Real-Time Monitoring of Ultrasound and Cavitation Mediated Drug Delivery

Shuning Bian

Linacre College

University of Oxford

Supervised by

Prof. Eleanor Stride

Dr. Robert Carlisle

November, 2016

Submitted to the Department of Engineering Science, University of Oxford, in fulfilment of the requirements for the degree of Doctor of Philosophy.

Statement of Originality

I hereby declare that this submission is my own work and, to the best of my knowledge, it contains no materials previously published or written by another person, or substantial proportions of material which have been accepted for the award of any other degree of diploma at the University of Oxford or any other educational institution, except where due acknowledgement is made in the thesis.

Any contribution made to the research by others, with whom I have worked at the University of Oxford or elsewhere, is explicitly acknowledged in the thesis.

I also declare that the intellectual content of this thesis is a product of my own work, except to the extent that assistance from others in the project's design and conception or in style, presentation and linguistic expression is acknowledged.

Shuning Bian

November 2016

Abstract

Drug delivery plays a crucial role in the chemotherapeutic treatment of cancerous solid tumours. A drug, no matter how potent, is only truly effective when it can be delivered to all targeted cells. In recent years it has been recognised that the poor response of tumours to chemotherapy is in part due to inadequate drug delivery. Numerous strategies have been developed to overcome this issue. Of particular interest to the present work is the application of ultrasound and cavitation, which has been shown to be capable of enhancing drug delivery in solid tumours. These enhancements are attributed to the acoustic cavitation of microbubbles and the effects cavitation induces in the surrounding tissue.

To better understand how ultrasound and cavitation can enhance drug delivery, an instrument was developed that is capable of monitoring in real-time and *in-situ* the effect of ultrasound and cavitation on drugs and drug analogues within flow channel models. The developed instrument was used to investigate the effect of ultrasound and cavitation on drug-eluting beads used for chemoembolisation, the effects of drug loading on microbubble dynamics, the effects produced by different cavitation agents, and the performance of passive acoustic mapping as a means of cavitation monitoring.

The findings of the above investigations include: more physiologically relevant characterisations of drug-eluting beads pharmacokinetics, the possibility of significant changes in microbubble dynamics due to drug loading, a lack of general correlation between detected cavitation activity and induced effects, and the potential of passive acoustic mapping for monitoring cavitation and ultrasound induced effects. These and other findings also demonstrate the utility of the developed instrument for studying the many facets and applications of ultrasound and cavitation mediated drug delivery.

Publications

In Publication

- Shuning Bian, Anjali Seth, Dan Daly, Robert Carlisle, and Eleanor Stride. A multimodal instrument for real-time *in situ* study of ultrasound and cavitation mediated drug delivery. *Review of Scientific Instruments*.

In Preparation

- Shuning Bian, Richard Browning, Dan Daly, Robert Carlisle, and Eleanor Stride. Effects of nanoparticle loading on microbubble dynamics.
- Shuning Bian, Erasmia Lyka, Dan Daly, Robert Carlisle, and Eleanor Stride. Concurrent real-time *in-situ* monitoring of cavitation activity and effect with confocal imaging and passive acoustic mapping.
- Shuning Bian, Marcus Caine, Yiqing Tang, Andrew Lewis, Dan Daly, Robert Carlisle, and Eleanor Stride. Real-time *in-situ* characterisation of DC and RO beads pharmacokinetic in vessel models.

Dedication

To my parents, 卞文锦 and 余冰影. This work would not have been possible without their countless sacrifices.

Acknowledgements

I would like to thank the members of BUBBL, past and present, for their friendship and advice. In particular, Dr Sunali Bhatnagar, Dr James Kwan, and Dr Jamie Collin for teaching me how to BUBBL; Dr Anjali Seth, Dr Luca Bau, and Anne Charlotte Van Blokland for meeting my unending demands for cavitation agents; Erasmia Lyka for a fruitful collaboration; and last but not least, Dr Richard Browning, for the many late nights and take away dinners.

I would also like to thank members of the IBME, especially the workshop technicians, Jim Fisk and David Salisbury. Not only did they manufacture many of my widgets they also taught me how to weld and change the tires on a bicycle.

To my external collaborators, sincere thanks for enriching my work. Specifically, Dr Kim Buttenschön, from Lein Applied Diagnostics (Reading, UK), for her assistance in instrument design and development; Marcus Caine, Dr Yiqing Tang, and Dr Andrew Lewis from Biocompatibles UK (Farnham, UK) for a productive partnership.

To my supervisors, Prof. Eleanor Stride and Prof. Robert Carlisle at BUBBL, and Dr Dan Daly from Lein Applied Diagnostics, I extend my deepest gratitude. They were my unfailing champions and guided me true. In particular, Prof. Stride always had time to answer my questions and ensured I never lost sight of the big picture.

Finally, to my family and friends, my heartfelt thanks for keeping me on a level keel. In particular, Nick Beeton for his mathematical insights and encouragements; and my wife, Ariella Adler, for leaving behind family, sunshine, and the possibility of pet cats to keep my heart warm in chilly England.

My research was supported by Lein Applied Diagnostics, Research Councils UK (Digital Economy Programme grant number EP/G036861/1), the National Centre for the Replacement Refinement and Reduction of Animals in Research, Linacre College

(EPA Cephalosporin Scholarship), and the Royal Commission for the Exhibition of 1851 (Industrial Fellowship 2014).

Errata

Due to typesetting errors the units µm and µM are rendered respectively as “um” and “uM” in all figures.

Table of Contents

List of Figures

List of Tables

Nomenclature

e_T	Fluorescence front displacement residual at the centre of the channel
S_C	Fluorescence front displacement at the centre of the channel
S_T	Fluorescence front displacement at the top of the channel
ACM	Agarose channel model
ADC	Analogue-to-digital converter
AFP	Actual focus position
ASF	Axial scaling factor
BVM	Bovine vessel model
CLSM	Confocal laser scanning microscopy
CPU	Central processing unit
DEB	Drug-eluting beads
DI	de-ionised
DLS	Dynamic light scattering
DOF	Depth of field
FOV	Field of view
FWHM	Full-width half-maximum
GPU	Graphics processing unit

GUI	Graphical user interface
HIFU	High-intensity focused-ultrasound
HSA	Human serum albumin
IFP	Interstitial fluid pressure
LSB	Least significant byte
MFM	Multiphoton fluorescence microscopy
MRI	Magnetic resonance imaging
MSB	Most significant byte
MTVM	Mouse tail vein model
MWCO	Molecular weight cut-off
NA	Numerical aperture
NFP	Nominal focus position
PAM	Passive acoustic mapping
PBS	Phosphate buffered saline
PCD	Passive cavitation detection
PMT	Photomultiplier tube
PRF	Pulse repetition frequency
PSF	Point spread function
RAM	Random access memory
RF	Radio-frequency
SLOC	Source lines of code
SPIM	Selective plane illumination microscopy
TACE	Transarterial chemoembolisation

Chapter 1

Introduction

Drug delivery plays a crucial role in the chemotherapeutic treatment of cancerous solid tumours. A drug, no matter how potent, is only truly effective when it can be delivered to all targeted cells. In recent years it has been recognised that the poor response of solid tumours to chemotherapy is in part due to the inadequate delivery of drugs within tumours [1, 2]. This difficulty arises primarily as a result of the tumour microenvironment.

1.1 Tumour Microenvironment

There are several reasons why the tumour microenvironment (Figure 1.1) plays a large role in determining drug penetration and cancer treatment efficacy. Firstly, due to their rapid rate of proliferation, tumours acquire their own vasculature through unregulated angiogenesis. Vessels so produced have poor pericyte coverage, and gaps between neighbouring endothelial cells have been shown to be as large as 1 to 8 µm [3, 4]. Combined with the collapse of interior lymphatic vessels that normally drain fluids away, the result is high interstitial fluid pressure (IFP) within the tumour [5], creating a pressure gradient that decreases towards the periphery. This pressure gradient retards the movement of drug molecules towards the core of a tumour, resulting in incomplete drug delivery [5–8].

The lack of functioning lymphatic vessels and high IFP at the core of a tumour also result in a hypoxic and acidic environment. This acidic environment is thought to

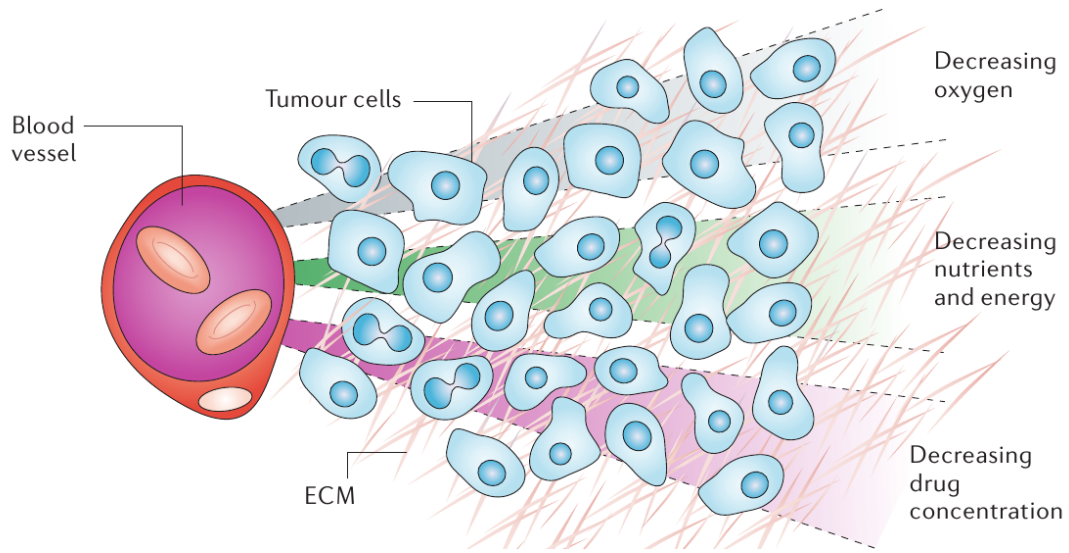

Figure 1.1: The tumour microenvironment, sourced from [2]. The concentration of drugs, oxygen, and nutrients rapidly decreases away from the vessels due to high IFP and dense ECM. As a result tumour cells distant from blood vessels are hypoxic and rarely exposed to drug molecules, leading to a poor response to treatment.

further impede the active transport of some drugs, such as methotrexate [9] and reduce the uptake of others, such as doxorubicin, mitoxantrone, and daunorubicin [10, 11].

Secondly, the extra-cellular matrix (ECM) expressed by tumours consists of collagens, proteoglycans, and other molecules that impede the movement of macromolecules, such as those used in gene and immunotherapy [12–14]. As a result, despite the "leaky" nature of tumour vasculature, cells distant from blood vessels do not readily encounter drug molecules [15]. For example, it has been reported that, in murine tumours, the concentration of doxorubicin drops to half its perivascular concentration at a distance of 40 to 50 µm from blood vessels, while the mean distance to hypoxic cells is between 90 to 140 µm [16]. Consequently, a large population of cancer cells are not exposed to a therapeutically relevant concentration of the drug.

It is worth mentioning that the hypoxic region at the core of a tumour is known to also directly affect the efficacy of drugs. Drugs such as cisplatin [17], doxorubicin [17] and methotrexate [17, 18] have been shown to be less effective against hypoxic cancer cells.

These features of the tumour microenvironment result in incomplete and inefficient drug delivery to tumours, jeopardise the success of chemotherapy treatments and adversely affect patient well-being and increase the cost of treatment.

1.2 Ultrasound and Cavitation Mediated Drug Delivery

Various strategies have been developed to counter the effects of the tumour microenvironment; for example using vascular endothelial growth factor (VEGF) blockade to achieve vascular normalisation [19–21], or dosing with glyceryl trinitrate to inhibit hypoxia induced resistance to doxorubicin [22]. Of particular interest in the present work is the application of ultrasound and cavitation, which has been shown to be capable of enhancing drug delivery in solid tumours [23–27]. These enhancements are attributed to the acoustic cavitation of microbubbles and the effects cavitation induces in the surrounding tissue.

Acoustic cavitation arises when a gas void, i.e. a bubble, within a fluid oscillates in response to a time-varying pressure, where during periods of compression the applied pressure is considered positive, and during periods of rarefaction the applied pressure is deemed negative. These oscillations give rise to various phenomena in the surrounding liquid and can be classified as either stable or inertial cavitation [28]. Stable cavitation occurs when bubbles oscillate around their equilibrium size, while inertial cavitation occurs when microbubbles expand to many times their initial size due to negative pressure, then violently collapse when positive pressure is applied[1]. Inertial cavitation is so called because the collapse of the bubble is dominated by the inertia of the surrounding medium. Whether cavitation takes place, and whether it is stable or inertial cavitation occurs depends on the driving frequency, the peak negative pressure experienced by the bubble, the size and composition of the microbubble, as well as the surrounding environment.

1.2.1 Microbubbles

In a medical context, cavitation in the human body is most often induced by introducing microbubbles into the body, which are gas bubbles less than 10 µm in diameter [29, 30]. To increase their longevity in the bloodstream, microbubbles are typically coated with a stabilising shell [29]. When driven at the right frequencies and pres-

[1] Despite the lack of a stable qualifier, inertial cavitation can also occur in a repeating "stable" manner.

sures, microbubbles undergo cavitation as described previously, producing a range of effects in its surrounding environment such as microstreaming [31, 32] and shockwaves [33, 34].

For a specific microbubble formulation within a given environment, there exists a range of ultrasound frequency and pressures for which cavitation activity, and therefore cavitation effect is maximised. The optimal parameters for different microbubble formulations can vary considerably such that the optimal settings for one formulation will not elicit any response from another.

1.2.2 Enhanced Permeability

The permeability of biological membranes can be temporarily enhanced by cavitation without long term damage, an effect that is variously referred to as sonoporation or sonophoresis, and encompasses a range of different processes. Sonoporation has been observed in many different tissues, such as the blood-brain-barrier [35], blood vessel walls [36, 37], and cell membranes [38–41]. The wide applicability of sonoporation makes it an attractive method for enhancing drug delivery.

The physical mechanisms underpinning sonoporation are not yet fully understood but are thought to be associated with cavitation induced effects such as microstreaming [31, 42, 43], microjets [33, 44], and shockwaves [33].

1.2.3 Microstreaming

Microstreaming is a phenomenon that occurs during both stable and inertial cavitation, whereby microbubbles create circulating flows in the surrounding fluid (Figure 1.2) as they oscillate in response to ultrasound [31, 32]. The shear stresses these flows impose on cells are predicted to be an order of magnitude (19 Pa vs 0.5–2 Pa) higher than those caused by normal circulation [45]. Evidence suggests that deformation of cell membranes due to microstreaming increases their permeability [42, 46, 47].

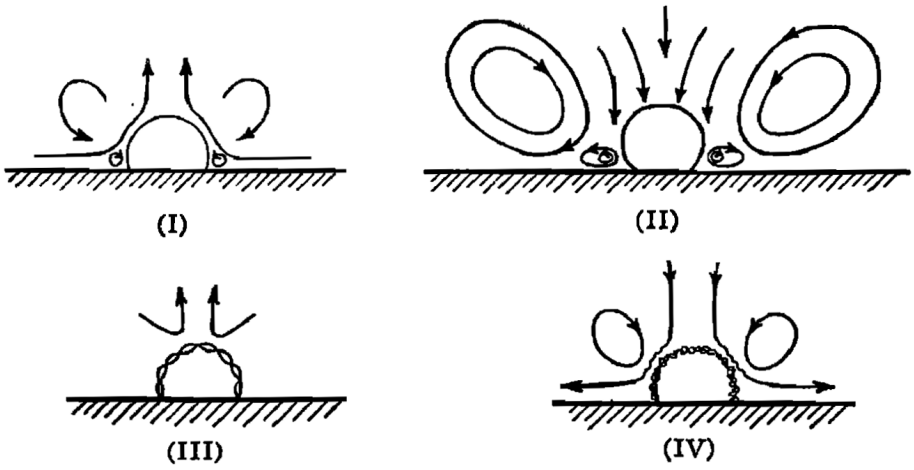

Figure 1.2: Microstreaming regimes of a microbubble near a surface [31]. The dominant regime depends on the viscosity of the surrounding fluid and the applied pressure.

1.2.4 Microjets

Microjets are produced when microbubbles collapse asymmetrically during inertial cavitation (Figure 1.3), typically near a boundary such as a blood vessel wall [33, 48, 49]. These jets are capable of inducing transient perforations in cell membranes [44, 50], and can also create pits in cells with diameters of up to 16 µm [51]. Both of these effects can increase the permeability of cells.

The direction of microjets, either towards or away from the boundary, is dependent on the boundary's elasticity [52]. In experiments with rat mesenteric microvessels, it has been observed that jetting occurs away from vessel walls [48].

1.2.5 Shockwaves

Shockwaves are produced whenever a microbubble collapses during inertial cavitation. These shockwaves exert enough pressure to damage the membrane of nearby cells, and may be an additional mechanism by which the permeability of cells are enhanced [33, 34]. It is noted, however, that much of the shockwave energy is dissipated within 100 µm of the bubble, and thus its effects will be localised [53].

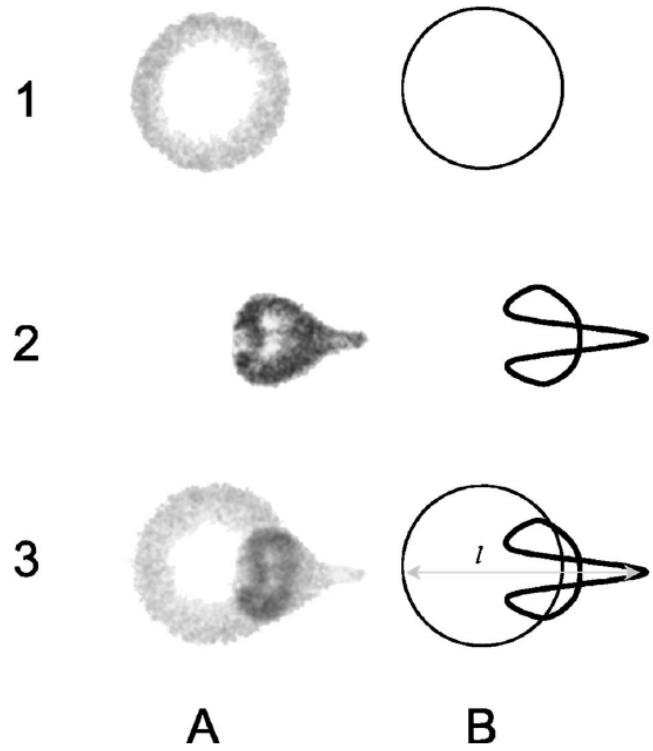

Figure 1.3: Microjetting of a single microbubble, sourced from [49]. Images A1 and A2 are high speed photographs of a microbubble before and after microjetting. A3 is a composite of A1 and A2. Images B1-B3 are schematic representations of A1-A3. The labelled distance l is 26 µm, and the elapsed time between A1 and A2 is 0.33 µs.

1.2.6 Acoustic Radiation Force

Acoustic radiation force is the force a particle experiences when it absorbs or scatters ultrasound [54], and can be decomposed into primary and secondary radiation forces. The primary radiation force is produced by the incident pressure field, and acts generally in the direction of ultrasound propagation [55]. It is capable of displacing and slowing microbubbles in blood vessels [55], as well as deforming tissue [56].

Oscillation of bubbles due to the incident pressure field produces a secondary pressure field, which gives rise to the secondary radiation force. Depending on the bubble size and the ultrasound frequency, secondary radiation force manifests as an attractive or repulsive force between bubbles [55].

1.3 Motivation

Due to its potential, the study of how drug delivery is affected by the interactions between ultrasound, cavitation and the surrounding tissue is an important and growing field of research. A particular difficulty is that while cavitation occurs at the microsecond scale and over distances measured in micrometres, it produces mechanical, biological and chemical responses that last from milliseconds to hours, affecting single cells as well as bulk tissue. For example, a microbubble can disrupt a cell's actin cytoskeleton within microseconds but the cell's response to the disruption can still be measured 40 minutes after the initiating event [41]. The multi-scale nature of these interactions necessitates the use of different monitoring and measurement techniques, each specialising in a particular range of time and length scales, in order to obtain a comprehensive understanding of ultrasound and cavitation mediated drug delivery.

Of particular interest to the current work is real-time monitoring during ultrasound exposure. Typically, the effects of ultrasound and cavitation on drug delivery are characterised only at the start and the end of an experiment, and while these endpoints can provide information on drug delivery, cellular uptake and cell destruction, the exact occurrences during ultrasound exposure can only be inferred. Therefore, a means of measuring in real-time the interactions between ultrasound, cavitation and drug delivery is necessary for a complete understanding of the underlying mechanisms.

1.4 Requirements

The present work aims to build an instrument capable of measuring in real-time and *in situ* the effects of ultrasound and cavitation on drug distribution within tissue mimicking flow channel models with minimal perturbation, and use it to study ultrasound and cavitation mediated drug delivery. For clinical relevance, the instrument should have a field of view on the order of hundreds to thousands of micrometres, comparable to the size of tumours, and to be ultrasound compatible, it must have a sufficiently large working distance to avoid interference with the ultrasound focus. For clinical high-intensity focused-ultrasound machines, the ultrasound focus has a $-3\,\mathrm{dB}$

Characteristic	Requirement
Working Distance	$\geq 15\,\text{mm}$
Field-of-view	$\geq 3\,\text{mm} \times 3\,\text{mm}$
Imaging Depth	$\geq 2\,\text{mm}$
Imaging Speed (3 mm × 3 mm FOV)	$\leq 30\,\text{s}$
Imaging Resolution (axial and lateral)	45 to 70 µm or better

Table 1.1: Design requirements of the new instrument.

contour with dimensions of 8 to 20 mm along the axis and 1 to 3 mm transversely at frequencies of 0.5 to 3 MHz[1]. Furthermore, the instrument should have an imaging depth of at least 2 mm to cope with flow channel models, and have a spatial resolution of at least 45 to 70 µm, sufficient to detect clinically significant improvements in drug penetration, and a temporal resolution of 30 s or better to capture the changes in drug distribution over time.

These desired instrument characteristics were translated into the design requirements tabulated in Table 1.1.

1.5 Chapter Overview

In the following chapters, Chapter 2 reviews imaging modalities that are, or could be, compatible with ultrasound with the goal of determining a suitable modality for the new instrument. Chapter 3 details the design and development of the instrument. Chapter 4 discusses the requirements for a suitable model to use with the instrument, and Chapter 5 describes common materials and methods. Chapters 6 to 9 presents the results of studies using the instrument into the pharmacokinetics of drug-eluting beads, the effect of nanoparticle loading on microbubble cavitation dynamics, the induced effects of different cavitation agents, and the efficacy of passive acoustic mapping. Finally, Chapter 10 summarise the current work and its contributions, and Chapter 11 presents proposals for future research and development.

[1] At these frequencies ultrasound exposure is not expected to interfere with imaging.

References

[1] Olivier Trédan, Carlos M Galmarini, Krupa Patel, and Ian F Tannock. Drug resistance and the solid tumor microenvironment. *Journal of the National Cancer Institute*, 99(19):1441–1454, 2007.

[2] Andrew I Minchinton and Ian F Tannock. Drug penetration in solid tumours. *Nature Reviews Cancer*, 6(8):583–592, 2006.

[3] Hiroya Hashizume, Peter Baluk, Shunichi Morikawa, John W McLean, Gavin Thurston, Sylvie Roberge, Rakesh K Jain, and Donald M McDonald. Openings between defective endothelial cells explain tumor vessel leakiness. *The American journal of pathology*, 156(4):1363–1380, 2000.

[4] Susan K Hobbs, Wayne L Monsky, Fan Yuan, W Gregory Roberts, Linda Griffith, Vladimir P Torchilin, and Rakesh K Jain. Regulation of transport pathways in tumor vessels: role of tumor type and microenvironment. *Proceedings of the National Academy of Sciences*, 95(8):4607–4612, 1998.

[5] Carl-Henrik Heldin, Kristofer Rubin, Kristian Pietras, and Arne Östman. High interstitial fluid pressure—an obstacle in cancer therapy. *Nature Reviews Cancer*, 4(10):806–813, 2004.

[6] Rakesh K Jain. Delivery of molecular and cellular medicine to solid tumors. *Advanced drug delivery reviews*, 64:353–365, 2012.

[7] Michael F Milosevic, Anthony W Fyles, Raimond Wong, Melania Pintilie, Mary-Claire Kavanagh, Wilfred Levin, Lee A Manchul, Thomas J Keane, and Richard P Hill. Interstitial fluid pressure in cervical carcinoma. *Cancer*, 82(12):2418–2426, 1998.

[8] Yves Boucher, Laurence T Baxter, and Rakesh K Jain. Interstitial pressure gradients in tissue-isolated and subcutaneous tumors: implications for therapy. *Cancer research*, 50(15):4478–4484, 1990.

[9] David SM Cowan and Ian F Tannock. Factors that influence the penetration of methotrexate through solid tissue. *International journal of cancer*, 91(1):120–125, 2001.

[10] Leo E Gerweck, Shashirekha Vijayappa, and Sergey Kozin. Tumor pH controls the in vivo efficacy of weak acid and base chemotherapeutics. *Molecular cancer therapeutics*, 5(5):1275–1279, 2006.

[11] Brent P Mahoney, Natarajan Raghunand, Brenda Baggett, and Robert J Gillies. Tumor acidity, ion trapping and chemotherapeutics: I. Acid pH affects the distribution of chemotherapeutic agents in vitro. *Biochemical pharmacology*, 66(7):1207–1218, 2003.

[12] Paolo A Netti, David A Berk, Melody A Swartz, Alan J Grodzinsky, and Rakesh K Jain. Role of extracellular matrix assembly in interstitial transport in solid tumors. *Cancer research*, 60(9):2497–2503, 2000.

[13] C de L Davies, DA Berk, A Pluen, and RK Jain. Comparison of IgG diffusion and extracellular matrix composition in rhabdomyosarcomas grown in mice versus in vitro as spheroids reveals the role of host stromal cells. *British journal of cancer*, 86(10):1639–1644, 2002.

[14] Edward Brown, Trevor McKee, et al. Dynamic imaging of collagen and its modulation in tumors in vivo using second-harmonic generation. *Nature medicine*, 9(6):796–800, 2003.

[15] Ian F Tannock, Carol M Lee, Jonathon K Tunggal, David SM Cowan, and Merrill J Egorin. Limited penetration of anticancer drugs through tumor tissue a potential cause of resistance of solid tumors to chemotherapy. *Clinical cancer research*, 8(3):878–884, 2002.

[16] Andrew J Primeau, Augusto Rendon, David Hedley, Lothar Lilge, and Ian F Tannock. The distribution of the anticancer drug Doxorubicin in relation to blood vessels in solid tumors. *Clinical Cancer Research*, 11(24):8782–8788, 2005.

[17] Xianrang Song, Xianxi Liu, Weiling Chi, Yonglei Liu, Ling Wei, Xingwu Wang, and Jinming Yu. Hypoxia-induced resistance to cisplatin and doxorubicin in non-small cell lung cancer is inhibited by silencing of HIF-1α gene. *Cancer chemotherapy and pharmacology*, 58(6):776–784, 2006.

[18] Kirsten Sanna and Einar K Rofstad. Hypoxia-induced resistance to doxorubicin and methotrexate in human melanoma cell lines in vitro. *International journal of cancer*, 58(2):258–262, 1994.

[19] Peter Carmeliet and Rakesh K Jain. Principles and mechanisms of vessel normalization for cancer and other angiogenic diseases. *Nature reviews Drug discovery*, 10(6):417–427, 2011.

[20] Christopher G Willett, Yves Boucher, Emmanuelle Di Tomaso, Dan G Duda, Lance L Munn, Ricky T Tong, Daniel C Chung, Dushyant V Sahani, Sanjeeva P Kalva, Sergey V Kozin, et al. Direct evidence that the VEGF-specific antibody bevacizumab has antivascular effects in human rectal cancer. *Nature medicine*, 10(2):145–147, 2004.

[21] Rakesh K Jain. Normalization of tumor vasculature: an emerging concept in antiangiogenic therapy. *Science*, 307(5706):58–62, 2005.

[22] Lisa J Frederiksen, D Robert Siemens, Jeremy P Heaton, Lori R Maxwell, Michael A Adams, and Charles H Graham. Hypoxia induced resistance to doxorubicin in prostate cancer cells is inhibited by low concentrations of glyceryl trinitrate. *The Journal of urology*, 170(3):1003–1007, 2003.

[23] IV Larina, BM Evers, TV Ashitkov, C Bartels, KV Larin, and RO Esenaliev. Enhancement of drug delivery in tumors by using interaction of nanoparticles with ultrasound radiation. *Technology in cancer research & treatment*, 4(2):217, 2005.

[24] Miriam Bazan-Peregrino, Bassel Rifai, Robert C Carlisle, James Choi, Costas D Arvanitis, Leonard W Seymour, and Constantin C Coussios. Cavitation-enhanced delivery of a replicating oncolytic adenovirus to tumors using focused ultrasound. *Journal of Controlled Release*, 169(1):40–47, 2013.

[25] Siv Eggen, Stein-Martin Fagerland, Ýrr Mørch, Rune Hansen, Kishia Søvik, Sigrid Berg, Håkon Furu, Audun Dybvik Bøhn, Magnus B Lilledahl, Anders Angelsen, et al. Ultrasound-enhanced drug delivery in prostate cancer xenografts by nanoparticles stabilizing microbubbles. *Journal of Controlled Release*, 187:39–49, 2014.

[26] Ralf Seip, Chien Ting Chin, Christopher S Hall, Balasundar I Raju, Alexander Ghanem, and Klaus Tiemann. Targeted ultrasound-mediated delivery of nanoparticles: on the development of a new HIFU-based therapy and imaging device. *Biomedical Engineering, IEEE Transactions on*, 57(1):61–70, 2010.

[27] Steven Mo, Constantin-C Coussios, Len Seymour, and Robert Carlisle. Ultrasound-enhanced drug delivery for cancer. *Expert opinion on drug delivery*, 9(12):1525–1538, 2012.

[28] Constantin C Coussios and Ronald A Roy. Applications of acoustics and cavitation to noninvasive therapy and drug delivery. *Annu. Rev. Fluid Mech.*, 40:395–420, 2008.

[29] E Stride and N Saffari. Microbubble ultrasound contrast agents: a review. *Proceedings of the Institution of Mechanical Engineers, Part H: Journal of Engineering in Medicine*, 217(6):429–447, 2003.

[30] SR Sirsi and MA Borden. Microbubble compositions, properties and biomedical applications. *Bubble Science, Engineering & Technology*, 1(1-2):3–17, 2009.

[31] Samuel A Elder. Cavitation microstreaming. *The Journal of the Acoustical Society of America*, 31:54, 1959.

[32] Junru Wu and Wesley L Nyborg. Ultrasound, cavitation bubbles and their interaction with cells. *Advanced drug delivery reviews*, 60(10):1103–1116, 2008.

[33] EA Brujan, T Ikeda, and Y Matsumoto. Jet formation and shock wave emission during collapse of ultrasound-induced cavitation bubbles and their role in the therapeutic applications of high-intensity focused ultrasound. *Physics in medicine and biology*, 50(20):4797, 2005.

[34] Tetsuya KODAMA, Yukio TOMITA, Yukiko WATANABE, Kenichiro KOSHIYAMA, Takeru YANO, and Shigeo FUJIKAWA. Cavitation bubbles mediated molecular delivery during sonoporation. *Journal of Biomechanical Science and Engineering*, 4(1):124–140, 2009.

[35] Feng-Yi Yang, Yu-Shi Lin, Kai-Hsiang Kang, and Tai-Kuang Chao. Reversible blood–brain barrier disruption by repeated transcranial focused ultrasound allows enhanced extravasation. *Journal of Controlled Release*, 150(1):111–116, 2011.

[36] Danny M Skyba, Richard J Price, Andre Z Linka, Thomas C Skalak, and Sanjiv Kaul. Direct in vivo visualization of intravascular destruction of microbubbles by ultrasound and its local effects on tissue. *Circulation*, 98(4):290–293, 1998.

[37] MR Böhmer, CHT Chlon, BI Raju, CT Chin, T Shevchenko, and AL Klibanov. Focused ultrasound and microbubbles for enhanced extravasation. *Journal of Controlled Release*, 148(1):18–24, 2010.

[38] Annemieke Van Wamel, Klazina Kooiman, Miranda Harteveld, Marcia Emmer, Folkert J Ten Cate, Michel Versluis, and Nico De Jong. Vibrating microbubbles poking individual cells: drug transfer into cells via sonoporation. *Journal of controlled release*, 112(2):149–155, 2006.

[39] Sophie Mehier-Humbert, Thierry Bettinger, Feng Yan, and Richard H Guy. Plasma membrane poration induced by ultrasound exposure: implication for drug delivery. *Journal of controlled release*, 104(1):213–222, 2005.

[40] Cheri X Deng, Fred Sieling, Hua Pan, and Jianmin Cui. Ultrasound-induced cell membrane porosity. *Ultrasound in medicine & biology*, 30(4):519–526, 2004.

[41] Xian Chen, Ruen Shan Leow, Yaxin Hu, Jennifer MF Wan, and CH Alfred. Single-site sonoporation disrupts actin cytoskeleton organization. *Journal of The Royal Society Interface*, 11(95):20140071, 2014.

[42] Philippe Marmottant and Sascha Hilgenfeldt. Controlled vesicle deformation and lysis by single oscillating bubbles. *Nature*, 423(6936):153–156, 2003.

[43] WL Nyborg. Ultrasonic microstreaming and related phenomena. *The British journal of cancer. Supplement*, 5:156, 1982.

[44] Claus-Dieter Ohl, Manish Arora, Roy Ikink, Nico de Jong, Michel Versluis, Michael Delius, and Detlef Lohse. Sonoporation from jetting cavitation bubbles. *Biophysical journal*, 91(11):4285–4295, 2006.

[45] Anthony Novell, James Collis, Alexander A Doinikov, Andrew Ooi, Richard Manasseh, and Ayache Bouakaz. Theoretical and experimental evaluation of microstreaming created by a single microbubble: Application to sonoporation. In *Ultrasonics Symposium (IUS), 2011 IEEE International*, pages 1482–1485. IEEE, 2011.

[46] Nilanjana Bose, Dario Carugo, Tapas Kumar Maiti, Xunli Zhang, and Suman Chakraborty. The role of cell membrane strain in sonoporation characterised by microfluidic-based single-cell analysis. In *15th International Conference on Miniaturized Systems for Chemistry and Life Sciences. Seattle, Washington, USA*, pages 1743–5, 2011.

[47] Seyedeh Moosavi Nejad, S Hamid R Hosseini, Hidenori Akiyama, and Katsuro Tachibana. Optical observation of cell sonoporation with low intensity ultrasound. *Biochemical and biophysical research communications*, 413(2):218–223, 2011.

[48] Hong Chen, Andrew A Brayman, Wayne Kreider, Michael R Bailey, and Thomas J Matula. Observations of translation and jetting of ultrasound-activated microbubbles in mesenteric microvessels. *Ultrasound in medicine & biology*, 37(12):2139–2148, 2011.

[49] Michiel Postema, Annemieke van Wamel, J Folkert, and Nico de Jong. High-speed photography during ultrasound illustrates potential therapeutic applications of microbubbles. *Medical physics*, 32(12):3707–3711, 2005.

[50] Nobuki Kudo, Kengo Okada, and Katsuyuki Yamamoto. Sonoporation by single-shot pulsed ultrasound with microbubbles adjacent to cells. *Biophysical journal*, 96(12):4866–4876, 2009.

[51] Paul Prentice, Alfred Cuschieri, Kishan Dholakia, Mark Prausnitz, and Paul Campbell. Membrane disruption by optically controlled microbubble cavitation. *Nature Physics*, 1(2):107–110, 2005.

[52] Emil-Alexandru Brujan, Kester Nahen, Peter Schmidt, and Alfred Vogel. Dynamics of laser-induced cavitation bubbles near an elastic boundary. *Journal of Fluid Mechanics*, 433:251–281, 2001.

[53] EA Brujan, T Ikeda, and Y Matsumoto. On the pressure of cavitation bubbles. *Experimental Thermal and Fluid Science*, 32(5):1188–1191, 2008.

[54] GR Torr. The acoustic radiation force. *American Journal of Physics*, 52(5):402–408, 1984.

[55] Paul Dayton, Alexander Klibanov, Gary Brandenburger, and Kathy Ferrara. Acoustic radiation force< i> in vivo: a mechanism to assist targeting of microbubbles. *Ultrasound in medicine & biology*, 25(8):1195–1201, 1999.

[56] Kathryn Nightingale, Mary Scott Soo, Roger Nightingale, and Gregg Trahey. Acoustic radiation force impulse imaging: in vivo demonstration of clinical feasibility. *Ultrasound in medicine & biology*, 28(2):227–235, 2002.

Chapter 2

Literature Review

2.1 Introduction

This chapter reviews published imaging modalities that have been, or could be, used concurrently with ultrasound for real-time *in situ* monitoring. Of particular interest are modalities will minimally affect ultrasound delivery while also satisfying the requirements of a long working distance ($\geq$ 15 mm), a large field of view ($\geq$ 3 mm $\times$ 3 mm), and an imaging depth of $\geq$ 2 mm.

2.2 Widefield Microscopy

Widefield microscopy, both light and fluorescence, has been used in ultrasound compatible setups to study microbubble dynamics [1], cavitation mediated drug delivery [2], and effects of cavitation on cells [3–7] and blood vessels [8, 9]. Typically, a widefield microscope is modified to accommodate a small water tank in which ultrasound transducers and samples are placed. High speed cameras (18,000 to 250,000 frames per second) are then used to enable real-time monitoring during ultrasound exposure. Both upright (Figure 2.1) and inverted (Figure 2.2) microscopes can be used, with upright microscopes having the advantage of being able to use water-immersion objectives and thereby eliminating the air-tank-water optical interfaces.

In addition to standard upright and inverted microscopes, long-distance microscopes have also been used, achieving working distances of up to 120 mm in air (Figure

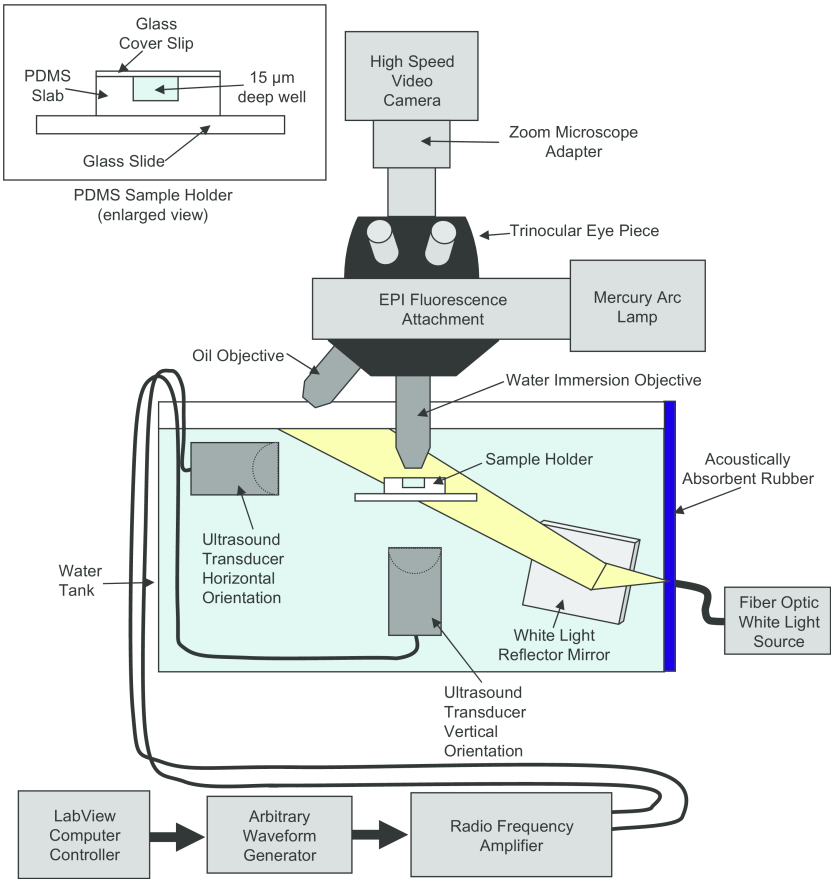

Figure 2.1: A modified upright microscope for real-time monitoring of interactions between focused ultrasound, echogenic drug delivery vehicles, and live cell membranes [2].

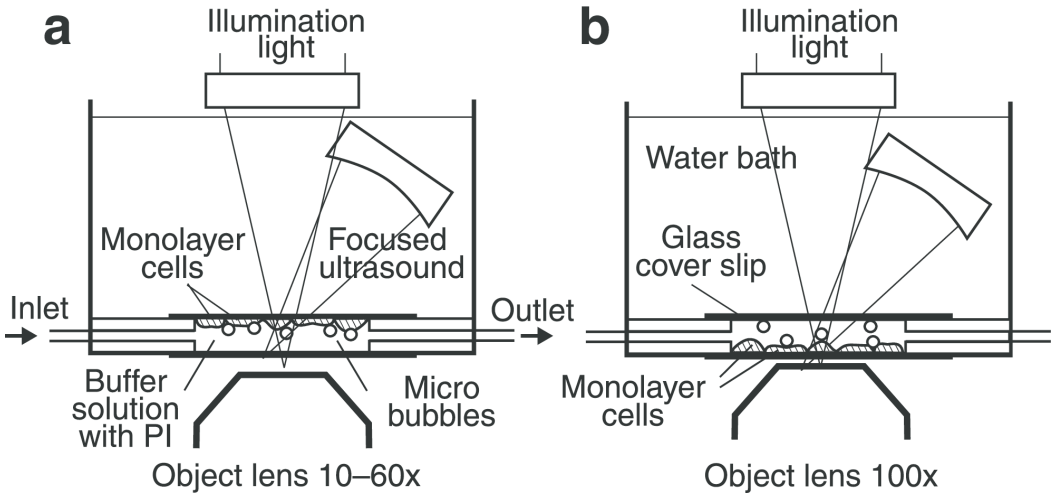

Figure 2.2: A modified inverted microscope for real-time monitoring of sonoporation of cells by adjacent microbubbles [3]. **(a)** imaging with a $10-60\times$ objective **(b)** imaging with a $100\times$ objective.

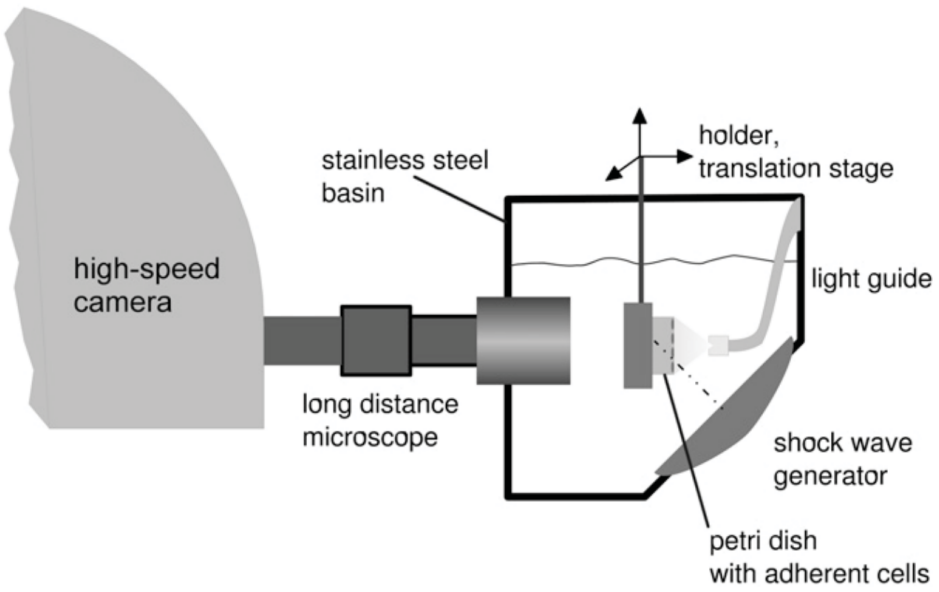

Figure 2.3: A long-distance microscope for real-time monitoring of sonoporation via jetting [10]. The high-speed camera in this setup allows imaging of bubble cavitation dynamics such as jetting.

2.3) [10].

While light microscopy cannot directly visualise drug molecules, using fluorescence microscopy it is possible to detect and measure, with a high degree of accuracy, the distribution and concentration of drugs that are fluorescent or have been fluorescently tagged.

The major limitation of widefield microscopy is the lack of optical sectioning capability, restricting observable samples to cell monolayers or thin tissue sections. This limitation is present in the studies cited here and is addressed by confocal, multi-photon and selective plane illumination microscopy.

2.3 Confocal Microscopy

Confocal microscopy is a technique that achieves good optical sectioning by using pinholes to eliminate light from outside the focal plane. As shown in Figure 2.4, light from the focal plane comes to a focus at the pinhole and passes through unimpeded, while light from out-of-focus planes comes to a focus before or after the pinhole, and is stopped. Consequently, confocal microscopy has excellent optical sectioning capability compared to widefield microscopy, and is capable of imaging within thick samples.

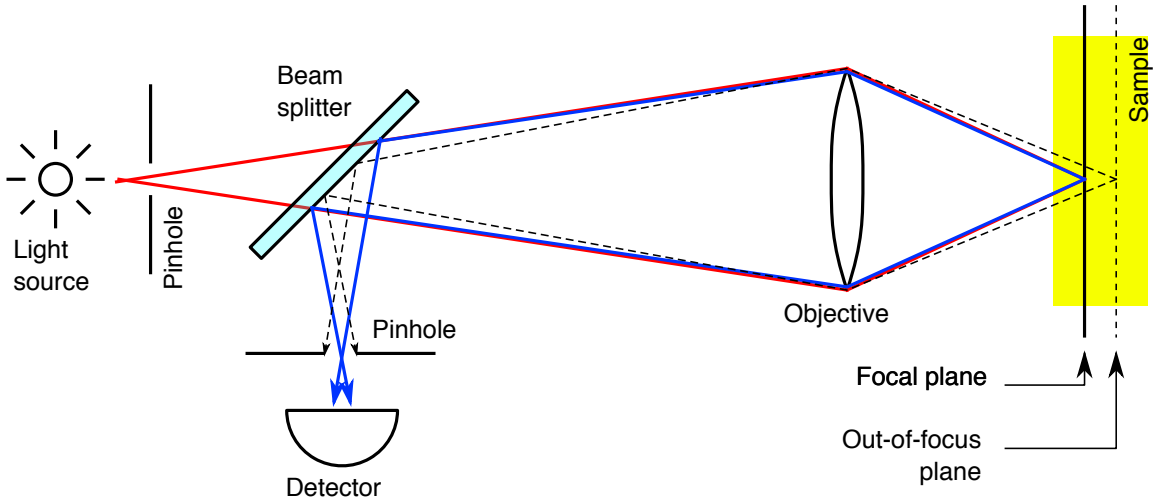

Figure 2.4: Principles of confocal microscopy. Light from the focal plane comes to a focus at the pinhole and passes through to the detector, while light from elsewhere is blocked.

Because the effective field-of-view of a confocal microscope is point-like, raster scanning is required to produce an image similar to that of a widefield microscope. Both scattered light and fluorescence imaging are possible with confocal microscopes.

High intensity light sources are required in confocal microscopy as most of the light from the sample, either backscattered or fluorescence, is blocked by the pinhole. Modern confocal microscopes make use of lasers, which provide high optical power output in a compact form factor. This technique is referred to as confocal laser scanning microscopy (CLSM).

Confocal microscopes with long working distances between 10 to 40 mm have been reported [11–13].

The major disadvantages of confocal microscopy are the longer image acquisition time and the side-effects of high intensity illumination, e.g. photobleaching and phototoxicity.

2.4 Multiphoton Fluorescence Microscopy

Multiphoton fluorescence microscopy (MFM) is a microscopy technique that exploits that fact that when certain fluorophores absorb two photons simultaneously (within 10^{-18} second [14]), they behave as if they had absorbed a single photon with half the

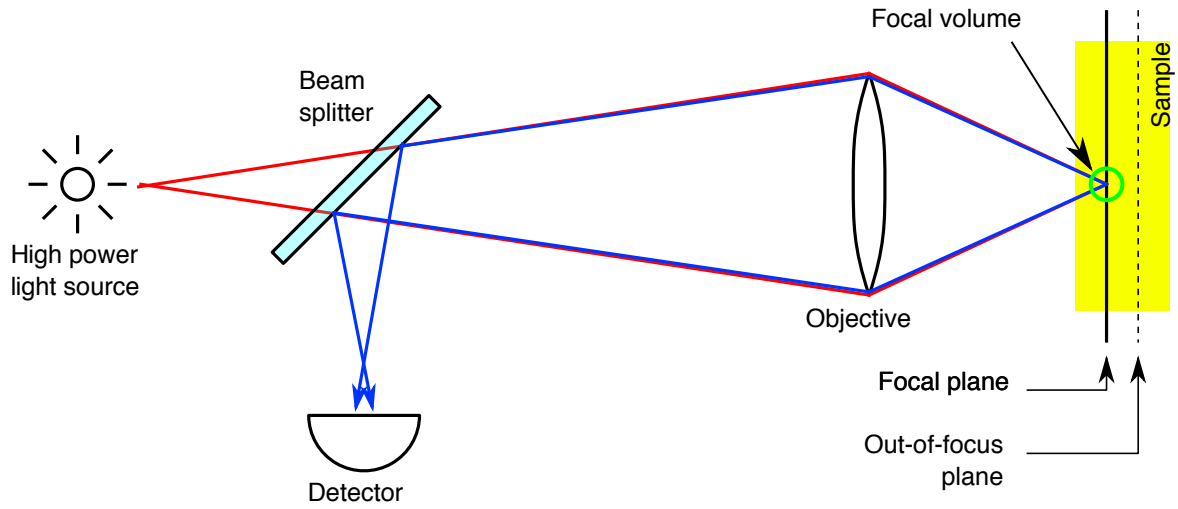

Figure 2.5: Principles of MFM microscopy. Fluorescence is effectively only generated from within the focal volume as photon flux elsewhere is insufficient for appreciable two-photon absorption.

wavelength, producing a fluorescence signal.

A typical MFM features the components shown in Figure 2.5. MFMs require a high intensity light source (much higher than in CLSM) to produce the necessary photon flux to facilitate two-photon absorption. Because the probability of two-photon absorption scales with the square of intensity, effectively only fluorophores at the focus are excited, resulting in excellent optical sectioning comparable to that achieved by confocal microscopy without the need for spatial filtering via pinholes.

MFM has a number of advantages compared to confocal microscopy. Firstly, the excitation wavelength of MFM, for the same fluorophore, is twice that used in confocal microscopy, as each photon only needs to carry half the excitation energy. Consequently, MFM excitation wavelengths are typically in the near-infrared, which is subject to less scattering and absorption by tissue, allowing for deeper sectioning of samples. Secondly, effects of scattering are reduced in MFM because fluorescence is only produced at the focus (Figure 2.6a), and the "haze" that scattering creates in confocal microscopy is not present (Figure 2.6b), resulting in better image contrast. Lastly, photobleaching and phototoxicity are reduced because fluorescence occurs only within the focal plane.

The disadvantages of MFM include the increased likelihood of sample heating as a result of high intensity illumination with near-infrared photons, and the need for light

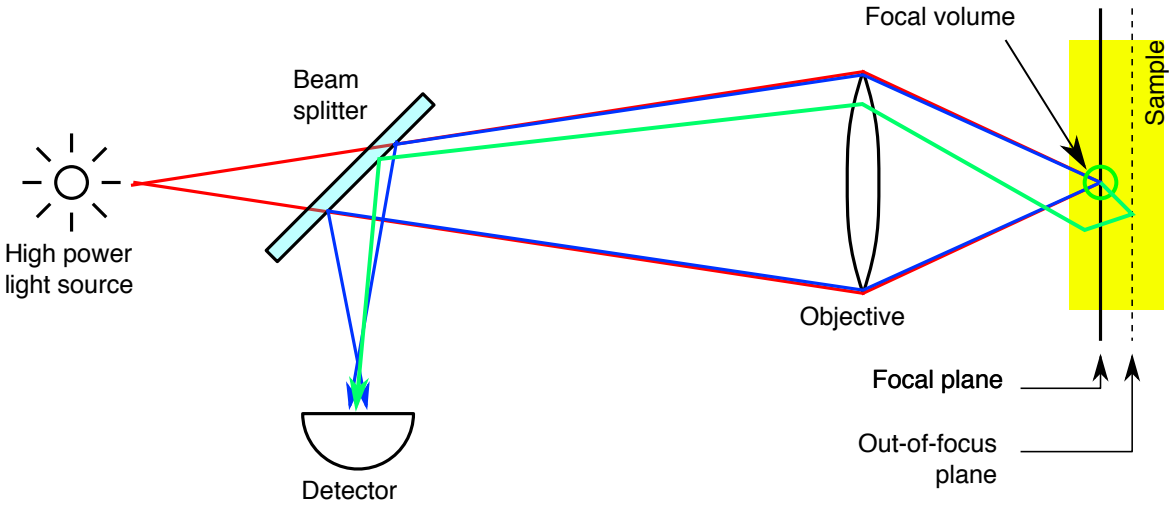

(a)

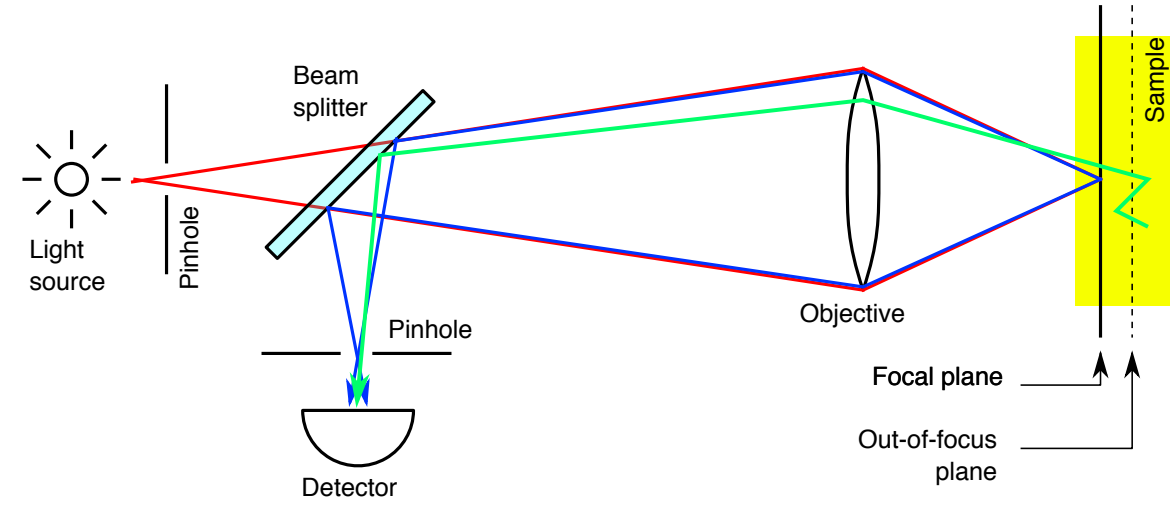

(b)

Figure 2.6: Effect of scattering on **(a)** MFM **(b)** confocal microscopy. In confocal microscopes scattering allows fluorescence from out-of-focus planes to reach the detector, reducing the contrast of images. In comparison, scattering has little effect on MFM as fluorescence emission only occurs at the focal volume.

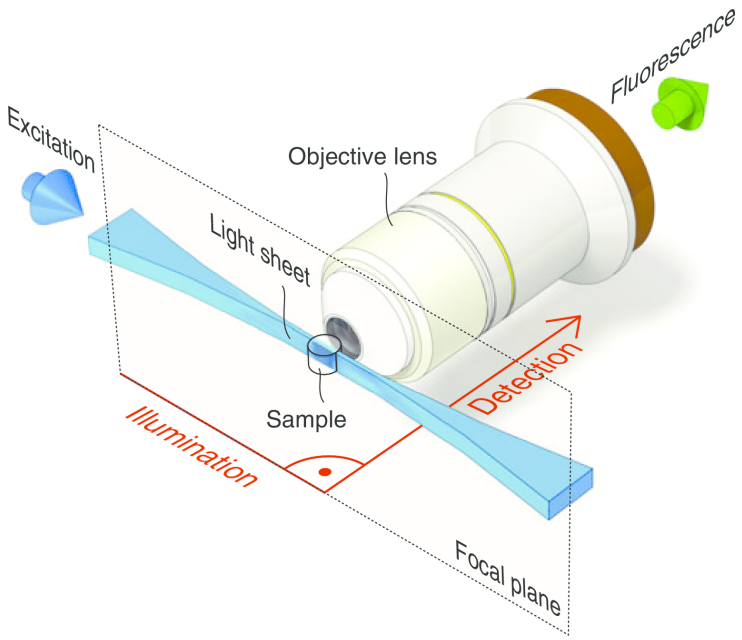

Figure 2.7: Principle of selective plane illumination microscopy [15]. A light-sheet, generated orthogonally to the detection axis, is used to illuminate the focal plane of the objective within the sample. This restricts fluorescence emission to the focal plane, providing optical sectioning capabilities whilst allowing for widefield imaging.

sources capable of generating the necessary photon flux. Typically, such light sources are substantially more expensive than what is required for CLSM and demand more stringent safety measures due to their output power and wavelength.

2.5 Selective Plane Illumination Microscopy

Selective plane illumination microscopy (SPIM) is a fluorescence microscopy technique that uses a light-sheet to illuminate only the focal plane of the imaging objective (Figure 2.7), providing optical sectioning in a manner similar MFM. Unlike MFM however, SPIM does not require raster scanning to form an image, as the whole of the visible focal plane is illuminated, allowing for instantaneous image formation.

Compared to MFM and CLSM, SPIM has comparable optical sectioning capabilities [16] and faster image acquisition. Due to its use of selective illumination, SPIM produces less photobleaching and phototoxicity than CLSM.

The main drawbacks of SPIM are its relative immaturity compared to CLSM and MFM, and its use of two orthogonal objectives for illumination and detection. The former increases the technical expertise required for a custom instrument, and the lat-

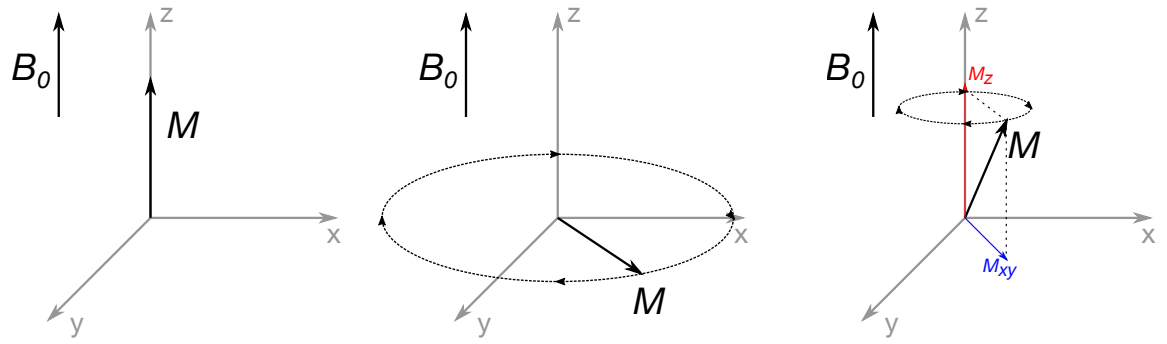

(a) (b) (c)

Figure 2.8: Principle of magnetic resonance imaging. (a) The macroscopic magnetisation vector M is aligned with the static magnetic field B_0 (b) M is deflected away from B_0 and into the x-y plane by the application of a time-varying magnetic field perpendicular to B_0 (c) M_{xy} continues to rotate about B_0 after removal of the time-varying magnetic field while M_z is stationary.

ter complicates integration with ultrasound equipment by requiring an additional window into the focus area.

2.6 Magnetic Resonance Imaging

Magnetic resonance imaging (MRI) is a non-ionising imaging technique that exploits nuclear magnetic resonance to detect the presence of various nuclei, typically hydrogen, within the human body. The process of MRI involves imposing a strong static magnetic field, B_0, on the sample, which causes the nuclear magnetic moments of affected nuclei to align themselves with the imposed field, resulting in a net nuclear magnetisation vector, M, that is aligned with B_0 (Figure 2.8a). In order to form an image, a time-varying magnetic field perpendicular to B_0 is created by applying a radio-frequency (RF) pulse to an RF coil. When the frequency of this time-varying magnetic field corresponds to the resonant frequency of the system, it causes the net magnetic moment M to deflect away from B_0 and rotate in the x-y plane (Figure 2.8b). When the RF pulse ceases, M begins to realign itself with B_0. In this state M_z is stationary while M_{xy} precesses about B_0 (Figure 2.8c). The rotation of M_{xy} is analogous to that of a rotating bar magnet, and will therefore induce a voltage in nearby coils. It is this induced voltage that is detected as the magnet resonance signal. Eventually, M will realign itself completely with B_0 and the induced voltage will go to zero [17]. By varying the ap-

plied RF pulse, the static magnetic field B_0, and measuring how the detected voltages decay over time, the location and type of different nuclei can be determined [18].

The spatial resolution of MRI depends on the strength and steepness of the generated magnetic field gradient, the sensitivity of detectors, and the number of phase-encoding steps. In magnetic resonance microscopy, it ranges from tens to hundreds of micrometres [19], while clinical MRI images have resolutions ranging from hundreds of micrometres to millimetres [20]. As spatial resolution increases, the amount of time required for phase-encoding also increases, resulting in a longer image acquisition time and therefore a lower temporal resolution. For example, with an acquisition time of 13 ms, a spatial resolution of 4.1 mm can be achieved. If the acquisition time is increased to 27 ms, then a spatial resolution of 2.6 mm is possible [21].

MRI has been used to measure *in-vivo* the concentration of liposomes containing both doxorubicin and an MRI contrast agent [22], and it is possible to use MRI and ultrasound concurrently by using MRI compatible ultrasound transducers [23–25]. The main disadvantages of MRI are the substantial purchase and running costs.

2.7 Evaluation

Amongst the modalities reviewed here, only widefield microscopy and MRI have been used concurrently with ultrasound. Of the remainder, only CLSM instruments currently feature a working distance in the desired range of 10 to 30 mm. While SPIM and MFM offer the best optical sectioning capability, no current system features a long working distance.

Ideally, the modality with the most advantageous characteristics is implemented, and of the modalities reviewed here, SPIM offers the best combination of good optical sectioning, fast image acquisition, and low photobleaching and phototoxicity. Realistically, however, the capabilities of each modality must also be weighed against the time and resources available, as well as the risks of attempting a wholly new configuration. Against these considerations, CLSM has a particular advantage due to the availability of the F410 [13, 26], an existing bench-top instrument with a long working distance, enabling accurate and realistic evaluation of CLSM's compatibility with intended ul-

trasound setups, its performance under anticipated experimental conditions, and the cost and technical difficulty of implementation.

The F410 was evaluated over a three month period. It was found to be ultrasound compatible and with sufficient resolution to detect the effects of interest. More importantly, it was determined that an instrument based on the F410 could be implemented with the time, resources, technical expertise available. These findings led to the decision to adopt CLSM as the imaging modality for the new instrument despite MFM and SPIM potentially offering superior performance.

References

[1] V Garbin, D Cojoc, Enrico Ferrari, E Di Fabrizio, MLJ Overvelde, SM Van Der Meer, N De Jong, D Lohse, and M Versluis. Changes in microbubble dynamics near a boundary revealed by combined optical micromanipulation and high-speed imaging. *Applied physics letters*, 90(11):114103, 2007.

[2] Stuart Ibsen, Michael Benchimol, and Sadik Esener. Fluorescent microscope system to monitor real-time interactions between focused ultrasound, echogenic drug delivery vehicles, and live cell membranes. *Ultrasonics*, 53(1):178–184, 2013.

[3] Nobuki Kudo, Kengo Okada, and Katsuyuki Yamamoto. Sonoporation by single-shot pulsed ultrasound with microbubbles adjacent to cells. *Biophysical journal*, 96(12):4866–4876, 2009.

[4] Paul A Dayton, James E Chomas, Aaron FH Lum, John S Allen, Jonathan R Lindner, Scott I Simon, and Kathy W Ferrara. Optical and acoustical dynamics of microbubble contrast agents inside neutrophils. *Biophysical Journal*, 80(3):1547–1556, 2001.

[5] B Wolfrum, R Mettin, T Kurz, and W Lauterborn. Observations of pressure-wave-excited contrast agent bubbles in the vicinity of cells. *Applied physics letters*, 81(26):5060–5062, 2002.

[6] Kengo Okada, Nobuki Kudo, Koichi Niwa, and Katsuyuki Yamamoto. A basic study on sonoporation with microbubbles exposed to pulsed ultrasound. *Journal of Medical Ultrasonics*, 32(1):3–11, 2005.

[7] Larisa A Kuznetsova, Sanjay Khanna, Nazar N Amso, W Terence Coakley, and Alexander A Doinikov. Cavitation bubble-driven cell and particle behavior in an ul-

trasound standing wave. *The Journal of the Acoustical Society of America*, 117(1):104–112, 2005.

[8] Hong Chen, Andrew A Brayman, Michael R Bailey, and Thomas J Matula. Blood vessel rupture by cavitation. *Urological research*, 38(4):321–326, 2010.

[9] Hong Chen, Andrew A Brayman, Wayne Kreider, Michael R Bailey, and Thomas J Matula. Observations of translation and jetting of ultrasound-activated microbubbles in mesenteric microvessels. *Ultrasound in medicine & biology*, 37(12):2139–2148, 2011.

[10] Claus-Dieter Ohl, Manish Arora, Roy Ikink, Nico de Jong, Michel Versluis, Michael Delius, and Detlef Lohse. Sonoporation from jetting cavitation bubbles. *Biophysical journal*, 91(11):4285–4295, 2006.

[11] Robert H Webb and Fran Rogomentich. Confocal microscope with large field and working distance. *Applied optics*, 38(22):4870–4875, 1999.

[12] Thomas D Wang, Michael J Mandella, Christopher H Contag, and Gordon S Kino. Dual-axis confocal microscope for high-resolution in vivo imaging. *Optics letters*, 28(6):414–416, 2003.

[13] Kim-Kristin Buttenschon. *A novel fluorophotometer for measuring concentration and diffusion of autofluorescent ophthalmic medication in the human eye*. PhD thesis, Durham University, 2013.

[14] Richard KP Benninger and David W Piston. Two-photon excitation microscopy for the study of living cells and tissues. *Current protocols in cell biology*, pages 4–11, 2013.

[15] Jan Huisken and Didier YR Stainier. Selective plane illumination microscopy techniques in developmental biology. *Development*, 136(12):1963–1975, 2009.

[16] Peter A Santi. Light sheet fluorescence microscopy a review. *Journal of Histochemistry & Cytochemistry*, 59(2):129–138, 2011.

[17] William E Brant and Eduard E de Lange. *Essentials of Body MRI*. OUP USA, 2012.

[18] Dominik Weishaupt, JM Froehlich, D Nanz, Victor D Köchli, KP Pruessmann, and Borut Marincek. *How does MRI work?: an introduction to the physics and function of magnetic resonance imaging*. Springer, 2008.

[19] Paul Glover and Peter Mansfield. Limits to magnetic resonance microscopy. *Reports on Progress in Physics*, 65(10):1489, 2002.

[20] Arno Klein, Jesper Andersson, Babak A Ardekani, John Ashburner, Brian Avants, Ming-Chang Chiang, Gary E Christensen, D Louis Collins, James Gee, Pierre Hellier, et al. Evaluation of 14 nonlinear deformation algorithms applied to human brain MRI registration. *Neuroimage*, 46(3):786–802, 2009.

[21] Markus Weiger, Klaas P Pruessmann, and Peter Boesiger. Cardiac real-time imaging using SENSE. *Magnetic Resonance in Medicine*, 43(2):177–184, 2000.

[22] Benjamin L Viglianti, Ana M Ponce, Charles R Michelich, Daohai Yu, Sheela A Abraham, Linda Sanders, Pavel S Yarmolenko, Thies Schroeder, James R MacFall, Daniel P Barboriak, et al. Chemodosimetry of in vivo tumor liposomal drug concentration using MRI. *Magnetic resonance in medicine*, 56(5):1011–1018, 2006.

[23] Bruno Quesson, Jacco A de Zwart, and Chrit TW Moonen. Magnetic resonance temperature imaging for guidance of thermotherapy. *Journal of Magnetic Resonance Imaging*, 12(4):525–533, 2000.

[24] K Hynynen, A Darkazanli, E Unger, and JF Schenck. MRI-guided noninvasive ultrasound surgery. *Medical physics*, 20(1):107–115, 1993.

[25] Holger Grüll and Sander Langereis. Hyperthermia-triggered drug delivery from temperature-sensitive liposomes using MRI-guided high intensity focused ultrasound. *Journal of Controlled Release*, 161(2):317–327, 2012.

[26] KK Buttenschön, JM Girkin, and D Daly. Tracking ophthalmic drugs in the eye using confocal fluorescence microscopy. In *SPIE BiOS*, pages 821403–821403. International Society for Optics and Photonics, 2012.

Chapter 3

Instrument Design and Development

3.1 Introduction

This chapter details the design and development of SIOS, a long working distance confocal laser scanning fluorescence microscope based on the F410 [1, 2] (Figure 3.1). As shown in Table 3.1, SIOS meets all design requirements set out in Chapter 1.

3.2 Optics

The optical schematic of SIOS is shown in Figure 3.2. Excitation light from the 15 mW 516 nm laser diode is collimated by L1 after reflection off the dichroic mirror, then focused into samples by L2. Fluorescence generated in phantoms is then collected by L2 and focused onto the pinhole by L1 after transmission through the dichroic mirror and the 550 nm long-pass filter. The pinhole allows fluorescence originating from the

Characteristic	Requirement	SIOS
Working Distance	$\geq 15\,\text{mm}$	51 mm
Field-of-view	$\geq 3\,\text{mm} \times 3\,\text{mm}$	$5\,\text{mm} \times 5\,\text{mm}$
Imaging Depth	$\geq 1\,\text{mm}$	15 mm
Imaging Speed (3 mm × 3 mm FOV)	$\leq 30\,\text{s}$	$< 30\,\text{s}$
Axial Resolution	45 to 70 µm or better	$63 \pm 6\,\mu\text{m}$
Lateral Resolution	45 to 70 µm or better	$50 \pm 1\,\mu\text{m}$

Table 3.1: SIOS characteristics vs requirements.

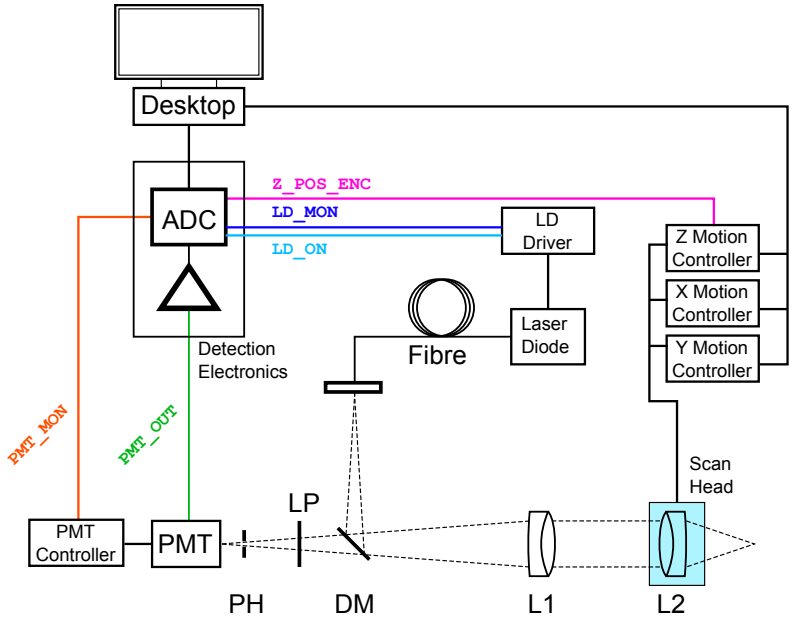

(a) Instrument schematic, showing all major components and their connections. All motion controllers and the ADC are connected to the desktop via USB-serial.

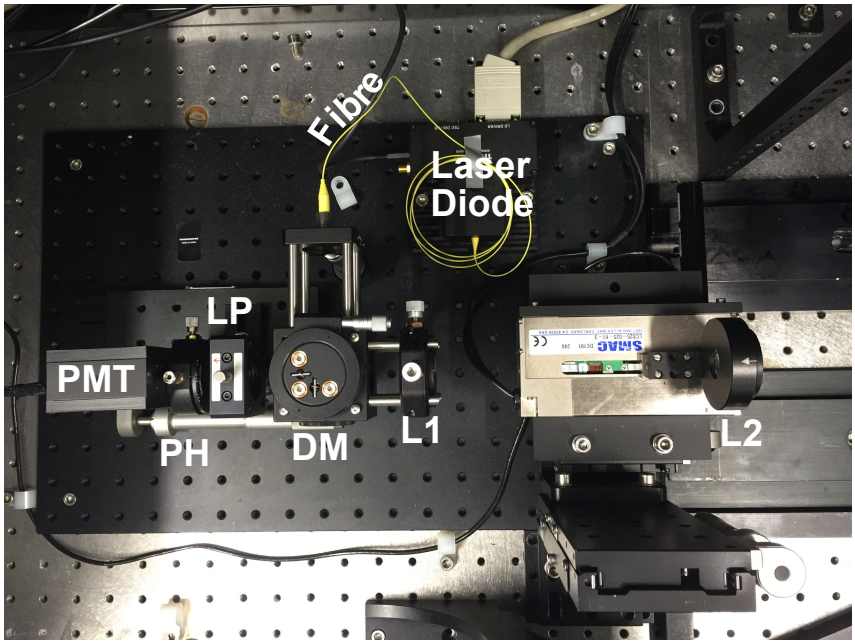

(b) Photograph of the instrument. The instrument is housed within a light-proof enclosure to minimise interference from ambient lighting.

Figure 3.1: Schematic and photograph of the instrument.

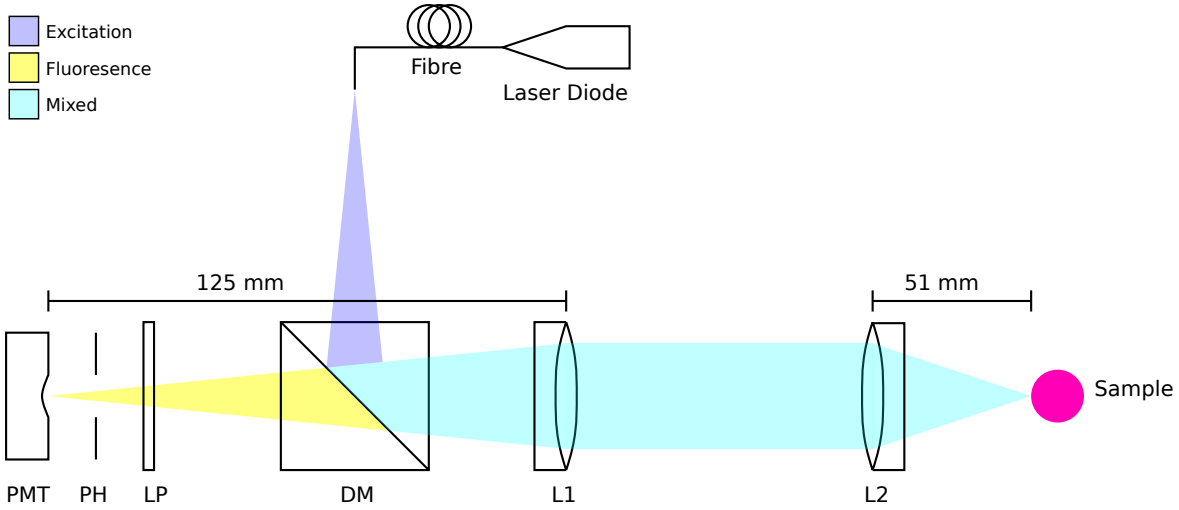

Figure 3.2: Optical schematic of SIOS. **Laser Diode**: 516 nm (LP520-SF15; Thorlabs, US); **DM**: dichroic mirror (DMLP550; Thorlabs); **L1**: collimating lens $f = 125\,\text{mm}$, ⌀25 mm (AC254-125-A-ML; Thorlabs); **L2**: multi-element objective, $f = 51\,\text{mm}$, 15 mm clear aperture (CA) (AMP-75.0-15.0-425-675-PM with companion lens; Acal BFi, UK); **LP**: 550 nm long-pass filter; **PH**: pinhole, ⌀15 µm; **PMT**: photomultiplier tube (H9306-04; Hamamatsu Photonics, JP).

focal plane of L2 to pass through and be detected by the photomultiplier tube (PMT).

SIOS' optical design derives from that of the F410 [1, 2], an instrument designed to perform non-invasive fluorescence measurements within the human eye. The F410 featured a Z stage for measuring fluorescence profiles along the optical axis and a reflection arm for determining the location of the cornea. In adapting the F410 design for the purpose of *in situ* monitoring of cavitation effects, the reflection arm was removed to simplify and improve alignment, and an XYZ scanning head was added to allow image formation via raster scanning. Additionally, the positioning and mounting of components were revised to improve instrument resolution, vibration isolation and instrument rigidity. Due to these changes, the axial resolution of SIOS is substantially better than that of the F410.

During ultrasound and cavitation mediated drug delivery experiments, samples are submerged within a water tank for ultrasound exposure. Accordingly, SIOS features a 51 mm working distance in order to image samples *in situ* through a water tank wall and the intervening volume of water. A water-immersion lens embedded within a water tank wall was considered. Such a lens, however, would require movement of samples and the ultrasound transducer along the optical axis during imaging, and its

fixed position limits the flexibility of the system in accommodating different models and samples.

Conventional wisdom recommends that the size of the pinhole in a confocal microscope should be about the size of the objective's imaged Airy disk [3]. At a wavelength of 550 nm, L2's Airy disk has a radius of 2.28 µm, calculated using $r_{Airy} = 1.22\lambda(F/D)$. After magnification by the instrument ($M = \frac{125\,\text{mm}}{51\,\text{mm}} = 2.45$), the imaged Airy disk has a radius of 5.59 µm, and thus a diameter of 11.18 µm. Accordingly, the smallest available pinhole that could accommodate L2's imaged Airy disk, with a diameter of 15 µm, was used.

3.2.1 Axial Scaling Factor

As implemented the instrument operates in air and images samples submerged in water. When focusing through two mediums with different refractive indices, the nominal focus position (NFP), when $n_2 = n_1$, does not coincide with the actual focus position (AFP) when $n_1 \neq n_2$ (Figure 3.3). Consequently, when the objective moves along the optical axis, the displacement of the AFP (ΔAFP) differs to that of the NFP (ΔNFP). By geometric consideration of the marginal rays, the relationship between ΔAFP and ΔNFP is given by Equation 3.1 [4, 5], where NA is the numerical aperture of the objective.

$$\Delta AFP = \frac{\tan(\sin^{-1}(NA/n_1))}{\tan(\sin^{-1}(NA/n_2))}\Delta NFP \tag{3.1}$$

If n_1 and n_2 are assumed to be always greater than or equal to 1, then for NA less than 0.176, as is the case currently, Equation 3.1 can be simplified using the small-angle approximation:

$$\Delta AFP = \frac{\tan(\sin^{-1}(NA/n_1))}{\tan(\sin^{-1}(NA/n_2))}\Delta NFP = \frac{\tan(NA/n_1)}{\tan(NA/n_2)} = \frac{n_2}{n_1}\Delta NFP \tag{3.2}$$

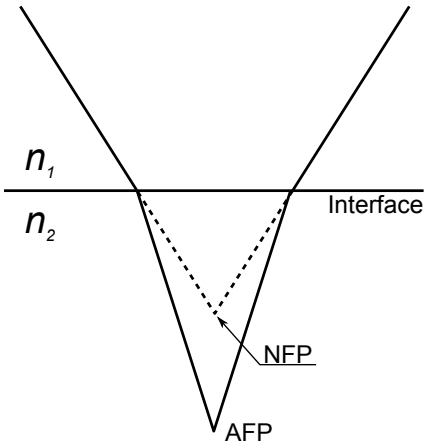

Figure 3.3: Actual and nominal focus positions when $n_1 < n_2$. **AFP**: actual focus position. **NFP**: nominal focus position. The dashed line shows the focus position when $n_1 = n_2$.

From Equation 3.2 we can derive the axial scaling factor (ASF) for the current instrument, where $n_2 = 1.33$ and $n_1 = 1.00$:

$$ASF = \frac{\Delta AFP}{\Delta NFP} = \frac{n_2}{n_1} = 1.33 \tag{3.3}$$

Distance measurements along the optical axis reported by the instrument were scaled using the value of ASF calculated from Equation 3.3. For example, if the instrument reports two fluorescent peaks 1 mm apart when measuring a sample submerged in water, then the actual distance between the peaks is 1.33 mm. Within agarose samples at 2% w/v concentration or less, the ASF is not significantly affected by local changes in refractive index, e.g. water-agarose, agarose-cell, due to the similar refractive indexes of water, agarose, and cells.

In these calculations, the effects of the glass tank wall have been ignored because while it causes a shift in AFP (Figure 3.4), the shift is constant for all focal positions and therefore $\Delta AFP' = \Delta AFP$, i.e. the ASF is unaffected.

Lastly, when imaging within agarose samples, changes in the ASF due to local variations in refractive index, e.g. water-agarose, agarose-cell, are negligible as water is the primary component of these materials and objects.

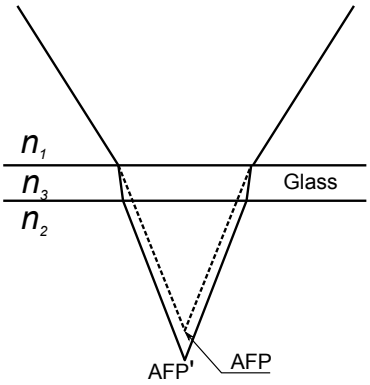

Figure 3.4: Effect of glass tank wall on AFP when $n_3 > n_1 > n_2$. Due to refraction within the glass wall, AFP shifts to AFP'. Dashed lines show AFP in the absence of the glass layer.

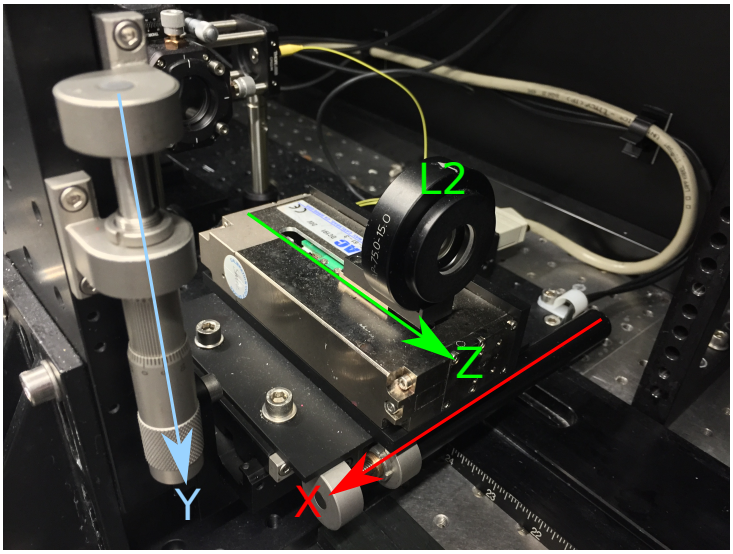

Figure 3.5: Linear stages for raster scanning. The stages are connected in an Z-X-Y arrangement, with the Y stage bearing the vertical load of both the X and Z stages.

3.3 Scan Head

SIOS' scan head consists of three linear stages that move the objective along the X, Y and Z axis (Figure 3.5). This scanning mechanism is possible because the diameter of the collimated beam produced by L1 overfills the objective, L2. While this scan head is slow compared to those using galvanometer mirrors or spinning disks, it offered a large field-of-view (FOV) and minimised aberrations from the air-water interface by keeping the optical axis perpendicular to the water tank wall.

The arrangement of the stages is such that the Y motion stage bears the most weight, making it the slowest axis. This decision was made to allow for faster XZ plane scans, which during trial experiments proved the most useful.

The fast axis of the scan head, the Z axis, is driven by a linear motor (LCS25-025-51; SMAC Corporation, USA) while the X and Y axes are driven by screw-drive systems (X-LSM025A-E03; Zaber Technologies Inc, CA and TRB25CC; Newport Corporation, US). In operation, the Z axis has a maximum speed of $100\,\mathrm{mm\,s^{-1}}$ while the X and Y axes both have a maximum speed of $2\,\mathrm{mm\,s^{-1}}$.

Each motion stage is paired with a motion controller connected via USB-serial to the desktop computer.

3.4 Detection Electronics

The detection electronics consist of circuitry primarily responsible for measuring the outputs of the instrument. Whereas the optical aspects of SIOS derive from the F410, the detection electronics consists of original designs. Shown in Figure 3.6, it consists of several modules, demarcated with dotted blue lines. Inputs signals, shown on the left, consist of the laser driver's monitor voltage (`LD_MON`), the PMT control voltage (`PMT_CTL`), the PMT output voltage (`PMT_OUT`), and the output from the Z stage's position encoder (`Z_POS_ENC`). The detection electronics has one output signal, `LD_ON`, that controls the on-off state of the laser diode.

The PMT output voltage, corresponding to the level of fluorescence at the optical focus, is the primary signal of interest. Due to its low magnitude, it is first amplified

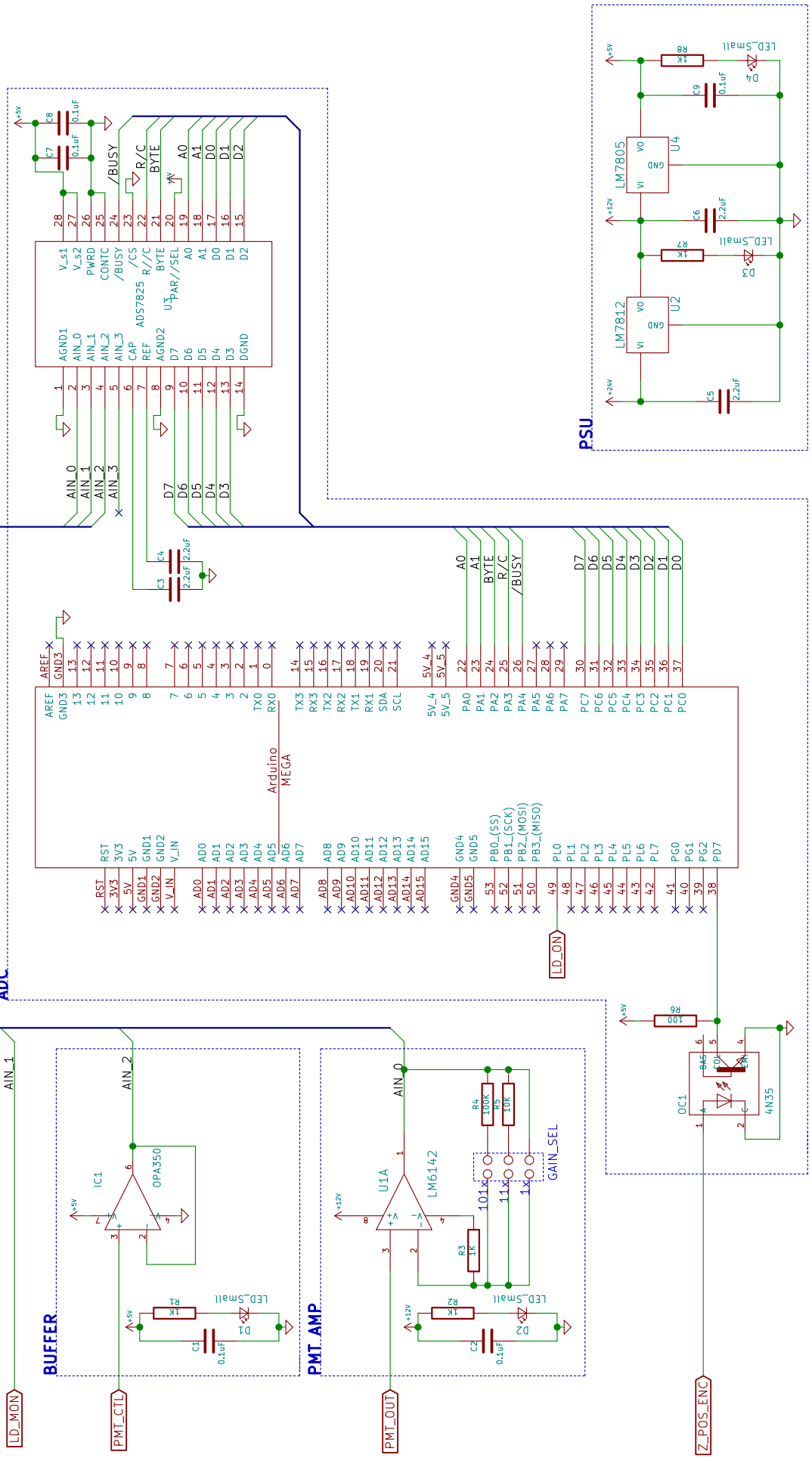

Figure 3.6: Schematic of detection electronics. The different modules are demarcated with dotted blue lines.

by PMT_AMP then sampled by ADC. The inputs PMT_CTL and LD_MON allows the state of the instrument to be captured at the time of measurement: PMT_CTL determines the sensitivity of the PMT, and LD_MON relates to the forward current (I_{fwd}) through the laser diode via Equation 3.4. Lastly, the input Z_POS_ENC is the phase A output of the Z stage's quadrature encoder, and allows ADC to be triggered based on the Z distance travelled.

$$I_{fwd} = \frac{200mA \times LD_{mon}[V]}{10V} \tag{3.4}$$

Each detection electronics module was implemented as a separate physical unit for ease of development and testing.

3.4.1 BUFFER

The BUFFER module exists to allow sampling of the PMT control voltage without unduly affecting the load presented to the PMT controller. It has a much higher input impedance than the ADS7825, which has an input impedance of approximately 40 kΩ.

3.4.2 ADC

The ADC module consists of an ATmega2560 microcontroller (Atmel Corporation, US) and an ADS7825 (Texas Instruments, US). The ADS7825 is a 4 channel 16-bit analogue-to-digital converter (ADC) with a maximum sampling rate of 40 kHz across all channels. Custom firmware running on the ATmega2560 interfaces between the ADS7825 and the desktop software.

The input signal Z_POS_ENC is used to triggered the ADC module. Triggering is currently configured to occur on the rising edge, which occurs once for every 4 µm of travel along the Z axis.

3.4.3 PMT_AMP

The PMT_AMP is a non-inverting selectable-gain amplifier built around an LM6142, a single-supply rail-to-rail operational amplifier with a slew rate of 13 V µs^{-1} and a gain

bandwidth product of 10 MHz. Gain selection is via the `GAIN_SEL` header, and allows the amplification to be adjusted as required, e.g. for instrument alignment and troubleshooting.

3.4.4 PSU

The `PSU` module, consisting of two linear regulators, supplies 12 V and 5 V power to the other modules. While less efficient than switching-mode regulators, linear regulators do not produce switching noise and the fixed nature of the instrument renders their inefficiency largely irrelevant.

3.5 Software

As with the detection electronics, the software written for SIOS is original and does not derive from that of the F410.

3.5.1 ADC Module Firmware

The ADC module firmware, running on the ATmega2560 within the `ADC` module, interfaces between the desktop control software and the ADS7825 analogue-to-digital converter. Written in C, it is responsible for configuring the ADS7825, triggering analogue-to-digital conversions based on `Z_POS_ENC`, and buffering the conversion result. Additionally, the firmware also controls the on-off state of the laser diode via `LD_ON`.

The primary function of the ADC module firmware is to obtain measurements of the PMT output when triggered by the movement of the Z stage. An overview of this process is shown in Figure 3.7. The variables `trig_lim` and `exp_limt` are set by the desktop control software. `trig_lim` configures the number of triggers required before sampling occurs, i.e. the distance between measurements. `exp_lim` implements a form of exposure control, in which the PMT output is sampled multiple times, equal to `exp_lim`, with the results accumulated into a 16-bit unsigned integer for storage and transmission. In the event of an integer overflow, `0xFFFF` is stored. This mechanism allows an additional level of control over the instrument sensitivity, but must be used

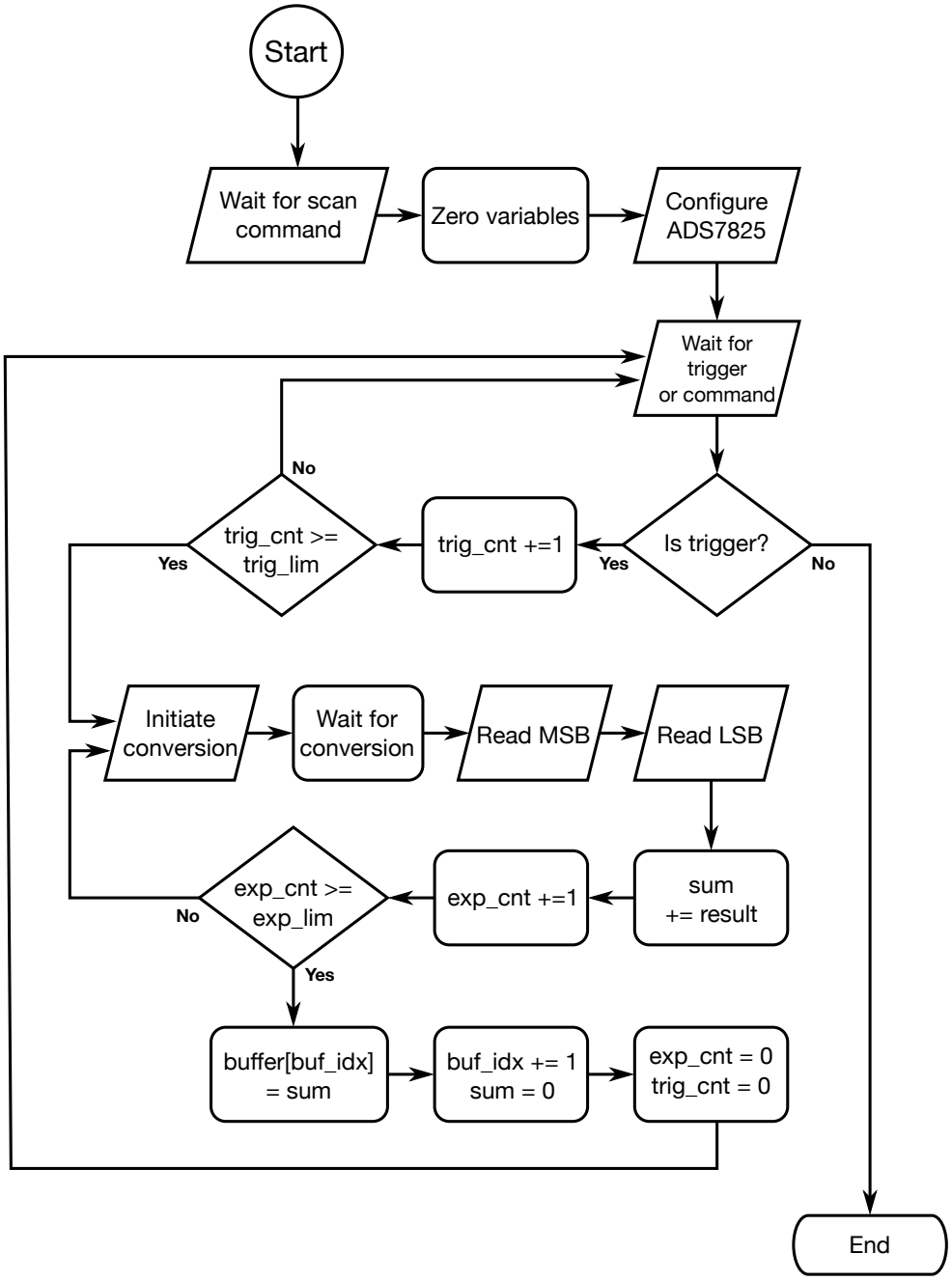

Figure 3.7: ADC module firmware data acquisition flow diagram. Parallelograms indicate input/output operations, including serial communication. As the data bus to the ADS7825 is only 8-bit wide, two read operations are required to obtain the 16-bit conversion result. Limit checks have been omitted for clarity. **MSB**: most significant byte; **LSB**: least significant byte.

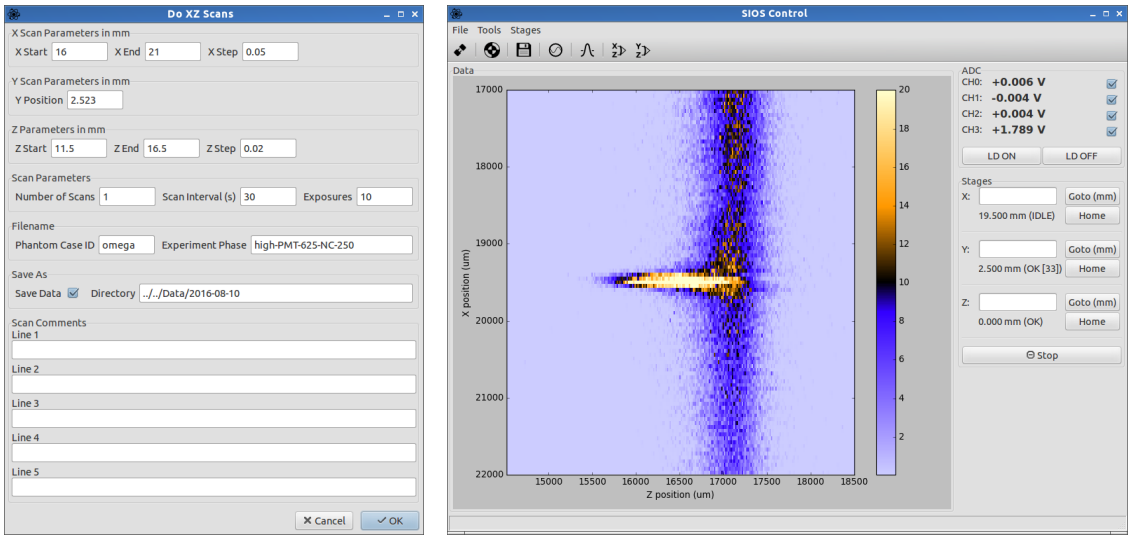

(a) (b)

Figure 3.8: Screen shot of the desktop control software. **(a)** Configuration of an XZ plane scan. A similar dialogue exists for scans in the YZ plane. **(b)** Image from an XZ plane scan.

carefully as each measurement takes at least 25 µs. Therefore, if `exp_lim` is set too high, the per-trigger measurement time may exceed the time between triggers, resulting in missing samples and signal distortions.

The number of measurements that can be stored is limited by the size of the `buffer` array, and therefore by the amount of random-access memory (RAM) available. The ATmega2560 has 8 kB of RAM, capable of holding $8192/2 = 4096$ 16-bit integers. In practice, however, some RAM must be reserved for the program stack. Based on the rule-of-thumb that up to 75 % of available RAM can be safely used, the current size of `buffer` is 6144 bytes, equal to 3072 16-bit integers.

3.5.2 Desktop Control Software

The desktop control software, written in Python, has three major functions: allow the user to set scan parameters, execute raster scans according to user specifications, and displaying the results. The first and last functions are accomplished via a graphical user interface (GUI), shown in Figure 3.8. Using the GUI, the user is able to configure the field-of-view by setting the scan range in X, Y and Z axes, and the spatial resolution by specifying the step size. For the X and Y axes, the step size is the movement between Z scans, while the step size along the Z axis (Δz, in micrometres) translates

into a value for `trig_lim` using Equation 3.5. In addition, the user can also specify the number of images to acquire, the time between each image, and the number of exposures (`exp_lim`) per trigger. Together these settings allow for automatic acquisition of images at set time intervals.

$$\texttt{trig\_lim} = \left\lfloor \frac{\Delta z}{4\,\mu\text{m}} \right\rfloor \tag{3.5}$$

The last and most important function of the desktop control software is image formation via raster scanning. This is accomplished by executing the steps shown in Figure 3.9, which performs a series of Z scans at different X positions in order to build up an XZ plane image. The variable `t_interval` corresponds to the interval, in seconds, between image acquisition; `scan_lim` is the number of images to acquire; and `X_position` is an array of generated X positions based on the start and end X positions and the desired step size. A similar algorithm is executed for acquiring YZ plane images.

3.5.2.1 Optimisations

The procedure shown in Figure 3.9 contains two optimisations that significantly improved the image acquisition speed of the system.

The first optimisation exploits parallelism offered by asynchronous commands to motion controllers. Commands to motion controllers, indicated by parallelograms with filled top-right corners, can be synchronous (shaded) or asynchronous (unshaded). A synchronous command is where a move is commanded and execution is halted until the motion controller signals the move has occurred successfully. In contrast, when a motion command is issued asynchronously, execution proceeds immediately after issuing the command. Use of asynchronous commands affords a degree of parallelism, whereby the desktop control software performs other tasks while the motion controllers execute the commanded movement. This is parallelism is used in the steps demarcated in green, where the X and Z stages are commanded to move to their next positions while the data is read from the ADC.

The second optimisation, demarcated in blue, is specific to the motion controllers

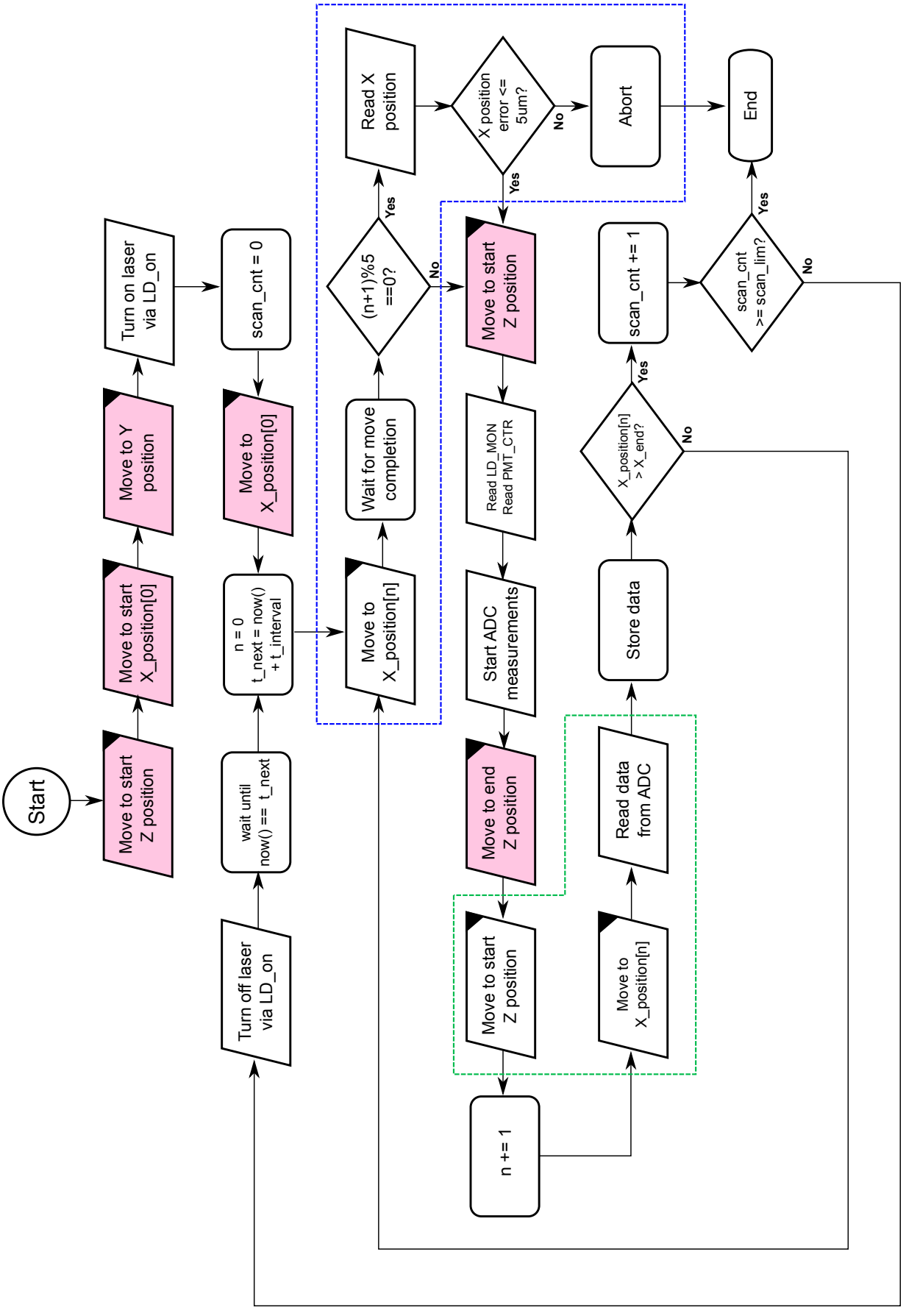

Figure 3.9: XZ image acquisition flowchart. Parallelograms with filled top-right corners indicate communication with motion controllers. Shaded parallelograms indicate synchronous commands that wait for a response. Limit checks have been omitted for clarity.

used. The time needed to read the controller position from the X or Y motion controller is much longer than the time required to complete the commanded move, typically 50 to 100 µm, due to the nature of USB-serial communication. As a result, it is faster to issue an asynchronous move command and assumed that, after some time, t_{move}, the stage has complete the movement. Heuristics are used to calculate t_{move}, which differ for the X and Y stages due to their different acceleration profiles. This optimisation, however, requires that the motion stage is able to complete the move in the time allowed, as otherwise the Z stage would start its movement while the X or Y stages are still in motion, leading to image skew. To guard against this possibility, for every 5 steps taken by the X or Y stage, the stage position is read and compared against the expected value. If the error between actual and anticipated position is greater than 5 µm the scan is aborted. The value of this check has been proven in practice, identifying several instances where the X or Y stage has not been able to complete the required movement in the time allocated[1].

3.5.2.2 Error Checking

As mentioned earlier in Subsection 3.5.1, it is possible to configure a scan such that the sampling time required per trigger exceeds the shortest time between triggers[2], resulting in missed measurements. To guard against this scenario, the desktop control software calculates the number of measurements it expects per Z scan and compares this against what is returned by the ADC. In the event that triggers are missed, the number of measurements returned will be smaller than expected, and the scan is flagged as invalid. This mechanism is, however, not perfect due to overshoot of the Z stage when coming to a stop, resulting in extra triggers and samples that can mask previously missed measurements.

[1] When these instances occurred heuristics were updated to increase t_{move}.

[2] As the Z stage is triggered based on distance travel, the time between triggers is not constant due to stage acceleration and deceleration.

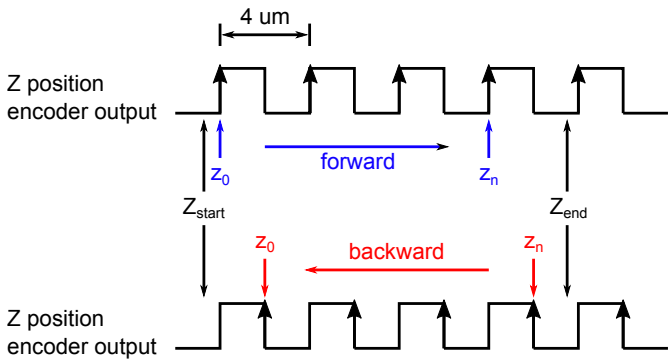

Figure 3.10: ADC triggering in forward and backward Z scans. Z_{start} and Z_{end} denote the physical stopping and starting position of the Z motion stage. $z_{0..n}$ denote the position assigned to the measurements.

3.5.2.3 Two-Way Z Scanning

An obvious optimisation that is missing in Figure 3.9 is two-way scanning, where instead of moving back to the starting position after each scan, the Z stage can remain where it is and perform the next scan "backwards", moving from the end position to the starting position. This would reduce the total distance travelled by the Z stage and therefore the total scan time.

Implementing two-way scanning would require resolving the issue where the ADC is triggered at different positions in forward and backward scans due to the rising and falling edges being swapped (Figure 3.10). Due to this issue, PMT measurements at different Z positions may be assigned the same Z position, resulting in registration errors of up to 2 µm. A further complication is the fact that the starting phase can differ, e.g. the phase of Z_{start} in the forward scan differs to the phase of Z_{end} in the backward scan, introducing an additional 2 µm of error in each direction, for a worse case error of 6 µm.

In practice, implementing two-way scanning does not produce significant savings. A typical plane scan configuration uses a step size of 50 µm along the X and Y axis and a Z scan range of 4 mm. Under these settings, the X and Y stages require at least 96 ms to move 50 µm, while the Z stage takes 104 ms to travel 4 mm, and the total time per Z scan, taking into account communication and data transfer times, is approximately 258 ms. Implementing two-way scanning would save $104 - 96 = 8$ ms, an improve-

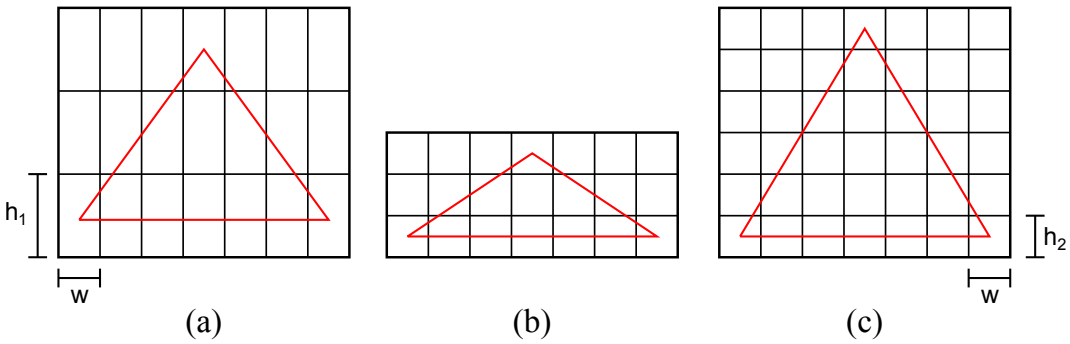

Figure 3.11: Conversion of non-square pixels to square pixels. **(a)** The real size of pixels where $h_1 > w$ **(b)** Distortion from being displayed with physically square pixels **(c)** Scaling so displayed features sizes are in proportion, with new pixel height $h_2 = w$.

ment of 3 %, which was deemed insufficient to justify the effort required.

3.5.3 Data Conversion Software

In order to convert measurements obtained by the instrument into 2D bitmaps suitable for analysis with programs such as ImageJ/Fiji[1], custom data conversion software was written[2]. A particular challenge in the conversion that the step size in X and Y axes is typically larger than the step size in the Z axis, resulting in non-square pixels (Figure 3.11a). While software like ImageJ can handle non-square pixels for measurement purposes, it nonetheless results in distortion when displayed due to monitors having physically square pixel (Figure 3.11b). To ensure displayed features are not distorted, the data conversion program, `wzdata2tif.py`, first produces a 2D bitmap with non-square pixels, then scales the image upwards along the longer axis, reducing the height of each pixel, to produce a bitmap that contains square pixels (Figure 3.11c). The value of new pixels in the final image is computed using the nearest-neighbour algorithm to avoid interpolation artefacts.

In addition to handling non-square pixels, `wzdata2tif.py` also takes into account the path lengthening effect due to refractive index mismatch, discussed in Subsection 3.2.1, and ensures that the features in the output images have dimensions that match their true physical size.

[1] http://imagej.net/and http://imagej.net/Fiji
[2] https://github.com/freespace/dphil-data-tools/

3.5.4 Development Effort

A total of 16,858 source lines of code were written in order to drive the instrument and to produce images for analysis. Using the `sloccount` utility[1], the software development effort was estimated to be the equivalent of approximately 3.88 person-years of work. Some of this development effort has published and made available for general use[2].

3.6 Instrument Characterisation

3.6.1 Optical Power Output

Figure 3.12 shows the optical power output of the instrument measured using an optical power meter (1830C with 818SL head, ND filtered fitted; Newport, US) placed in front of the collimator. The accuracy of the 818SL detector is generally between 2 % to 7 %.

To ensure consistent optical power output across experiments, the instrument operates in a climate controlled environment at 20 °C, and the laser housing is equipped with a heatsink. These measures keep the laser's temperature constant, removing thermal effects that increase the threshold current and reduces optical power output.

3.6.2 Axial Resolution

The axial resolution of a confocal microscope is commonly defined by the full-width half-maximum (FWHM) of its axial point-spread function (PSF), which can be measured by removing the long-pass filter and scanning against a stationary mirror. Figure 3.13 shows the PSF of SIOS so measured using a water submerged mirror and scanning through the intervening glass wall of a water tank. The distance between the mirror and the glass tank wall was 12.5 mm. These conditions simulate experimental conditions and the PSF so obtained is a more accurate estimate of the instrument's capabilities when used as intended.

[1] `http://www.dwheeler.com/sloccount/`

[2] List of modules and their URLs are listed in the Appendix.

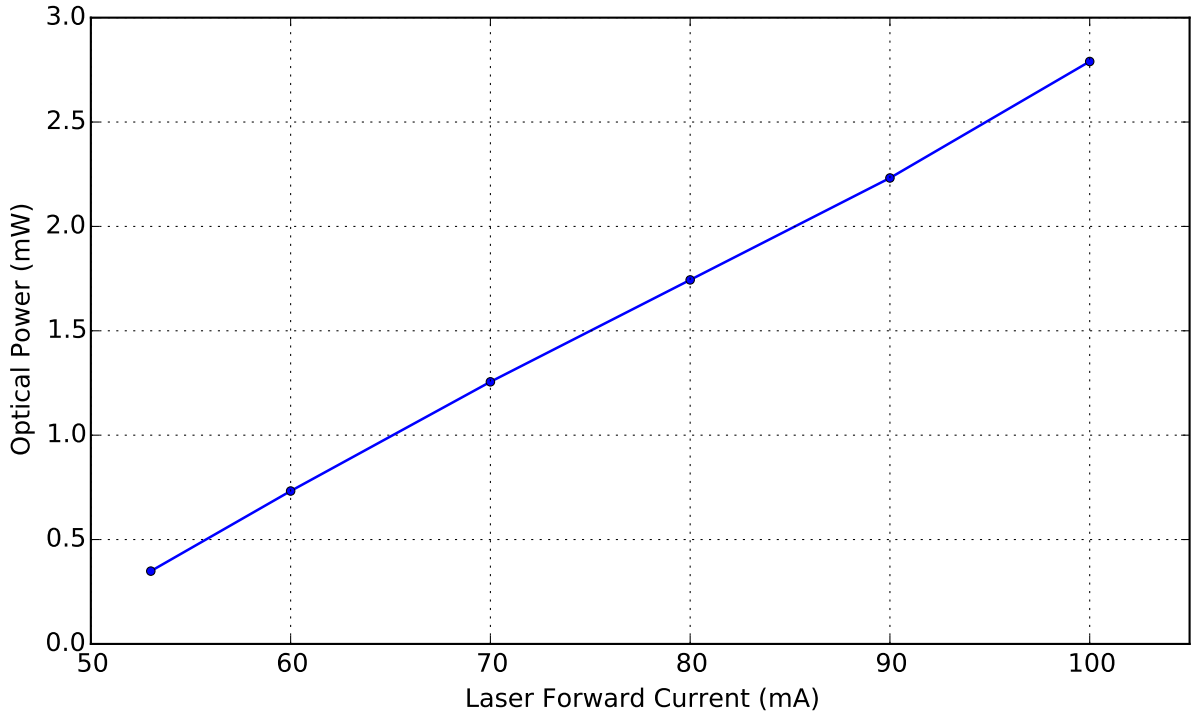

Figure 3.12: Optical power output of the instrument as a function of laser diode forward current.

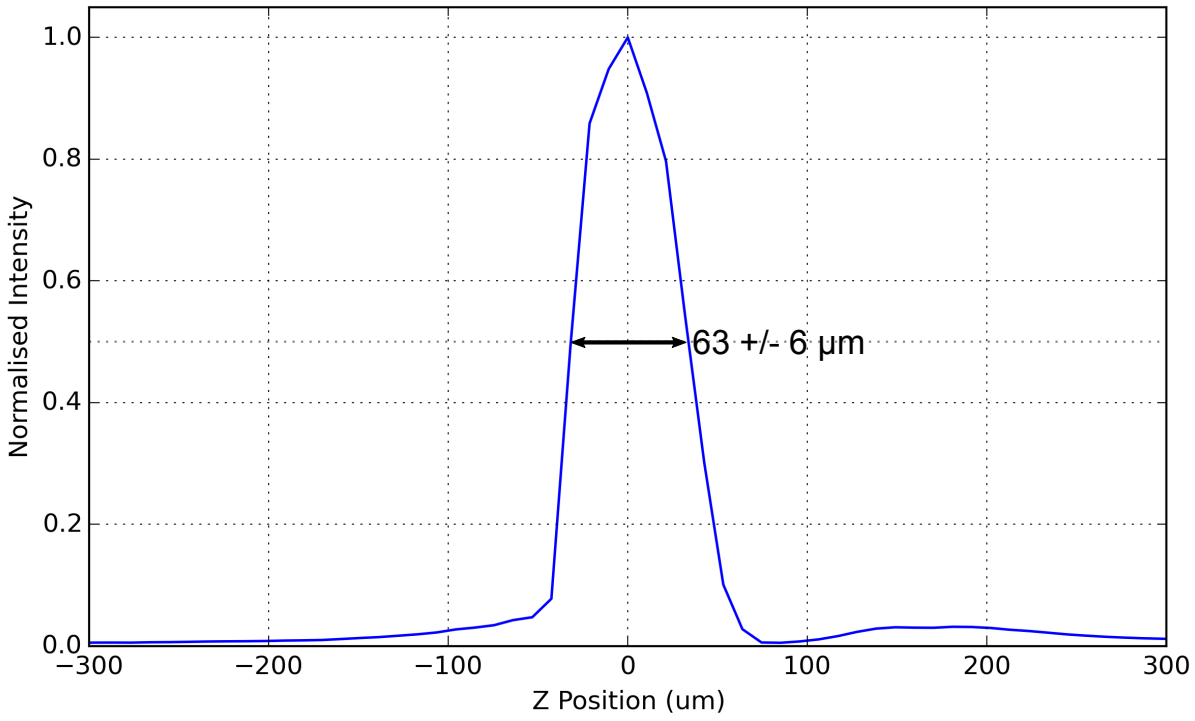

Figure 3.13: Point spread function of the instrument (average of 3 measurements), obtained by scanning against a mirror target submerged in water. Asymmetries in the PSF are attributed spherical aberrations.

The measured PSF, shown in Figure 3.13, has a FWHM of 63 ± 6 µm which is within an acceptable agreement with the expected value of 57.14 µm, calculated using Equation 3.6 [6] with $\lambda = 516$ nm, and meets the requirements listed in Table 1.1 in Chapter 1. The error derives principally from the 4 µm positional accuracy of the Z stage, which translates into an error of 5.32 µm $\approx$ 6 µm after applying the ASF.

$$FWHM_z = \frac{0.88\lambda}{n - \sqrt{n^2 - NA^2}} \tag{3.6}$$

The instrument's PSF is stable over long time periods with measurements of the FWHM taken 14 months apart deviating by less than 2 µm.

3.6.3 Lateral Resolution

Using the Rayleigh criterion, the lateral optical resolution of the instrument is expected to be 2.17 µm, calculated using $\frac{0.61\lambda}{NA}$. However as image formation is via raster scanning, the lateral resolution also depends on the step size along the X and Y axes, which at 50 µm is significantly larger than the optical resolution. Consequently, the lateral resolution of the instrument is 50 µm with an error of ± 1 µm based on the 1 µm positional accuracy of the motion stages.

3.6.4 PSF Degradation

In addition to axial scaling, the mismatch in refractive indices of the objective and sample media also causes attenuation and aberrations due to the fact that both phase and amplitude are both affected by the optical interface. One consequence is the aforementioned axial scaling, another is increased spherical aberrations [5]. The effect of these and other aberrations degrade the PSF, increasing its width and reducing its amplitude, with the degree of degradation expected to increase with optical depth [5, 7].

To characterise the degradation of the PSF with increasing optical depth, a series of PSF measurements were taken with the submerged mirror placed at increasing distances from the objective (Figure 3.14). It was found that both the amplitude and the width of the PSF decrease with increasing optical depth. For each millimetre of ad-

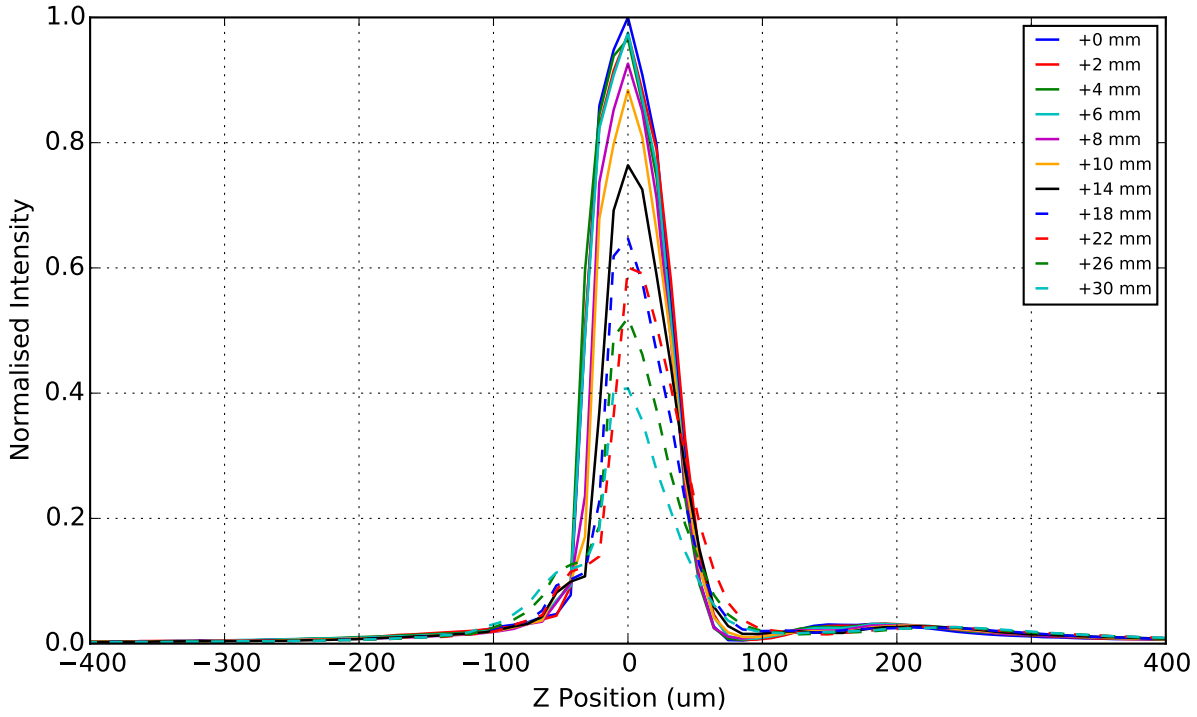

Figure 3.14: PSF at different optical depths. Positions are relative to $z_0' = 12.5\,\text{mm}$ away from the tank wall. Each trace corresponds to a single measurement.

ditional optical depth, the amplitude was reduced by approximately 2.0 %, and the FWHM by approximately 0.57 %. The reduction in the FWHM run contrary to the previous findings [7], and may be the result of distorted FWHM measurements when the lower portion of the PSF clips below the detection limits of the system.

Lastly, an additional symptom of PSF degradation is that the size of the irregularity at $Z \approx -50\,\mu\text{m}$ increases with optical depth (Figure 3.14).

3.6.5 Scanning Speed

SIOS can perform a 5 mm by 5 mm XZ plane scan with an X axis resolution of 50 µm in 30 s. Scanning speed is primarily limited by the acceleration of the X stage, which determines how quickly the Z stage can be repositioned, and secondarily by the number of samples required per trigger. Note due to axial scaling, when imaging in water the effective FOV is 5 mm by 6.65 mm.

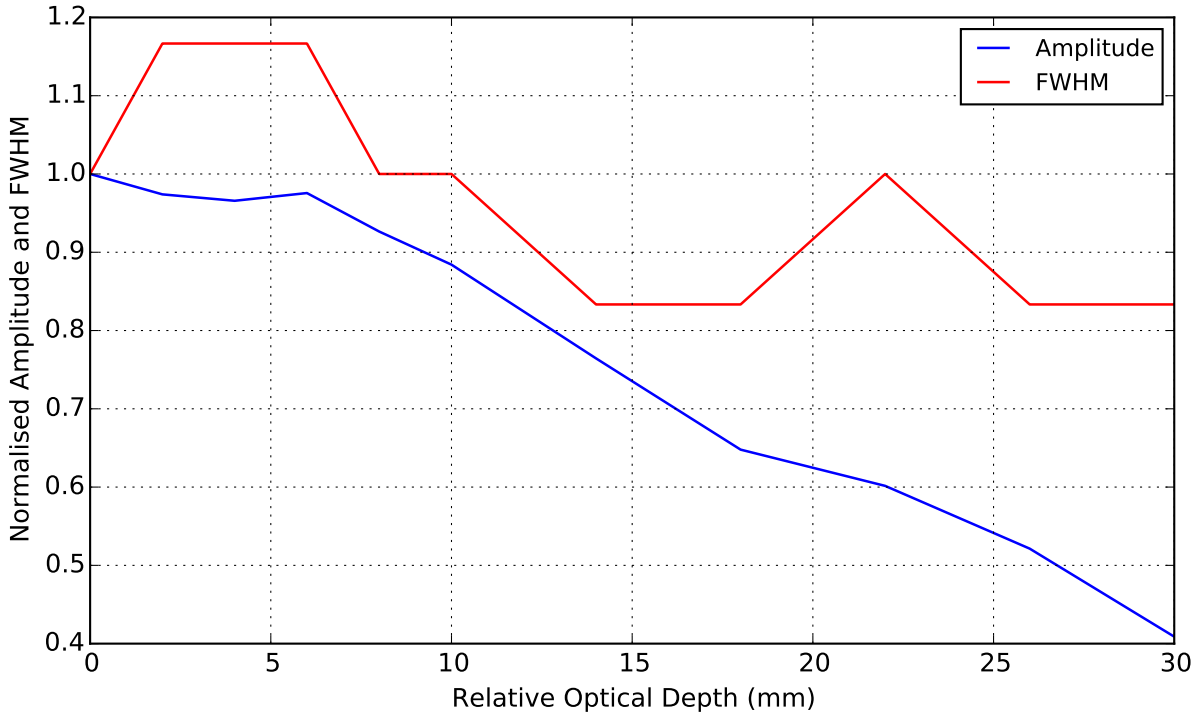

Figure 3.15: Normalised PSF amplitude and FWHM with increasing optical depth.

3.7 Summary

A new confocal instrument, SIOS, based on the F410 was developed. It features a new scan head and original detection electronics and software. SIOS meets or exceeds its engineering design goals with a 50 mm working distance, a 5 mm by 5 mm FOV, an axial resolution of 63.84 µm, and an 3 mm $\times$ 3 mm image acquisition time of less than 30 s.

Appendix

Published Software Modules

All modules are published under the MIT license.

Module	URL and Description
`pylecroy`	`https://github.com/freespace/pylecroy` Python class for loading binary Lecroy `trc` files.
`dphil-data-tools`	`https://github.com/freespace/dphil-data-tools` Python scripts for data plotting, conversion and analysis. Includes programs to convert instrument output to TIF images.
`pySMC100`	`https://github.com/freespace/pySMC100` Python module for interfacing with SMC100 motion controllers from Newport, US. Provides motion control, position query and controller configuration.
`smalc-lac-1`	`https://github.com/freespace/smac-lac-1` Python module for interfacing with LAC-1 motion controllers from SMAC, US. Provides motion control, position query and controller configuration.
`pyAPT`	`https://github.com/freespace/pyAPT` Python module for interfacing with APT motion controllers from Thorlabs, US. Provides motion control, position query and controller configuration.
`arduino-ADS7825`	`https://github.com/freespace/arduino-ADS7825` AVR firmware and python module to interface with an ADS7825. Provides command and control of ADS7825 and facilitates data transfer between ADS7825 and desktop software.

References

[1] Kim-Kristin Buttenschon. *A novel fluorophotometer for measuring concentration and diffusion of autofluorescent ophthalmic medication in the human eye*. PhD thesis, Durham University, 2013.

[2] KK Buttenschön, JM Girkin, and D Daly. Tracking ophthalmic drugs in the eye using confocal fluorescence microscopy. In *SPIE BiOS*, pages 821403–821403. International Society for Optics and Photonics, 2012.

[3] Denis Semwogerere and Eric R Weeks. Confocal microscopy. *Encyclopedia of Biomaterials and Biomedical Engineering*, pages 1–10, 2005.

[4] K Carlsson. The influence of specimen refractive index, detector signal integration, and non-uniform scan speed on the imaging properties in confocal microscopy. *Journal of Microscopy*, 163(2):167–178, 1991.

[5] TD Visser, JL Oud, and GJ Brakenhoff. Refractive index and axial distance measurements in 3-d microscopy. *SPIE MILESTONE SERIES MS*, 131:286–289, 1996.

[6] Stefan Wilhelm, Bernhard Grobler, Martin Gluch, and Hartmut Heinz. Confocal laser scanning microscopy. principles. *Microscopy from Carl Zeiss, microspecial*, 2003.

[7] S Hell, G Reiner, C Cremer, and Ernst HK Stelzer. Aberrations in confocal fluorescence microscopy induced by mismatches in refractive index. *Journal of microscopy*, 169(3):391–405, 1993.

Chapter 4

Model Selection

4.1 Introduction

When investigating the *in vivo* effects of a treatment, models are indispensable tools during the exploratory phase as they allow rapid iteration of experimental parameters. The ideal model is one that is practical, realistic, robust, and reproducible. A practical model is one that can be manufactured or prepared without excessive cost in time or resources, allowing for a large number of experiments. A realistic model is one that mimics *in vivo* conditions, e.g. with the similar mechanical properties as the target tissue and containing vessels of similar sizes. Realistic models increase the likelihood that results obtained are reproducible *in vivo*. A robust model is one that can withstand experimental conditions without catastrophic failure. Robust models maximise experimental efficiency and reduce resource consumption. Finally, a reproducible model is one where its characteristics can be well controlled. Reproducible models minimise variability and improve data quality.

The goal of model selection is to determine which of the models available best meet the criteria. In general, the models considered here are flow channel models, where a channel, representing a blood vessel, is embedded within a hydrogel, which models the surrounding tissue (Figure 4.1). Fluids are flown through the channels during experiments in order to delivery drug analogues and cavitation agents to the ultrasound focus and the surrounding hydrogel.

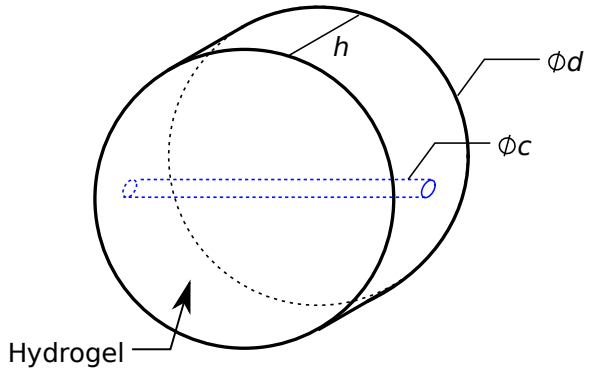

Figure 4.1: Schematic of a flow channel model. The flow channel, shown in blue, is embedded within a hydrogel such as agarose. Typical dimensions are $h = 10\,\text{mm}$; $d = 25\,\text{mm}$; $c = 0.2$ to $1.6\,\text{mm}$.

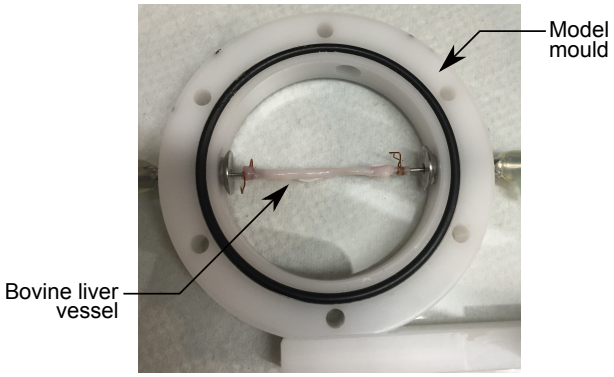

Figure 4.2: Mounted bovine liver vessel. The vessel at the centre of the model mould has been excised from a commercially sourced bovine liver and mounted using copper wires.

4.2 Excised Blood Vessels

The best approximation to an *in vivo* blood vessel is an excised blood vessel. Attempts were made to create flow channel models containing blood vessels extracted from bovine livers and mouse tails.

4.2.1 Bovine Vessel Model

Bovine vessel models (BVMs) were made from blood vessels excised from bovine livers obtained from a commercial butcher. Blood vessels approximately 2 to 4 mm in diameter and 25 to 40 mm long were extracted, flushed with PBS, and mounted on model moulds (Figure 4.2). The moulds were then made water tight and filled with 1 % w/v molten agarose. The filled moulds were then allowed to set overnight at 4 °C, resulting in flow channel models consisting of a bovine blood vessel embedded in agarose. Due

to the difficulties involved in identification, extraction and mounting of vessels, only one to two BVM were produced per liver per day. In experiments performed at 20 °C, BVMs proved to be relatively robust with few failures.

BVMs have two major shortcomings: low reproducibility and lack of realism. The low reproducibility of BVMs stems from the lack of control over the animal from which the liver is taken, e.g. breed, age, gender; and the difficulty in extracting the "same" vessel each time. The lack of realism is a consequence of the fact that the blood vessels used in BVMs are necessarily larger than those found in tumour vasculature, as the extraction of smaller, more representative vessels, proved impractical. These larger blood vessels have thicker and more complex vessel walls compared to vessels induced via tumour angiogenesis, and because they are healthy, do not exhibit the enhanced permeability and retention (EPR) effect [1].

4.2.2 Mouse Tail Vein Model

Mouse tail vein models (MTVMs) were an attempt to address the shortcomings of BVM. Mouse tail veins are smaller (<1 mm), are easily identified and consistently located. In theory, these characteristics make MTVM a more realistic and reproducible model, and the location of the vessels, just below the dermis and above tail bones, should ease extraction.

In practice, separation of the mouse tail vein from the tail's sub-dermal layer proved beyond available capabilities, and despite many attempts, an MTVM was never realised. Additionally, even if MTVMs were practical, the model depends on a sporadic supply of mice. Whereas bovine livers can be sourced readily and on-demand from commercial butchers, mice are available only when another experiment's control group is sacrificed. It would be ethically untenable to sacrifice tens of animals for a single piece of tissue.

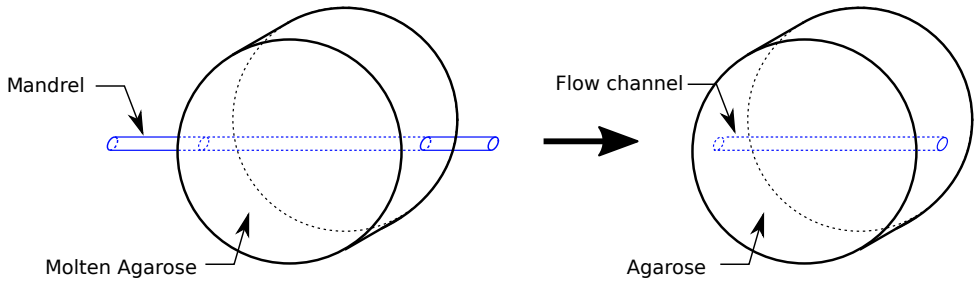

Figure 4.3: Manufacture of agarose channel model. Molten agarose is allowed to set around a mandrel, which is removed after setting, resulting in a flow channel within the agarose.

4.3 Agarose Channel Model

Agarose channel models (ACMs) are flow models constructed by casting agarose around a mandrel, e.g. steel rod or fishing wire, which is then later withdrawn, leaving behind a channel cavity (Figure 4.3). ACMs are practical, with production rates of more than nine models a day, reproducible and robust. By controlling the diameter of the channel and the agarose concentration, ACMs can be tuned to mimic *in vivo* conditions. For example, the flow channel can have sub-millimetre diameters to better simulate vessels found near tumours, and the Young's modulus of agarose can be controlled by varying the agarose percentage, allowing it to mimic a range of tissues such as liver and kidney. Furthermore, the pharmacokinetics of agarose can also be modified, e.g. via the addition of alginate, to more closely model drug diffusion in tissue.

ACMs also have the unique advantage that they can be seeded with living cells, offering the possibility of observing biological effects of ultrasound and cavitation.

4.3.1 Regenerated Cellulose Capillary Model

Regenerated cellulose capillary models (RCCMs) are a variation of ACMs, where a 200 µm diameter regenerated cellulose capillary (Cuprophan RC55 8/200, Membrana GMBH) is embedded within agarose and becomes the flow channel. The capillaries were intended for haemodialysis, and feature a maximum weight cut-off (MWCO) of approximately 10,000 kDa. The small size of the capillaries along with an MWCO that resembles liver tissue made RCCMs attractive in terms of realism. They were also robust, capable of withstanding high pressures and flow rates, and were easy to

Model	Practicality	Realism	Robustness	Reproducibility
BVM	1	1	2	1
MTVM	0	-	-	-
ACM	3	3	2	3
RCCM	3	0	3	3

Table 4.1: Evaluation of flow channel models. Scores are out of 3. MTVM was only scored on practicality as its performance under the other criteria are unknown.

produce.

The major shortcoming of RCCMs was that while the capillaries that were realistic in terms of diameter and diffusion characteristics, the tensile strength and the elasticity of the capillaries far exceeded that of similarly sized vessels. For example, cellulose haemodialysis membranes have a Young's modulus of approximately 20 MPa [2], while the Young's modulus of arteries and veins range from 6.5 to 560 kPa [3]. The robustness of the capillaries was such that they proved invulnerable to the effects of cavitation, rendering RCCMs highly unrealistic.

4.4 Evaluation

Table 4.1 summarises how well each flow channel model meets the requirements of practicality, realism, robustness and reproducibility. Based on these results, the ACM was chosen as the standard model for experiments.

4.4.1 Limitations of the ACM

The main limitation of the ACM is the lack of biological modelling. Specifically, the lack of living cells within ACMs prevents it from being used to study the biological response to ultrasound, limiting ACM studies to those concerned with purely physical effects. Additionally, as the elasticity of agarose can differ substantially from that of living tissue, results obtained with in ACMs concerning physical effects cannot be used to directly predict response *in vivo*. Lastly, ACMs tend to use agarose at concentrations of 1 % or higher, producing significant optical scattering which negatively affects image quality.

4.5 Summary

A variety of flow channel models were tested, and the ACM was found to best meet the requirements of practicality, realism, robustness and reproducibility. Accordingly, despite its limitations, the ACM was chosen as the standard model for ultrasound and cavitation experiments.

References

[1] Jun Fang, Hideaki Nakamura, and Hiroshi Maeda. The epr effect: unique features of tumor blood vessels for drug delivery, factors involved, and limitations and augmentation of the effect. *Advanced drug delivery reviews*, 63(3):136–151, 2011.

[2] E Klein, F Holland, A Lebeouf, A Donnaud, and JK Smith. Transport and mechanical properties of hemodialysis hollow fibers. *Journal of Membrane Science*, 1:371–396, 1976.

[3] Clayton T McKee, Julie A Last, Paul Russell, and Christopher J Murphy. Indentation versus tensile measurements of young's modulus for soft biological tissues. *Tissue Engineering Part B: Reviews*, 17(3):155–164, 2011.

Chapter 5

Materials and Methods

5.1 Introduction

In the present work, the different experiments share in common many of the materials used and methods employed for data collection and analysis. To avoid duplication, oft-used materials and methods are described here and are referred to in the following chapters as needed.

5.2 Materials

5.2.1 Agarose Channel Models

Agarose channel models, introduced in Chapter 4, are agarose cylinders with a diameter of 40 mm and height of 10 mm, each featuring an embedded flow channel (Figure 4.1, Chapter 4). The channel models were formed by injecting molten agarose into model moulds with mandrels inserted. The agarose was then allowed to set overnight at 4 °C. Immediately before use, mandrels were removed, exposing the flow channels.

Two flow channel sizes were used: 1.6 mm and 370 µm. For 1.6 mm channels, stainless steel rods of the same diameter were used as mandrels, while 370 µm channels were formed using fishing lines.

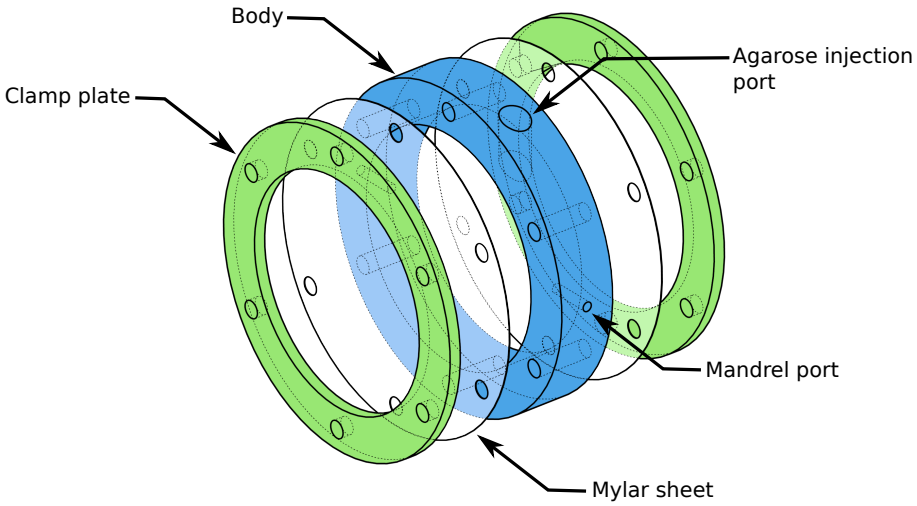

Figure 5.1: Schematic of model moulds. Moulds have an outer diameter of 55 mm with an internal cutout of 40 mm. Agarose channel models were contained within the body, which has a height of 10 mm and features agarose injection and mandrel insertion ports. Clamp plates secure Mylar sheets to the body, creating two optically and acoustically transparent windows. Accessories for attaching tubing and mounting to motion stages are not shown.

5.2.1.1 Channel Model Moulds

The channel model moulds were constructed from polyoxymethylene and feature two ultrasound and optically transparent windows (Figure 5.1). In addition to shape-forming the agarose, the moulds also served as holders, providing the means by which the flow channels are connected to external tubing, and facilitating the mounting of channel models to motion stages. The moulds were water tight and isolated the channel models from the surrounding body of water.

The channel model moulds were designed and manufactured by Jim Fisk and David Salisbury at the Institute of Biomedical Engineering, Department of Engineering Science, University of Oxford.

5.2.1.2 Agarose Hydrogels

Agarose hydrogels were prepared by first adding agarose powder (UltraPure Agarose-1000; Thermo Fisher Scientific, USA) to de-ionised water at the required w/v concentration in a 1000 mL borosilicate glass bottle. Then, to account for losses during the degassing step, an additional 20 mL of de-ionised water was also added. The weight of the mixture was recorded, and then the mixture was heated in a microwave until the

agarose powder had completed dissolved. To account for water loss during heating, the mixture was replenished with de-ionised water to recover its pre-heating weight.

In order to avoid unwanted cavitation within the agarose hydrogel, the heated mixture was then degassed for 30 min. Following degassing, the mixture was poured into model moulds and allowed to set overnight at 4 °C.

5.2.2 TRITC-Dextran

To make flow channels visible to SIOS, and to introduce a drug analogue with which the effect of ultrasound and cavitation on drug distribution and penetration can be monitored, fluids-under-test were made fluorescent with the addition of TRITC-Dextran (44 kDa, Tetramethylrhodamine isothiocyanate–Dextran, 42874; Sigma-Aldrich, US). A high concentration stock solution was made by adding 175 mg of TRITC-Dextran powder to 1 mL of de-ionised water. When needed, the stock solution was added to experimental fluids at a concentration of 1 µL per 1 mL.

5.2.3 Fluorescent Nanoparticles

Fluorescent nanoparticles (FluoSpheres, 42874; Life Technologies, US) were used post ultrasound exposure to enhance widefield fluorescence microscopy of flow channels and deformations. The nanoparticles, supplied in suspension, have a mean diameter of 0.2 µm with excitation and emission peaks at 580 nm and 605 nm respectively. When required, 100 µL of the stock suspension was diluted into 10 mL of de-ionised water, then introduced into flow channels.

5.2.4 Widefield Microscopy

All widefield microscopy was carried out using an inverted microscope (Eclipse Ti; Nikon Inc, USA) and a 4× objective ($NA = 0.13$, CFI Plan Fluor DL 4×; Nikon);

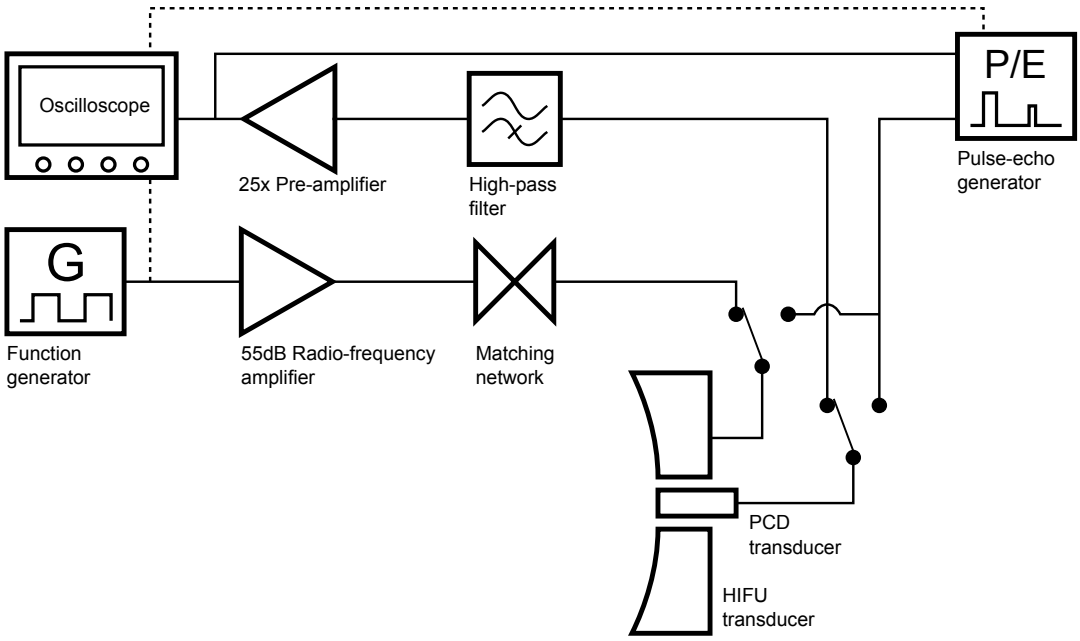

Figure 5.2: Ultrasound setup for ultrasound and cavitation mediated drug delivery experiments. **Oscilloscope**: WaveRunner 104Xi, LeCroy Corporation, US; **Pre-amp**: SR445A, Standford Research Systems, US; **High-pass Filter**: F5081-5P00-B, Allen Avionics Inc, US; **Pulse-echo generator**: DPR 300, JSR Ultrasonics, US; **Function generator**: 33250A, Agilent Technologies, US; **RF amplifier**: 1140LA, Electronics & Innovation Ltd, US; **Matching network**: H102-28D, Sonic Concepts, US; **HIFU transducer**: H102-28D, Sonic Concepts; **PCD transducer**: V319, Panametrics-NDT, US; Dashed lines indicated trigger signals.

5.3 Methods

5.3.1 Ultrasound Setup

The ultrasound setup (Figure 5.2) used two ultrasound transducers: a high-intensity focused ultrasound (HIFU) transducer and a single-element coaxial passive cavitation detection (PCD) transducer. Both transducers can be connected to the pulse-echo unit for alignment. During ultrasound exposure, the HIFU transducer was driven by the amplified output waveform of the function generator, and induced cavitation noise was detected by the PCD transducer. The PCD signal was then high-pass filtered and amplified before being sampled and stored by the oscilloscope.

The HIFU transducer used has a fundamental frequency of 1.067 MHz and a focal length of 62.64 mm, while the PCD transducer has a centre frequency of 15 MHz and a focal length of 76.2 mm. In order to accommodate the PCD transducer in a coaxial arrangement, the HIFU transducer features a central circular cutout.

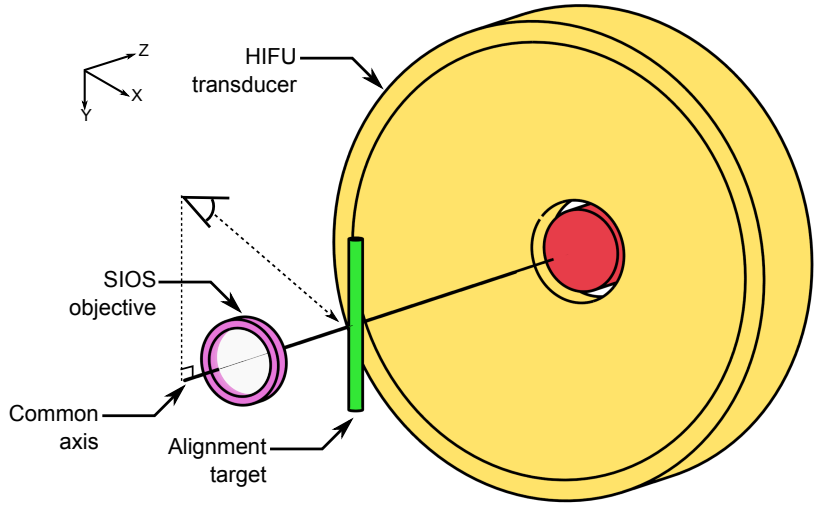

Figure 5.3: Alignment of the optical and acoustic axes along X. Alignment target is a 2 mm diameter metal cylinder. Reflections off the alignment target were observed from the indicated position above the common axis and maximised. As shown, the alignment target is coincident with the optical and ultrasound foci. All components other than the objective were immersed in water.

5.3.2 Alignment of Flow Channel Models

In order to monitor in real-time the effects of ultrasound and cavitation on flow channels, the channels must be simultaneously aligned to the ultrasonic focus whilst within the field-of-view (FOV) of SIOS. This is achieved using a successive series of alignments, beginning with the alignment of the optical and acoustic axes along X. First, the optical focus was moved to the centre of the FOV, and the alignment target, a 2 mm diameter metal cylinder, was aligned to the focus by illuminating it with the instrument and maximising back reflections. With the alignment target at the optical focus, the HIFU transducer was then translated along the X axis to maximise the strength of pulse-echoes returns from the target, thus bringing the optical and acoustic axes into alignment along the X axis (Figure 5.3). During this process, both the alignment target and the HIFU transducer were submerged in water.

Following alignment of the optical and acoustic axes along X, the alignment target was replaced with a flow channel model (Figure 5.4). The model's flow channel was then filled with air to create an optical and acoustic reflector. Using back reflections, the flow channel was then placed at the optical focus such that the optical axis passes through the channel waist. This was then followed by the alignment of the acoustic focus to the channel along the Y and Z axes using pulse-echoes returns, thereby bring-

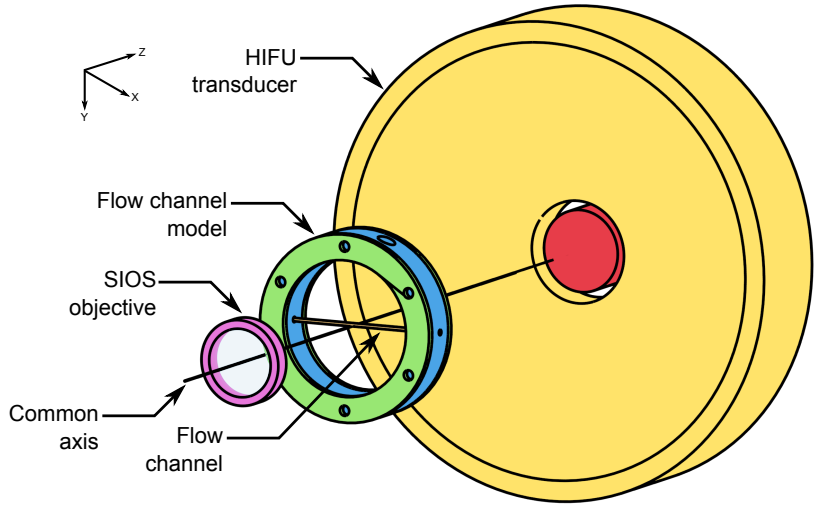

Figure 5.4: Alignment of the flow channel, the optical focus and the acoustic focus. As shown the flow channel is at the optical and ultrasound foci. Both the flow channel model and the HIFU transducer were immersed in water.

ing the flow channel, the optical focus, and the acoustic focus into coincidence at the centre of the SIOS' FOV. Finally, the focus of the single-element PCD transducer was aligned to the flow channel along the Z axis.

For channel models with 370 µm diameter flow channels, the alignment of the optical axis to the channel waist using back reflections suffered from errors ($\approx$ 200 µm) that were comparable to the channel diameter, and thus additional fine-tuning was required. Fine-tuning consisted of imaging a flow channel transversely in the YZ plane to determine the position of the channel waist along the Y axis, and then configuring the desktop control software so that subsequent longitudinal XZ scans occurred at this position. As the instrument lacks a reflection arm, fine-tuning requires the flow channel to be filled with a fluorescent fluid.

5.3.3 Ultrasound Exposure and Real-Time Monitoring

In general, real-time monitoring of a flow channel was carried out immediately before, during, and after ultrasound exposure, and consisted of a series of XZ scans of the channel taken at fixed time intervals. The exact timings and scan interval durations were determined by the requirements of each experiment.

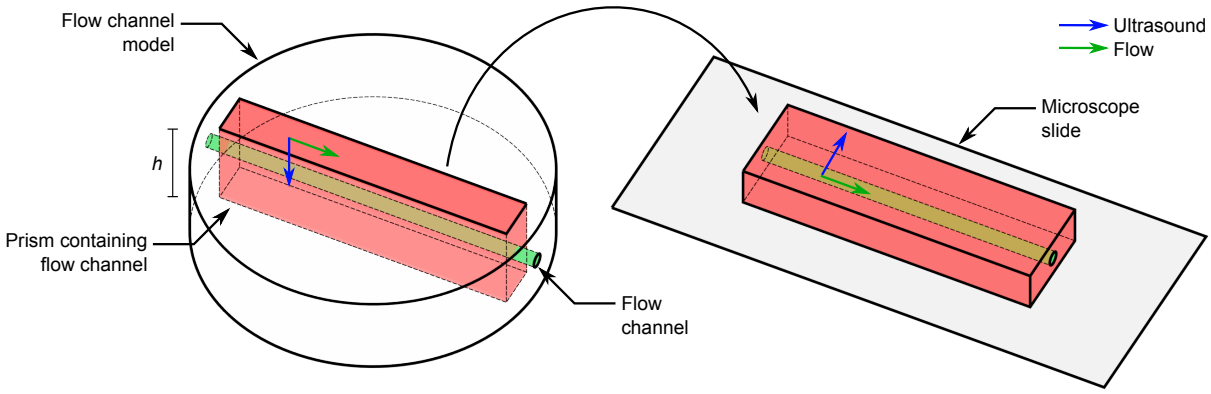

Figure 5.5: Excision of a flow channel for end-point microscopy. The rectangular block containing the flow channel, shown in red, was approximately 30 mm long, 10 mm heigh and 4 mm deep. Once excised from the flow channel model the block was then rotated and placed on a microscope slide for imaging.

5.3.4 End-Point Flow Channel Microscopy

When end-point microscopy images of the flow channels were required, flow channels were flushed with de-ionised water following ultrasound exposure to remove any fluorescent fluids, then flushed again with a suspension of fluorescent nanoparticles. These fluorescent nanoparticles adhere to the interiors of the flow channel and any deformations, improving contrast under widefield fluorescence microscopy. Flow channels were then excised for imaging.

Excision of a flow channel required the disassembly of the model mould in order to release the agarose channel model. A rectangular block containing the flow channel, approximately 30 mm long, 10 mm heigh and 4 mm deep was then excised using a custom-built guillotine. The excised block was then placed on a glass microscope slide for imaging (Figure 5.5). If needed, lateral cross section views of deformations were obtained by sectioning the block around the deformation and mounting as shown in Figure 5.6 for imaging.

The guillotine used for excisions was also designed and manufactured by Jim Fisk and David Salisbury.

5.3.5 Cavitation Noise Acquisition and Analysis

The oscilloscope shown in Figure 5.2 was used to sample the amplified output of the PCD transducer and to store the measurements to disk for later analysis. With each

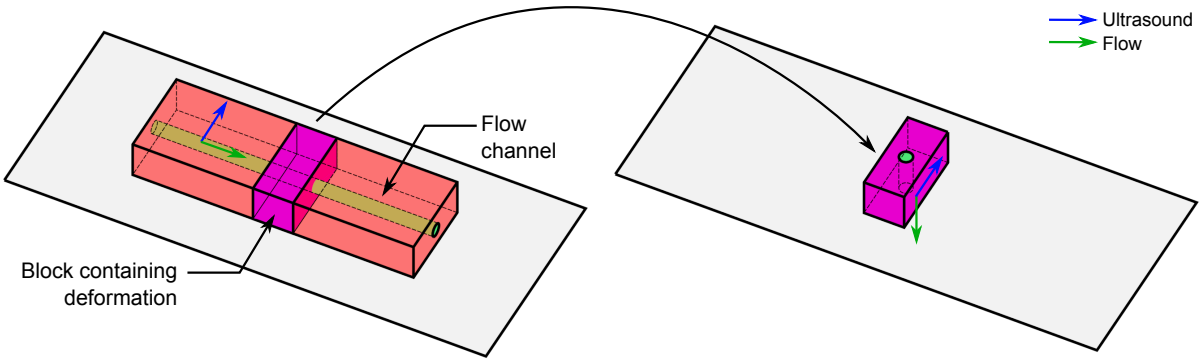

Figure 5.6: Sectioning of an excised block to enable cross section imaging of deformations.

outgoing ultrasound pulse 50,000 measurements were taken at a sampling frequency of 50 MHz, triggered by the `SYNC` output of the signal generator. Each set of 50,000 measurements constitutes a time series.

Due to the time-of-flight required for the HIFU pulse to reach the flow channel, and for cavitation noise from within the channel to reach the PCD transducer, cavitation signals appear approximately 100 µs after triggering (Figure 5.7a). While the oscilloscope can be configured to begin recording after a time delay, starting at the trigger time provides implicit measurements of background noise and allows for the detection of pre-focal cavitation, e.g. due to improperly degassed agarose or trapped air bubbles.

Analysis of detected cavitation noise was carried out on a per time series basis. For frequency content analysis, a fast Fourier transform (FFT) was applied to the mean-subtracted time series, i.e. $(x - \bar{x}) \xrightarrow{FFT} X(\omega)$ where x is a single time series. This treatment removes any DC bias in the signal. To obtain the power spectral density (Figure 5.7b) the output was squared then divided by the sampling frequency, F_s:

$$PSD(\omega) = |X(\omega)|^2 / F_s$$

From the power spectral density the power of detected cavitation noise can be estimated:

$$P = \int_0^{F_s/2} PSD(\omega) d\omega$$

And by combining the power spectral density from all time series, the cavitation

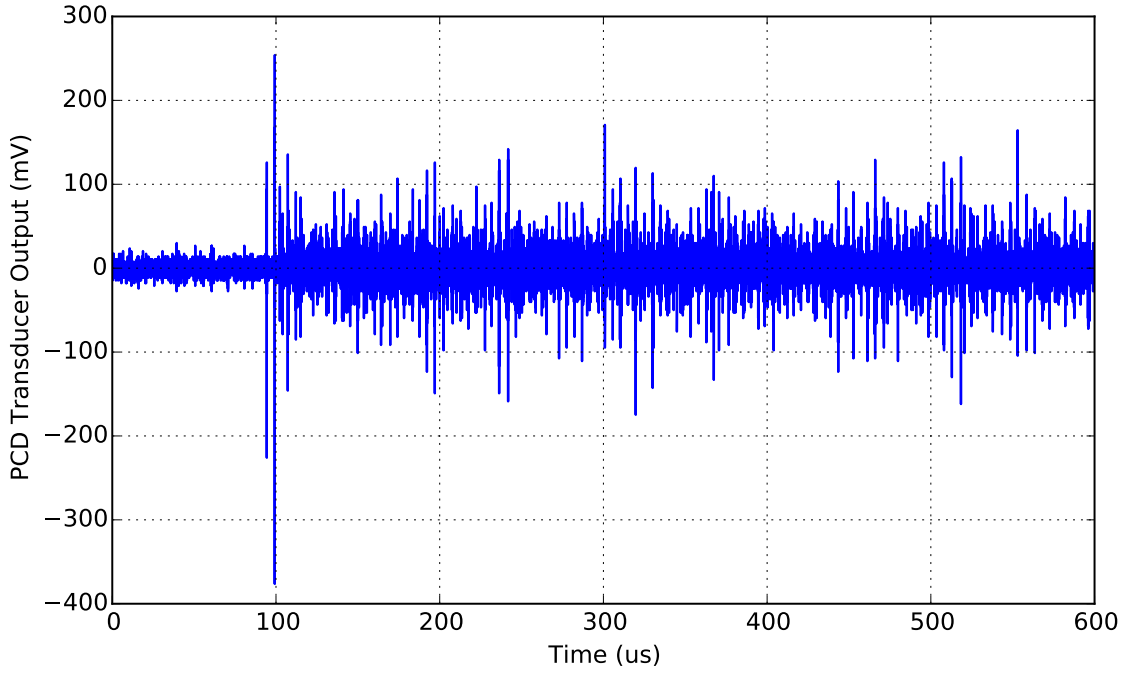

(a)

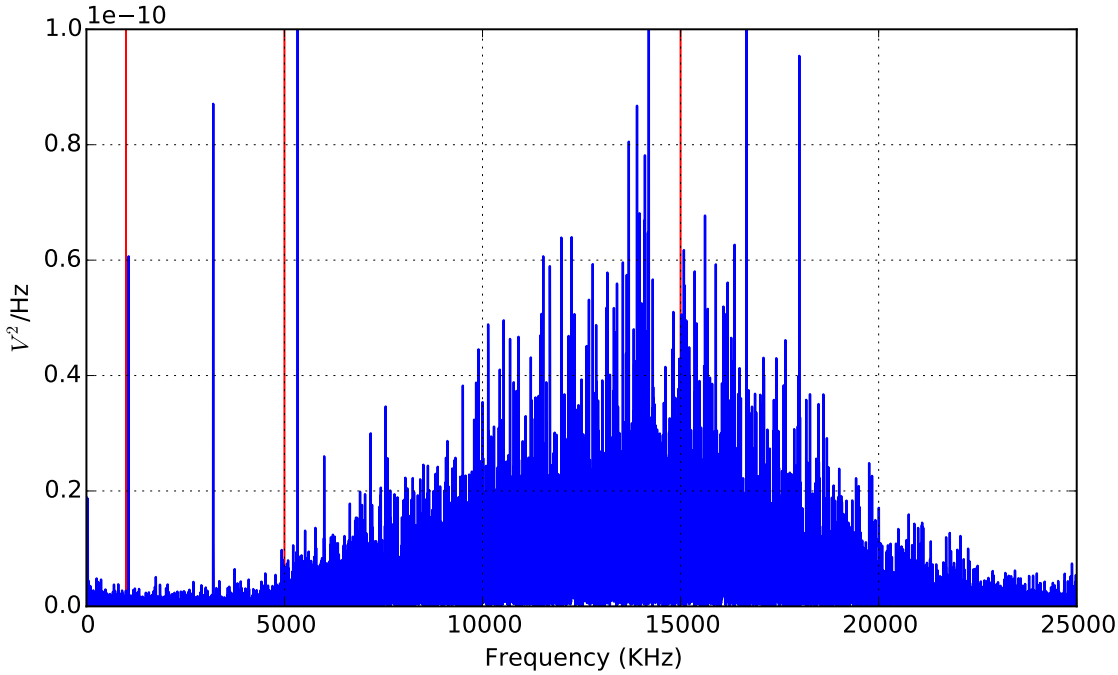

(b)

Figure 5.7: **(a)** A time series of 50,000 measurements and **(b)** its power spectral density. The vertical red lines in (b) indicate, left-to-right, the fundamental frequency of the HIFU transducer, the cut-on frequency of the high-pass filter, and the centre frequency of the PCD transducer.

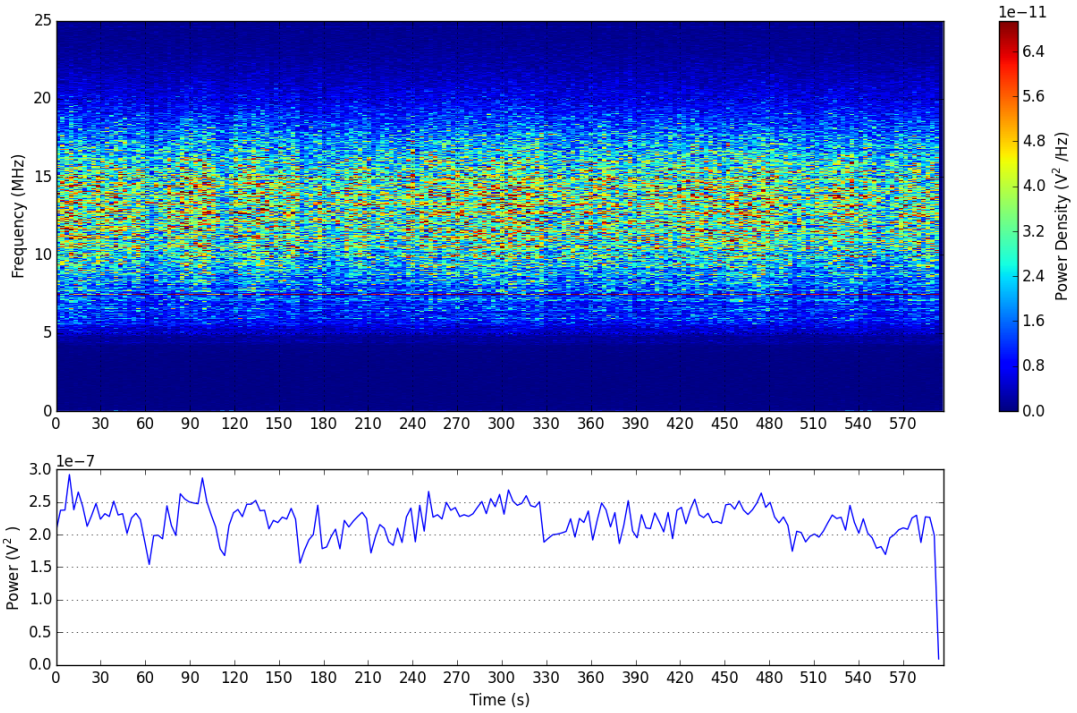

Figure 5.8: Example cavitation noise spectrogram and power curve.

noise spectrogram was produced (Figure 5.8).

Lastly, the total energy of detected cavitation noise was estimated by summing the power across all recording then multiplying by the time between triggers, T_{trig}:

$$E = T_{trig} \sum_{i=0}^{N} P_i$$

Where P_i is the power of time series x_i and N is the number of time series recorded in a single experiment.

5.3.6 SIOS Image Analysis

The real-time images of fluorescence distribution in and around flow channels reflect both the structure of the flow channels, including deformations, and the diffusion of fluorophores into the surrounding agarose. By tracking the movement of fluorescence contours, information about changes in the channel structures and rates of diffusion can be inferred.

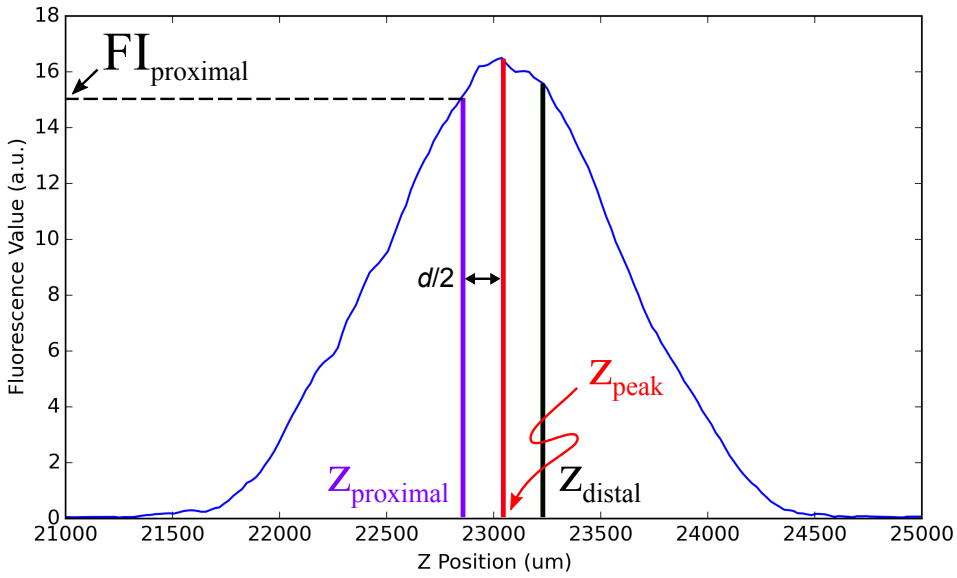

Figure 5.9: Determination of fluorescence value at the proximal channel boundary. For each of the first 25 rows in an image, the location of the fluorescence peak was taken to be the channel centre. Then using the nominal channel diameter d, the location of the channel boundaries were determined. Finally, using $z_{proximal}$, $FI_{proximal}$ was found.

Fluorescence front displacement is a technique for tracking changes in fluorescence contours developed for the present work. It begins by determining the fluorescence value at the proximal channel boundary ($FI_{proximal}$) across the first 25 rows of an image. For each row, the location of the fluorescence peak (z_{peak}) was taken to be the centre of the channel. Then, based on the nominal channel diameter, the proximal and distal channel boundaries locations were calculated using $z_{proximal} = z_{peak} - r_{channel}$ and $z_{distal} = z_{peak} + r_{channel}$ respectively. $FI_{proximal}$ was then simply the fluorescence value at $z_{proximal}$ (Figure 5.9).

Once $FI_{proximal}$ has been determined for each of the 25 rows, the average value of $FI_{proximal}$ was then used to define the fluorescence front, a point along an image row that splits it into two segments, one where the maximum fluorescence value is less than $\overline{FI_{proximal}}$ and one where the maximum fluorescence value is at least as large as $\overline{FI_{proximal}}$. For example, in Figure 5.9, the fluorescence front is at $z_{proximal}$. When applied to all rows of an image, the fluorescence front maps the proximal boundary of the channel and any deformation (Figure 5.10). By comparing the locations of the fluorescence front in the first images against subsequent images, the fluorescence front displacement in each image is calculated on a per-row basis using Equation 5.1, where $FF_r[n]$ is the Z coordinate of the fluorescence front in row r of the n-th image.

$$\Delta FF_r[n] = FF_r[0] - FF_r[n] \tag{5.1}$$

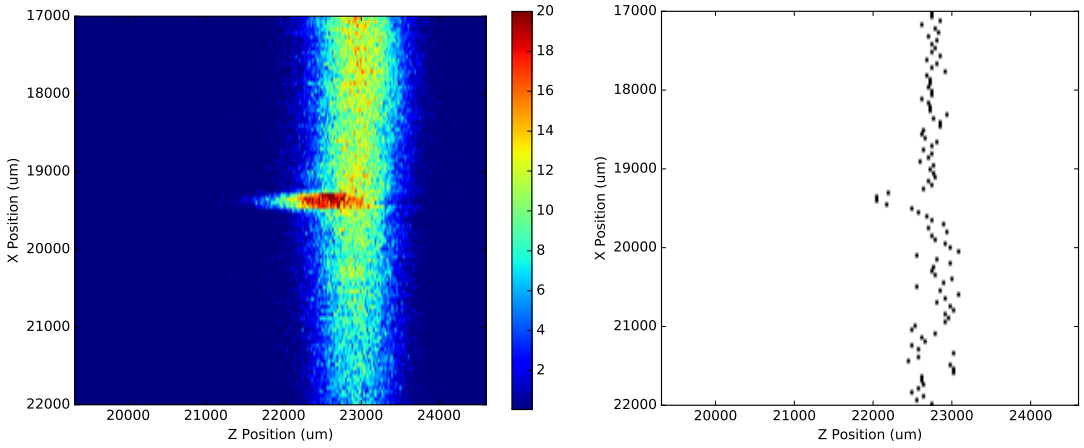

(a) (b)

Figure 5.10: **(a)** Fluorescence image of a flow channel and its **(b)** fluorescence front. In (a) the non-uniform fluorescence intensity along the flow channel is attributed to the skew of the channel relative to the imaging plane. For rows where the maximum intensity does not exceed the channel-boundary value, the half-maximum fluorescence value is used instead. Colour bar has units of fluorescence.

To simplify analysis, each image was partitioned into three horizontal sections with height ratios of 1:2:1, and only the largest fluorescence front displacement in each section is reported. By splitting the image into three sections, the fluorescence front displacement due to diffusion can be estimated from the top section, which is far from the ultrasound focus and cavitation effects; and by reporting the largest fluorescent displacement in each section as opposed to the mean or the median value, deformations were more readily detected and measured (Figure 5.11).

The largest fluorescence front displacement at the top, centre and bottom of an image is represented by S_T, S_C and S_B respectively. Using S_T and S_C, the channel-centre fluorescence front displacement residual, e_C, is calculated: $e_C = S_C - S_T$ (Figure 5.12). e_C provides an estimate of the amount fluorescence front displacement that is not accounted for by diffusion, i.e. due to ultrasound and cavitation effects.

5.4 Order of Execution

The procedures detailed in this chapter are executed in the order shown in Figure 5.13 for all experiments unless otherwise noted.

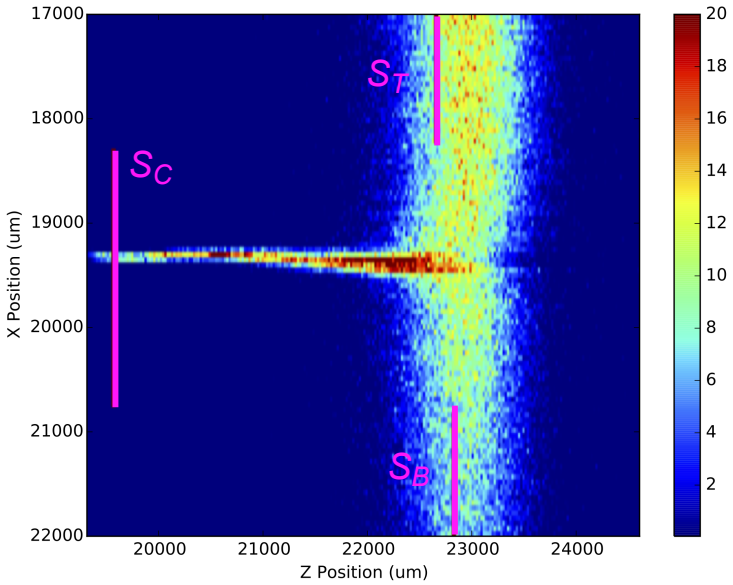

Figure 5.11: Fluorescence fronts with the largest displacements in top, centre and bottom section of an SIOS image. In each section, the height of the section and the location of the most displaced fluorescence front is indicated by a vertical dark red line.

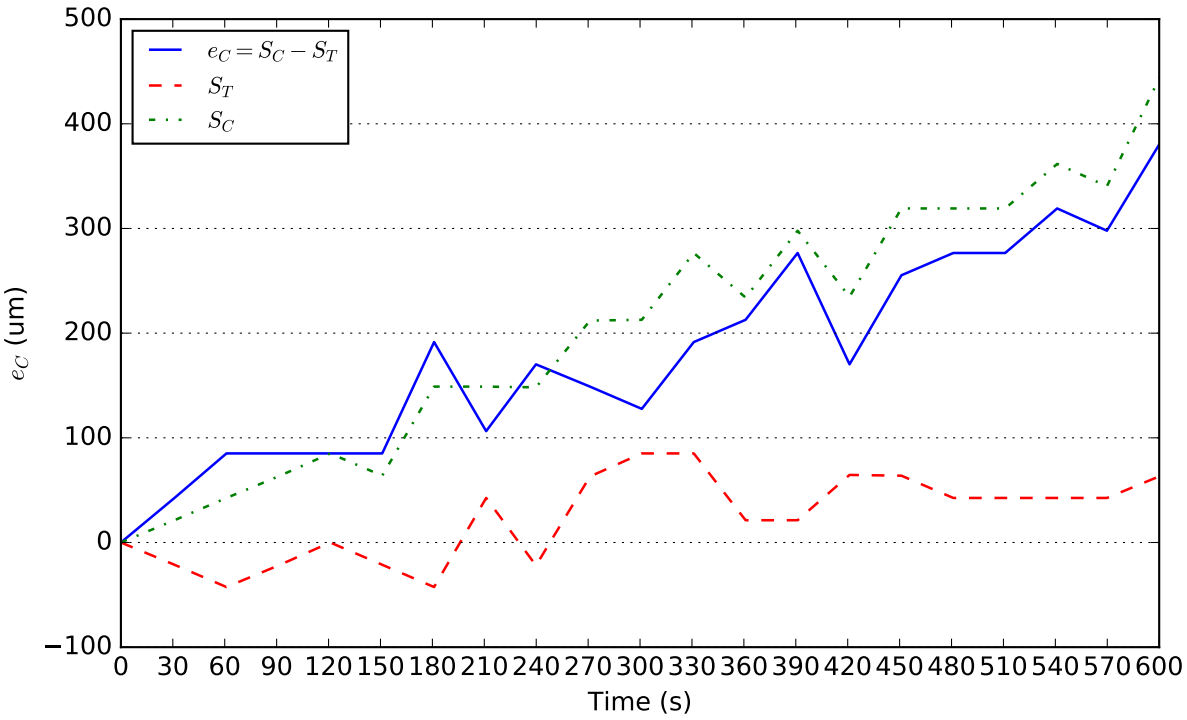

(a)

Figure 5.12: Derivation of channel-centre fluorescence front displacement residual, e_C, from fluorescence front displacement at the top (S_T) and centre of the image (S_C). Data derives from a sequence of 22 images captured during a single experiment.

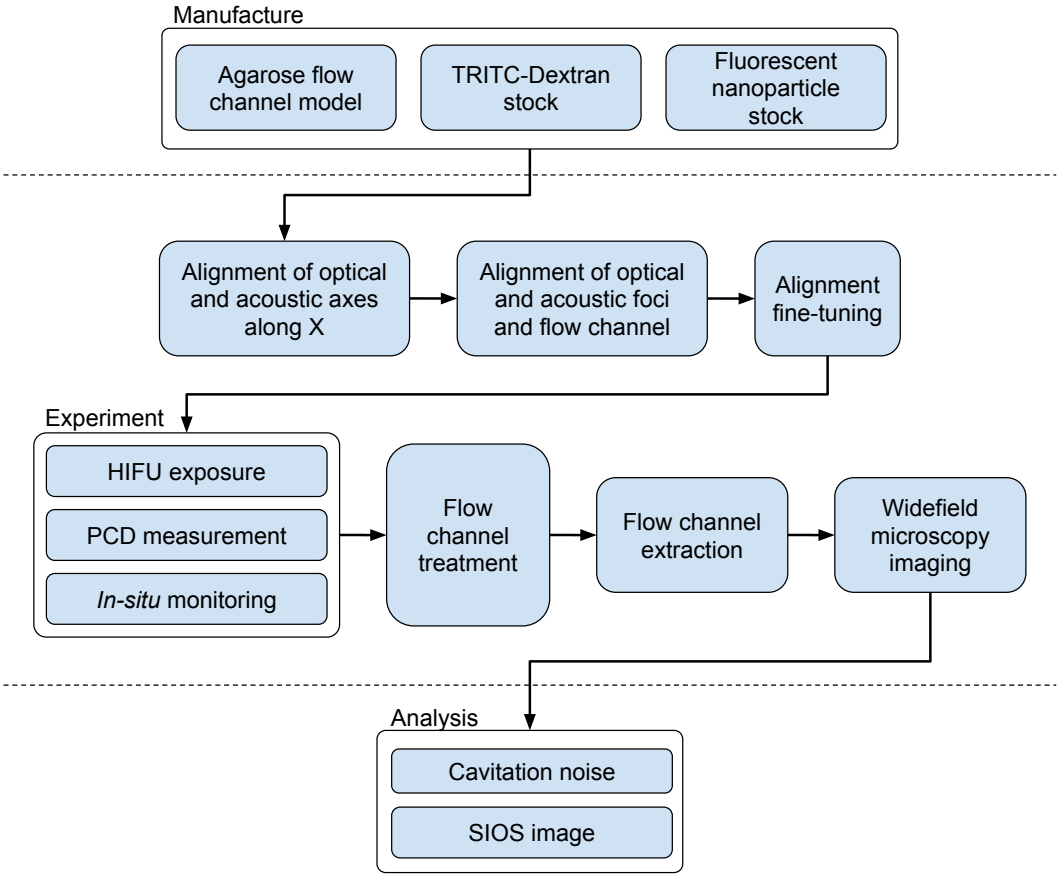

Figure 5.13: Order of execution for procedures detailed in this chapter. The procedures bounded by the dotted lines are performed on the same day.

5.5 Validation

The materials and methods described in this chapter were validated in experiments using nanoparticle loaded microbubbles, the results of which are presented in full in Chapter 7. Briefly, SIOS was used to detect and monitor the development of deformations within agarose channel models, with good correspondence between the *in situ* images produced by SIOS (Figure 5.14) and end-point images obtained with a wide-field microscope (Figure 5.15).

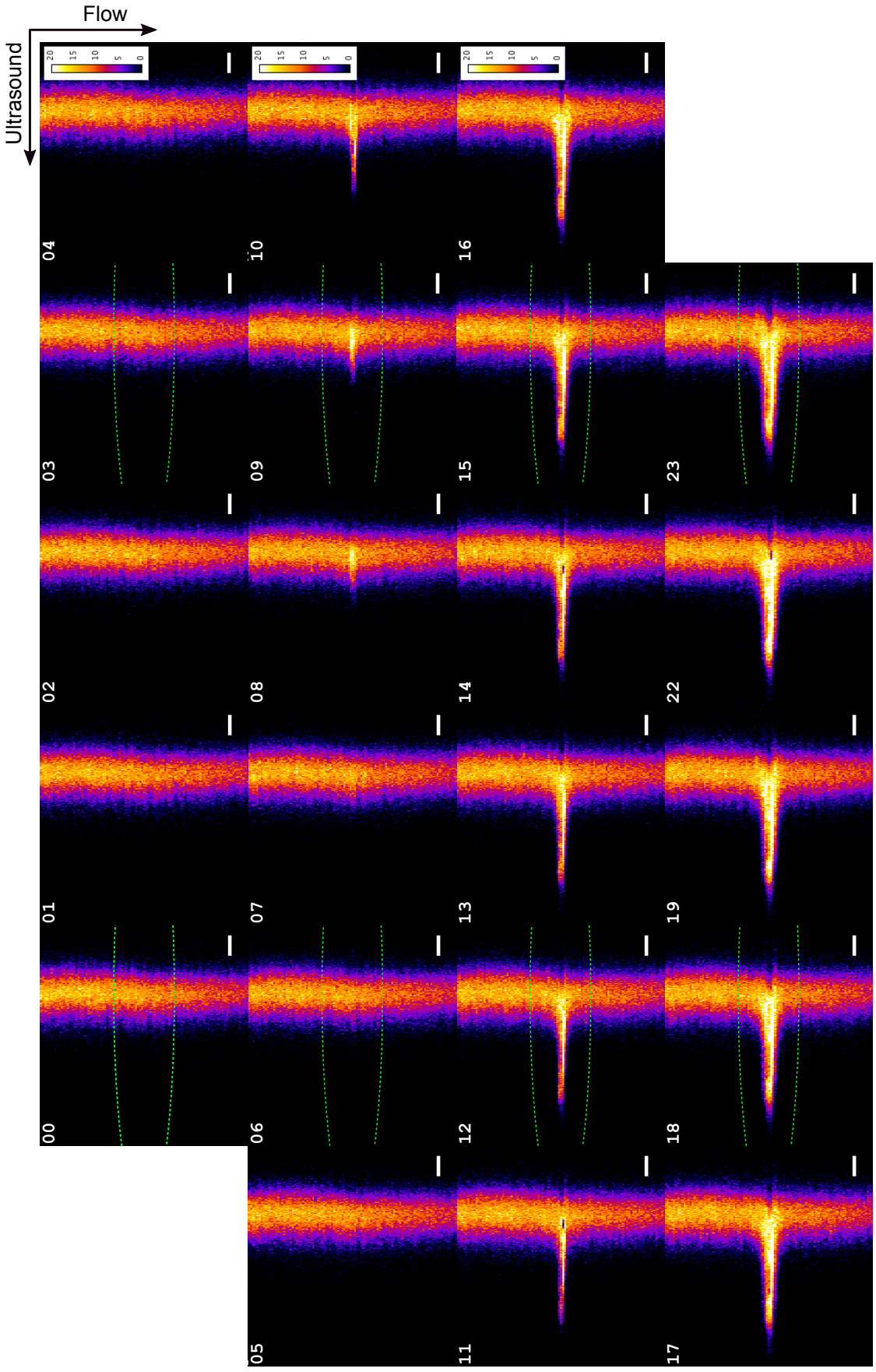

Figure 5.14: *In situ* images produced by SIOS during an experiment using nanoparticle loaded microbubble. Image 0 was taken immediately before ultrasound exposure. Images 1 to 22 were taken 30 s apart during ultrasound exposure. Image 23 was taken immediately after cessation of ultrasound exposure. Deformation in the direction of ultrasound propagation can be clear seen in images 08 to 23. Based on image 23, the deformation extended 2370 µm in the direction of ultrasound. The green dotted lines demarcate the −3 dB boundary of the ultrasound focus.

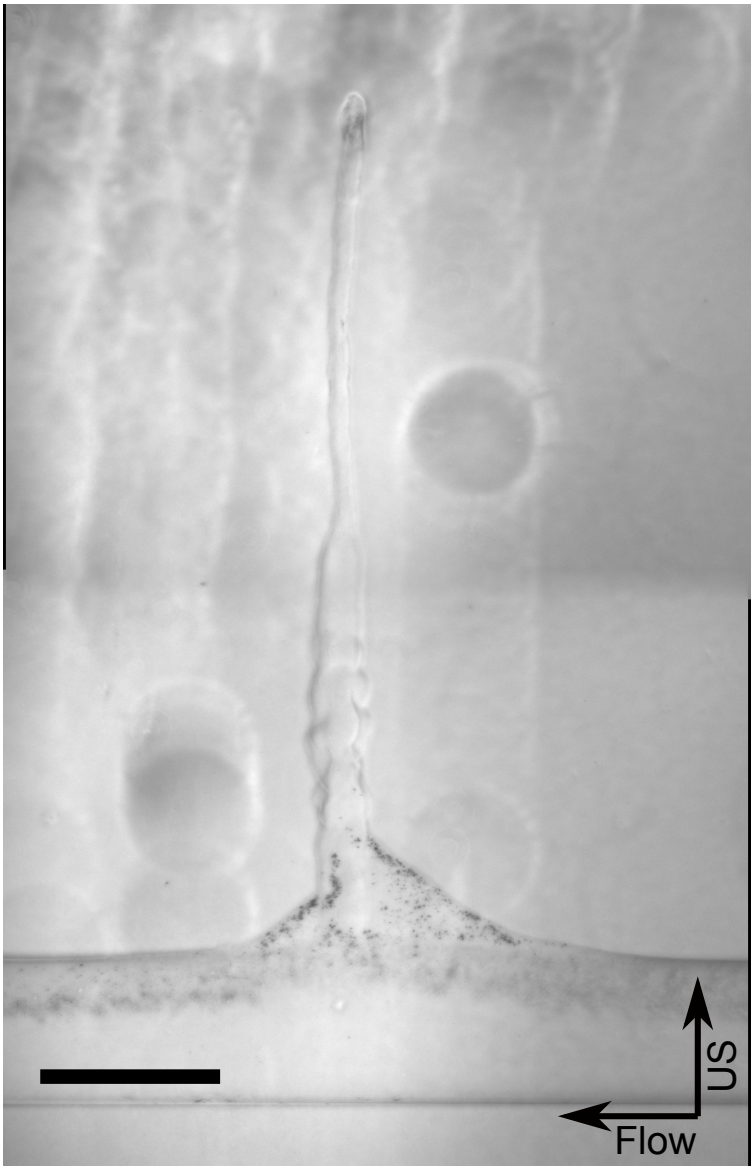

Figure 5.15: End-point microscopy image of the channel section at the ultrasound focus. The deformation measured 2411 µm in the direction of ultrasound.

Chapter 6

Drug Transport and Ultrasound Response of Drug-Eluting Beads

6.1 Introduction

Transarterial chemoembolisation (TACE) is a clinical treatment for hepatocellular carcinoma. Using a catheter placed in an artery directly connected to a tumour, TACE delivers a targeted dose of chemotherapy agents, such as doxorubicin or cisplatin. Following this, the artery is embolised using a blocking material to eliminate blood flow. By combining chemotherapy and embolisation, TACE simultaneously starves the tumour of nutrients while prolonging its exposure to chemotherapy agents, resulting in higher treatment response rates and reduced systematic drug levels and toxicity [1].

Drug-eluting beads (DEBs) are micrometre diameter beads loaded with chemotherapy drugs that are gradually released following implantation. When used in TACE (DEB-TACE), DEBs act as the drug delivery vehicle and the embolising material, and confer two advantages: the gradual release of chemotherapy agents further increases their contact time with tumours; and by delivering the drug dose at a slower rate, systematic toxicity is reduced. In published studies, the clinical outcomes of DEB-TACE have been found to be equal to or better than conventional TACE [2–5]. At the same time, DEB-TRACE resulted in significantly lower peak drug concentrations in serum and required a smaller total drug dose [2, 5].

Of interest to the current work is the pharmacokinetics of DEBs, specifically DC

Bead™ (Biocompatibles UK, UK) [6, 7] and RO Bead™ (Biocompatibles UK) [8], the latter of which is radiopaque and visible under X-ray imaging. The treatment efficacy of these DEBs is determined by their rate of drug release, and the penetration of the eluted drug into the surrounding tissue. By studying these characteristics in models that mimic *in vivo* conditions, both chemically and geometrically, the efficacy of these and other DEBs can be more readily determined, allowing for more rapid DEB development. Additionally, the effects of ultrasound exposure on DEBs are of interest as some evidence suggests it may enhance the rate of drug release [9]. Furthermore, ultrasound exposure could also increase the penetration of eluted drugs into the surrounding tissue, as well as enhance the permeability of cells [10, 11].

The aim of this chapter is to evaluate the utility of SIOS for the purposes of characterising, *in vivo*, DEB pharmacokinetics and the effects of ultrasound exposure on drug release and penetration.

6.2 Materials

6.2.1 Beads

70 to 150 µm diameter DC and RO beads, loaded with 37.5 mg mL^{-1} of doxorubicin, were received from Biocompatibles UK. As supplied, beads were suspended in deionised (DI) water in separate containers. In addition to the DEBs, Biocompatibles UK also provided acid washed glass beads with diameters of 150 to 212 µm.

A particular characteristic of DC and RO beads is that they both swell when releasing doxorubicin. Of the two, swelling is less in RO beads due to their added radiopaque moiety, which also reduces the rate of doxorubicin release.

6.2.2 Agarose-Alginate Channel Models

Agarose-alginate channel models were manufactured as described in Chapter 5, using 0.5 % alginate mixed with 1.5 % agarose. The addition of alginate increased the interactions between the hydrogel matrix and doxorubicin molecules, providing a more accurate simulation of *in vivo* conditions by slowing doxorubicin diffusion. In order to

simulate arteries, the channel models featured 1.6 mm diameter flow channels.

6.2.3 Doxorubicin Calibration Gels

Calibration gels, consisted of 1.0 % w/v agarose containing doxorubicin at concentrations of 10 µM, 15 µM, 20 µM, 30 µM, 40 µM, and 50 µM, were supplied by Biocompatibles UK.

6.3 Methods

6.3.1 Instrument Sensitivity

In order for fluorescence measurements to be comparable across experiments, the instrument sensitivity was kept constant by fixing the PMT control voltage at 600 mV and the laser forward current at 60 mA, with the latter corresponding to 0.73 mW of optical output power[1]. When triggered by the Z stage, the PMT output is sampled 8 times and accumulated into a single reading. The number of samples per trigger can be varied as needed because its effect on the measured value is linear, and therefore, measurements at different settings can be compared after appropriate scaling.

6.3.2 Doxorubicin Detection and Measurement

Doxorubicin is naturally fluorescent at the excitation wavelength used by SIOS and thus can be detected directly. In order to convert a fluorescence value into a measurement of doxorubicin concentration, a standard curve was obtained by measuring known concentrations of doxorubicin and noting the resulting output. To more accurately simulate experimental conditions, and to take into account the effects of scattering and attenuation due to the agarose-alginate gel, calibration gels were injected into flow channels and measured *in situ* while channel models were submerged in water.

For each calibration gel, lateral cross-section scans of gel filled channels were taken at 2 min intervals for one hour. By using lateral cross sections scans, the instrument

[1] Due to scattering and absorption by the air-water interface and the agarose-alginate gel, the optical power at focus within the channel model will be less.

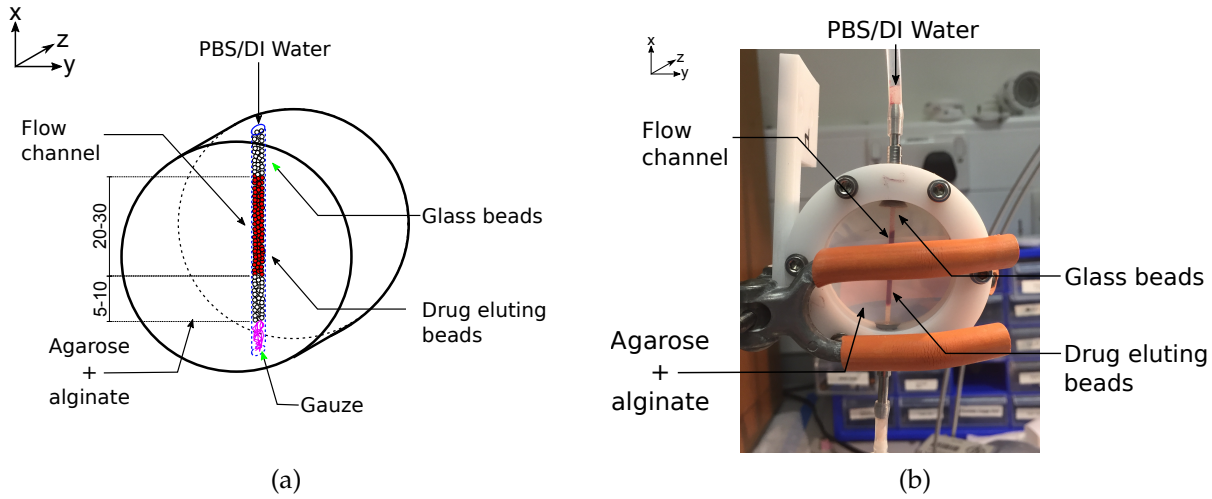

Figure 6.1: Packed agarose flow channel models. (a) Packing of an agarose flow channel with glass and drug-eluting beads (b) Photograph of a packed flow channel. Measurements are in millimetres.

need not be perfectly aligned to the same vertical position in each channel, reducing the effect of misalignments between samples. The scanning interval of 2 min was previously found to be sufficient to avoid overt photobleaching. Due to a limit supply of calibration gels and the destructive nature of measurement due to photobleaching, a single standard curve was derived and used for all results presented here.

In order for the standard curve to be applicable to experimental results, the laser forward current and PMT control voltage used to obtain the standard curve was also used in all experiments. While the optical power output was not checked each time, given the temperature controlled environment within which the laser operates, the optical power output is expected to be consistent across experiments.

6.3.3 Channel Packing

Embolisation was modelled by packing a flow channel with glass beads and DEBs. Such a channel is as shown in Figure 6.1. Channel packing was accomplished by first inserting gauze at the outflow end of the flow channel, then infusing the channel with DI water. When the channel was filled, the outflow end was blocked, resulting in a static column of DI water within the channel. Glass beads were then added to the top of the water column with a pipette and allowed to sink. When the height of the glass beads within the channel was between 5 to 10 mm, DEBs were added until the beads

were 5 to 10 mm from the top of the channel. The remaining space was then packed with glass beads.

After packing, the channel models are referred to as agarose-alginate packed channel models.

6.3.4 PBS Infusion

The mechanism of doxorubicin release from the DEBs requires the presence of ions in the surrounding liquid. To provide these ions, phosphate-buffered saline (PBS) at $1\times$ concentration (Cat. No. 14190250; ThermoFisher Scientific, US) was allowed to flow through packed channels for 30 min under gravity. Due to variabilities in the channel packing density, the flow rate, and therefore the volume, of PBS through the packed channels can differ drastically. Furthermore, due to swelling of DC and RO beads when eluting doxorubicin, the concentration of PBS within a channel is expected to be a gradient, with the highest concentration at the top of the channel, where PBS enters, and lower concentrations further away. As DC beads experience more swelling than RO beads, the PBS concentration gradient is expected to be more pronounced in channels packed with DC beads than in channels packed with RO beads.

6.3.5 DEB Elution and Ultrasound Exposure

Embolised channel models were placed within the experimental setup and aligned as described in Chapter 5. The models were oriented such that the packed channels were horizontal, and the top the channel was towards the origin of the X axis. Once aligned to optical and acoustic foci, the elution of doxorubicin from a packed channel was monitored over 120 min, with one XZ plane scan of the channel taken every 2 min, starting at $t = 0$. In total, each channel was scanned 61 times.

To determine if ultrasound exposure affects the release of doxorubicin from packed channels, or its penetration into the surrounding hydrogel, some packed channels were exposed to 10 min of ultrasound at $t = 55$ min at 1.067 MHz, 1.04 MPa peak-negative pressure, 1.0 kHz pulse-repetition frequency and 1.87 % duty cycle. These parameters were chosen to reflect what would be possible with commercially available ultrasound

machines. As the aim of these experiments was to determine the suitability of the system for investigating ultrasound effects, and not to investigate the ultrasound effects themselves, other exposure parameters were not considered.

By allowing embolised channels to passively diffuse prior to ultrasound exposure, doxorubicin release and distribution before, during and after ultrasound exposure can be compared. This approach, made possible with the real-time *in situ* imaging capabilities of SIOS, minimises the effect of variabilities in the channel packing density and PBS exposure, significantly reducing the number of experiments required.

Water temperature during monitoring and ultrasound exposure was kept at 18 °C to 19 °C.

6.3.6 Drug Transport Analysis

The rate of doxorubicin release from DC and RO bead packed channels was measured using total image fluorescence. Total image fluorescence is computed by summing the value of all pixels within an image, and is comparable across experiments provided the number of pixels, determined by the field-of-view and scan resolution, is kept constant, and the resulting sum is scaled by the number of samples per trigger.

The penetration of released doxorubicin into the surrounding agarose-alginate gel was determined using fluorescence front displacement analysis, described in Chapter 5.

6.3.7 Experimental Groups

Three ultrasound exposure experiments and one control experiment were performed using DC bead packed channels. For RO bead packed channels, one ultrasound exposure experiment and two control experiments were performed. The number of RO bead experiments was dictated by time constraints.

Doxorubicin Concentration (μM)	Mean 99th Percentile Fluorescence Value (a.u.)	SD
50	2.40	0.21
30	1.50	0.22
20	0.81	0.02

Table 6.1: Calibration values for Doxorubicin concentration. **SD**: standard deviation.

6.4 Results and Discussion

6.4.1 Doxorubicin Calibration and Detection Limit

Measurements of calibration gels within a flow channel produced images such as the one shown in Figure 6.2a, with fluorescence values distributed as shown in Figure 6.2b. Due to the localisation of the fluorescence signal towards the centre of the image, the histogram is biased towards zero. Eliminating the dark pixels by thresholding produces the histogram shown in the inset of Figure 6.2b. Due to the cylindrical distribution of the calibration gel within the flow channel, position-dependent scattering and absorption by the agar-alginate gel, and diffusion during measurements, the fluorescence intensity is broadly distributed. Under the assumption that the brightest measured values are produced by regions with the highest concentrations of doxorubicin, the 99th percentile was chosen as the measure that best reflects the "true" fluorescence value that corresponds a given doxorubicin concentration. This approach yielded the calibration curve shown in Figure 6.3, where data for 20 μM was at the limits of detection, with measurements falling to the noise-floor after 10 min. Table 6.1 tabulates the calibration values.

Based on these results, and with the instrument settings used here, the lower limit of doxorubicin detection is 20 μM. It is possible to lower this limit by increasing the number of exposures, which would improve the SNR; lowering the agarose concentration, which would reduce scattering and absorption at the expense of model robustness; and increasing the PMT sensitivity, which would require better light shielding.

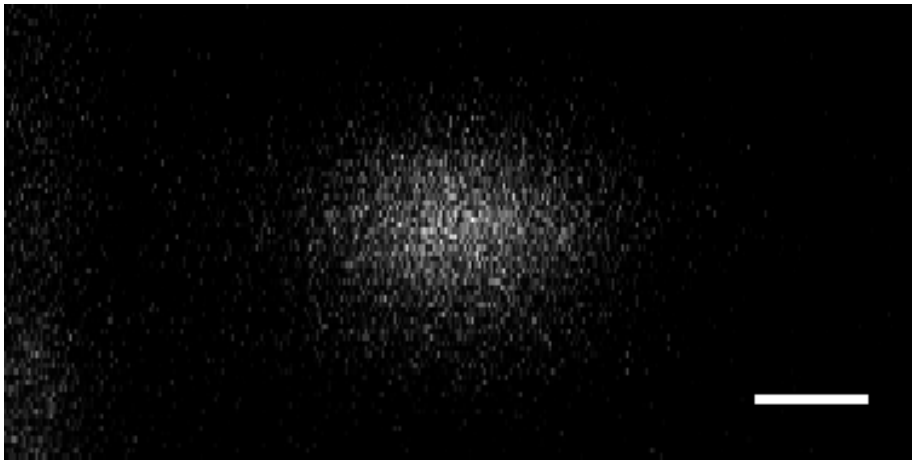

(a)

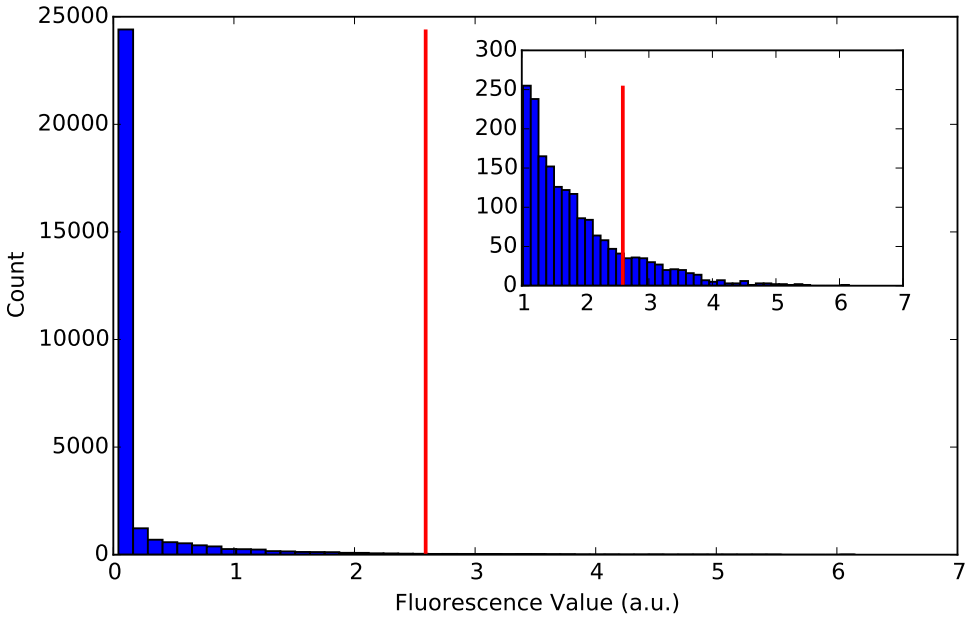

(b)

Figure 6.2: **(a)** YZ plane scan of 50 µM doxorubicin calibration gel within a flow channel. Fluorescence at the left edge of the image is due to reflection and scattering by the optical window. **(b)** Histogram of pixel values in (a) with 99th percentile (2.59) indicated. A close up is shown in the inset to better illustrate the distribution of bright pixels. Scale bar is 1000 µm.

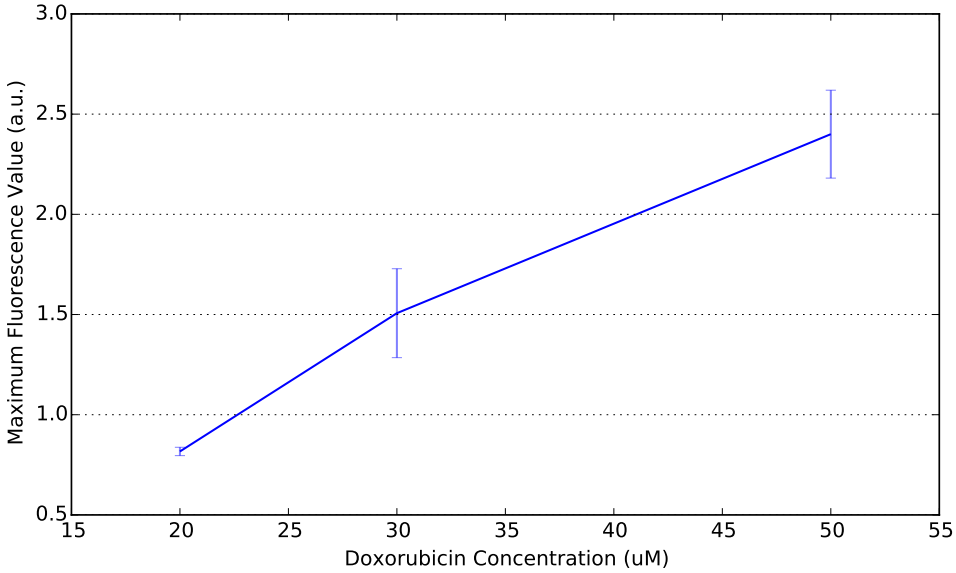

Figure 6.3: Calibration curve for doxorubicin within ACMs. Each value is the mean of 3 measurements and the error bars represent one standard deviation.

6.4.2 Effect of Ultrasound Exposure

6.4.2.1 DC Bead Packed Channels

Images of DC bead packed channels were analysed to assess the effect of ultrasound exposure. If ultrasound exposure increased the rate at which doxorubicin was released by DC beads, or the penetration of doxorubicin into the surrounding agarose-alginate gel, then the fluorescence values within the ultrasound focus are expected to increase during and after ultrasound exposure. By inspection of Figure 6.4, there is no evidence of such enhancement.

In order to more quantitatively assess the effect of ultrasound, the channel-centre fluorescence front displacement residual, e_C, was calculated as described in Chapter 5. If doxorubicin release and penetration were increased by ultrasound exposure, then values of e_C should also increase post ultrasound exposure. Alternatively, ultrasound exposure may reduce doxorubicin release and penetration, in which case the values of e_c should decrease following ultrasound exposure. Based on Figure 6.5 and Table 6.2, the values of e_C before and after ultrasound exposure were not significantly different.

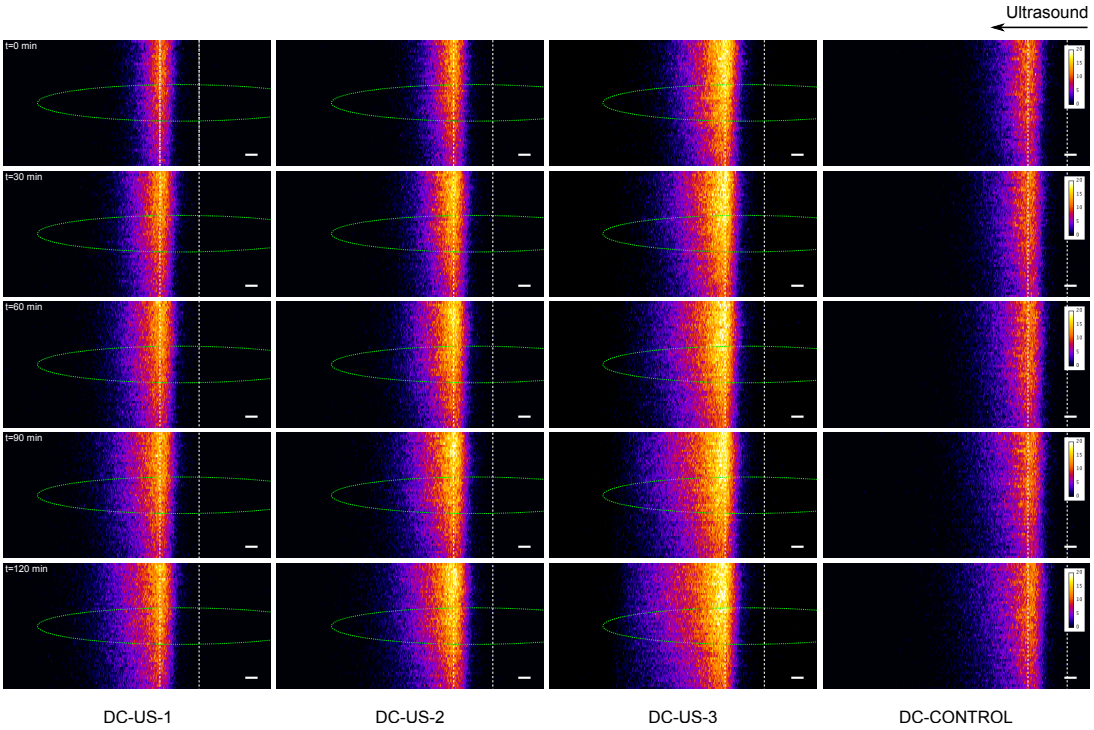

Figure 6.4: Selected XZ plane scans of DC bead packed channels over 120 min with (DC-US) and without ultrasound exposure (DC-CONTROL). As shown, the top of each image corresponds to the top of the channel during the packing process (Figure 6.1). The boundaries of the packed channels are indicated by the dashed white lines, and the estimated -3 dB boundary of the ultrasound focus is demarcated in green. Due to the opaqueness of DC beads, only the outer shell of DC beads is visible. The non-uniform distribution of doxorubicin is attributed to the aforementioned PBS concentration gradient, with higher PBS concentrations resulting in faster rates of doxorubicin release. Differences in the brightness of images from DC-US experiments are attributed to variation in the channel packing density and PBS exposure. In DC-CONTROL, experimenter error resulted in images being acquired with twice the X resolution of images in DC-US experiments, resulting in increased photobleaching and lower image brightness. Scale bars are 500 µm.

					Two-tailed dependent t-test	
Experiments	μ_0	SD	μ_1	SD	t	p
DC-US-1	12.15	122.74	6.06	159.65	0.20	0.8422
DC-US-2	23.55	92.58	-20.51	146.74	1.47	0.1529
DC-US-3	86.60	134.88	85.07	233.49	0.03	0.9774
DC-CONTROL	-126.83	125.48	-161.01	157.14	0.93	0.3615

Table 6.2: Mean value of e_C in models with DC bead packed channels before (μ_0) and after (μ_1) ultrasound exposure. μ_0 and μ_1 have units of µm.

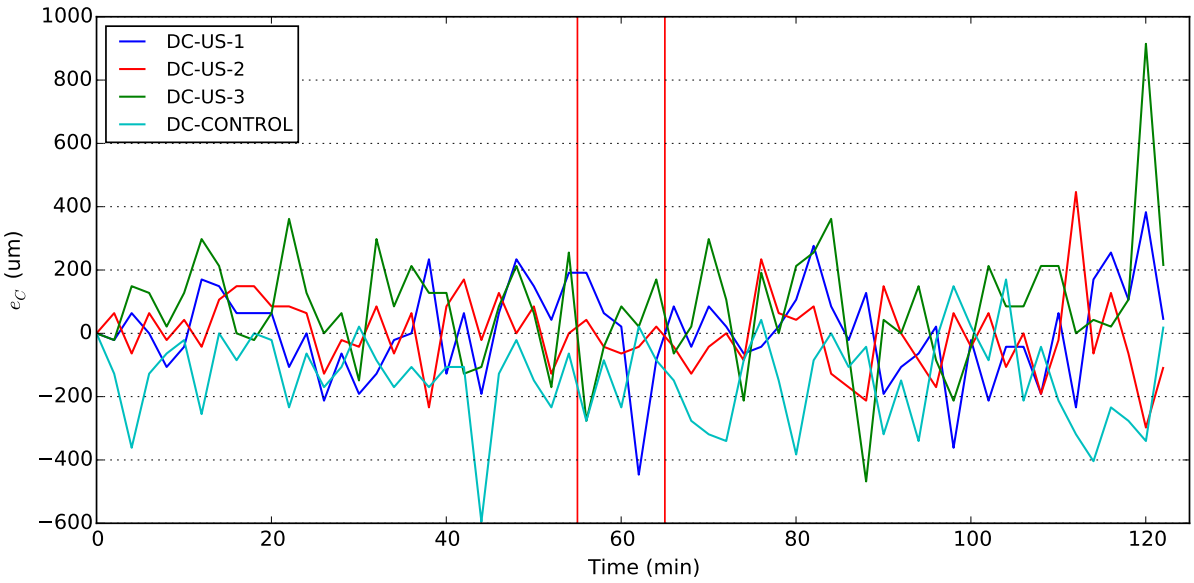

(a)

Figure 6.5: Channel-centre fluorescence front displacement residual, e_C, in models with DC bead packed channels. The vertical red lines indicate the start and end of ultrasound exposure during non-control experiments.

					Two-tailed dependent t-test	
Experiments	μ_0	SD	μ_1	SD	t	p
RO-US-1	48.63	92.17	94.21	138.61	-1.23	0.2280
RO-CONTROL-1	-220.26	97.16	-246.08	99.82	0.89	0.3829
RO-CONTROL-2	36.46	135.47	18.23	98.08	0.57	0.5718

Table 6.3: Mean value of e_C in models with RO bead packed channels before ultrasound exposure (μ_0) and after (μ_1). μ_0 and μ_1 have units of µm.

6.4.2.2 RO Bead Packed Channels

The effect of ultrasound exposure on RO bead packed channels was similarly analysed, and no localised enhancement of fluorescence was observed in any experiment (Figure 6.6). Similarly, ultrasound exposure produced no significant change in the values of e_C (Figure 6.7 and Table 6.3). These results indicate that ultrasound exposure has no detectable effect on doxorubicin release and penetration in models with RO bead packed channels.

6.4.2.3 Discussion

While ultrasound exposure was previously found to increase doxorubicin elution from DEBs in microfluidic devices [9], no similar increase was observed in experiments with

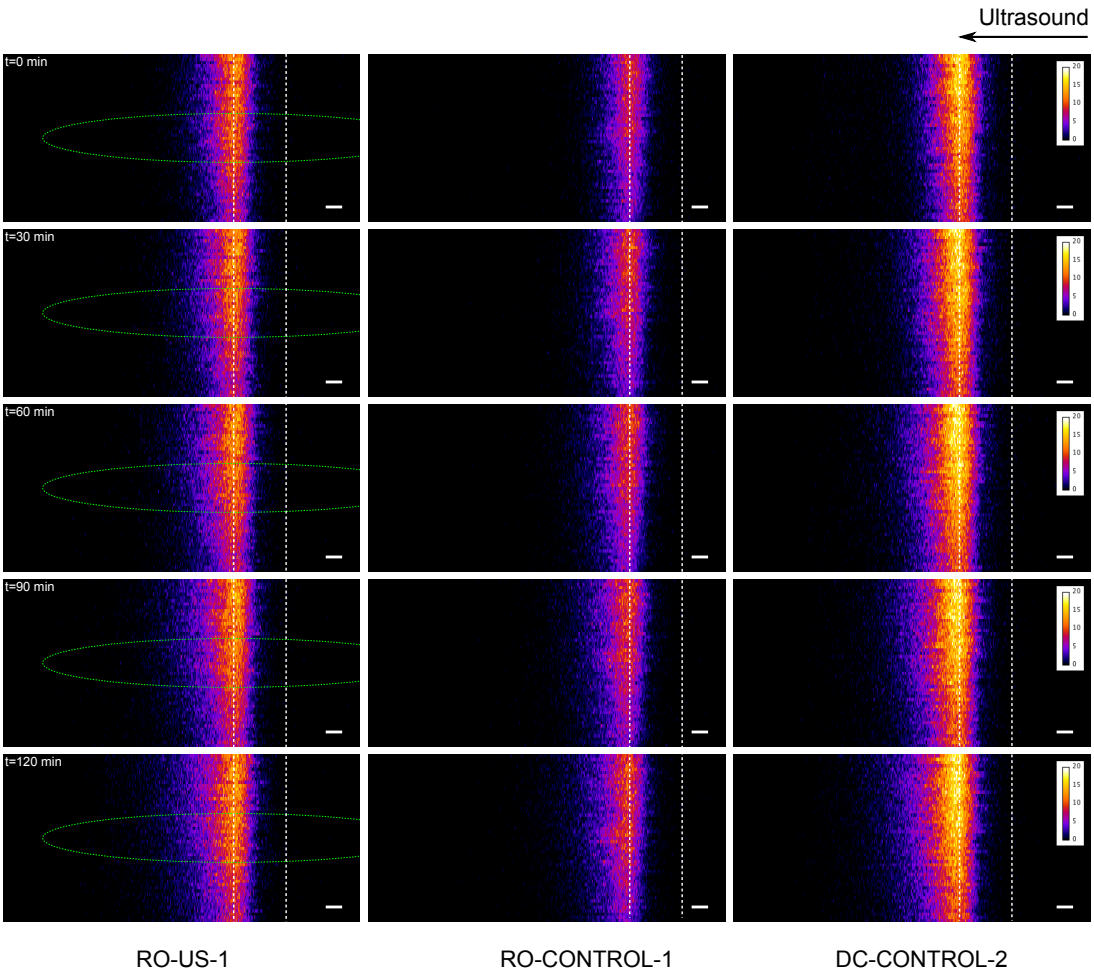

Figure 6.6: Selected XZ plane scans of RO bead packed channels over 120 min with (RO-US) and without ultrasound exposure (RO-CONTROL). As shown, the top of each image corresponds to the top of channels during the packing process (Figure 6.1). The boundaries of the packed channel are indicated by the dashed white lines, and the estimated -3 dB boundary of the ultrasound focus is demarcated in green. Due to the more uniform distribution of PBS in RO bead packed channels, the distribution of doxorubicin is more uniform than in models with DC bead packed channels (Figure 6.4). Differences in the brightness of images are attributed to variations in the channel packing density and PBS exposure. Scale bars are 500 µm.

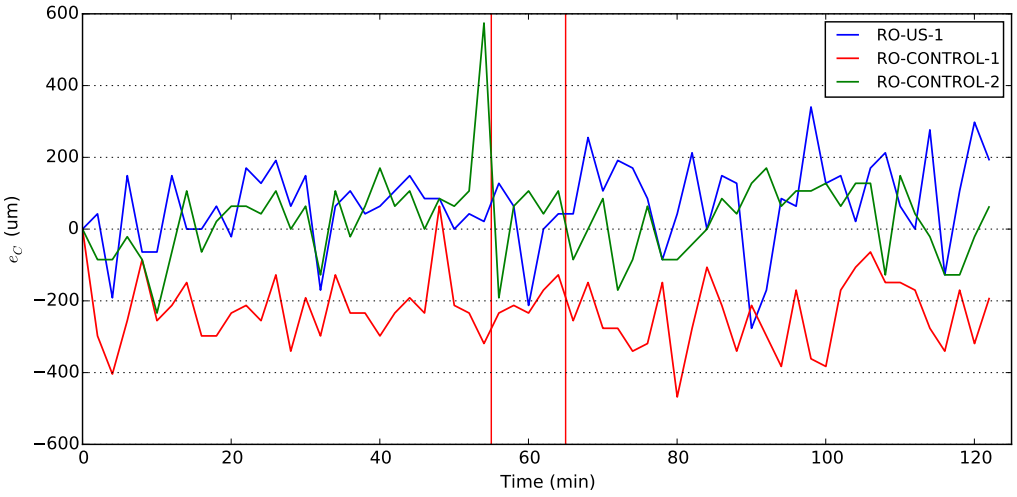

Figure 6.7: Channel-centre fluorescence front displacement residual, e_C, in models with RO bead packed channels. The vertical red lines indicate the start and end of ultrasound exposure during non-control experiments. The sudden increase seen in RO-CONTROL-2 immediately prior to ultrasound exposures was due to an unexpected increase in the ambient lighting.

DC or RO bead packed channels. These contradictory findings can be explained if, as suggested in [9], the increase in doxorubicin elution in microfluidic devices was due to heating by the ultrasound transducer. In the experiments presented here, heat transfer between the HIFU transducer and the channel models was negligible due to the 62 mm separation distance, and heating due to ultrasound exposure is extremely unlikely due to the low frequency and duty cycle used. The thermal isolation of channel models is one of the advantages of the current system, and may account for the discrepancies between previous findings and those reported here.

6.4.3 Drug Transport

6.4.3.1 Doxorubicin Release

The release of doxorubicin from DC beads has been previously characterised, *in situ*, by suspending the beads in PBS, and measuring the absorption of UV light by eluted doxorubicin [12]. This approach yielded a logarithmic release profile (Figure 6.8). In contrast, the release of doxorubicin from DC and RO bead packed channels followed a linear trend (Figure 6.9). The difference between these results can explained by the slower diffusion of doxorubicin through the agarose-alginate gel, the result of interactions between the alginate salt ions in the gel matrix and the doxorubicin molecules.

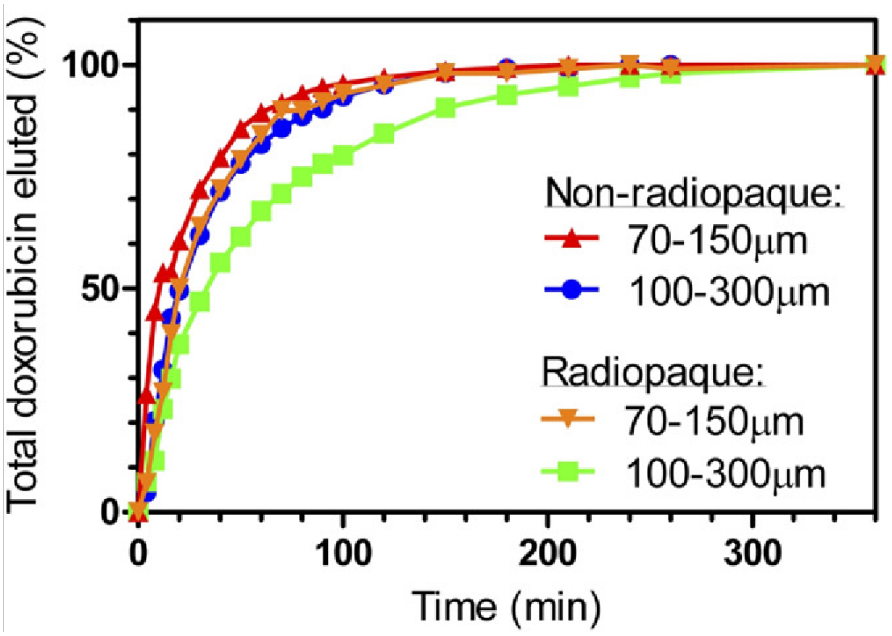

Figure 6.8: Doxorubicin release profile from DEBs in PBS solution [12]. DC beads labelled as non-radiopaque. The radiopaque curves are not applicable to the RO beads due to the difference in composition. The size of interest is 70 to 150 µm. Each curve is the result of one experiment.

Compared with previous findings, the present results, obtained with SIOS and packed channel models, are much more realistic, mimicking not only the interaction between tissue and doxorubicin, but also the geometry of embolised vessels.

Lastly, the rate of doxorubicin release cannot be used to distinguish between experiments with ultrasound exposure and those without, lending further support to the above finding that ultrasound exposure has no detectable affect on drug elution from DC or RO beads.

6.4.3.2 Doxorubicin Penetration

Penetration of doxorubicin into the agarose-alginate gel was approximately 4000 µm channel models with DC bead packed channels, and 2500 µm in models with RO bead packed channels (Figure 6.10). This is consistent with the fact that DC beads elute doxorubicin faster than RO beads.

For comparison, doxorubicin from a 500 µm diameter swine liver vessel packed with radiopaque DC beads[1] was found to penetrate approximately 700 µm into the surrounding tissue (Figure 6.11). Given the slower elution rate of radiopaque DC beads

[1] An alternative formulation of DC beads that is distinct from RO beads.

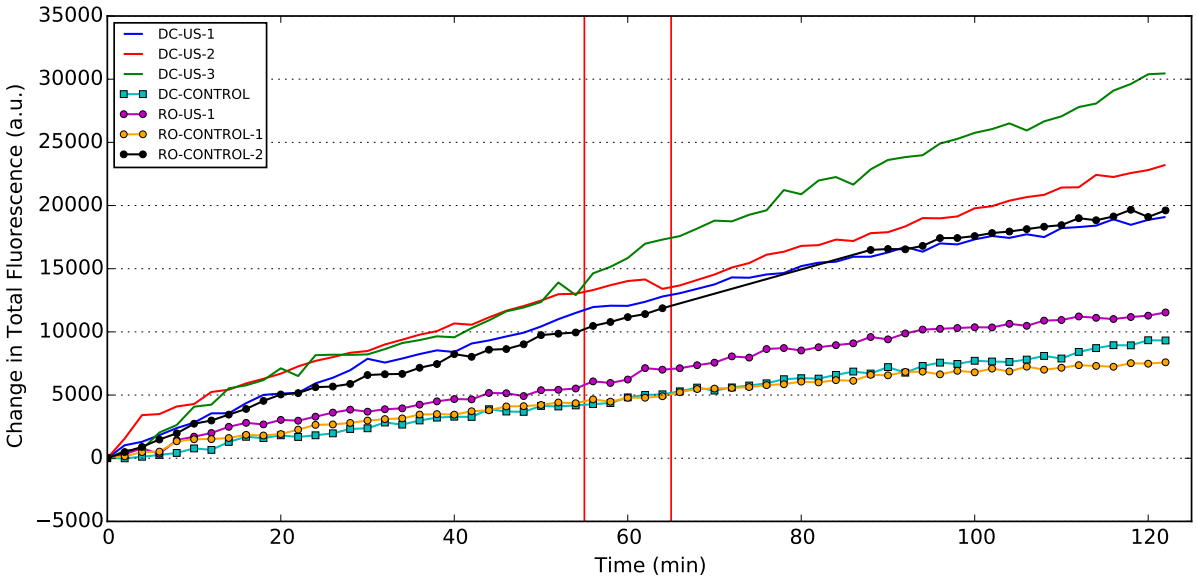

Figure 6.9: Change in total fluorescence in images of DC and RO bead packed channels over 2 h. The red lines indicate the start and end of ultrasound exposure during non-control experiments. Plots have been adjusted to correct for external factors, e.g. the expected increase in ambient lighting conditions seen in RO-CONTROL-2. Data from DC-CONTROL, which experienced more photobleaching than other DC bead experiments, is presented unmodified as the necessary correction factor is not known.

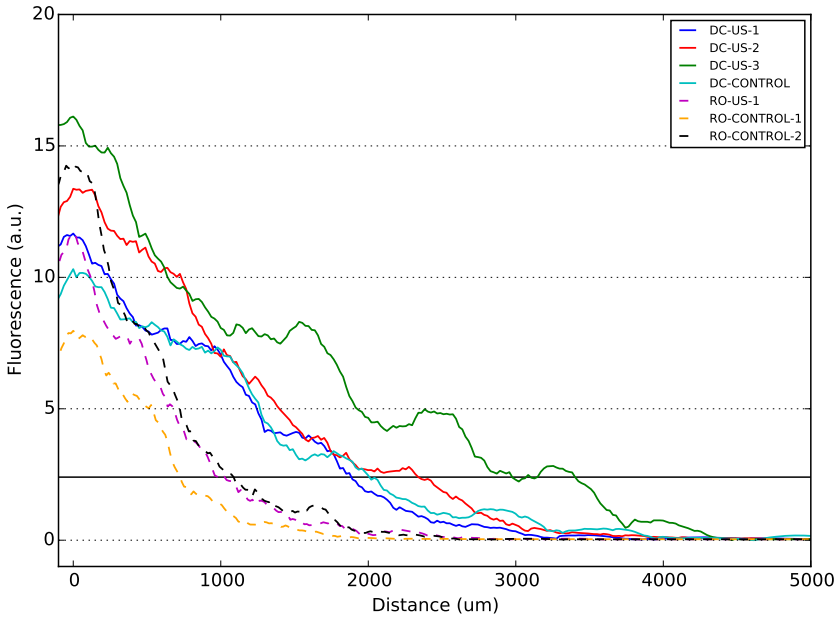

Figure 6.10: Line profiles of fluorescence intensity at $t = 2$ h in models with DC and RO bead packed channels. Using the images taken at $t = 2$ h, profiles are extracted from the centre row of each image, starting from the fluorescence maximum and extend towards the instrument objective. The black horizontal line denotes the fluorescence value that corresponds a doxorubicin concentration of 50 µM. Each curve was filtered using a second order Savitzky–Golay filter with a window size of 31.

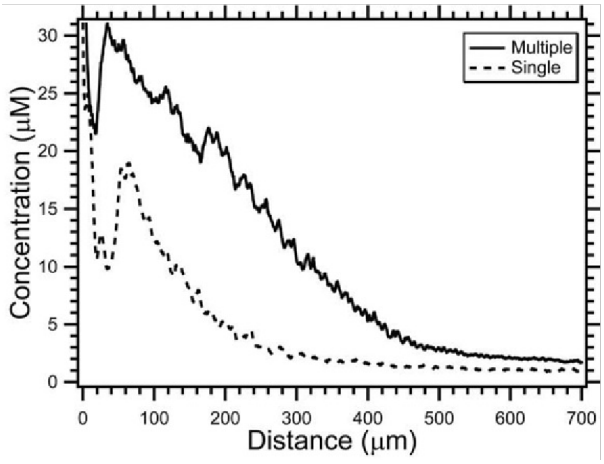

Figure 6.11: Penetration of doxorubicin from radiopaque DC beads into swine liver tissue [12]. Single and multiple refers to doxorubicin released by a single bead or multiple beads within a 500 μm diameter vessel.

(Figure 6.8) and the size difference between the liver vessel and packed channels, the difference in penetration distance is not unreasonable.

6.4.3.3 Agarose-Alginate Packed Channel Model

The agarose-alginate packed channel model appears to be a promising model for simulating DEB-TACE. It is capable of modelling not only the interactions between tissue and doxorubicin, but also the geometry of embolised vessels. A key component of the model is the agarose-alginate gel, which mimics the *in vivo* interactions between tissue and doxorubicin. By tuning the concentration of alginate and channel diameters, different tissue types and target vessel sizes can be modelled *in vitro*, enabling faster development and testing of DEB.

The use of agarose-alginate packed channel models is possible due to the *in situ* imaging capabilities of SIOS. The *in situ* images provided eliminated the need to section the models, significantly reducing the number of experiments required for drug transport studies. Furthermore, SIOS enabled the release and penetration of doxorubicin within these packed channel models to be measured directly and in real-time, whereas experiments using swine [12], rabbit [13] and human livers [14] relied on indirect or time-delayed techniques, e.g. plasma liver enzyme concentration, tissue sectioning and histology.

Together, SIOS and agarose-alginate packed channel models form a promising plat-

form for the *in vitro* study of DEB pharmacokinetics.

6.5 Summary

The pharmacokinetics of DC and RO bead packed channels was studied *in situ* with the developed instrument in agarose-alginate packed channel models. The doxorubicin release profile for DC and RO bead packed channels were found to be linear over a period of 2 h, with the rate of doxorubicin release higher in DC bead packed channels than in RO bead packed channels. Compared to previous pharmacokinetic studies in PBS, the results presented here is much more representative of *in vivo* conditions, with the agarose-alginate packed channel models simulating not only the geometry of embolised vessels but also the interactions between tissue and doxorubicin. Based on these results, the combination of SIOS and agarose-alginate packed channel models offer a promising platform for the *in vitro* study of DEB pharmacokinetics.

In addition to the pharmacokinetic studies, the effect of ultrasound exposure on DEB packed channels was also investigated. With the settings used, ultrasound exposure did not produce detectable effects on doxorubicin release or penetration. However as the experiments were primarily exploratory, further investigations may yield fruit.

References

[1] Sung Wook Shin. The current practice of transarterial chemoembolization for the treatment of hepatocellular carcinoma. *Korean journal of radiology*, 10(5):425–434, 2009.

[2] María Varela, María Isabel Real, Marta Burrel, Alejandro Forner, Margarita Sala, Mercé Brunet, Carmen Ayuso, Lluis Castells, Xavier Montañá, Josep M Llovet, et al. Chemoembolization of hepatocellular carcinoma with drug eluting beads: efficacy and doxorubicin pharmacokinetics. *Journal of hepatology*, 46(3):474–481, 2007.

[3] Philipp Wiggermann, Dominik Sieron, Christiane Brosche, Thomas Brauer, Fabian Scheer, Ivan Platzek, Wojciech Wawrzynek, and Christian Stroszczynski. Transarterial chemoembolization of child-a hepatocellular carcinoma: drug-eluting bead tace (deb tace) vs. tace with cisplatin/lipiodol (ctace). *Medical Science Monitor*, 17(4):CR189–CR195, 2011.

[4] Sheng Gao, Zhe Yang, Zhiyun Zheng, Jia Yao, Min Deng, Haiyang Xie, Shusen Zheng, and Lin Zhou. Doxorubicin-eluting bead versus conventional tace for unresectable hepatocellular carcinoma: a meta-analysis. *Hepato-gastroenterology*, 60(124):813–820, 2013.

[5] Eleni Liapi and Jean-Francois H Geschwind. Transcatheter arterial chemoembolization for liver cancer: is it time to distinguish conventional from drug-eluting chemoembolization? *Cardiovascular and interventional radiology*, 34(1):37–49, 2011.

[6] Andrew L Lewis, Matthew R Dreher, Vincent O'Byrne, David Grey, Marcus Caine, Anthony Dunn, Yiqing Tang, Brenda Hall, Kirk D Fowers, Carmen Gacchina John-

son, et al. Dc beadm1: towards an optimal transcatheter hepatic tumour therapy. *Journal of Materials Science: Materials in Medicine*, 27(1):1–12, 2016.

[7] Andrew L Lewis, M Victoria Gonzalez, Andrew W Lloyd, Brenda Hall, Yiqing Tang, Sean L Willis, Simon W Leppard, Laura C Wolfenden, Rosemary R Palmer, and Peter W Stratford. Dc bead: in vitro characterization of a drug-delivery device for transarterial chemoembolization. *Journal of vascular and interventional radiology*, 17(2):335–342, 2006.

[8] Rafael Duran, Karun Sharma, Matthew R Dreher, Koorosh Ashrafi, Sahar Mirpour, MingDe Lin, Ruediger E Schernthaner, Todd R Schlachter, Vania Tacher, Andrew L Lewis, et al. A novel inherently radiopaque bead for transarterial embolization to treat liver cancer-a pre-clinical study. *Theranostics*, 6(1):28, 2016.

[9] Dario Carugo. *Development of microfluidic systems for therapeutic applications*. PhD thesis, University of Southampton, 2012.

[10] Raffi Karshafian, Peter D Bevan, Ross Williams, Sanya Samac, and Peter N Burns. Sonoporation by ultrasound-activated microbubble contrast agents: effect of acoustic exposure parameters on cell membrane permeability and cell viability. *Ultrasound in medicine & biology*, 35(5):847–860, 2009.

[11] Cheri X Deng, Fred Sieling, Hua Pan, and Jianmin Cui. Ultrasound-induced cell membrane porosity. *Ultrasound in medicine & biology*, 30(4):519–526, 2004.

[12] Matthew R Dreher, Karun V Sharma, David L Woods, Goutham Reddy, Yiqing Tang, William F Pritchard, Oscar A Chiesa, John W Karanian, Juan A Esparza, Danielle Donahue, et al. Radiopaque drug-eluting beads for transcatheter embolotherapy: experimental study of drug penetration and coverage in swine. *Journal of Vascular and Interventional Radiology*, 23(2):257–264, 2012.

[13] Ali Gholamrezanezhad, Sahar Mirpour, Jean-Francois H Geschwind, Pramod Rao, Romaric Loffroy, Olivier Pellerin, and Eleni A Liapi. Evaluation of 70–150-μm doxorubicin-eluting beads for transcatheter arterial chemoembolization in the rabbit liver vx2 tumour model. *European radiology*, pages 1–9, 2016.

[14] Julien Namur, Steven J Citron, Marty T Sellers, Mark H Dupuis, Michel Wassef, Michel Manfait, and Alexandre Laurent. Embolization of hepatocellular carcinoma with drug-eluting beads: doxorubicin tissue concentration and distribution in patient liver explants. *Journal of hepatology*, 55(6):1332–1338, 2011.

Chapter 7

Effect of Nanoparticle Loading On Microbubble Cavitation

7.1 Introduction

Drug loaded microbubbles offer an attractive platform for targeted drug delivery. When exposed to ultrasound, the loaded drug is released from the microbubbles, and as they are co-located, drug release and uptake is localised to the treatment region, allowing for targeted drug delivery [1–3]. This is particularly useful when the drug is highly cytotoxic, e.g. paclitaxel [2], and systematic delivery of the drug is poorly tolerated. Additionally, as the drug is released by cavitation, sonoporation of nearby cells may further enhance drug uptake.

Drug loading of microbubbles can be accomplished by several methods, shown in Figure 7.1 [4]. Briefly, drugs can be loaded inside microbubbles, incorporated into the microbubble shell, and attached the bubble via electrostatic attraction or avidin biotin linkage.

An implicit assumption in the use of drug loaded microbubbles is that they are as least as safe as their unloaded counterparts. This assumption stems from the fact that, compared to unloaded microbubbles, loaded microbubbles exhibited a damped response to ultrasound [5]. For example, at the same pressures, the expansion of loaded microbubbles is less than that of unloaded microbubbles. It is this assumption of safety that the experiments presented in this chapter will investigate using PLGA

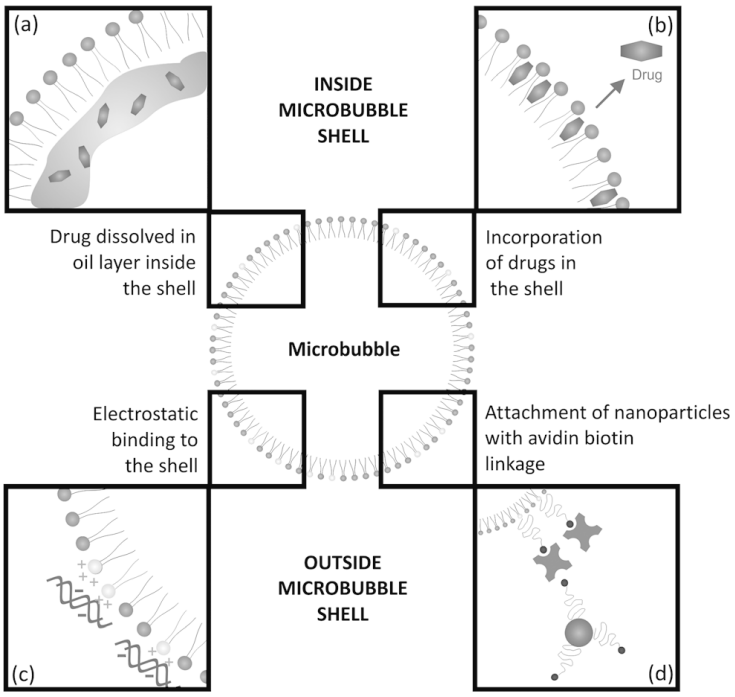

Figure 7.1: Methods for drug loading of microbubbles [4]. Drugs can be **(a)** loaded inside microbubbles, **(b)** incorporated into the microbubble shell, **(c)** attached via electrostatic attraction, **(d)** and attached via avidin biotin linkage.

nanoparticles and phospholipid coated microbubbles. At the same time, these experiments will evaluate the utility of SIOS for monitoring cavitation effects in real-time and *in-situ*.

7.2 Materials and Methods

The experiments described in this chapter utilises agarose channel models made from 2.0 % w/v agarose with 370 µm diameter flow channels. After aligning the system and channel models, fluorescent suspensions of loaded and unloaded microbubbles were flowed through the channels at 27 µL min^{-1}. The channels were then exposed to ultrasound and concurrently imaged using SIOS. Following ultrasound exposure channels were treated to improve widefield fluorescence microscopy, then excised and imaged with an inverted microscope.

Details on the manufacture of agarose channel models, the alignment procedures, and the treatment of flow channels following ultrasound exposure can be found in Chapter 5.

7.2.1 Microbubbles and Nanoparticles

Microbubbles were manufactured by first preparing a lipid solution containing 1,2-distearoyl-sn-glycero-3-phosphocholine (DSPC, 850365; Avanti Polar Lipids, US); 1,2-distearoyl-sn-glycero-3-ethylphosphocholine (DSEPC, 890703; Avanti); and polyoxyethylene (40) stearate (PEG40S, P3440; Sigma-Aldrich, US) in molar ratio of 19.3:9:1 respectively. The solution was then sonicated in the presence of sulphur hexafluoride gas (SF6), producing microbubbles with a mean diameter of $1.60 \pm 1.09\,\mu m$ and a zeta potential of $54.2 \pm 8.5\,mV$. Henceforth, these positively charged microbubbles will be referred to as DSEPC microbubbles.

Poly(lactic-co-glycolic acid) (PLGA) nanoparticles (NP) were manufactured using a modified double emulsion technique based the work of McCall et al. [6] The resulting PLGA nanoparticles have a mean size of $0.31 \pm 0.10\,\mu m$ and a zeta potential of $-40.5 \pm 5.6\,mV$. Nanoparticles were stored in powder form and resuspended when required in de-ionised water.

Both microbubbles and PLGA nanoparticles were manufactured by Richard Browning at the Institute of Biomedical Engineering, Department of Engineering Science, University of Oxford. The zeta potential of nanoparticles and microbubbles were determined using a Zetasizer Nano ZS (Malvern, UK). The size of nanoparticles was measured using the same instrument, while a widefield microscope (DM500; Leica Microsystems, DE) with an attached digital imager (MicroPublisher 3.3; QImaging, CA) was used to measure the size of microbubbles.

Due to their zeta potentials, the nanoparticles are negatively charged in solution while the microbubbles are positively charged. Consequently, PLGA nanoparticles will attach to the surface of DSEPC microbubbles when mixed together, producing PLGA nanoparticle loaded DSEPC microbubbles, also referred to as loaded DSEPC microbubbles. For the experiments described in this chapter, microbubbles were used at a concentration of 1.0×10^7 to $5.0 \times 10^7\,ml^{-1}$, and PLGA nanoparticles at a concentration of $276\,ng\,mL^{-1}$.

In control experiments, DSEPC microbubbles and PLGA nanoparticles were used individually, and for test experiments they were mixed prior to infusion into the chan-

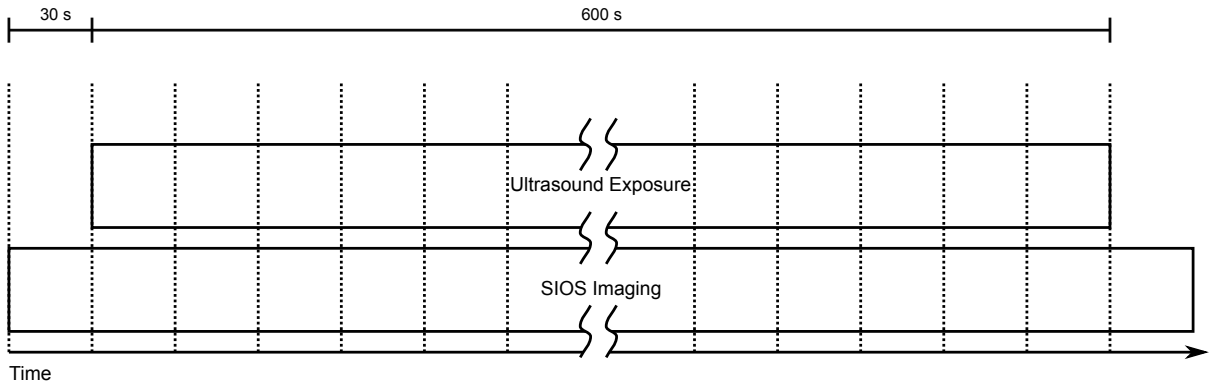

Figure 7.2: Experiment timeline. Dotted lines indicate the start of XZ plane scans of the flow channel. Time taken for each scan was kept below 30 s to avoid overruns.

nel models. In all instances, suspensions were made fluorescent via the addition of TRITC-Dextran.

7.2.2 Ultrasound Exposure and *In Situ* Monitoring

Ultrasound exposure and *in situ* monitoring of flow channels occurs concurrently as shown in Figure 7.2. The channels were first scanned by SIOS to obtain a pre-sonication image, and then exposed to high-intensity focused-ultrasound (HIFU) at 1.067 MHz, 1.8 MPa peak negative pressure, 5 Hz pulse repetition frequency, and 1.17 % duty cycle for 10 min. All SIOS scans were performed longitudinally in the XZ plane in order to fully capture the ultrasound focus and to provide sufficient coverage along the X axis to observe any potential effects occurring outside the ultrasound focus.

7.2.3 Deformation Detection and Measurement

Deformation detection and measurement were carried out using widefield fluorescence microscopy and the channel-centre fluorescence front displacement residual, e_C, as described in Chapter 5. Results obtained from widefield microscopy serve as the gold standard for the reported measurements.

7.2.4 Experimental Groups

Experiments comparing the effects produced by unloaded DSEPC microbubbles and PLGA nanoparticle loaded microbubbles were carried out in four groups, labelled I–IV.

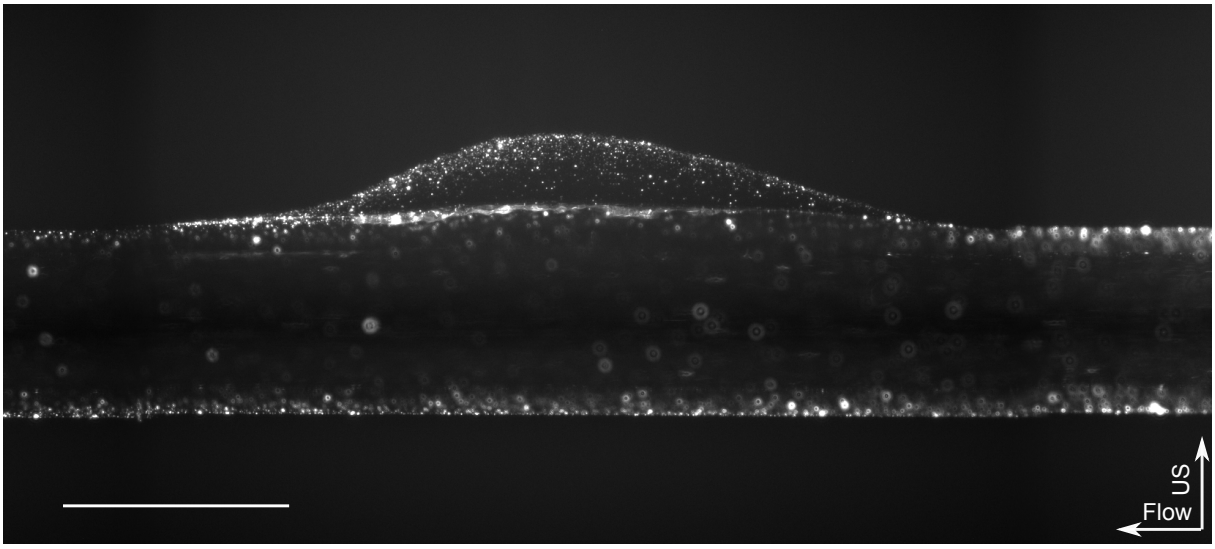

Figure 7.3: Widefield fluorescence microscopy of the focus region from experiment C-III, representative of experiments C-II to C-IV. A chamber-type deformation extending 218 µm in the direction of ultrasound is visible. The deformation is approximately 1500 µm wide. Scale bar is 500 µm.

Experiments in each group were performed the same day with the same equipment and materials. Specifically, a common stock of agarose was used to manufacture each channel model, and the same stocks of PLGA nanoparticles and DSEPC microbubbles were used for each experiment.

An experimental group consists of at least one control and one test experiment, with further test experiments performed according to the time available. Control experiments are labelled C-I through to C-IV, and test experiments are labelled L-I through to L-IV. Where two test experiments were performed the same day, they are differentiated by suffixes a and b, assigned in time order, e.g. L-Ia, L-Ib.

PLGA only control experiments were typically performed on their own, except for one experiment which was performed on the same day as experimental group IV. These experiments are labelled P-1 through to P-4, and P-IV respectively.

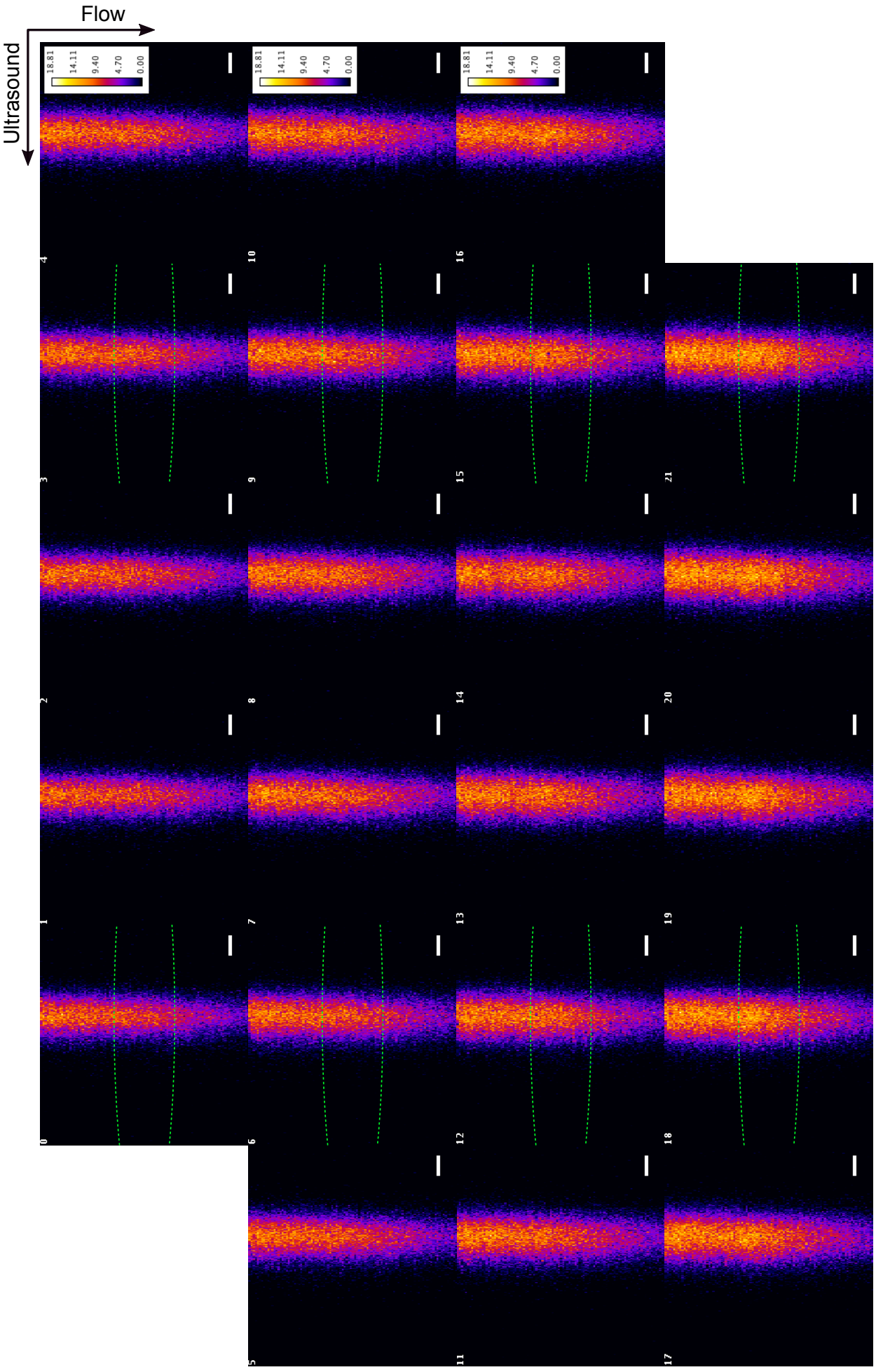

Figure 7.4: XZ scans of the flow channel in experiment C-III. Images were taken at 30 s intervals immediately before (0), during (1-20), and after (21) ultrasound exposure. The image sequence shown is representative of experiments C-II and C-IV. Colour bars have units of fluorescence value. Green lines demarcate the anticipated −3 dB boundary of the ultrasound focus. Scale bars are 500 µm.

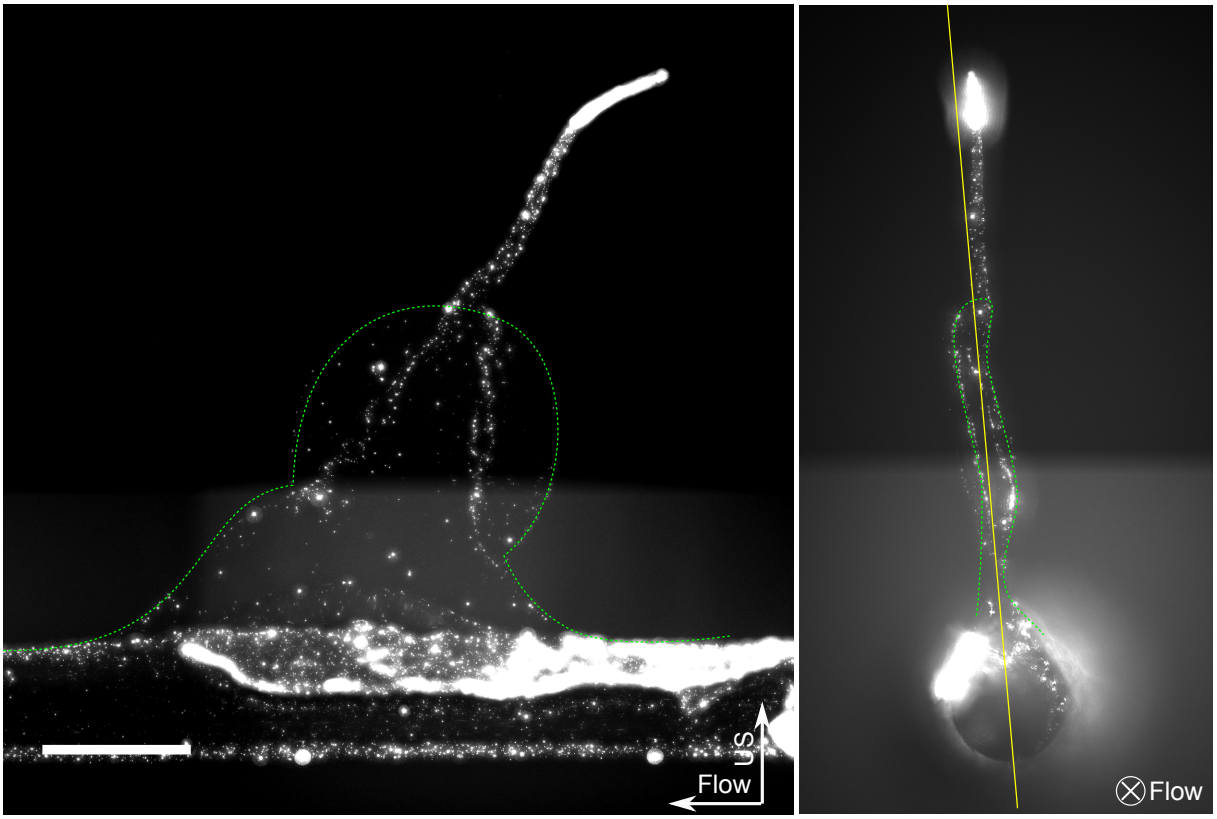

Figure 7.5: Widefield fluorescence microscopy of the focal region in experiment C-I. The cross section image of the deformation is shown on the right. The deformation, as a whole, extends 1969 µm in the direction of ultrasound propagation, while the region detected by SIOS, demarcated in green, extends 1128 µm. The estimated SIOS imaging plane is shown in yellow, and appears skewed as the deformation was used to align the image vertically. Images have been processed to improve contrast and brightness. The scale bar is 500 µm.

7.3 Results and Discussion

7.3.1 Unloaded DSEPC Microbubbles

7.3.1.1 Deformation Characteristics

In three of four control experiments with unloaded DSEPC microbubbles, C-II to C-IV, ultrasound exposure resulted in "chamber-type" deformations, extending approximately 200 µm in the direction of ultrasound (Figure 7.3[1]). These deformations appear as small localised enhancements in fluorescence intensity that extend in the direction of ultrasound exposure (Figure 7.4).

In the remaining experiment, C-I, a more extensive "wave-type" deformation was

[1]Cross section was produced using maximum intensity Z-projection in ImageJ: `http://imagej.net/Z-functions#Maximum_Intensity_Z-projection`

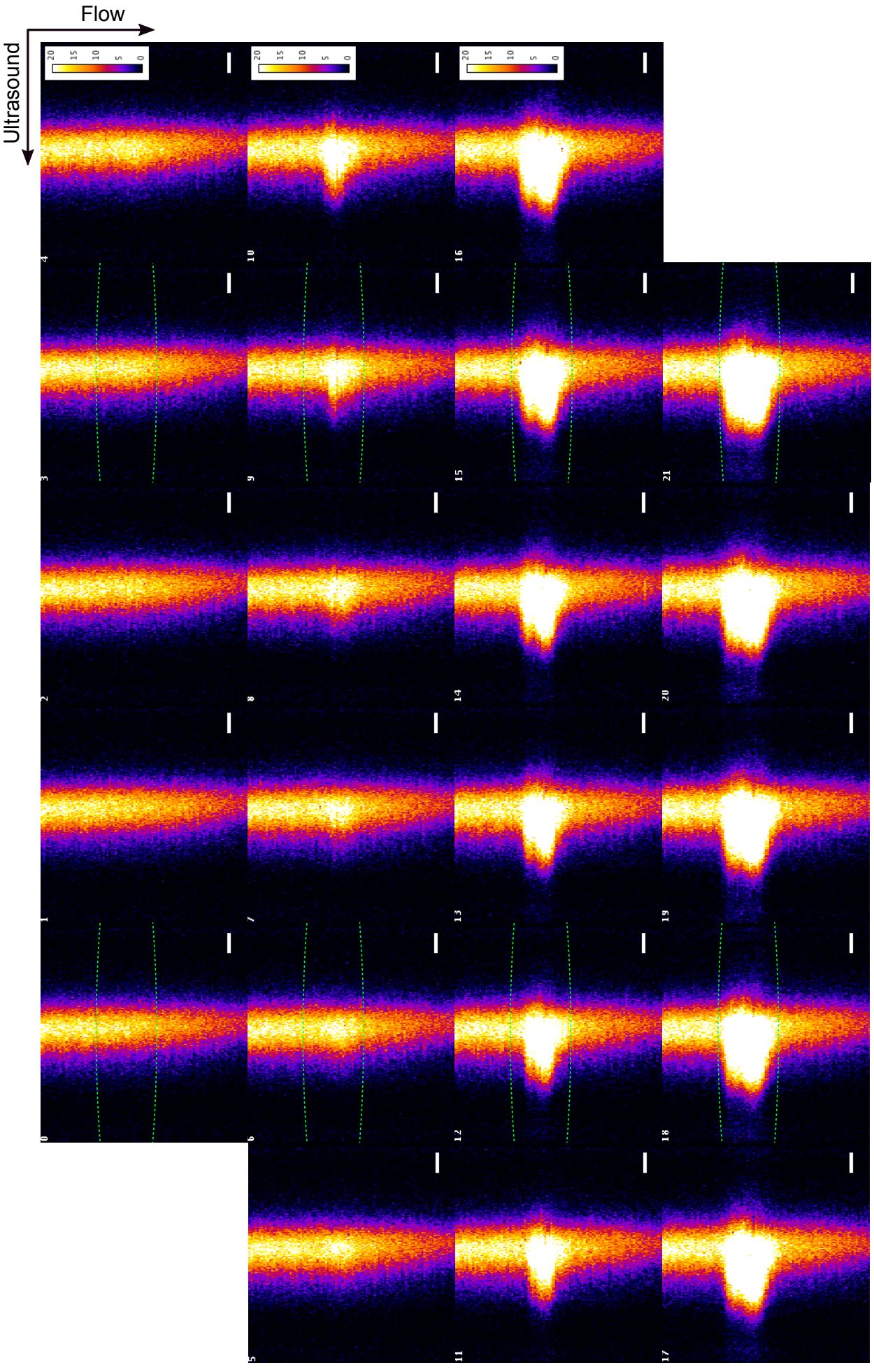

Figure 7.6: Longitudinal scans of the flow channel experiment C-I. Images were taken at 30 s intervals immediately before (0), during (1-20), and after (21) ultrasound exposure. Colour bars have units of fluorescence value. Green lines demarcate the anticipated −3 dB boundary of the ultrasound focus. Scale bars are 500 µm.

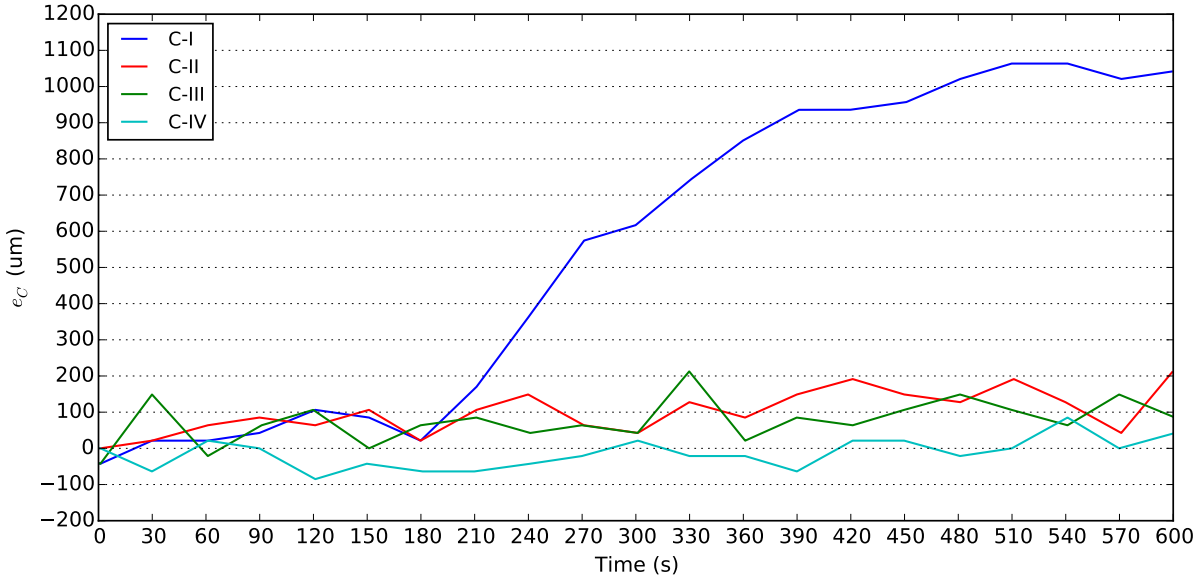

Figure 7.7: e_C during ultrasound exposure in unloaded DSEPC microbubble control experiments. Each curve presents one experiment.

observed (7.5). Whereas the chamber-type deformations were formed gradually, the formation of the wave-type deformation experienced a period of rapid growth (Figure 7.6 and 7.7). Additionally, due to the curvature of the deformation out of the imaging plane, it was only partially captured by SIOS, accounting for both the truncated appearance of the deformation in Figure 7.6 and the smaller apparent size in SIOS images.

The chamber-type deformations seen in experiments C-II to C-IV is thought to be the result of agarose erosion, where cavitating DSEPC microbubbles gradually break down the agarose matrix. Due to acoustic radiation force, which pushes microbubbles in the direction of ultrasound propagation, these chamber-type deformations are only seen on the side of the channel distal from the HIFU transducer. The asymmetric appearance of the chamber-type deformations is thought to be the result of flow, which causes the microbubbles within deformations to accumulate downstream, resulting in faster agarose erosion on one side of the deformation than the other.

Formation of the wave-type deformation in experiment C-I is thought to be largely similar to that of chamber-type deformations. At some point, however, due to a localised weakness in the agarose, the agarose cracked during erosion, i.e. separated along a thin plane. Microbubbles then infiltrated the newly created space and caused further damage. This theory is supported by the irregular nature of the wave-like deforma-

tion; and the observation that while the chamber-type deformations were aligned the acoustic axis, the wave-like deformation was not.

7.3.1.2 Cavitation Characteristics

During these experiments, the cavitation noise from unloaded DSEPC microbubbles was recorded by the single-element passive cavitation detection (PCD) transducer, located coaxially with the HIFU transducer. In experiment C-1, the rapid growth of the wave-type deformation, at $t = 180$ s was associated with a decrease in the power of the PCD signal (Figure 7.8a).

Meanwhile, in those experiments in which chamber-type deformations were formed, the PCD measurements showed a linear increase in power (e.g. Figure 7.8b; full dataset in Appendix). This increase could be explained by extra volume offered by the deformations, which allowed a greater number of microbubbles to be present within the ultrasound focus, resulting in higher levels of cavitation activity.

7.3.2 PLGA Nanoparticles

7.3.2.1 Deformation Characteristics

Ultrasound exposure of PLGA nanoparticles resulted in "short tunnel-type" deformations, defined as tunnel-like deformations shorter than 1500 µm, in three of five experiment (P-2, P-4 and P-IV; Figure 7.9). The formation of these short tunnel-type deformations involved a period of rapid growth with an abrupt onset (Figure 7.10 and Figure 7.11), a behaviour seen previously with the wave-type deformation in experiment C-1. Additionally, an earlier onset of rapid deformation formation appears to correlate with a larger deformation size (Figure 7.11).

In the other PLGA nanoparticle experiments, P-1 and P-3, there was minimal to nil deformation (e.g. Figure 7.12; full data set in Appendix).

7.3.2.2 Cavitation Characteristics

In the PCD data recorded during these experiments, there were no features that could be used to predict the presence of short tunnel-type deformation. For example, the

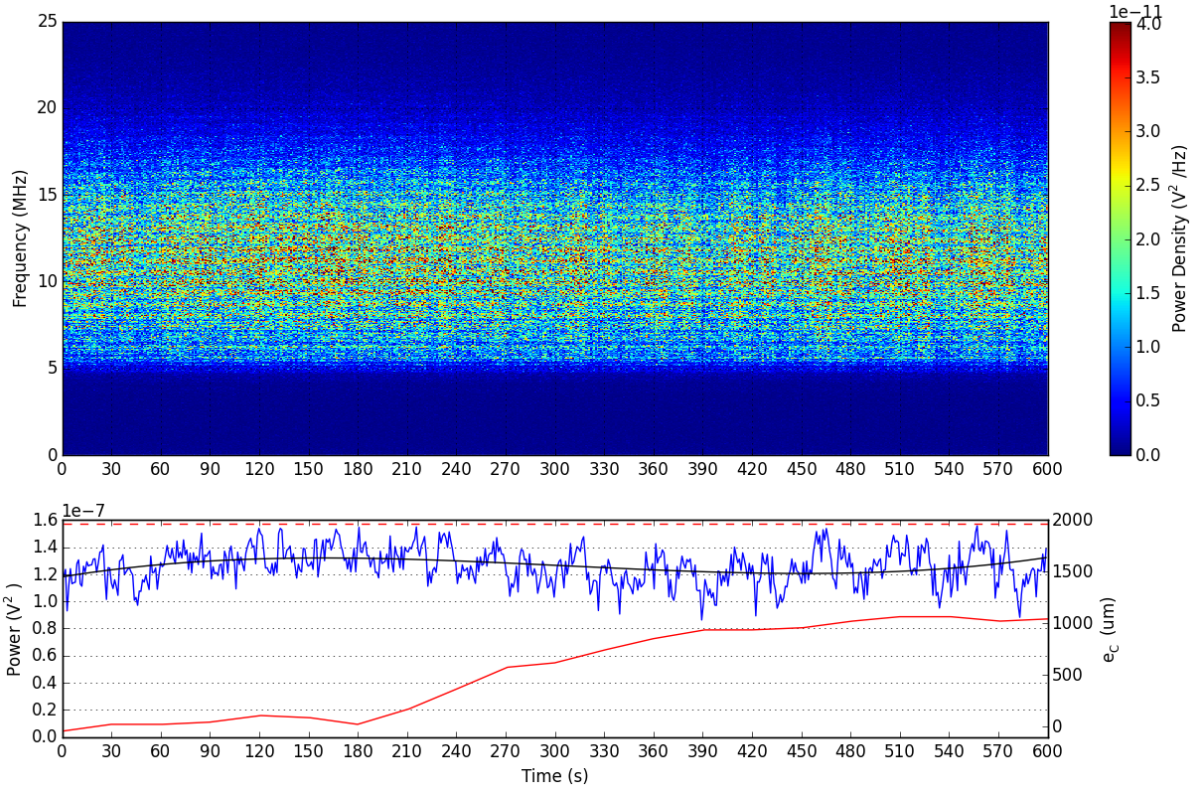

(a) C-I

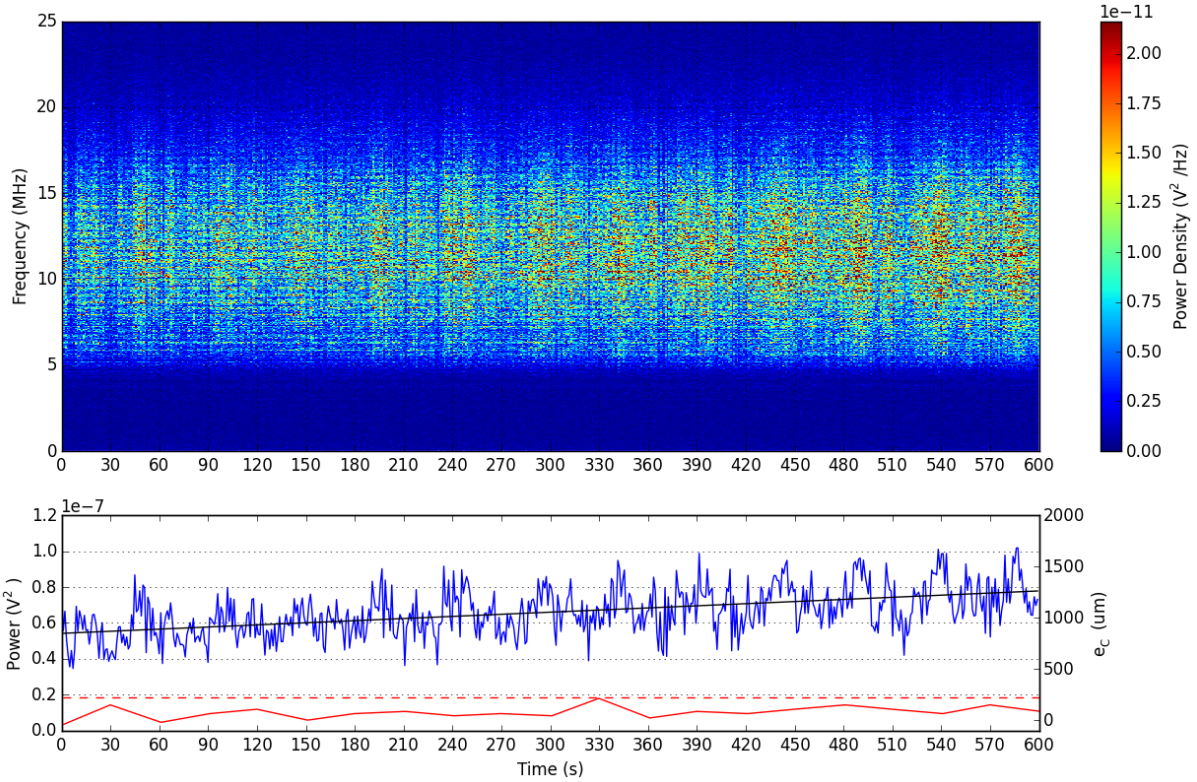

(b) C-III

Figure 7.8: Spectrogram of experiments C-I and C-III plotted together with the corresponding values of e_C. In the lower power plots, the black lines are fitted polynomials, the solid red lines are the e_C values, and the dotted red lines are the maximum extent of any deformations measured using widefield microscopy. The power plot for C-I is fitted with a 3rd degree polynomial while power plot for C-III is fitted with a 1st degree polynomial.

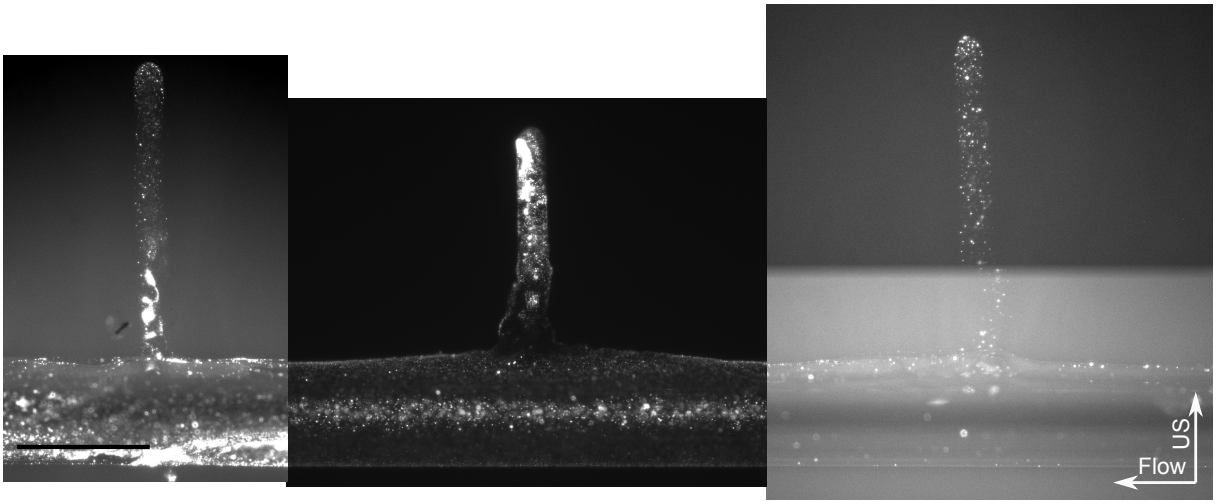

Figure 7.9: Widefield microscopy images of deformation post ultrasound exposure in experiments P-2, P-4 and P-IV. Left-to-right, images are from P-2, P-4 and P-IV, with deformation extend into the agarose 1115 µm, 887 µm and 1251 µm respectively. Scale bar is 500 µm.

PCD measurements from experiments P-1 and P-2 were similar, despite the fact that a short tunnel-type deformation was observed in experiment P-2 while no deformation occurred in experiment P-1 (Figure 7.13; full data set in Appendix). This is not surprising given that the level of detected cavitation noise is effectively nil, consistent with the fact that PLGA nanoparticles are not cavitation agents.

7.3.3 PLGA Nanoparticle Loaded DSEPC Microbubbles

7.3.3.1 Deformation Characteristics

In experiments with PLGA nanoparticle loaded DSEPC microbubbles, tunnel-like deformations longer than 2000 µm were produced during ultrasound exposure (Figure 7.14). These "extended tunnel-type" deformations, like short tunnel-type deformations, developed in two stages: a stage of slow growth followed by a stage of rapid enlargement (Figure 7.15 and Figure 7.16). As with short tunnel-type deformations, early onset of rapid growth was associated with larger deformations (Figure 7.17).

SIOS did not fully capture the deformation in experiment L-II as it deviated from the imaging plane, resulting in a smaller than expected value for e_C (Figure 7.18).

The extended tunnel-type deformations are hypothesised to have developed from chamber-type deformations. The asymmetry in a chamber-type deformation, previ-

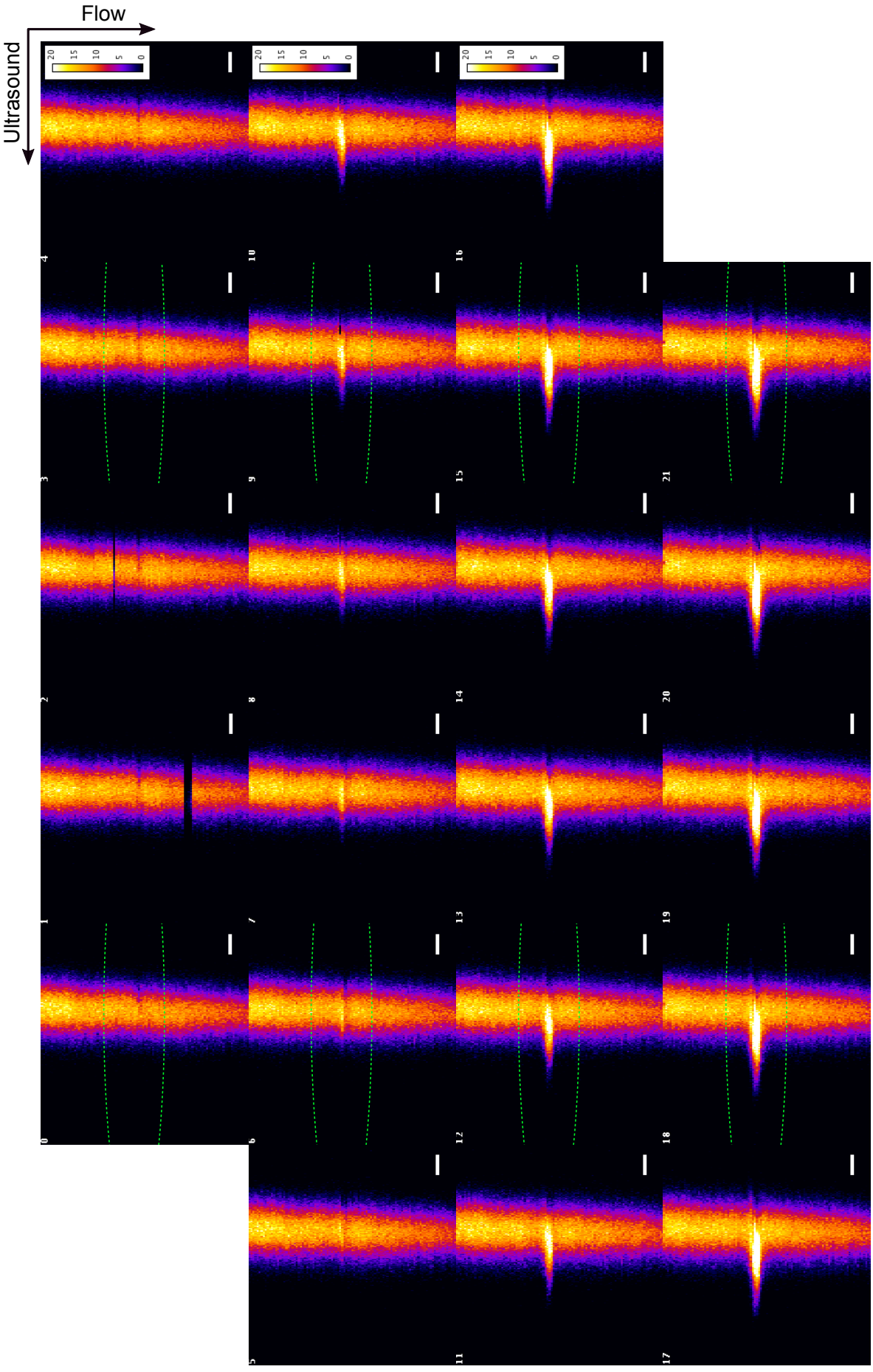

Figure 7.10: XZ scans from experiment P-2. Images were taken at 30 s intervals immediately before (0), during (1-20), and immediately after (21) ultrasound exposure. Green line demarcates the anticipated ultrasound focus. Colour bar has units of fluorescence and scale bars are 500 µm.

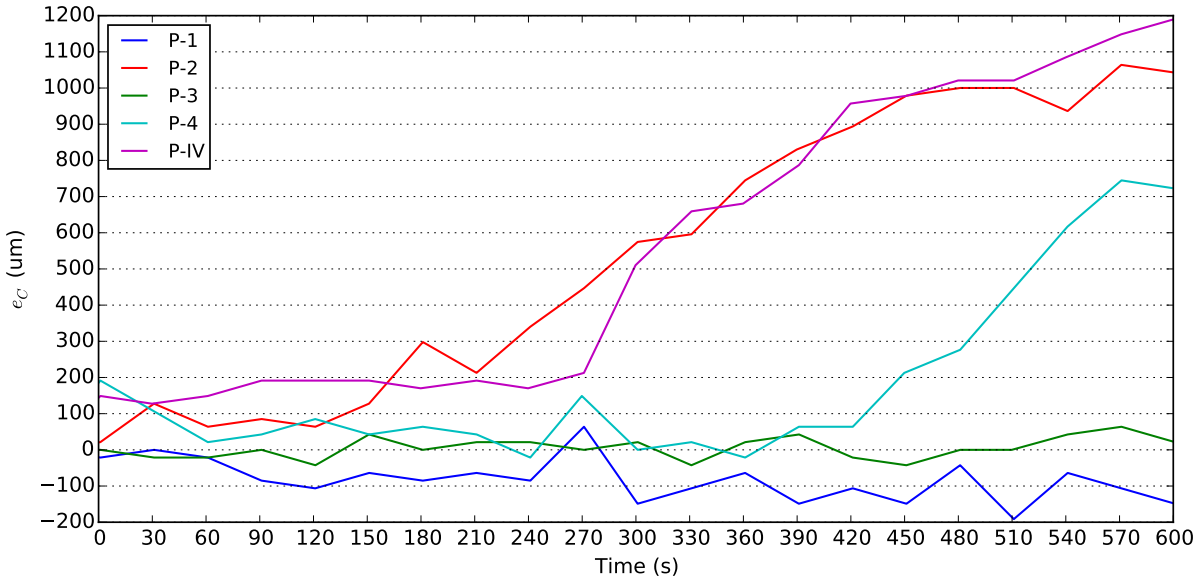

Figure 7.11: e_C during ultrasound exposure in PLGA nanoparticle control experiments. The negative trend of e_C for P-1 is due to S_C outpacing S_T and not due to retraction of the channel boundary.

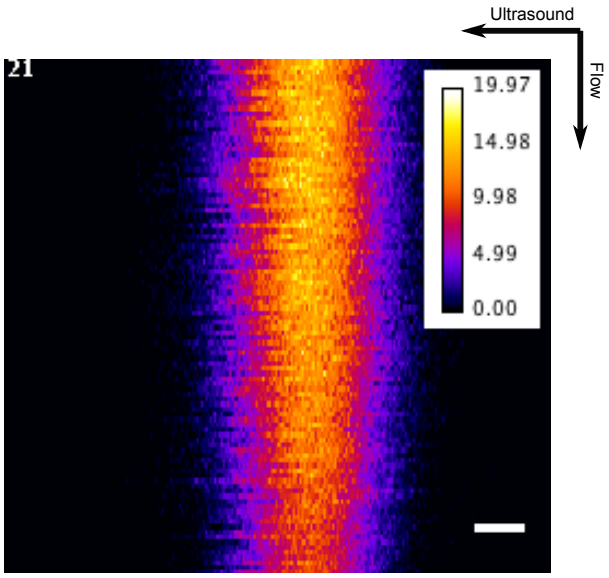

(a) XZ plane scan.

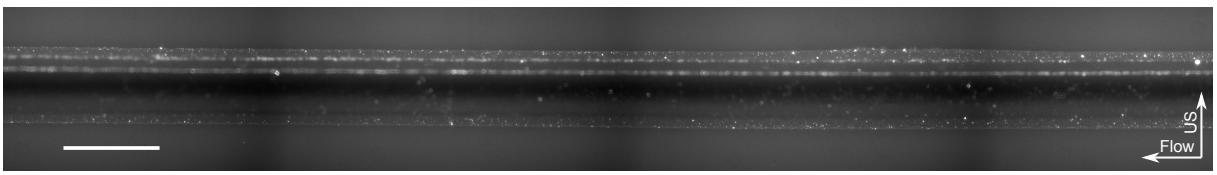

(b)

Figure 7.12: Post ultrasound **(a)** SIOS and **(b)** widefield fluorescence microscopy images of the flow channel in experiments P-1. Colour bar has units of fluorescence. Scale bar is 500 µm.

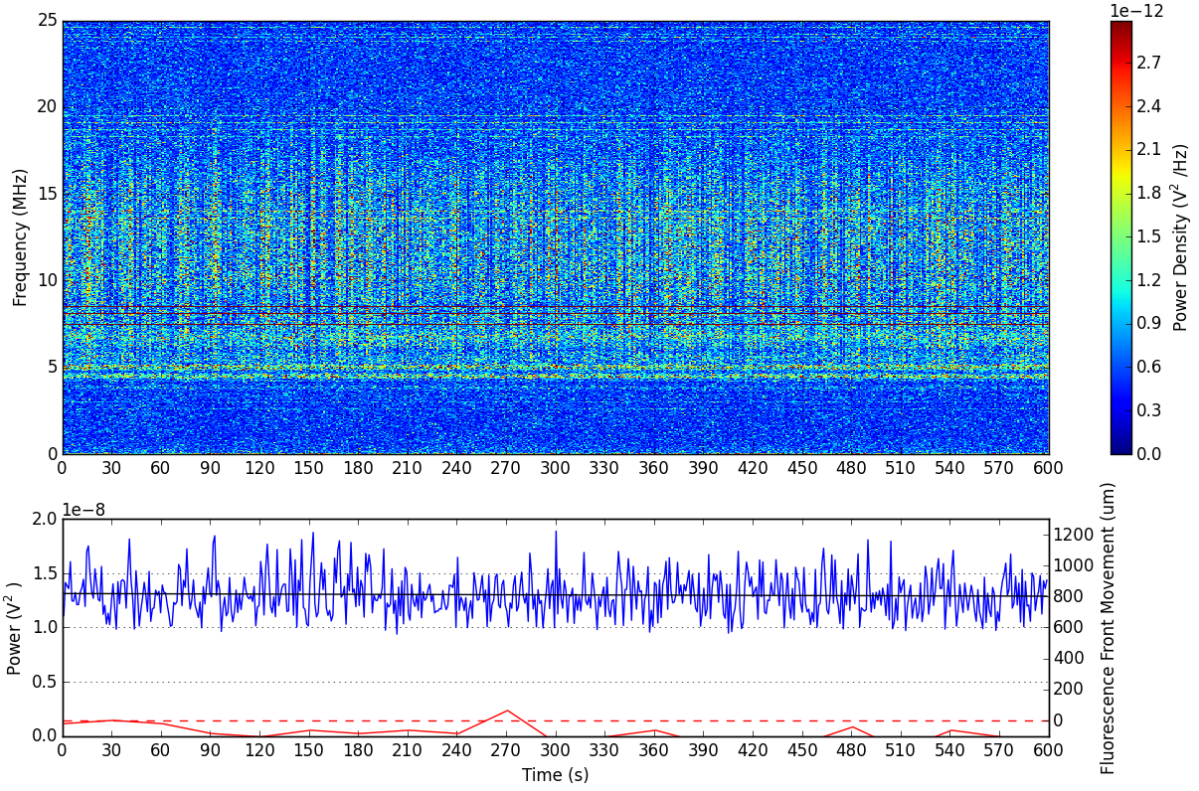

(a) P-1

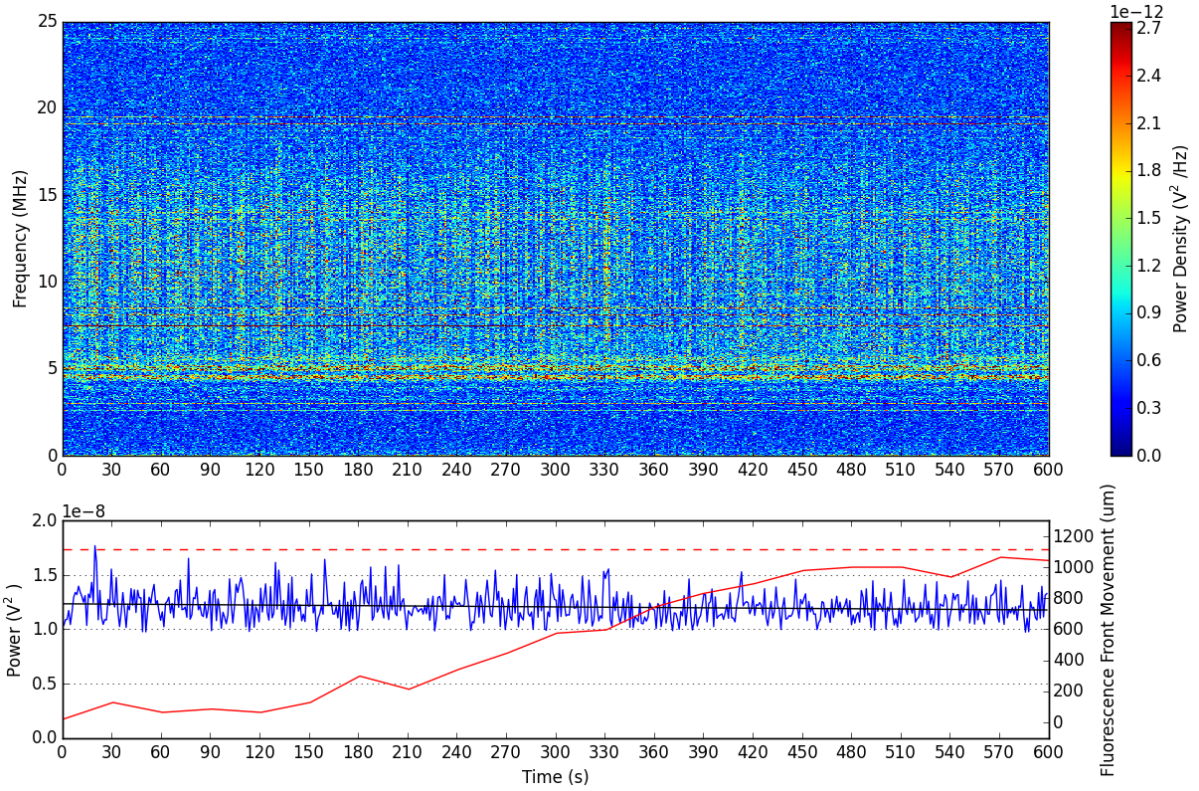

(b) P-2

Figure 7.13: Spectrogram of experiments P-1 and P-2 plotted together with the corresponding values of e_C. Power plots are fitted with first degree polynomials.

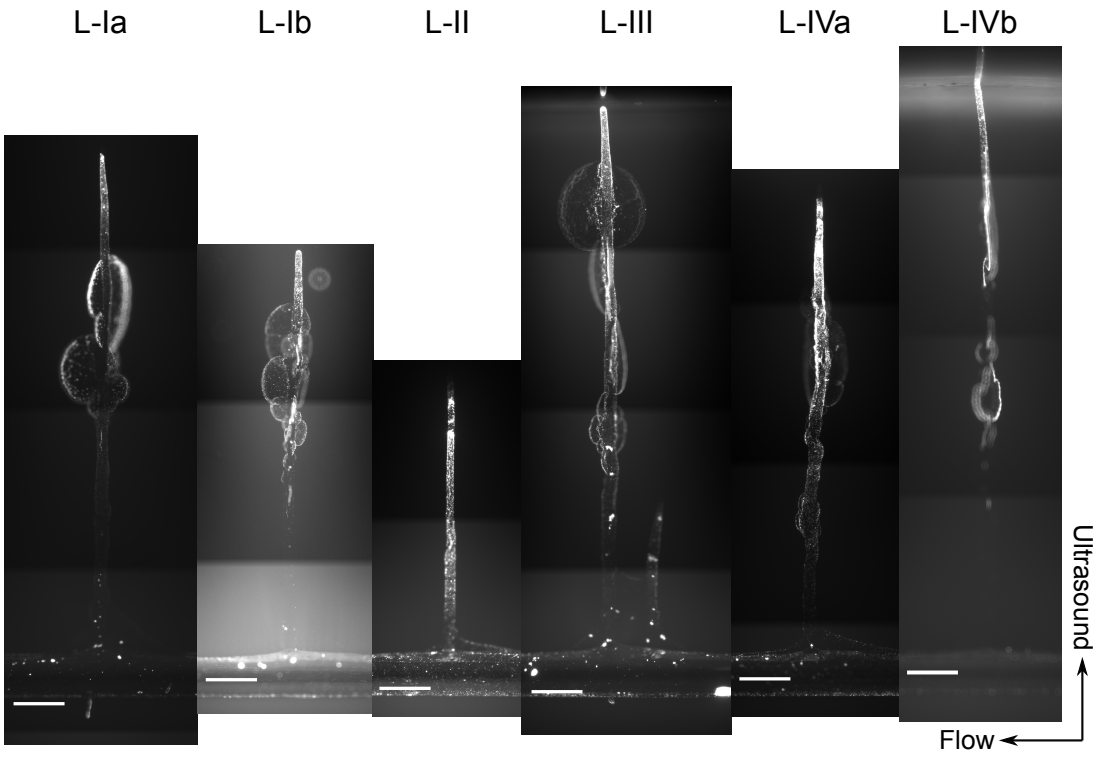

Figure 7.14: Endpoint widefield microscopy images of deformation caused by PLGA nanoparticle loaded DSEPC microbubbles after exposure to ultrasound. In experiment L-III and L-IVb reflection from the agarose-air interface can be seen. Left-to-right, the extent of deformation in the direction of ultrasound is 4949 µm, 4017 µm, 2722 µm, 5402 µm, 4658 µm and 5696 µm. Scale bars are 500 µm.

ously discussed in Subsection 7.3.1.1, develops until a tunnel-like region forms within the deformation, inside of which flow is stagnant. Within this region, primary acoustic radiation force is the dominant mode of transport, pushing new microbubbles into the region and maintaining the microbubble population against ultrasonic destruction. Due to confinement of the microbubbles by the tunnel-like region, cavitation damage to the surrounding agarose is increased, resulting in more rapid agarose erosion at the "tip" of the region and agarose cracking along its length. Together, these effects produce the extended tunnel-type deformations. This theory is illustrated in Figure 7.19, where microscope images from experiment C-III and experiment L-IVa were used as references for the starting and intermediate contours.

7.3.3.2 Cavitation Characteristics

During these experiments, there is a general trend where the power of the PCD signal increases prior to the onset of rapid deformation growth, and plateaus thereafter (e.g. Figure 7.20; full data set in Appendix). That the onset of rapid deformation growth

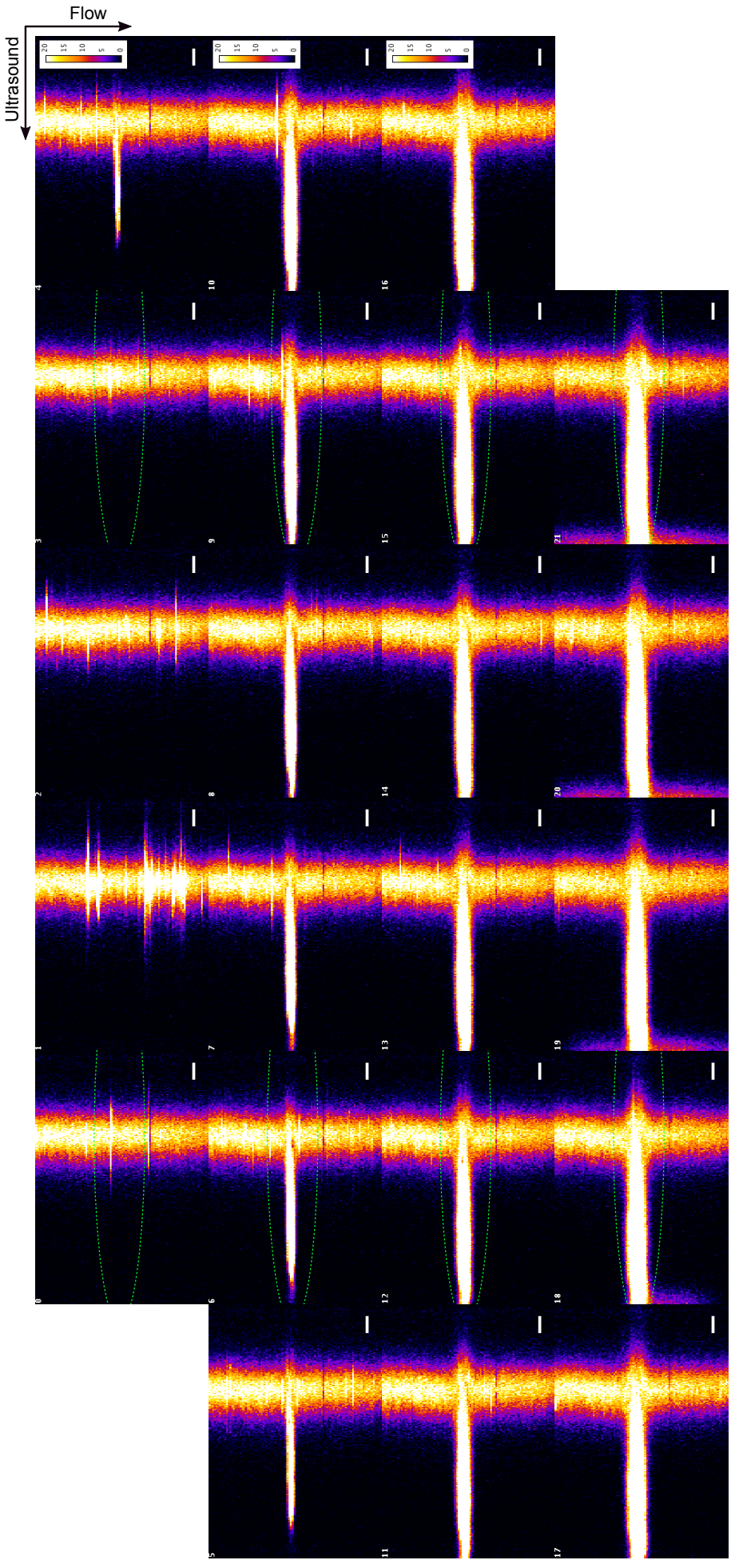

Figure 7.15: XZ scans of the flow channel carrying PLGA nanoparticle loaded DSEPC microbubbles from experiment L-IVb. Images were taken immediately before (0), during (1-20), and immediately after (21) ultrasound exposure. From image 17 onwards a new fluorescence signal can be seen at the left edge of the image. This is due to the deformation reaching the interface between the agarose and the mylar window, allowing the fluorescent mixture from the flow channel to infiltrate the agarose-mylar interface. Images are taken 30 s apart. Green line demarcates the anticipated ultrasound focus. Colour bars have units of fluorescence and scale bars are 500 µm.

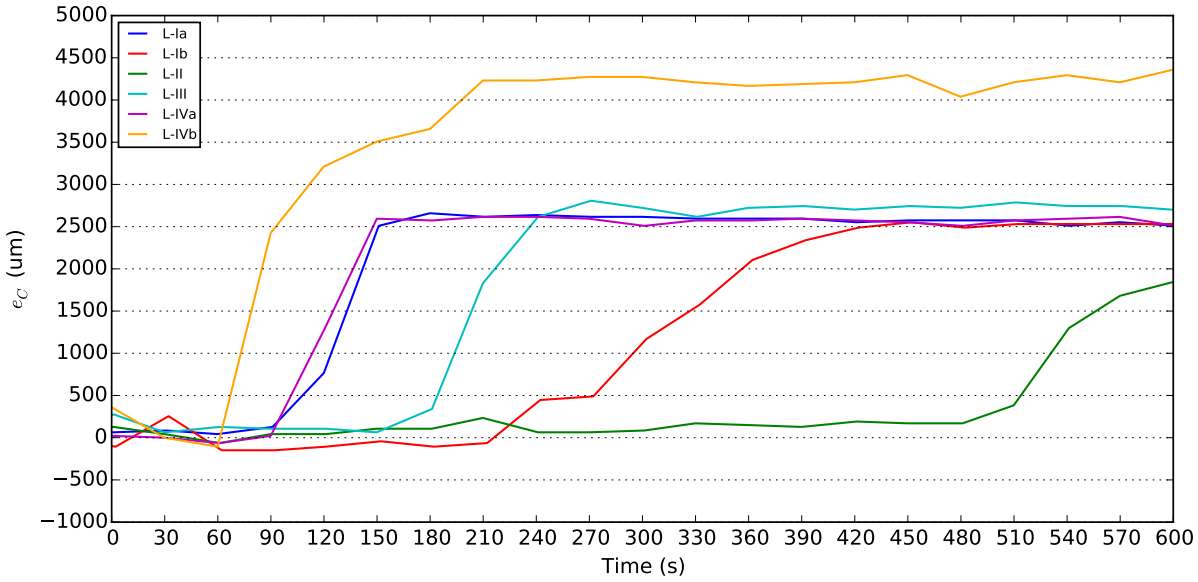

Figure 7.16: e_C during ultrasound exposure of channels containing PLGA nanoparticle loaded DSEPC microbubbles. Due to deformation extending beyond the FOV, values do not in general exceed um3000. For experiment L-IVb the FOV was extended in anticipation of substantial deformation occurring. Variations in e_C after deformation has exceeded FOV is due to variations in S_C.

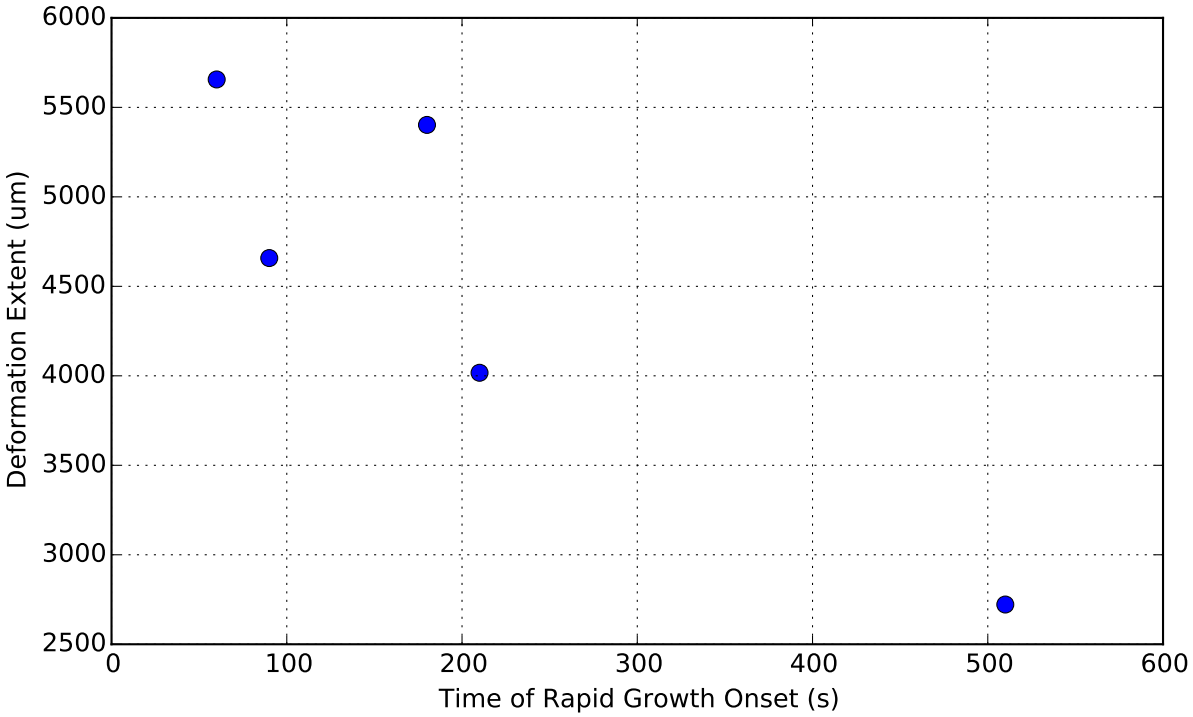

Figure 7.17: Correlation between time of rapid growth onset and deformation extent for extended tunnel-type deformations. Deformation extents were measured using widefield microscopy.

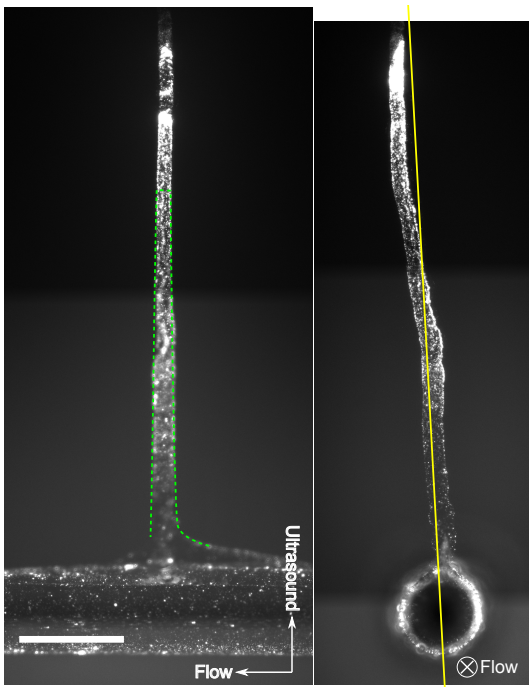

Figure 7.18: Widefield fluorescence microscope image the deformation in experiment L-II. The deformation extent measured by e_C is demarcated in green, and measures $\approx$ 1800 µm in the direction of ultrasound. The estimated SIOS imaging plane is indicated in yellow, and appears skewed as the image the deformation was used to vertical align the sample. Scale bar is 500 µm.

lags the increase in PCD signal power indicates increased cavitation activity leads to rapid deformation growth. Furthermore, based on data from unloaded DSEPC microbubbles experiments, the initial increase in PCD signal power may indicate the formation of chamber-type deformations such as those seen in Figure 7.3. Similar deformations can be seen at the base of the extended tunnel-type deformations (Figure 7.14). These observations lend support to the previously discussed theory, in which the extended tunnel-type deformations develop from chamber-type deformations. However, more experiments are necessary to establish the strength of the relationship between increases in cavitation power and the formation of chamber-type deformations.

7.3.4 Deformation Detection Limit of e_C

The use of e_C to detect deformations relies on the assumption that displacement of the fluorescence front due to deformations can be distinguished from displacement due to TRITC-Dextran diffusion. Therefore, in order for a deformation to be detected with a high degree of confidence, it must be large enough that the measured fluorescence

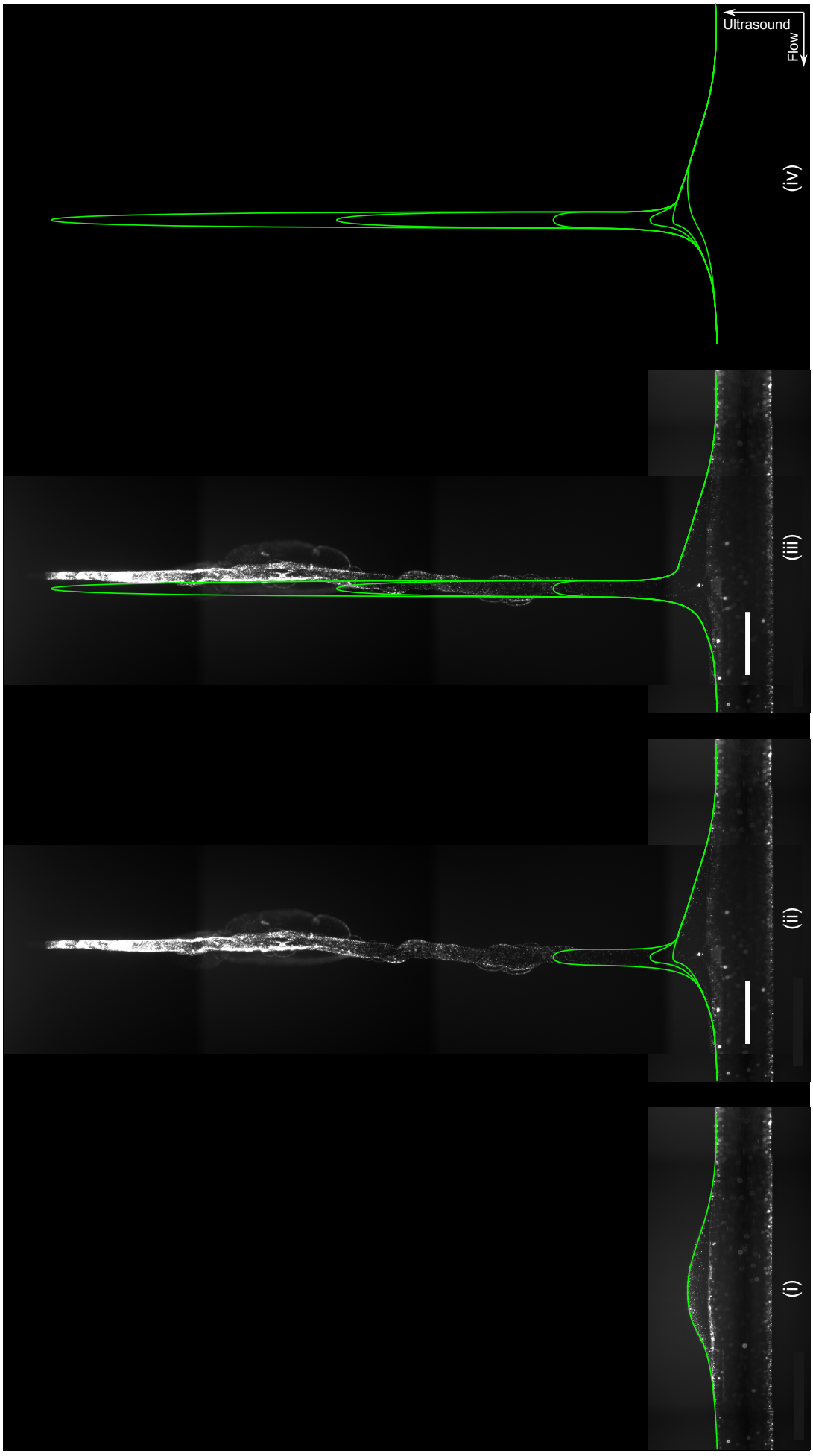

Figure 7.19: Development of extended tunnel-type deformation from chamber-type deformation. **(i)** Formation of the chamber-type deformation. **(ii)** Continued asymmetric erosion leads to the formation of a tunnel-like region at the apex. Confinement of microbubbles by the tunnel-like region leads to rapid erosion. Bubble population is replenished microbubbles pushed into the tunnel-like region by acoustic radiation force. **(iii)** Extended tunnel-type deformation is fully formed. **(iv)** Contours of the deformation at different development stages. In (i) image from C-III is used and in (ii) and (iii) image from L-IVa has been superimposed. The cracking of agarose which is hypothesised to lead to the formation of side-lobes characteristic of deformation by loaded microbubbles is not shown here. Scale bars are 500 µm.

Deformation Extent (µm)			
Experiment	e_C	Microscopy	Error (µm)
C-I†	1042	1969	
C-II*	213	202	
C-III*	85	218	
C-IV*	43	258	
P-1*	-149	0	
P-2	1042	1115	73
P-3*	21	46	
P-4	723	887	164
P-IV	1191	1251	60
L-Ia$^{\triangle}$	2510	4949	
L-Ib$^{\triangle}$	2531	4017	
L-II†	1851	2722	
L-III$^{\triangle}$	2701	5402	
L-IVa$^{\triangle}$	2509	4658	
L-IVb$^{\triangle}$	4358	5696	

Table 7.1: Catalogue of deformation extent in the direction of ultrasound from all experiments as measured by SIOS and widefield fluorescence microscopy. e_C values at the end of ultrasound exposure are shown. Errors are calculated by subtracting e_C from widefield measurements. (*) indicates cases where deformation is below the detection limit of 300 µm; (*) denotes cases where deformation extent exceeds the field-of-view; and (†) indicates cases where deformation exited the SIOS imaging plane.

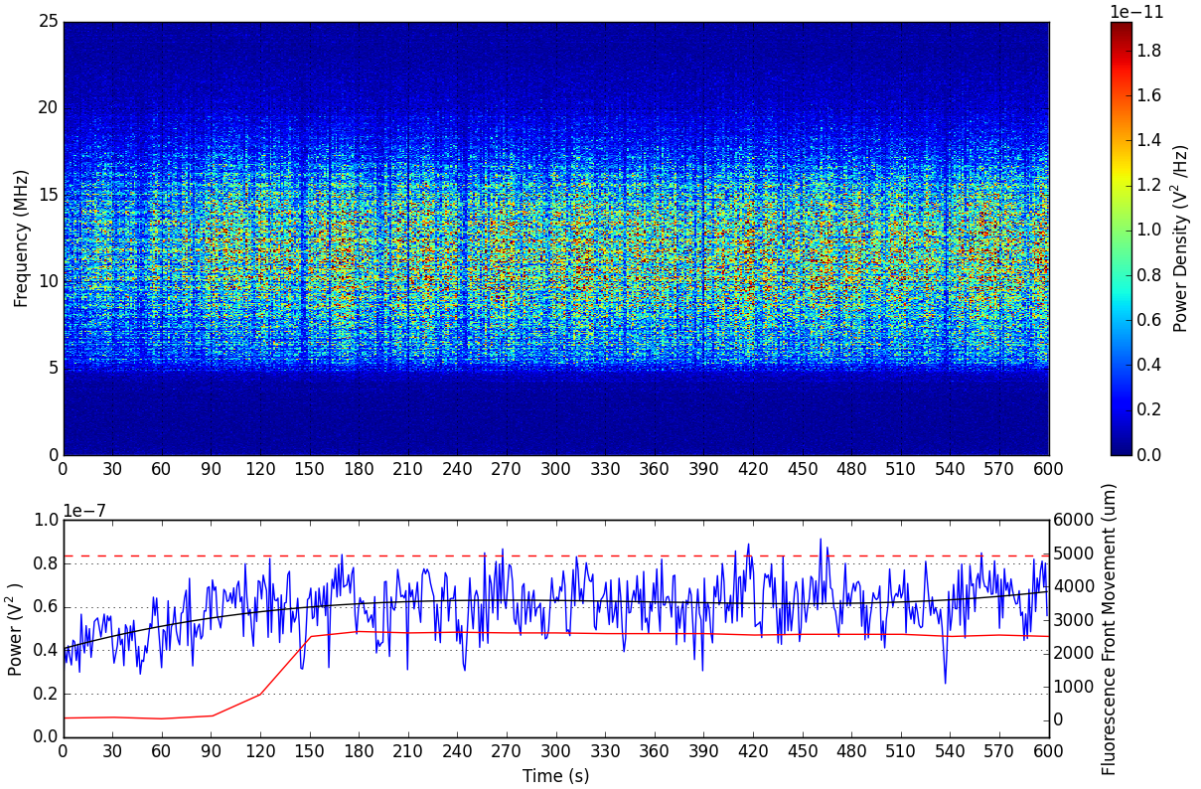

Figure 7.20: Spectrogram of detected cavitation noise in experiment L-Ia plotted together with e_C. Power plot was fitted with a 3rd degree polynomial.

front displacement cannot be attributed to diffusion and measurement noise alone. Using the non-negative values of S_T following ultrasound exposure, TRITC-Dextran diffusion was estimated to account for up to 127 µm SD 59 µm of fluorescence front displacement during an experiment. Consequently, a deformation needs to extend $127 + 3 \times 59 = 304$ µm or more in the direction of ultrasound before it can be detected with confidence. Rounding to one significant figure, the detection limit is 300 µm.

7.3.5 Estimating Deformation Extent

The extent of deformations in the direction of ultrasound propagation can be estimated from the post ultrasound exposure values of e_C. In experiments P-2, P-4 and P-IV, estimates based on e_C agreed reasonably with measurements obtained using widefield fluorescence microscopy. However, when deformations are well above the detection limit, as is the case in these experiments, deformation extents were better estimated using the post ultrasound values of S_C (Table 7.2). This is due to the fact that rapid agarose erosion, necessary for the formation of large deformations, significantly re-

Deformation Extent (μm)			
Experiment	S_C	Microscopy	Error
P-2	978	1115	137
P-4	851	887	36
P-IV	1277	1251	-26

Table 7.2: Estimates of deformation extent using the post ultrasound values of S_C and widefield fluorescence microscopy measurements. Errors are calculated by subtracting S_C from microscopy measurements.

duces the effect of diffusion on fluorescence front displacements.

7.3.6 Cavitation Energy and Deformation

It is generally accepted that higher levels of detected cavitation activity correlate with greater induced effects. In the experiments presented here, cavitation activity was measured in terms of total detected cavitation noise energy, and cavitation effect was measured by the degree of flow channel deformation. Figure 7.21 shows the total cavitation energy recorded in each experiment and the corresponding deformation extent in the direction of ultrasound propagation. Within each experimental group, higher cavitation noise energy is generally associated with larger deformations. However, this is not the case when considering all experimental groups. For example, the mean cavitation noise energy in experiments using loaded and unloaded DSEPC microbubbles were similar (t = -0.7135, df = 3.687, p-value = 0.5181, Welch Two Sample t-test), but the mean deformation size was significantly different (t = 6.3186, df = 7.55, p-value = 0.0003, Welch Two Sample t-test).

.

In addition to total cavitation noise energy, the variance and standard deviation of cavitation noise power were also examined, and no correlation to deformation extent. These results suggest that, despite the substantial and significant differences in induced effects, coaxial single-element PCD measurements cannot differentiate between loaded and unloaded DSEPC microbubbles.

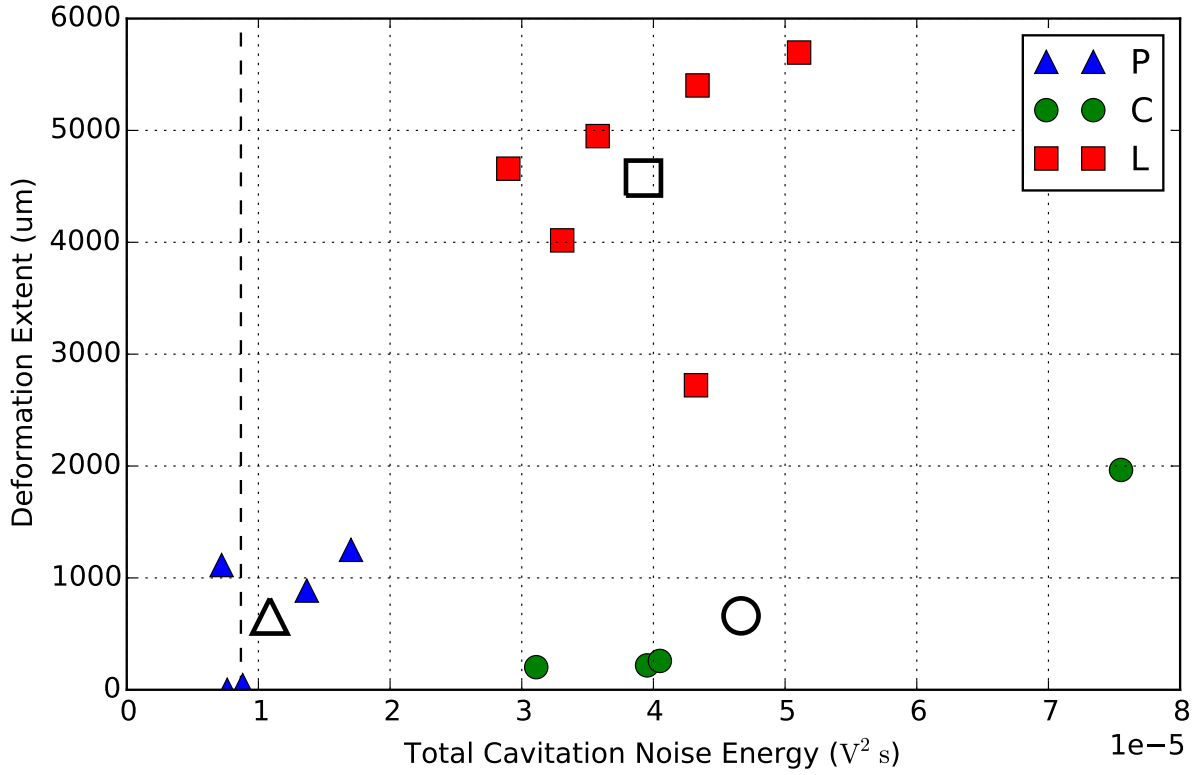

Figure 7.21: Total cavitation noise energy and deformation size across control and test experiments. **C**: unloaded DSEPC microbubble control experiments; **P**: PLGA nanoparticle control experiments; **L**: PLGA loaded DSEPC microbubble test experiments. Vertical dashed line indicates cavitation energy in de-ionised water only controls, i.e. energy measurement noise. Unfilled markers represent the arithmetic mean of each group.

7.3.7 Correspondence of Cavitation Features and Deformation Formation

Prior to these experiments, it was thought that, using PCD measurements, it would be possible to identify and track the development of deformations. In particular, the rapid growth experienced by the short and extended tunnel-type deformations were expected to produce readily identifiable features. The results presented here suggests that, using trends in the PCD signal power, it may be possible to track the development of chamber-type deformations and infer the existence of extended tunnel-type deformations. However, unlike SIOS measurements, no feature in PCD measurements could be used to identify the onset of rapid deformation growth in either PLGA nanoparticle experiments or loaded DSEPC microbubble experiments.

The lack of features in the PCD measurements that correspond with the onset of rapid deformation growth may be due to "shielding" of the PCD transducer by the microbubble population within the flow channel, preventing cavitation noise from inside deformations from reaching the transducer. An alternative explanation is that, due to the narrow focus of the PCD transducer ($\approx 488\,\mu m$ at $-3\,dB$), channels or deformations may not be in the field-of-view due to misalignments; and the fact that deformations do not always occur at the centre of the HIFU focus. Both of these are partly due to the use of a single-element coaxial PCD transducer.

Based on these results, the utility of PCD using a single-element coaxial transducer in a treatment context is limited. While measurements can determine whether or not cavitation is occurring at the ultrasound focus, the level of detected cavitation activity cannot be assumed to correlate with biological effects, e.g. sonoporation. Consequently, the degree of enhancement in drug penetration and uptake must be determined by other means, e.g. biopsies of the targeted tissue. Furthermore, from a safety perspective, single-element coaxial PCD measurements cannot be relied up on to detect sudden and rapid changes in induced effects.

7.3.8 Effect of PLGA Nanoparticle Loading

Loading of PLGA nanoparticle on DSEPC microbubbles substantially affected the cavitation behaviour of the microbubbles. Compared to their unloaded counterparts, loaded DSEPC microbubbles produced deformations were significantly different in appearance and in size. Whereas unloaded DSEPC microbubbles generally produced chamber-type deformations that extend $\approx 200\,\mu m$ in the direction of ultrasound propagation, loaded DSEPC microbubbles produced tunnel-type deformations with lengths of up to $5600\,\mu m$. To the best of the author's knowledge, this is the first reported observation of such an effect, and runs counter to expectations established based on previous reports of damped ultrasound response from liposome loaded microbubbles

The manner in which PLGA nanoparticles are affecting the DSEPC microbubbles so as to produce the observed effects remains an open question. However, if the formation of the extended tunnel-type deformations follows the theory described Subsection 7.3.3.1, then one possible explanation is that PLGA nanoparticles are increasing the dynamic stability of loaded DSEPC microbubbles, allowing them to survive longer when exposed to ultrasound. With their greater stability, loaded DSPEC microbubbles are able to erode agarose at a faster rate than unloaded DSEPC microbubbles, thus accelerating the development of chamber-type deformations so that extended tunnel-type deformations are formed during the ultrasound exposure period.

In support of the stabilisation theory, stabilisation of microbubbles by nanoparticles has been previously reported, where microbubbles with gold nanoparticles incorporated into the shell were found to be significantly more stable in storage, with the effect attributed to reduced gas diffusion and interfacial tension [7].

Lastly, there exists evidence that the extended tunnel-type deformations can be produced by unloaded DSEPC microbubbles. An experiment, D-1 was conducted using DSEPC microbubbles manufactured from an aliquot of DSEPC prepared in the 48 hours prior. The results of this experiment, shown in Figure 7.22 and Figure 7.23, demonstrate that DSEPC microbubbles are also capable of producing extended tunnel-type deformations. This finding suggests that the microbubble properties necessary for the formation of extended tunnel-type deformations are affected by the DSEPC stock

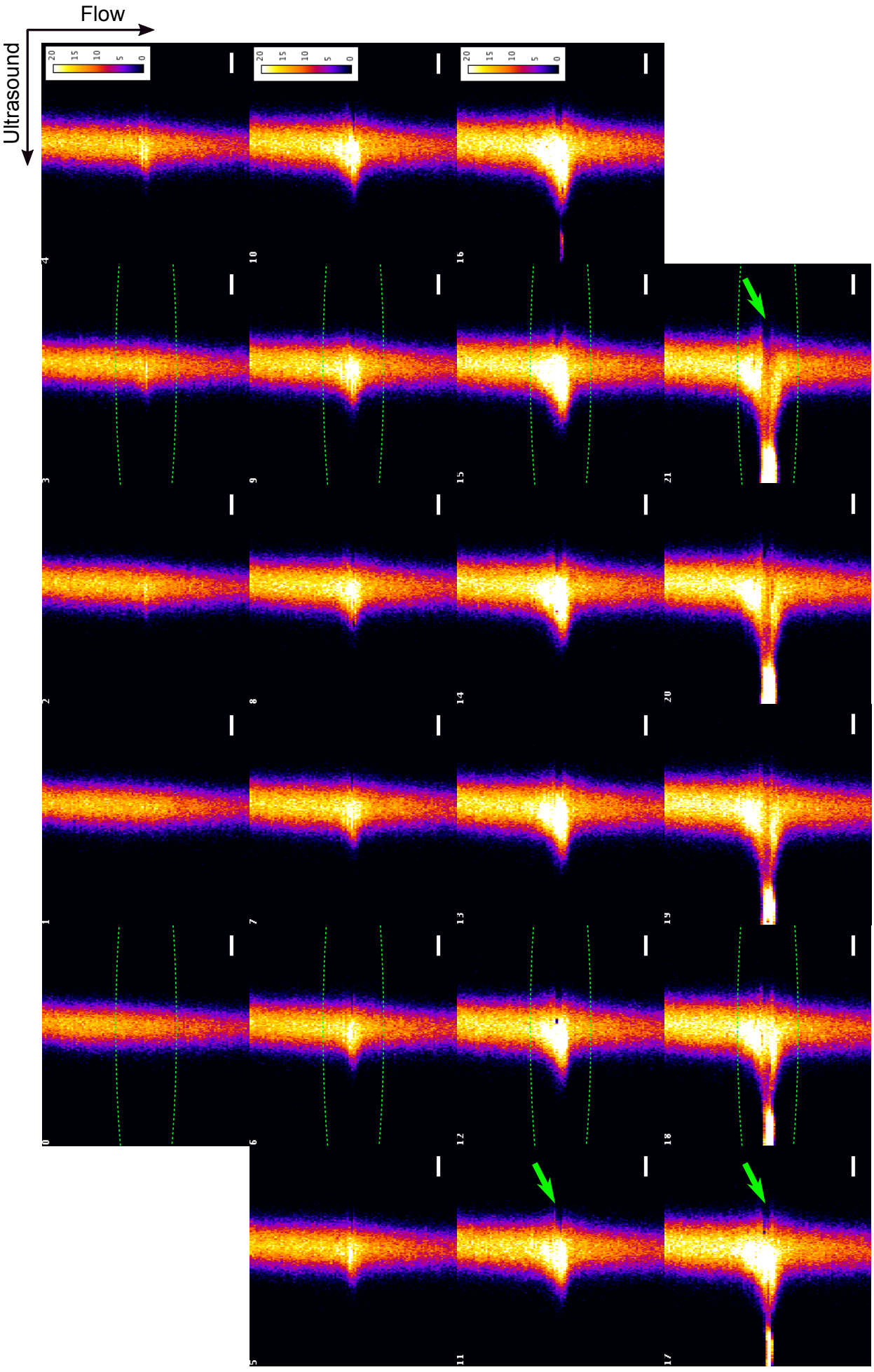

Figure 7.22: XZ scans of the flow channel from experiment D-1. Images were taken immediately before (0), during (1-20), and immediately after (21) ultrasound exposure. Starting from image 11, a persistent artefact, indicated by green allows, appears at the centre of the channel. This is attributed to the presence of an air pocket or similar structure that is inducing an optical distortion along the scan axis. Images are taken 30 s apart. Green line demarcates the anticipated ultrasound focus. Colour bars have units of fluorescence, and scale bars are 500 µm.

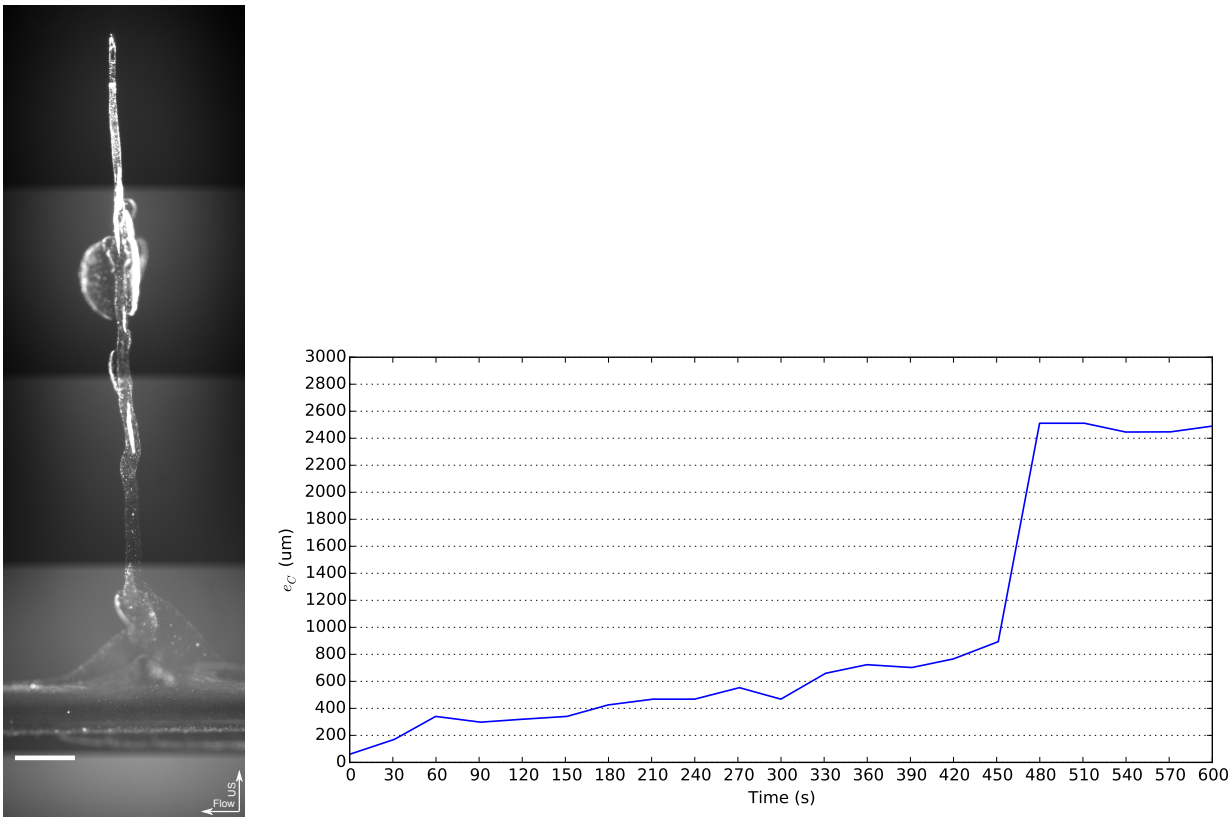

(a) (b)

Figure 7.23: **(a)** Widefield fluorescence microscopy of the central channel region and **(b)** e_C values duration ultrasound exposure in experiment D-1. Deformation extends 4276 µm into the agarose in the direction of ultrasound. Due to limited FOV displacement saturates at approximately 2500 µm. The image has been processed to improve contrast and brightness. Scale bar is 500 µm.

used to manufacture the bubbles, and that these properties can be conferred by PLGA nanoparticles. Additionally, this finding also suggests that DSEPC undergoes degradation when stored dissolved in chloroform at $-20\,^{\circ}\mathrm{C}$. This degradation may inherent to DSEPC, which has a typical shelf-life of one year.

7.3.9 Variations In Deformation Characteristics

There is a large variation in the deformation characteristics in the results presented here, even amongst deformations produced by the same cavitation agents. For example, in the deformations produced by PLGA nanoparticle loaded DSEPC microbubbles (Figure 7.14), some deformations feature prominent "side lobes" (L-Ia, L-Ib, and L-III) and some do not (L-II, L-IVa, L-IVb). These variations can be explained by inhomogeneities in the agarose hydrogel, resulting in local regions of enhanced or decreased mechanical strength; and variations in the nanoparticle and microbubble preparations, which affects the stability and ultrasound response of microbubbles and the loading efficiency of the nanoparticles.

7.4 Summary

The goals of this chapter were to test the assumption that loaded microbubbles do not produce more cavitation effect than their unloaded counterparts, and to evaluate the utility of SIOS for monitoring cavitation effects in real-time and *in-situ*. The data presented here demonstrated that PLGA nanoparticle loaded microbubbles, contrary to expectations, produced significantly more deformation in the flow channel model than either unloaded DSEPC microbubbles or PLGA nanoparticles. To explain the difference in deformations produced by loaded and unloaded DSEPC microbubbles, a theory was developed whereby PLGA nanoparticles, when loaded onto DSEPC microbubbles, increased the bubbles' dynamic stability, leading to the differences in deformation appearance and size.

The availability of *in-situ* images of the flow channel, provided by SIOS, allowed the development of deformations to be monitored in real-time. Combined with PCD

data, the images enabled the identification of possible correspondences between detected cavitation noise and deformation growth. Based on trends in the cavitation noise power, the presence of chamber-type and extended tunnel-type deformations could be detected. However, the onset of rapid deformation growth experienced by short and extended tunnel-type deformations produced no corresponding features in the PCD measurements. Furthermore, while cavitation activity, measured by total detected cavitation noise energy, showed some correlation with deformation size in experiments using the same cavitation agent, there was no general correlation across all cavitation agents.

Taken together, the results presented in this chapter suggest that loading of microbubbles can significantly affect their cavitation dynamics even though the difference may not be apparent from single-element coaxial PCD measurements. Consequently, extra care should be taken when characterising modified bubbles on the basis of PCD data alone, and it should not be assumed that safety data from unloaded microbubbles also applies to their loaded counterparts. Furthermore, the overall lack of correlation between PCD measurements and deformations suggest that, in a treatment context, single-element coaxial PCD should not be used as the sole means by which cavitation is monitored, as the level of cavitation activity does not, in general, reflect the magnitude of cavitation effect.

Finally, the utility of SIOS for monitoring cavitation effects in real-time and *in-situ* was demonstrated. Using the images provided by SIOS, it was possible to determine that the wave and tunnel-type deformations did not form gradually, but underwent a period of rapid growth with an abrupt onset. Furthermore, the images allowed the time of rapid growth onset to be determined, and this was instrumental in establishing that PCD measurements were unable to do the same.

Appendix

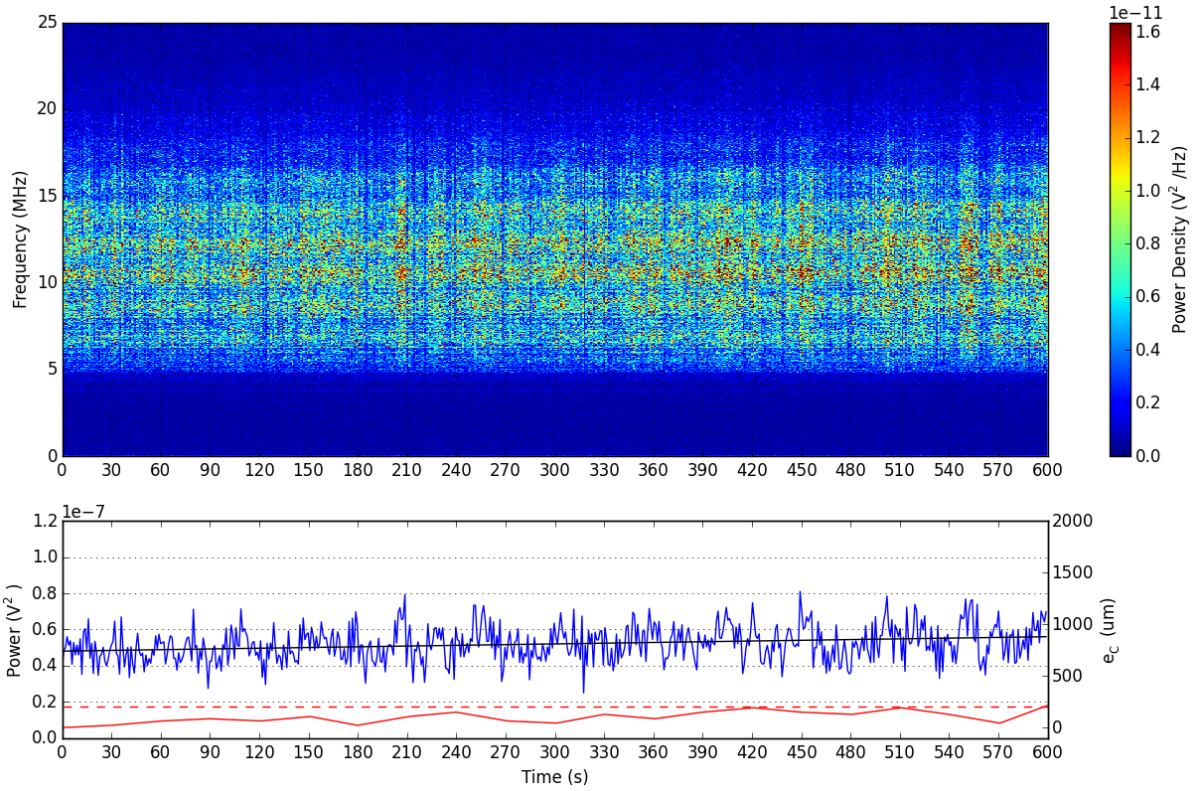

(a) C-II

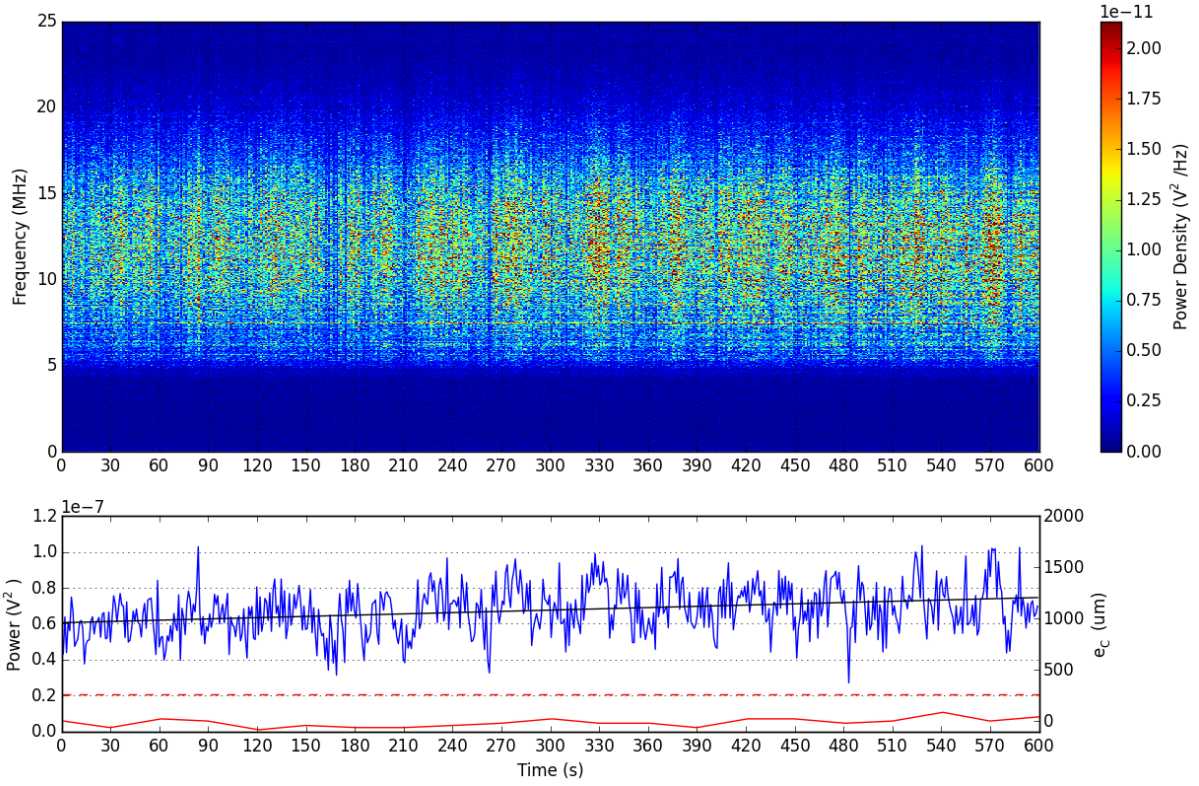

(b) C-IV

Figure 7.24: Spectrogram of experiments C-II and C-IV plotted together with the corresponding values of e_C. Power plots were fitted with 1st degree polynomials.

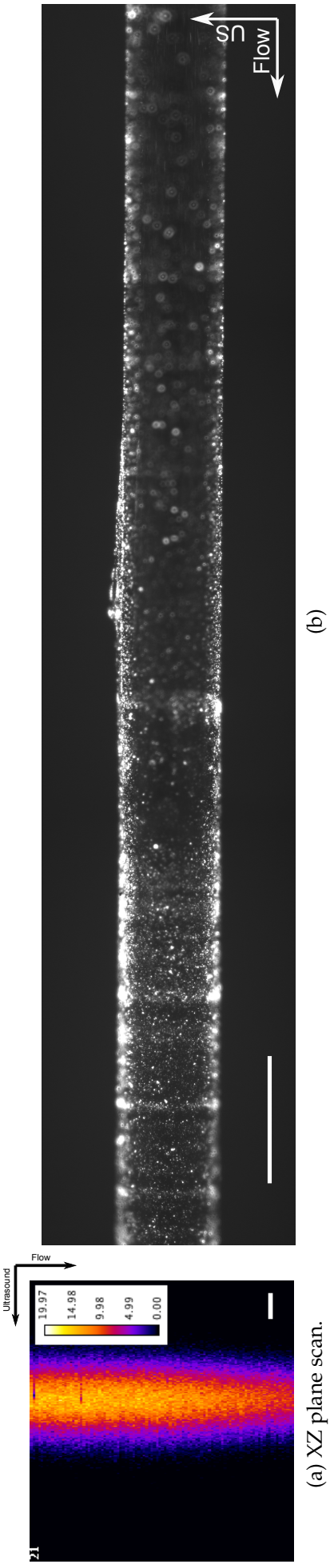

(a) XZ plane scan. (b)

Figure 7.25: Post ultrasound **(a)** SIOS and **(b)** widefield fluorescence microscopy images of the flow channel in experiments P-3. Deformation in (b) extended 42 µm in the direction of ultrasound propagation. Colour bar has units of fluorescence. Scale bar is 500 µm.

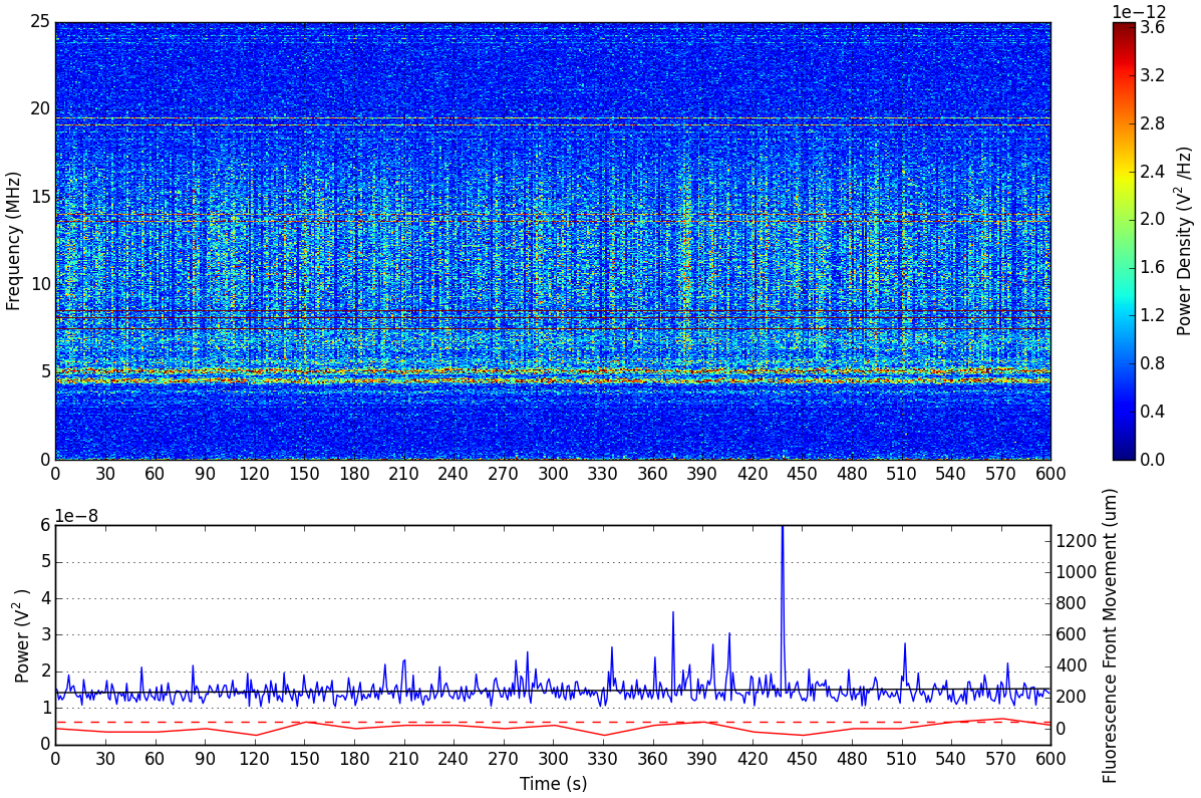

(a) P-3

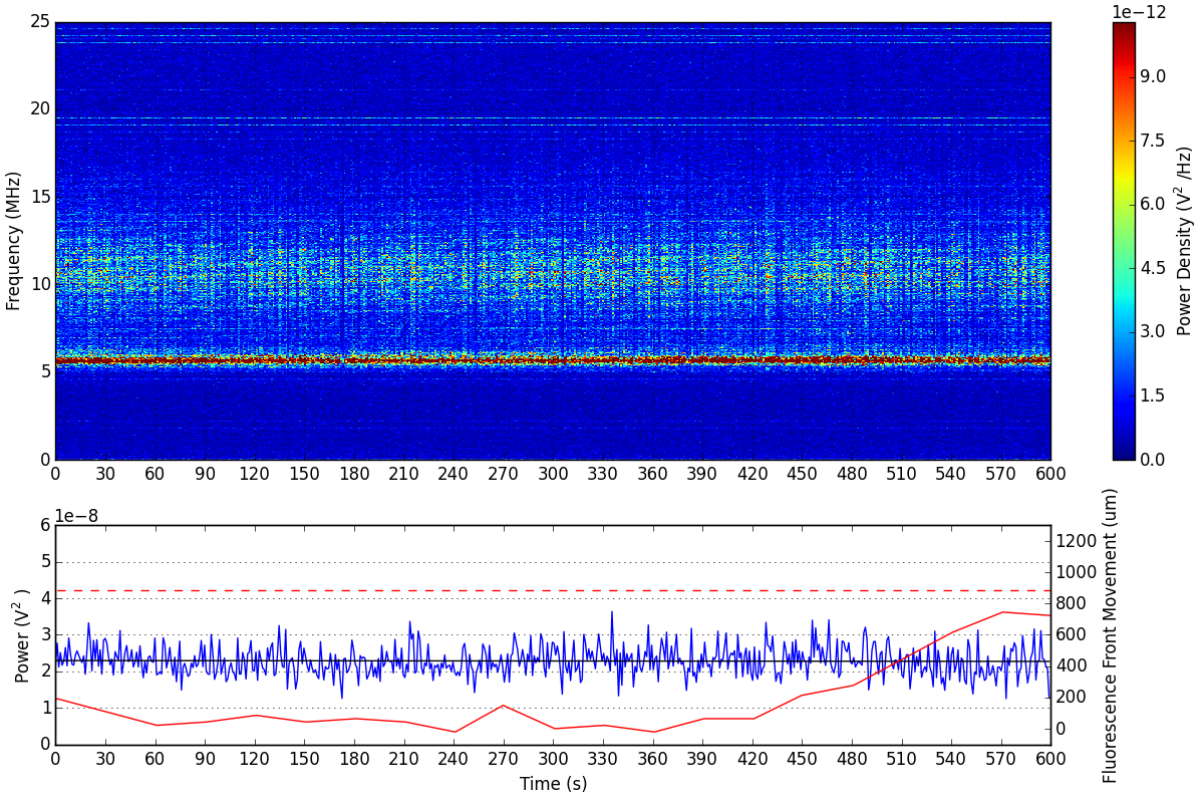

(b) P-4

Figure 7.26: Spectrogram of experiments P-3, P-4 and P-IV plotted together with the corresponding values of e_C. Power plots were fitted with 1st degree polynomials.

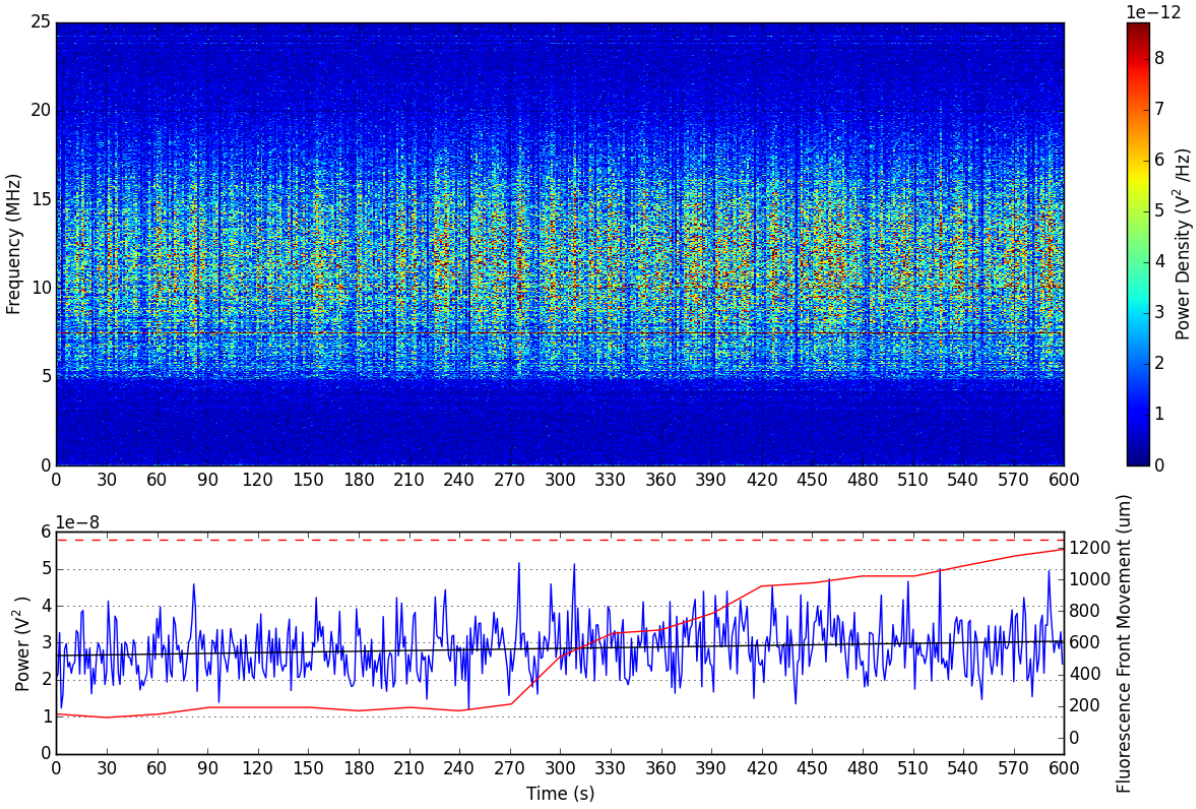

(c) P-IV

Figure 7.27: (continued)

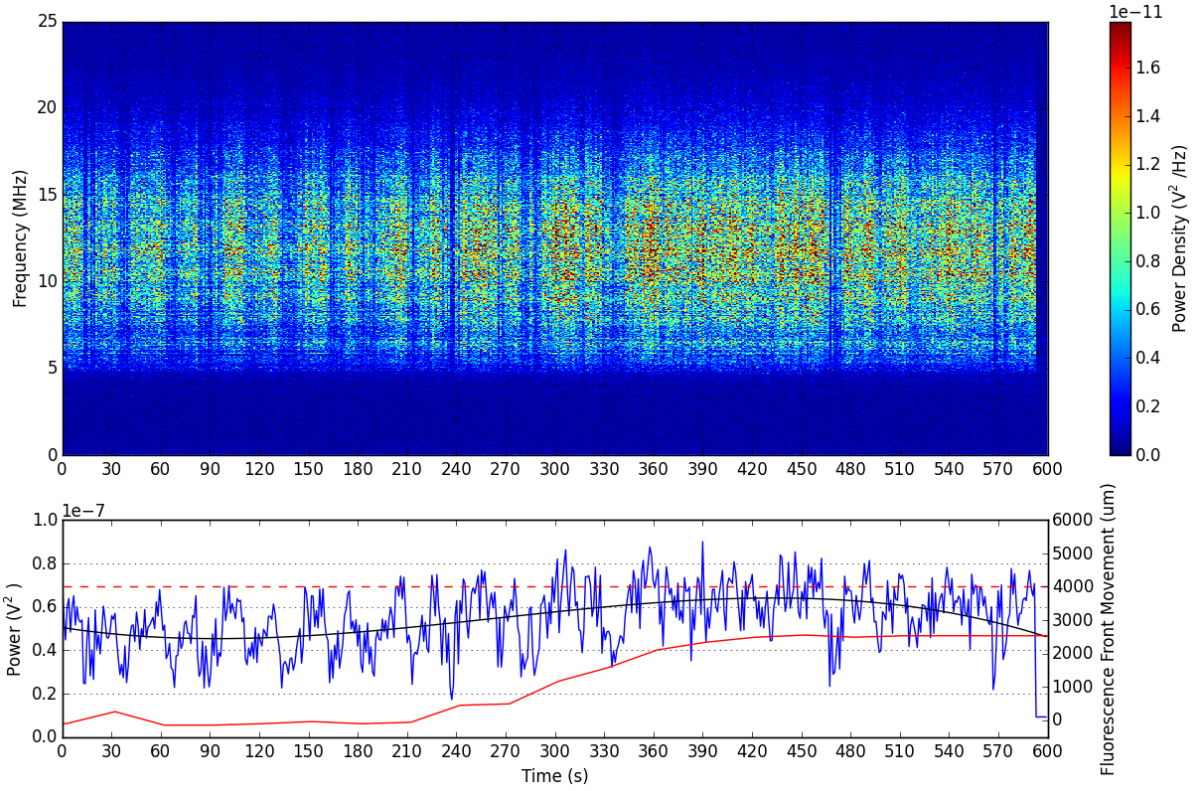

(a) L-Ib

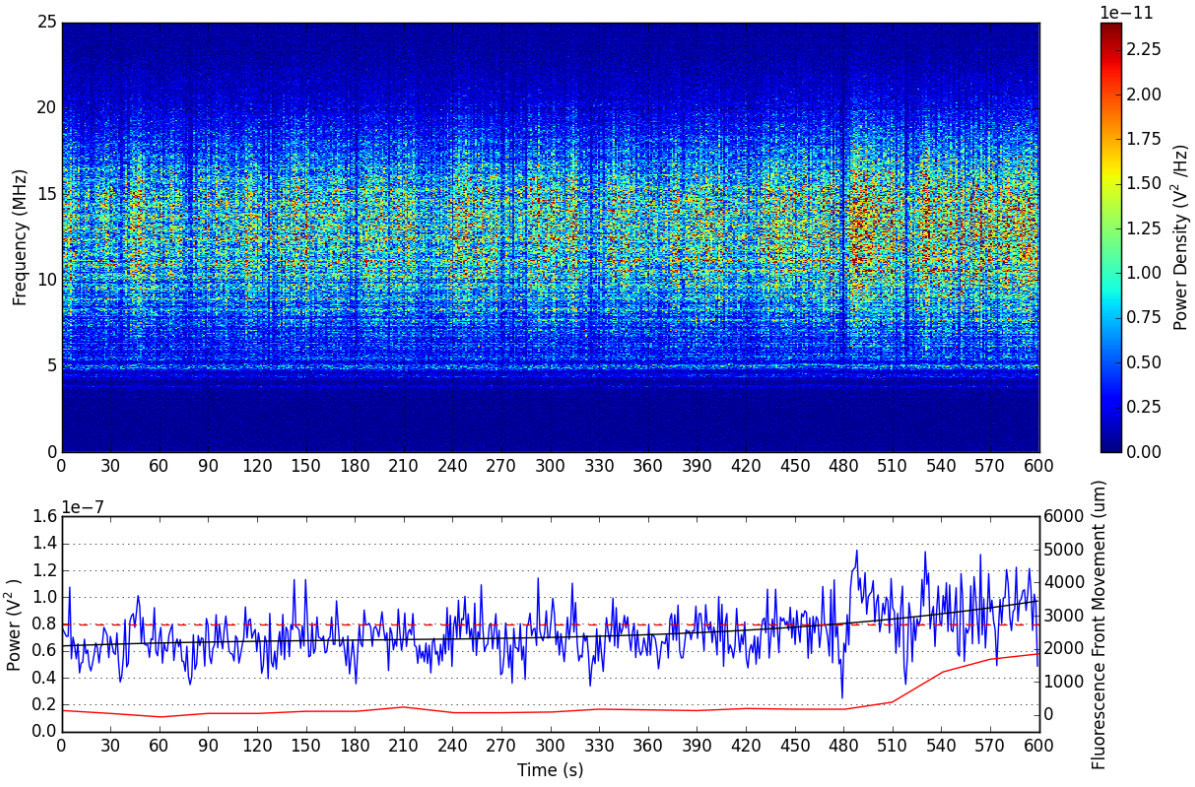

(b) L-II

Figure 7.28: Spectrogram of experiments L-Ib to L-IVb plotted together with the corresponding values of e_C. **(a)** is cut short due to experimenter error resulting in ultrasound exposure ending earlier than planned. Power plots were fitted with 3rd degree polynomials.

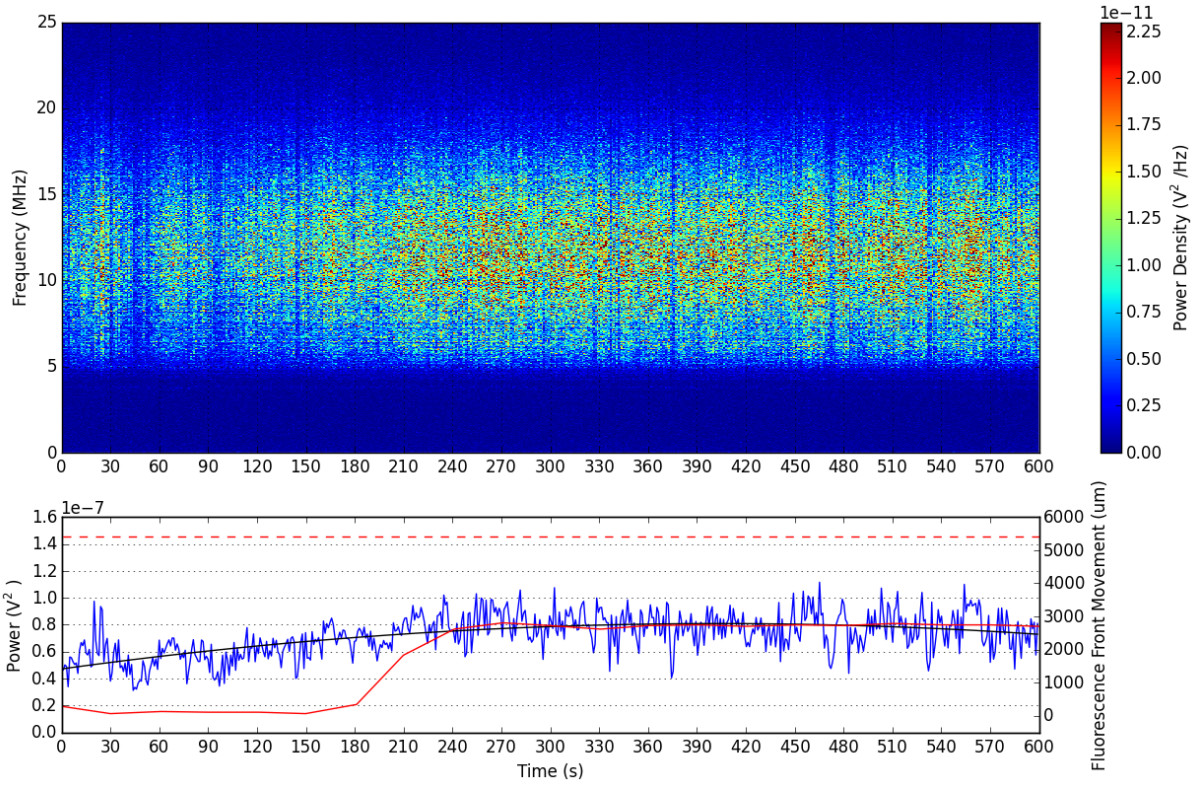

(c) L-III

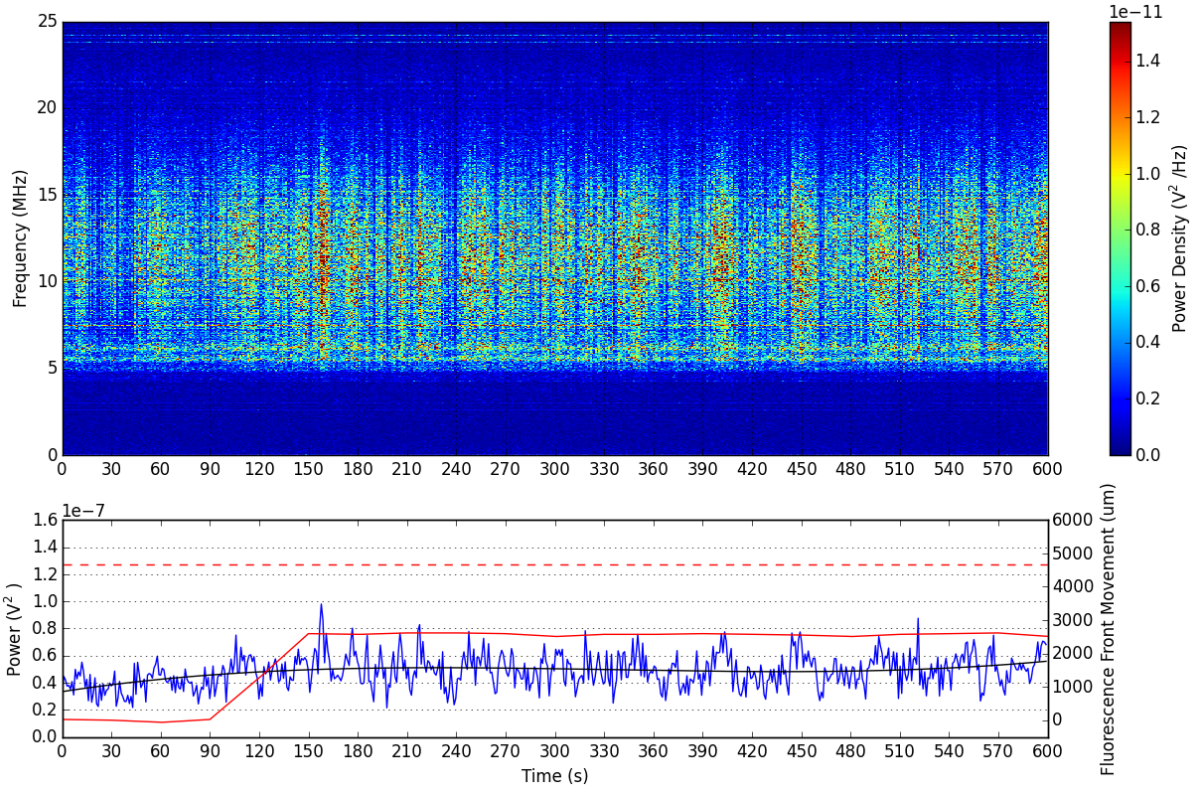

(d) L-IVa

Figure 7.28: (continued)

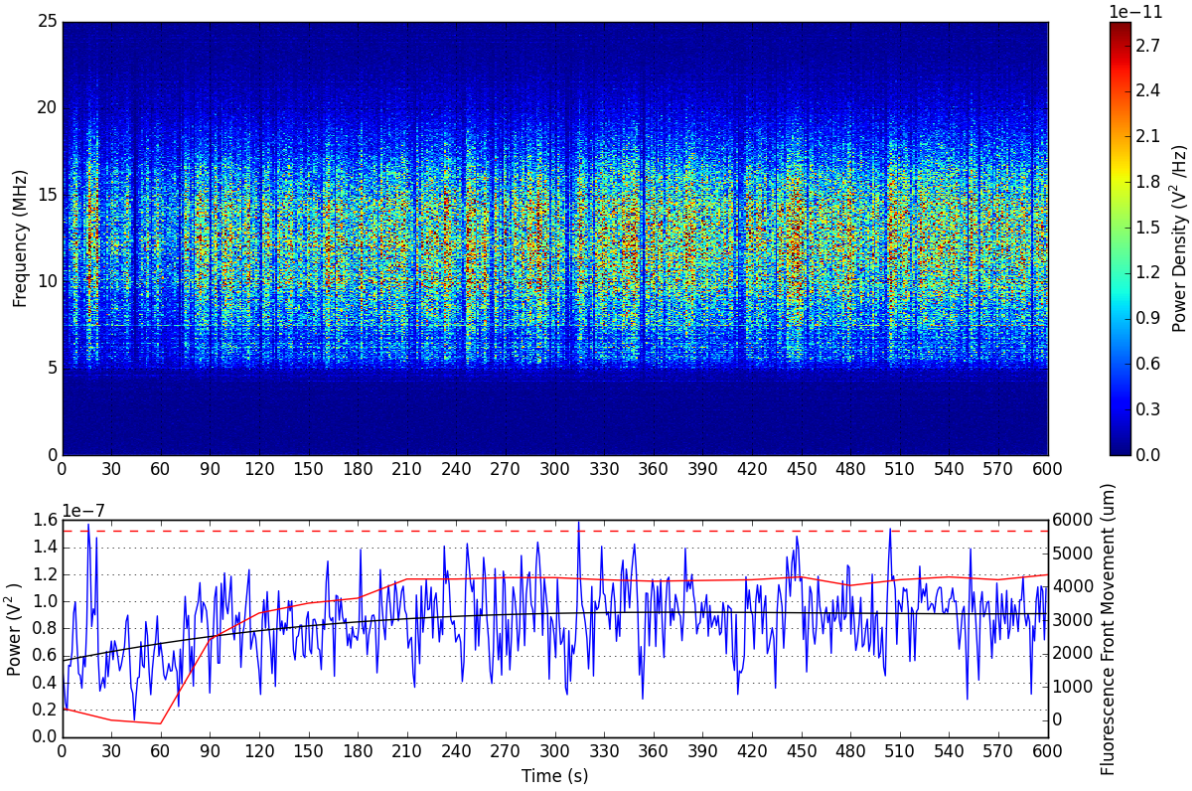

(e) L-IVb

Figure 7.29: (continued)

References

[1] Roosmarijn E Vandenbroucke, Ine Lentacker, Joseph Demeester, Stefaan C De Smedt, and Niek N Sanders. Ultrasound assisted sirna delivery using peg-siplex loaded microbubbles. *Journal of controlled release*, 126(3):265–273, 2008.

[2] Michael C Cochran, John Eisenbrey, Richard O Ouma, Michael Soulen, and Margaret A Wheatley. Doxorubicin and paclitaxel loaded microbubbles for ultrasound triggered drug delivery. *International journal of pharmaceutics*, 414(1):161–170, 2011.

[3] Bart Geers, Ine Lentacker, Niek N Sanders, Joseph Demeester, Stephen Meairs, and Stefaan C De Smedt. Self-assembled liposome-loaded microbubbles: The missing link for safe and efficient ultrasound triggered drug-delivery. *Journal of controlled release*, 152(2):249–256, 2011.

[4] Ine Lentacker, Stefaan C De Smedt, and Niek N Sanders. Drug loaded microbubble design for ultrasound triggered delivery. *Soft Matter*, 5(11):2161–2170, 2009.

[5] Ying Luan, Telli Faez, Erik Gelderblom, Ilya Skachkov, Bart Geers, Ine Lentacker, Ton van der Steen, Michel Versluis, and Nico de Jong. Acoustical properties of individual liposome-loaded microbubbles. *Ultrasound in medicine & biology*, 38(12):2174–2185, 2012.

[6] Rebecca L McCall and Rachael W Sirianni. Plga nanoparticles formed by single- or double-emulsion with vitamin e-tpgs. *JoVE (Journal of Visualized Experiments)*, (82):e51015–e51015, 2013.

[7] Graciela Mohamedi, Mehrdad Azmin, Isabel Pastoriza-Santos, Victoria Huang, Jorge Pérez-Juste, Luis M Liz-Marzán, Mohan Edirisinghe, and Eleanor Stride. Ef-

fects of gold nanoparticles on the stability of microbubbles. *Langmuir*, 28(39):13808–13815, 2012.

Chapter 8

Cavitation Agent Catalogue

8.1 Introduction

Ultrasound and cavitation mediated drug delivery typically utilises gas microbubbles as cavitation agents. The gas microbubbles, with diameters in the range of 1 to 10 µm, do not readily extravasate from tumour vasculature as they are much larger than the characteristic pore cutoff size of ≤ 1.2 µm [1]. As a result, cavitation effects are largely confined to the interior of tumour blood vessels and the immediate surroundings. Recently, nanometre-scale cavitation agents have been developed that can pass through tumour vasculature and travel into the surrounding tissue, delivering cavitation effects more directly and effectively. Furthermore, these nanometre-scale agents are prevented from infiltrating normal tissue due to the tighter endothelial junctions in healthy blood vessels, causing these agents to preferentially accumulate in tumours.

Two nanometre-scale cavitation agents are of interest in the present work. The first, referred to as nanocups, are cup-shaped nanoparticles with entrapped gas bubbles [2]. Under ultrasound exposure, the trapped bubbles detach from the nanocups and undergo inertial cavitation (Figure 8.1). The second, referred to as nanodroplets, are amphiphilic polymer coated droplets[1] with cores of liquid perfluorohexane. When exposed to ultrasound, the perfluorohexane cores are vaporised, resulting in microbubbles that then undergo acoustic cavitation (Figure 8.2). Nanodroplets can also be loaded with drugs and other agents, e.g. iron oxide for contrast under magnetic reson-

[1] Manuscript in preparation

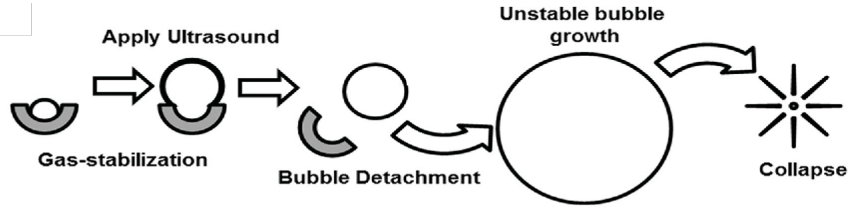

Figure 8.1: Detachment of en entrapped air bubble from a nanocup and subsequent bubble cavitation [2].

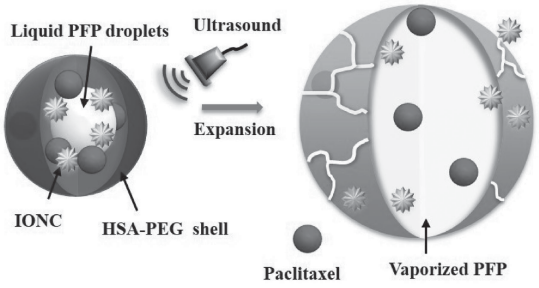

Figure 8.2: Ultrasound activation of a magnetically responsive nanodroplets loaded with paclitaxel [3]. **HSA**: human serum albumin; **PEG:** poly(ethylene glycol); **IONC**: iron oxide nanocrystals; **PFC**: liquid perfluorocarbon.

ance imaging and magnetic targeting.

To better understand these new nanometre-scale cavitation agents, the developed instrument was used to characterise the cavitation effects of nanocups, nanodroplets and gas microbubbles under a standard set of conditions. Such a catalogue is of scientific and clinical interest, allowing for the comparisons of cavitation effects and characteristics between cavitation agents of different sizes and modes of action. As the cavitation phenomena responsible for the induced effects are not fully understood, the scope of the present work is limited to the observation of cavitation effects, and does not include investigations into the underlying cavitation dynamics.

8.2 Materials and Methods

Agarose channel models made from 2 % w/v agarose and featuring 370 µm diameter flow channels were utilised for all catalogue experiments. After alignment of the system and channel models, fluorescent suspensions containing the cavitation agent under test were flowed through the channels at $27\,\mu L\,min^{-1}$. The channels were then exposed to ultrasound and were simultaneously imaged *in-situ* by SIOS. Post ultrasound exposure, the flow channels were treated to improve contrast under widefield

fluorescence microscopy, then excised and imaged with an inverted microscope.

Details on the manufacture of agarose channel models, the alignment procedures, and the post ultrasound exposure treatment of flow channels can be found in Chapter 5.

8.2.1 Cavitation Agents

The cavitation agents in the catalogue consist of DSEPC microbubbles, loaded and unloaded; SonoVue®; nanocups; and nanodroplets.

8.2.1.1 Concentration

To allow direct comparison all cavitation agents were prepared at a concentration of $\approx 1 \times 10^7$ cavitation nuclei per mL. Alternatives, such as maintaining a constant gas fraction, were considered and rejected due to the difficulties in quantifying the gas fraction of nanodroplets and nanocups, which when inert has a gas fraction of zero.

8.2.1.2 DSEPC Microbubbles

The catalogue includes DSEPC microbubbles, loaded and unloaded, previously described in Chapter 7. As the results from Chapter 7 are obtained using the same experimental parameters that are used here, they are included in the catalogue without modifications. In the interest of brevity, however, results from Chapter 7 will not be presented here in detail, but will be included in analyses.

8.2.1.3 SonoVue

SonoVue®(Bracco International B.V., Netherlands) is a commercially available ultrasound contrast agent, and consisting of gas microbubbles with a mean diameter of $\approx$ 2.5 µm. Each microbubble has a phospholipid shell and a core of sulphur hexafluoride gas. Supplied as a kit containing 25 mg of lyophilised powder and 5 mL of sodium chloride, SonoVue was prepared prior to each experiment according to the manufacturer instructions, then diluted using de-ionised water to achieve the desired concentration of 1×10^7 mL^{-1}.

8.2.1.4 Nanocups

Nanocups are cup-shaped nanoparticles 100 to 460 nm in size, containing trapped gas nanobubbles. They were manufactured by coating polystyrene template nanoparticles with a cross-linked polymethyl methacrylate polymer, resulting in cup-shaped nanoparticles suitable for trapping air bubbles [2]. To seed the nanocups with air bubbles, nanocups in suspension were air dried and then resuspended. Following resuspension, nanocups were diluted to a concentration $1\,\mu g\,mL^{-1}$, containing an estimated 1×10^7 nanocups per millilitre.

Due to their stability, the same nanocups suspension was used for all experiments. The stock suspension was prepared Anne Charlotte Van Blokland at the Institute of Biomedical Engineering, Department of Engineering Science, University of Oxford.

8.2.1.5 Nanodroplets

Nanodroplets are polymer-shelled nanoparticles, approximately 800 nm in diameter, containing a liquid perfluorocarbon core loaded with iron oxide nanoparticles. Nanodroplets were manufactured by ultrasonic emulsification of 5% v/v perfluorohexane in water in the presence of iron oxide nanoparticles ($2.5\,mg\,mL^{-1}$) and poly(ethylene glycol) methyl ether-block-poly(D,L-lactide)-block-decane ($2.5\,mg\,mL^{-1}$), an amphiphilic triblock copolymer of polyethylene glycol. The resulting emulsion was then washed and diluted down to the required concentration of $1 \times 10^7\,mL^{-1}$.

The nanodroplets were manufactured on the same day as each experiment by Luca Bau at the Institute of Biomedical Engineering, Department of Engineering Science, University of Oxford.

8.2.2 Ultrasound Exposure and *In Situ* Monitoring

As shown in Figure 8.3, ultrasound exposure occurred concurrently with *in situ* monitoring. Flow channels were imaged longitudinally in the XZ plane once every 30 s and a total of 22 images was acquired per channel. Depending on the field-of-view, image acquisition time was between 27 to 29 s. Immediately following the acquisition of the first image, flow channels were exposed to high-intensity focused-ultrasound (HIFU)

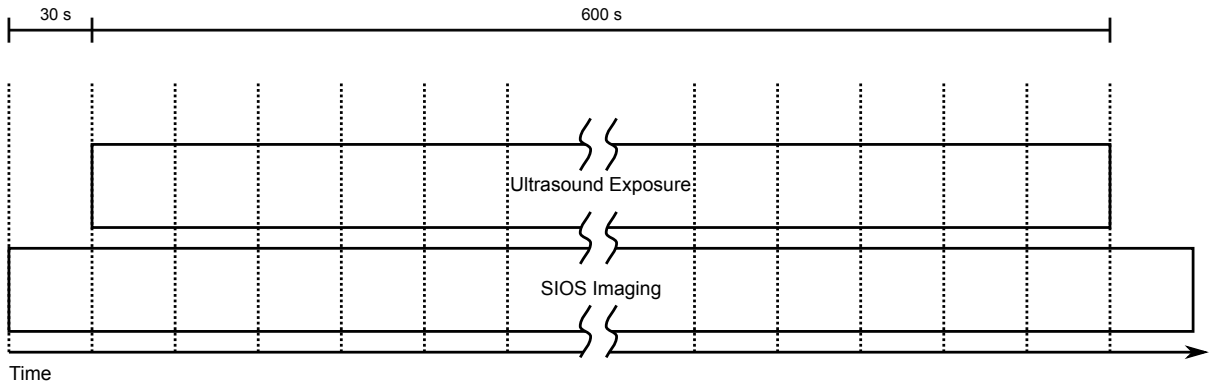

Figure 8.3: Experiment timeline. Dotted lines indicate the start of XZ plane scans of the flow channel. Time taken for each scan was kept below 30 s to avoid overruns.

Cavitation Agent	Labels
SonoVue	S-1 to S-4
Nanocups	N-1 to N-4
Nanodroplets	A-1 to A-3
DSEPC microbubbles	C-I to C-IV
PLGA nanoparticle loaded DSEPC microbubbles	L-I to L-IV

Table 8.1: Cavitation agent catalogue experiment labels.

at 1.067 MHz, 1.8 MPa peak negative pressure, 5 Hz pulse repetition frequency (PRF) and 1.17 % duty cycle for 10 min.

The ultrasound exposure parameters used were chosen to so that, at the same concentration, cavitation agents produced different levels of cavitation effects. While these parameters may be far from optimal for some agents, it allows for the direct comparison of cavitation effects and the analysis of commonalities and differences that would not be possible if cavitation-agent specific ultrasound parameters were used.

8.2.3 Experimental Groups

For ease of reference, experiments were grouped based on the cavitation agent used and are labelled as shown in Table 8.1.

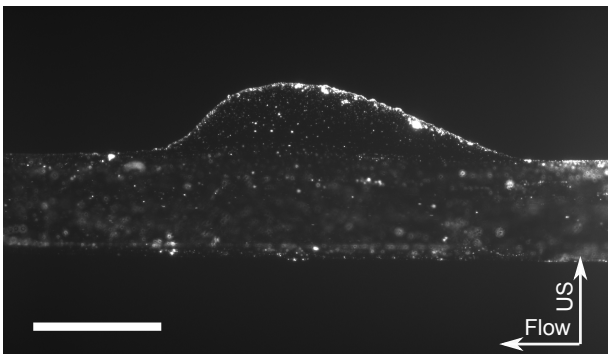

Figure 8.4: Widefield fluorescence microscopy of the chamber-type deformation produced in experiment S-2 during ultrasound exposure. The deformation extends 286 µm in the direction of ultrasound propagation. Scale bar is 500 µm.

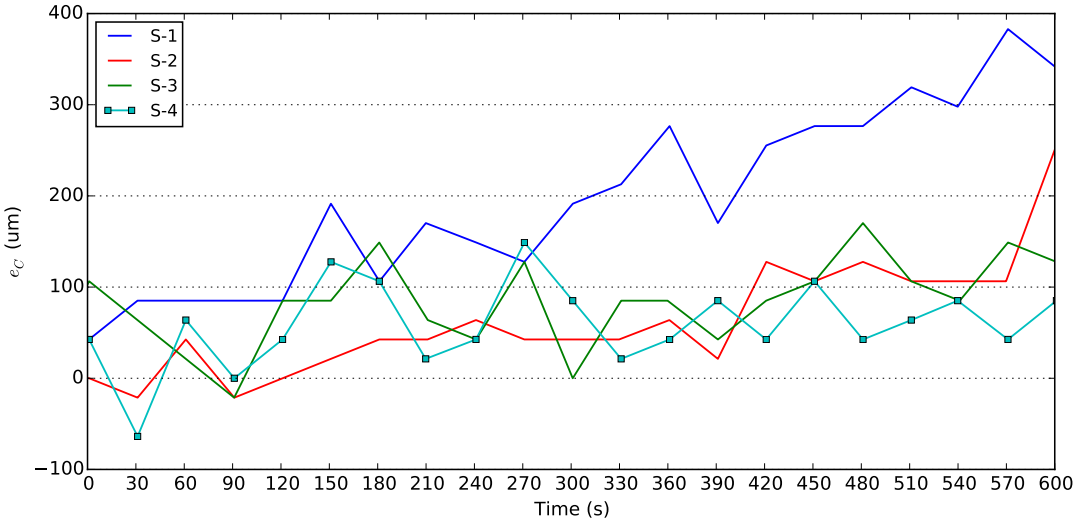

Figure 8.5: e_C from experiment S-1 to S-4.

8.3 Results and Discussion

8.3.1 SonoVue

8.3.1.1 Deformation Characteristics

Ultrasound exposure of SonoVue in flow channels produced "chamber-type" deformations similar in size and shape to those found in unloaded DSEPC microbubble experiments (Figure 8.4). This is consistent with the fact that SonoVue and DSEPC microbubbles are both phospholipid shelled gas microbubbles with similar mean diameters (SonoVue: 2.5 µm; DSEPC: 1.6 µm).

The channel-centre fluorescence front displacement, e_C, for experiments S-1 to S-4 is shown in Figure 8.5. The gradual increase in e_C in experiment S-1 supports the theory, advanced in Chapter 7, that chamber-type deformations are the result of gradual

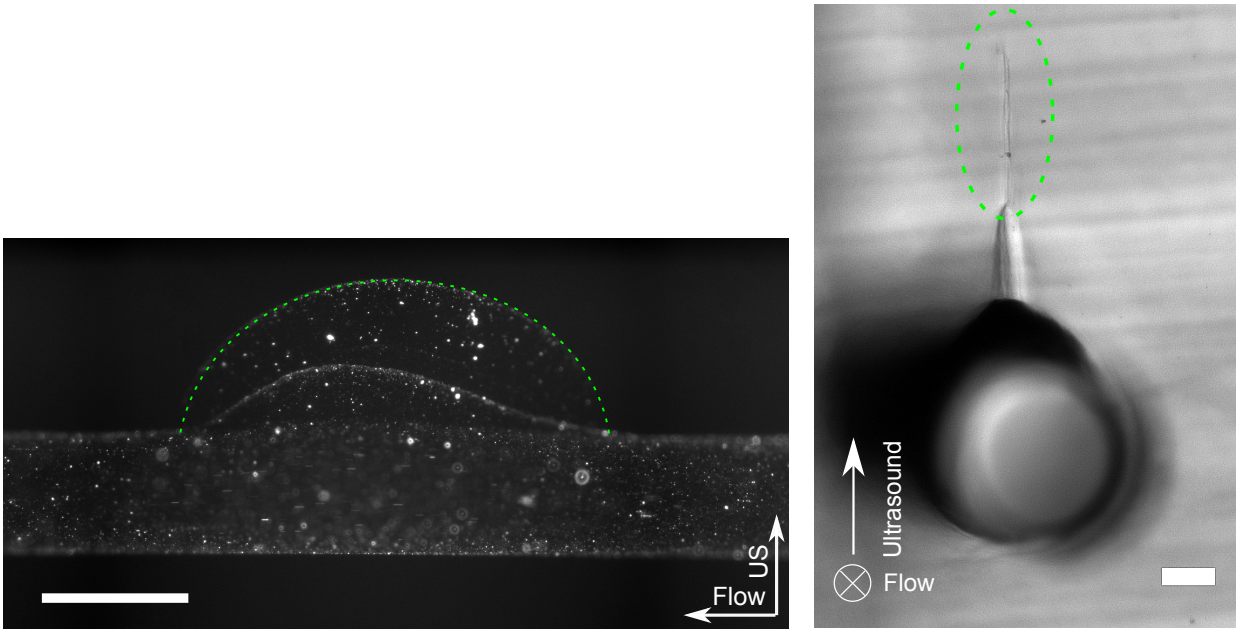

(a) (b)

Figure 8.6: Widefield fluorescence microscopy of chamber-type deformation and crevice in experiments S-4. **(a)** Fluorescence microscopy of the deformation and crevice. **(b)** Brightfield cross-section view of the deformation and crevice. The crevice, outlined in green, extends 536 µm in the direction of ultrasound propagation, while the deformation extends 251 µm. Scale bars are 500 µm and 100 µm in (a) and (b) respectively.

erosion by cavitation.

In experiment S-4, agarose cracking produced a crevice in the imaging plane that extended 536 µm in the direction of ultrasound propagation (Figure 8.6a). The presence of this crevice was not reflected in the e_C values from experiment S-4, a failure in detection that could be explained by the small volume of the crevice (Figure 8.6b), where the amount of fluorescent liquid contained within was below the limits of detection.

Deformation extents in the direction of ultrasound from all SonoVue experiments can be found in Table 8.2.

8.3.1.2 Cavitation Characteristics

The trend of linearly increasing cavitation power between the start and end of ultrasound exposure, previously associated with chamber-type deformation in Section 7.3.3.1, was observed in experiments S-2 (Figure 8.7b), S-3 and S-4 (see Appendix) where deformations were of a similar size to those observed with unloaded DSEPC microbubbles. It was not present in experiments S-1 (Figure 8.7a), where deformation

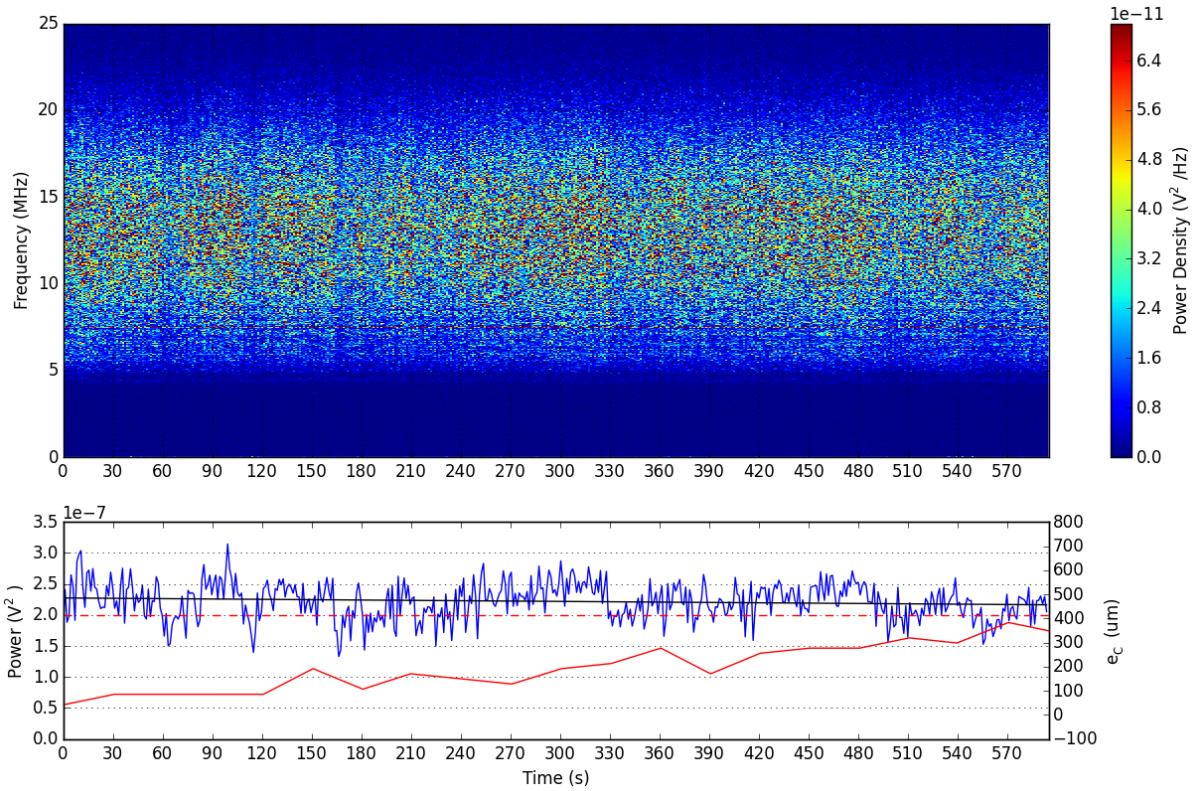

(a) S-1

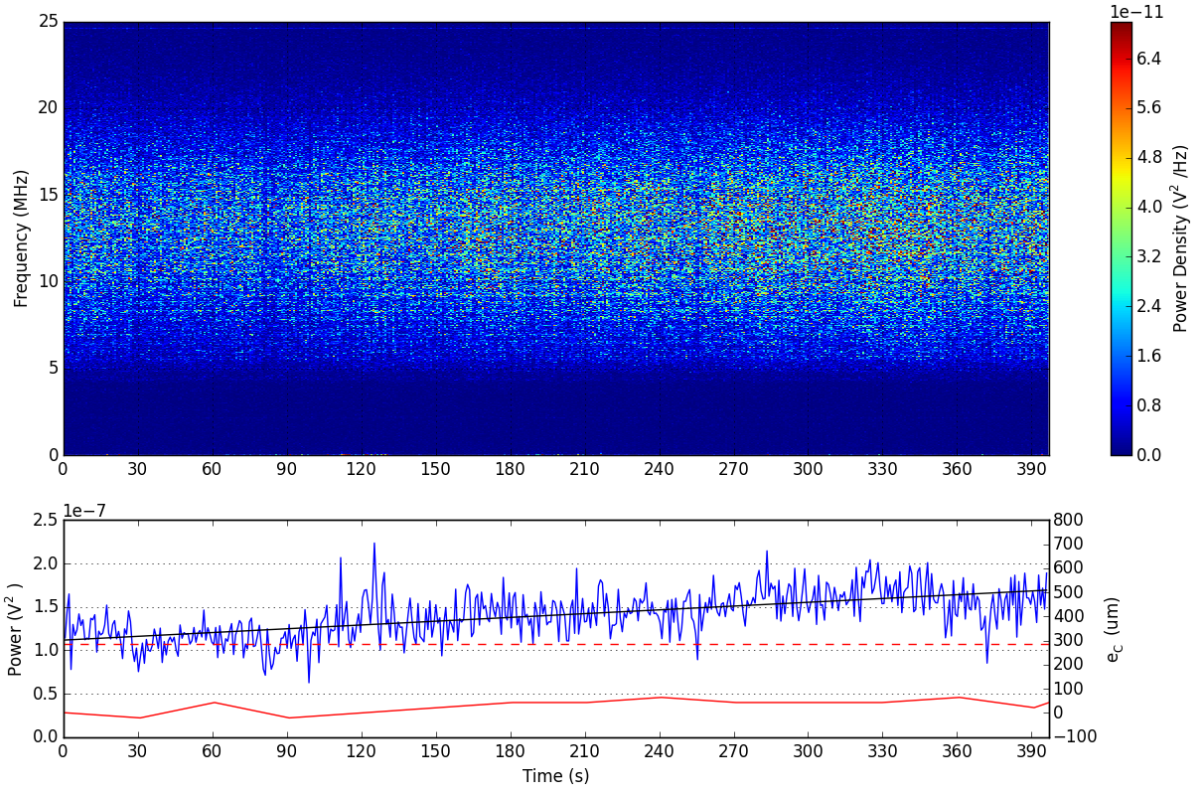

(b) S-2

Figure 8.7: PCD spectrogram and power in experiment S-1 and S2 plotted together with their corresponding e_C. Red dashed lines indicate the deformation extent in the direction of ultrasound propagation measured using widefield microscopy. Power plots have been fitted with 1st degree polynomials.

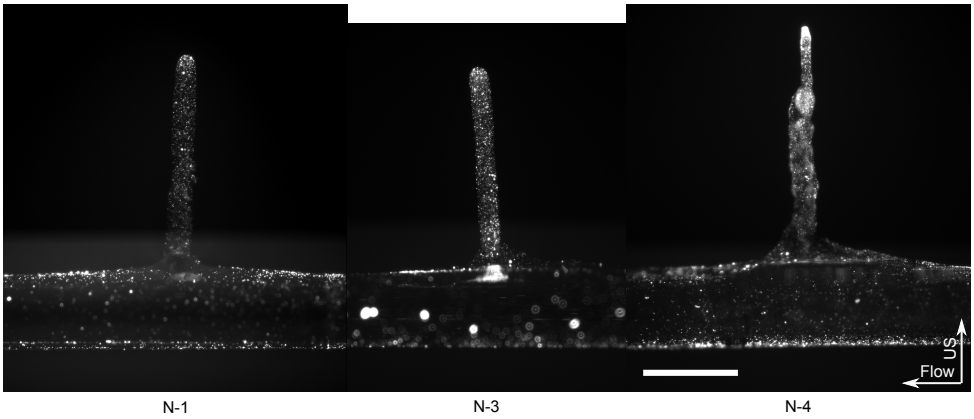

Figure 8.8: Widefield fluorescence microscopy of short tunnel-type deformations in experiments N-1, N3 and N-4. Left-to-right, deformation extend 1179 µm, 1096 µm, and 1266 µm in the direction of ultrasound propagation. Scale bar is 500 µm.

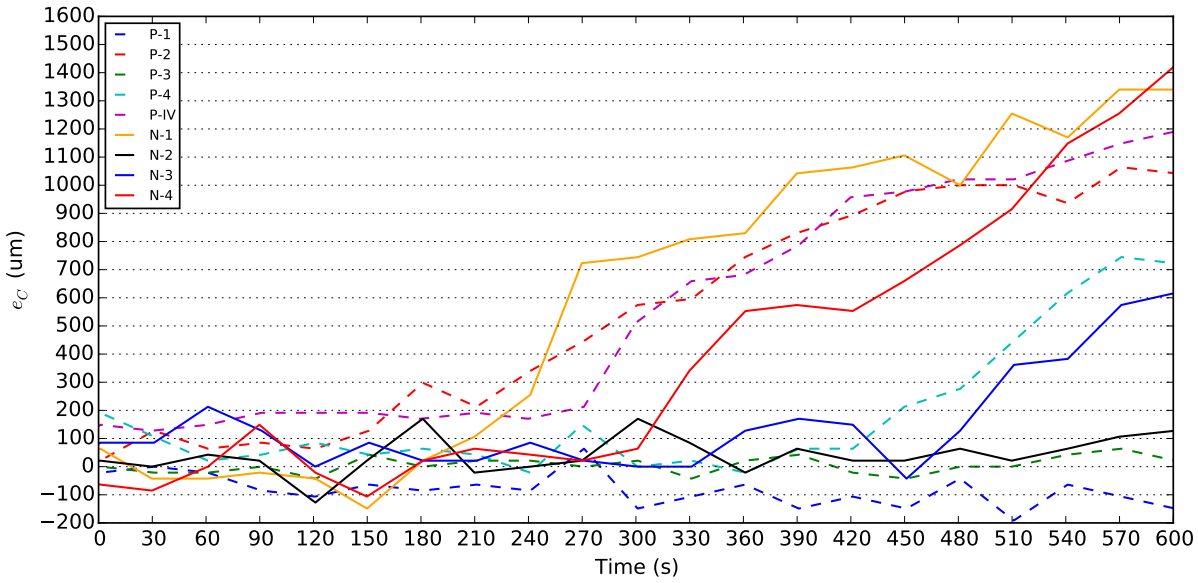

Figure 8.9: e_C values from nanocup and PLGA nanoparticle experiments.

extended 413 µm in the direction of ultrasound propagation.

8.3.2 Nanocups

8.3.2.1 Deformation Characteristics

In three of four nanocup experiments, short tunnel-type deformations similar to those produced in PLGA nanoparticles experiments (Chapter 7) were observed. The deformations were approximately 100 µm wide and 1000 µm in length, and were observed in experiments N-1, N-3, and N4 (Figure 8.8). In addition to their similarities in appearance, the deformations also exhibited similar rates of growth (Figure 8.9), suggesting

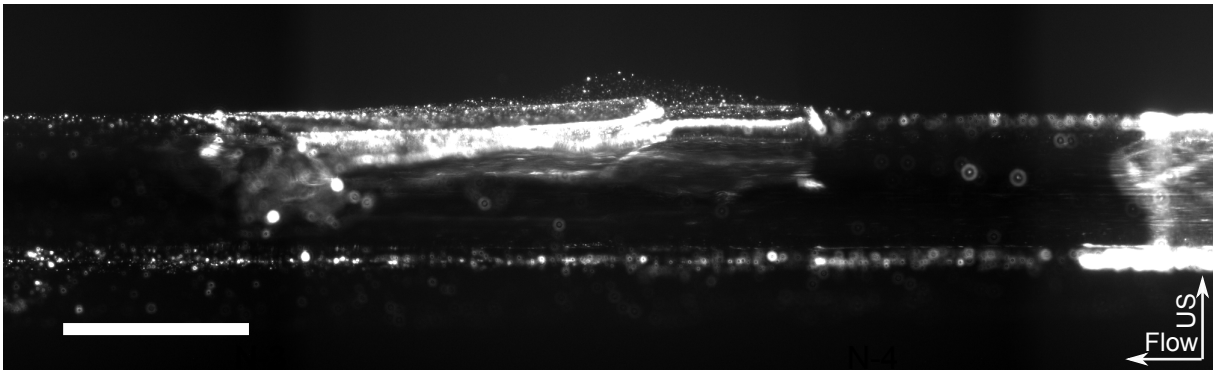

Figure 8.10: Widefield fluorescence microscopy of deformation in experiment N-2. Deformation extends 88 µm in the direction of ultrasound propagation. Scale bar is 500 µm.

that the same underlying mechanism was responsible. This implies that, under current experimental parameters, nanocups have no more effect than PLGA nanoparticles.

In the remaining experiment, N-2, minimal deformation occurred (Figure 8.10).

8.3.2.2 Cavitation Characteristics

Cavitation was detected in all experiments (e.g. Figure 8.11; full data set in Appendix). However no features in the spectrograms or the power plots could be consistently associated with the onset of rapid deformation growth. The power of recorded PCD signals, also referred to as PCD power, was found to increase in all experiments, with the rate of increase, determined from the fitted polynomials, bearing some relation to the deformation extent (Figure 8.12). A possible explanation for this relationship is that as the deformations enlarge the flow channels, the number of nanocups within the ultrasound focus increases, leading to increased cavitation activity and, therefore, cavitation noise.

8.3.3 Nanodroplets

8.3.3.1 Deformation Characteristics

Deformations resulting from the ultrasound exposure of nanodroplets (Figure 8.13) took on different shapes and appearances. The first experiment (A-1) produced a deformation similar to those seen with PLGA nanoparticles and nanocups, the second experiment (A-2) produced an irregular deformation due to agarose cracking, and the

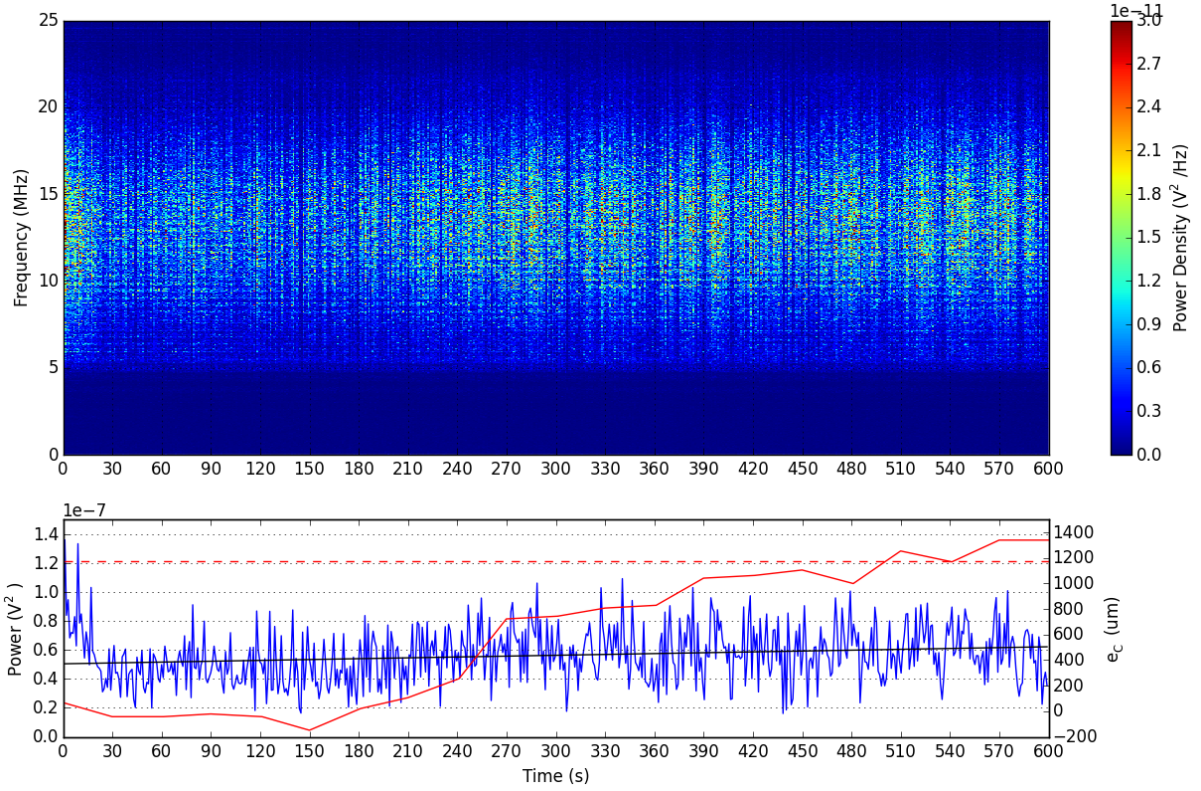

Figure 8.11: PCD spectrogram and power from experiment N-1 plotted with e_C. The red dashed line indicates deformation extent in the direction of ultrasound propagation measured using widefield microscopy. Power plot has been fitted with a first degree polynomial.

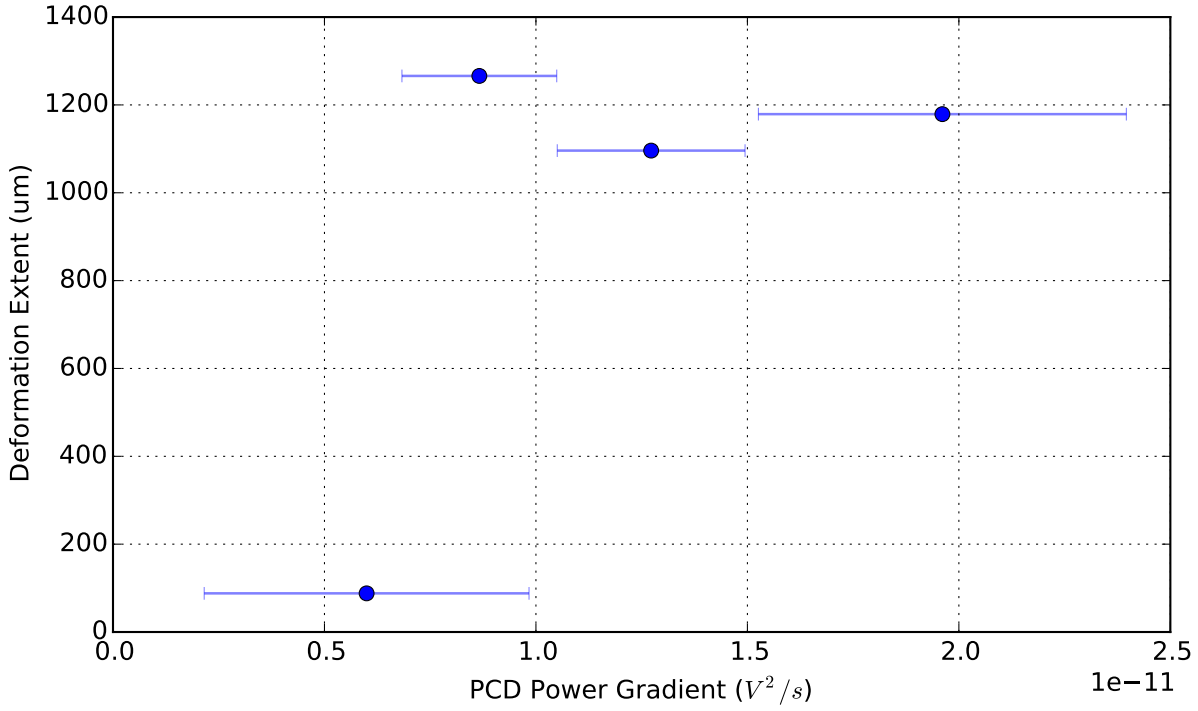

Figure 8.12: Deformation extent vs PCD power gradient. Deformation extents are in the direction of ultrasound and were determined by widefield microscopy. PCD power gradients were determined by fitting straight lines to the PCD power curves. Error bars represent the standard error of gradient estimates.

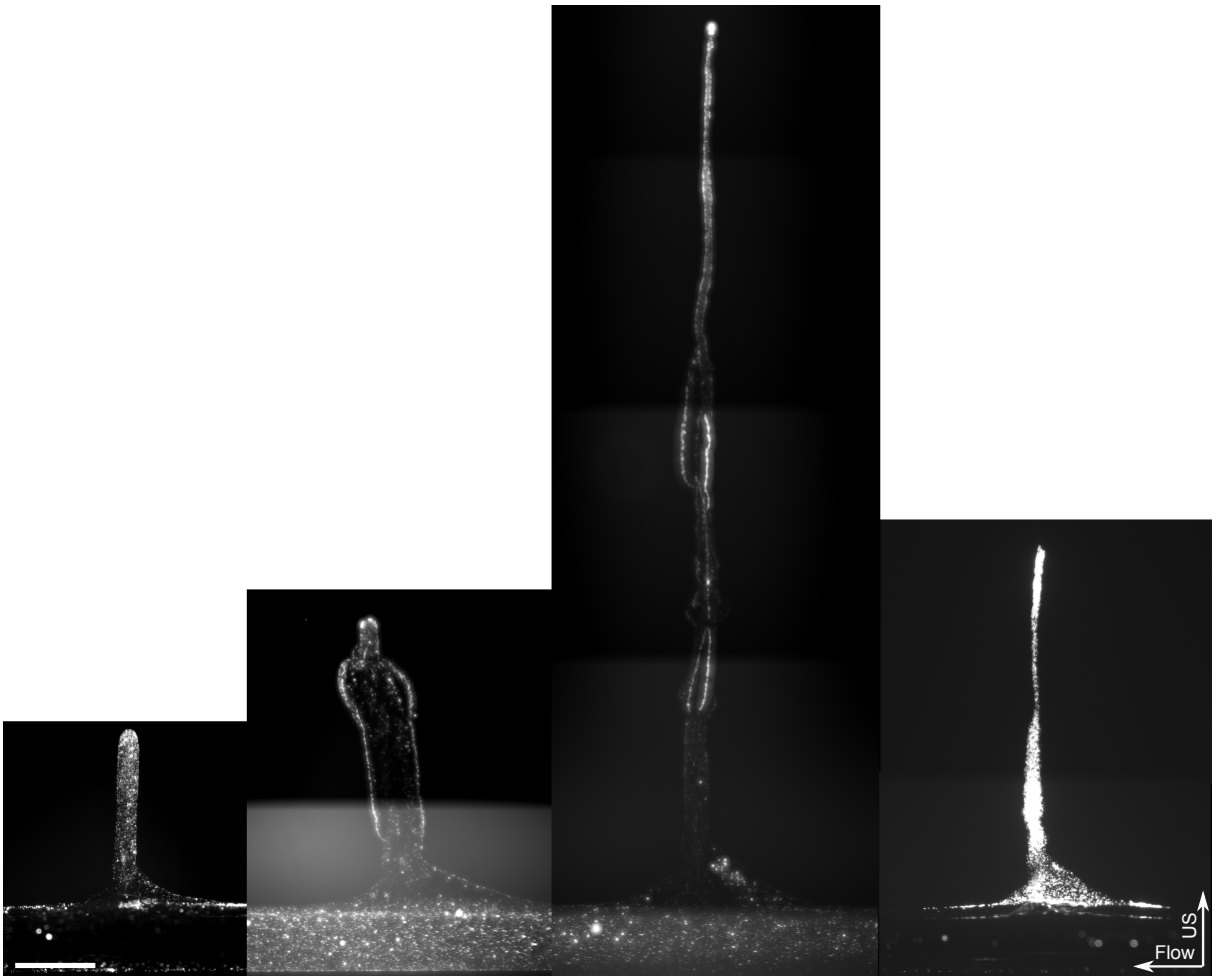

Figure 8.13: Widefield fluorescence microscopy of deformations in nanodroplet experiments A-1 to A-4. Deformation in A-1 resembles those in PLGA nanoparticle and nanocup experiments. Agarose cracking occurred in experiment A–2. In A-3 and A-4, deformations resemble those seen in PLGA nanoparticle loaded DSEPC microbubble experiments. Left-to-right, deformations extend 1111 µm, 1848 µm, 5584 µm, 2290 µm in the direction of ultrasound propagation. Images have been adjusted to improve contrast. Scale bar is 500 µm.

third (A-3) and fourth (A-4) experiments produced extended tunnel-type deformations similar to those seen with PLGA nanoparticle loaded DSEPC microbubbles.

The mechanism responsible for producing the short tunnel-type deformation in A-1, which may also be responsible for similar deformations in PLGA nanoparticle and nanocup experiments, created an optical artefact in the *in-situ* images of the flow channel (Figure 8.14). The artefact, indicated by the green arrow, manifests as a localised region of reduced or zero fluorescence, and is first seen at the start of ultrasound exposure (image 1) and appears in all subsequent images. In the absence of ultrasound, its effects appear reduced (image 21). Currently, there are two explanations: optical aberration due to air bubbles trapped at the ultrasound focus, or an accumulation of iron oxide nanoparticles released from nanodroplets. Both theories rely on primary acoustic radiation force to maintain a locally high concentration of bubbles or iron oxide particles, thereby accounting for the appearance of the artefact with ultrasound exposure, and the lessening of its effects in the absence of ultrasound. The appearance of the artefact shortly after ultrasound exposure favours the theory of iron oxide particle accumulation. However, there is no explanation for why such accumulation was not seen in the other nanodroplet experiments.

Due to this artefact, the deformation extent in experiment A-1 was severely underestimated by e_C measurements.

The deformation in experiment A-2 experienced a rate of growth similar to that seen in nanocup and PLGA nanoparticle loaded DSEPC microbubble experiments (Figure 8.15), suggesting that in the absence of agarose cracking it would have produced a tunnel-type deformation similar to that in experiment A-1. Due to the deformation deviating from the imaging plane (Figure 8.16), the deformation extent in the direction of ultrasound was underestimated by e_C measurements.

Further analysis of Figure 8.15 showed that in experiments A-3 and A-4, deformations grew at a rate comparable to that measured in PLGA nanoparticle loaded DSEPC microbubble experiments. These similarities in deformation growth are consistent with the similarities deformation morphology.

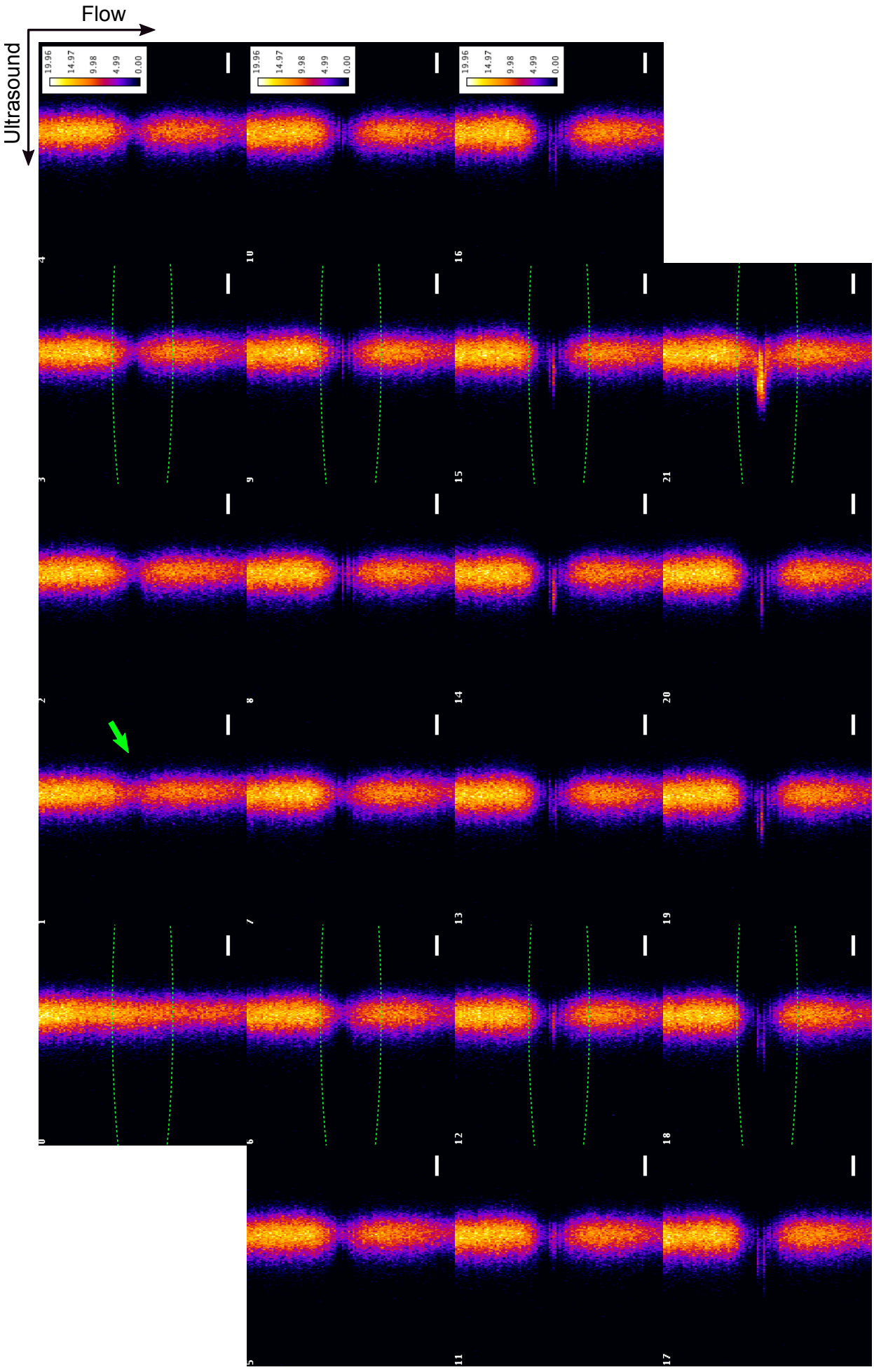

Figure 8.14: SIOS images of the flow channel centre from experiment A-1. Images were taken immediately before (0), during (1-20), and immediately after (21) ultrasound exposure. The green allow indicates the location of an optical artefact. Green lines demarcate the anticipated ultrasound focus. Colour bars have units of fluorescence. Scale bars are 500 µm.

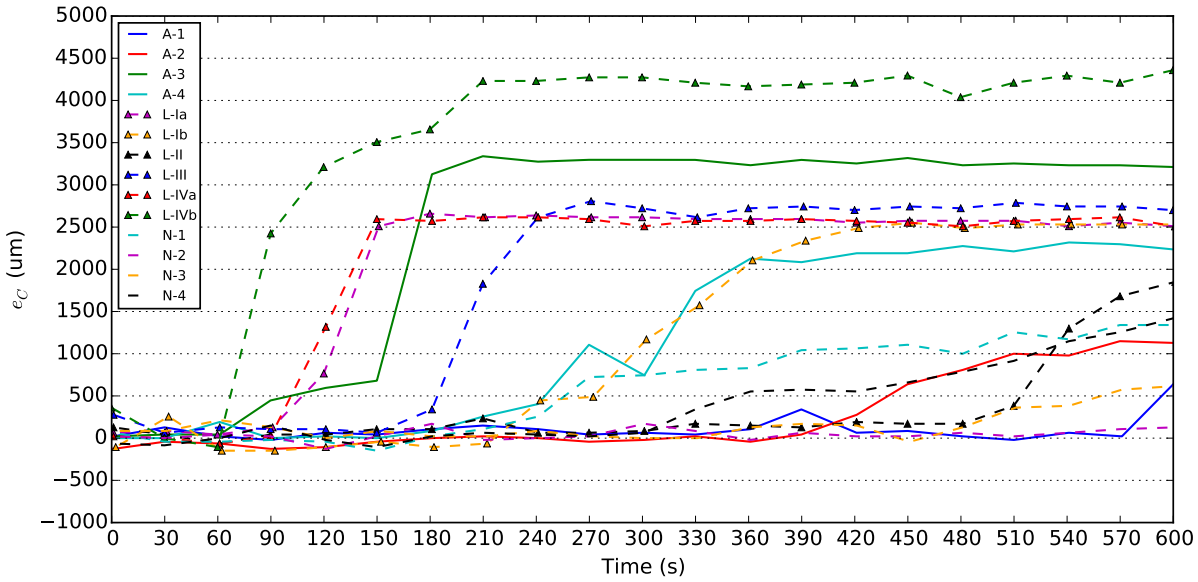

Figure 8.15: e_C during nanodroplet, PLGA nanoparticle loaded DSEPC microbubble, and nanocup experiments. The "plateauing" of e_c values at approximately 2600 µm is due to deformation extending past the field-of-view. Variation in the plateau region is due to variations in S_T, the fluorescence front displacement at the top of the channel.

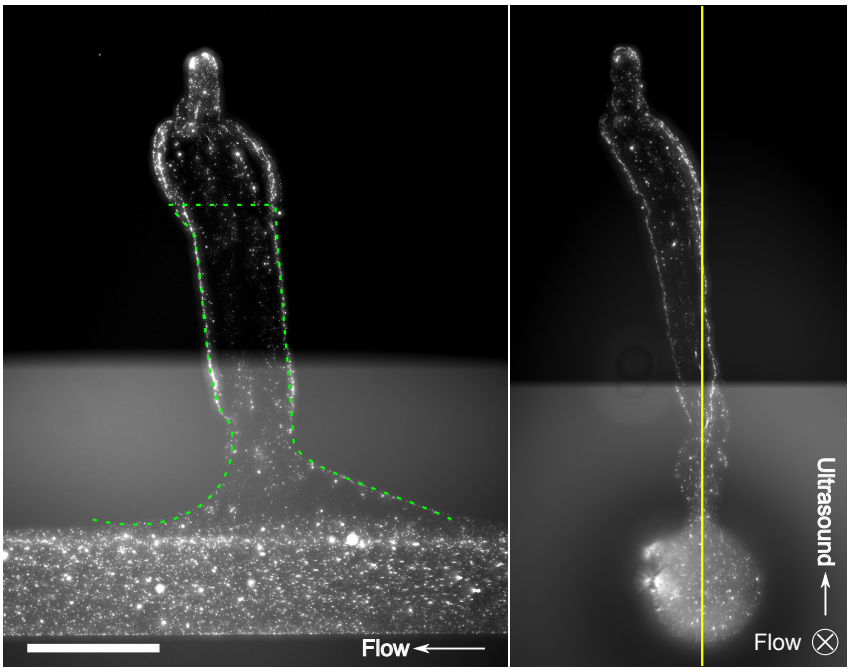

Figure 8.16: Widefield fluorescence microscope image of deformation in experiment A-2. The deformation extent measured by e_C is demarcated in green, and measures ≈ 1200 µm in the direction of ultrasound. The estimated SIOS imaging plane is indicated in yellow. Scale bar is 500 µm.

8.3.3.2 Cavitation Characteristics

PCD power was found to increase over time in all nanodroplet experiments (e.g. Figure 8.17a; full dataset in Appendix), and may once again be attributed to increases in the flow channel volume at the ultrasound focus. The rate of cavitation power increase was found to correlate well with deformation extent (Figure 8.18).

In experiments A-3 (Figure 8.17b) and A-4 (see Appendix), transient increases in cavitation power, with durations of approximately 10 s, were observed immediately prior to the onset of rapid deformation growth at $t \approx 150$ s and $t \approx 270$ s respectively. It is hypothesised that these increases in cavitation power may be the result of cascading vaporisations, where the vaporisation of one nanodroplet produces a bubble that then collapses, producing a shockwave [4] with sufficient amplitude to trigger the vaporisation of several more nearby droplets.

8.3.4 Data Catalogue

Data from all experiments, including those from Chapter 7, is summarised in Table 8.2 in the Appendix.

8.3.5 Deformation Classification

Based purely on their appearance, the deformations produced by the different cavitation agents presented in this chapter and in Chapter 7 fall into three categories: chamber-type deformations produced by gas microbubble (e.g. Figure 8.4); short tunnel-type deformations, with extents below 1500 µm, seen in nanocups experiments; and extended tunnel-type deformations, over 2000 µm in length, found in experiments using nanodroplets and PLGA nanoparticle loaded DSEPC microbubbles.

The distinction between short and extended tunnel-type deformations goes beyond appearances. When the maximum rate of growth, measured using S_C, is plotted against deformation size, measured with widefield microscopy, the short and extended tunnel-type deformations fall into two distinct groups (Figure 8.19). Furthermore, there is also a reasonable correlation between the maximum S_C gradient and the de-

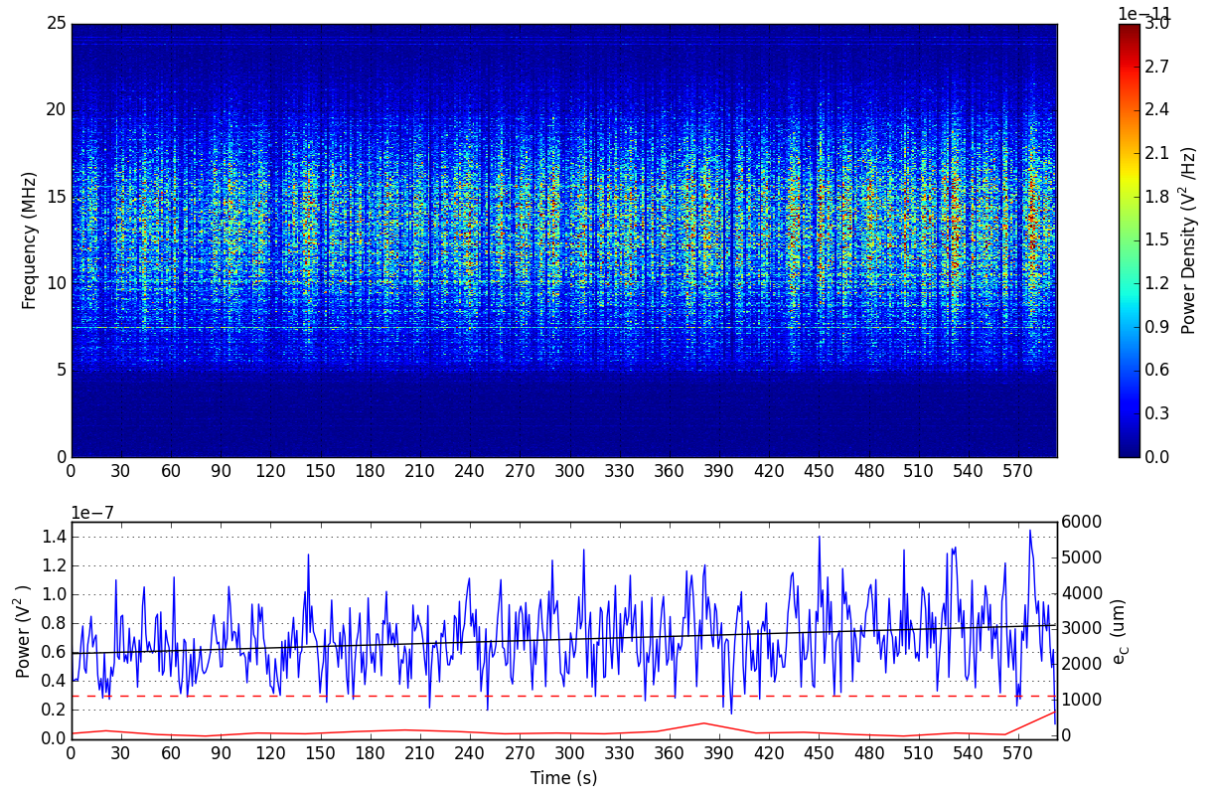

(a) A-1

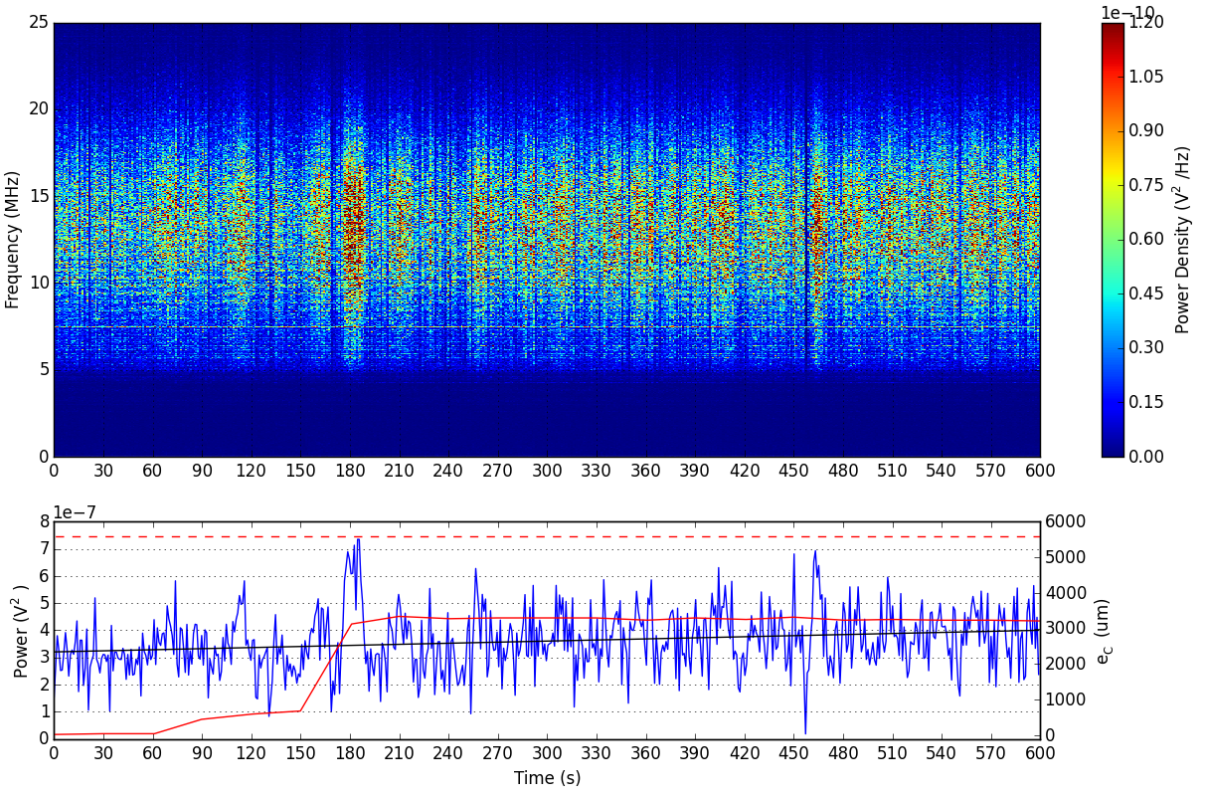

(b) A-3

Figure 8.17: PCD spectrogram and power from experiments A-1 and A-3 plotted with the corresponding e_C values. The red dashed line indicates deformation extent in the direction of ultrasound propagation measured using widefield microscopy. Power plots were fitted with 1st degree polynomials.

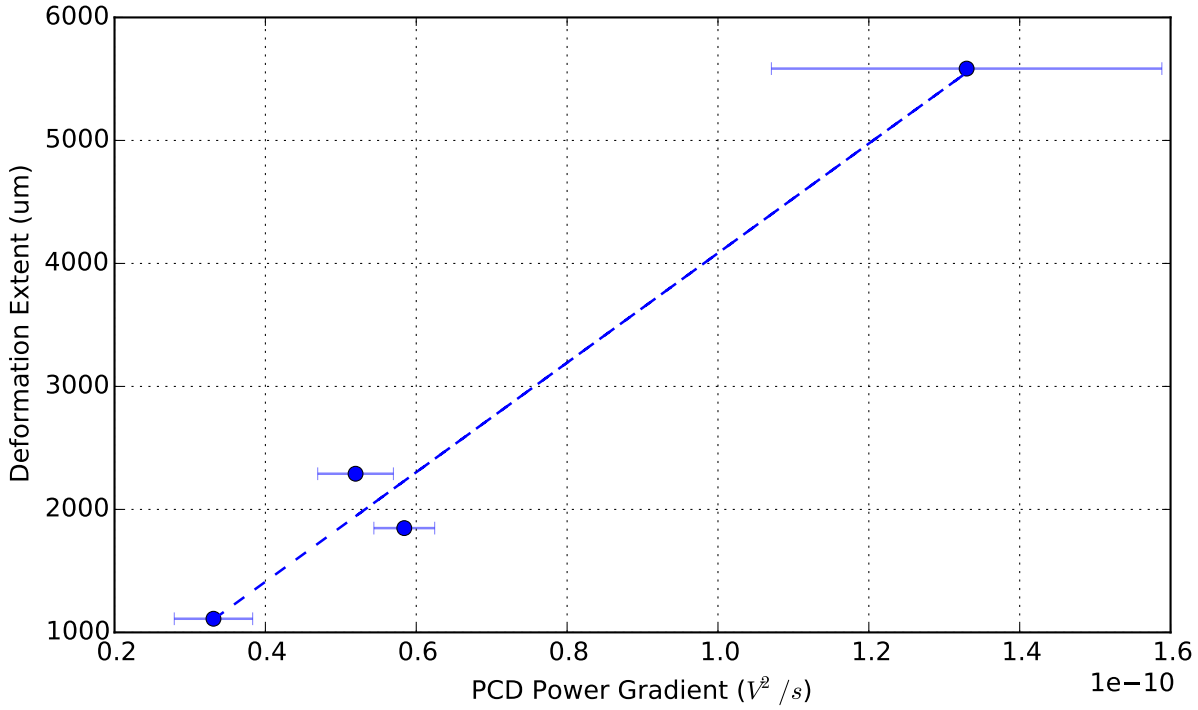

Figure 8.18: Deformation extent vs PCD power gradient. Deformation extents were in the direction of ultrasound propagation. PCD power gradients were estimated from straight lines fitted to power curves. Error bars represent standard error. The dashed line has been fitted to the data using $y = 44.5 \times 10^{12}x - 369.79$ with $r^2 = 0.98$.

formation extent[1] ($r^2 = 0.86$). In contrast, cavitation activity, as measured by detected cavitation noise energy, cannot differentiate between short and extended type deformations (Figure 8.20), with no significant difference between the cavitation energies of the two groups (t = 2.0239, df = 7.552, p-value = 0.07969, Welch Two Sample t-test).

8.3.6 Short Tunnel-Type Deformation

The short tunnel-type deformations, observed in experiments with nanocups (Figure 8.8), nanodroplets (A-1; Figure 8.13). Additionally, they were also produced in experiments with PLGA nanoparticles (Chapter 7, Figure 7.9). These deformations are characterised by their uniform width (mean 1129 µm SD 126 µm) and length (mean 133 µm SD 22 µm), and are found in experiments with high levels of cavitation activity, e.g. nanodroplets experiments, and in experiments where cavitation activity borders on the detection limit, e.g. PLGA nanoparticle experiments. This suggests that the mechanism responsible is independent of cavitation. Several possibilities are presen-

[1] Due to deformations reaching the agarose-mylar interface, the right-most two data points in Figure 8.19 is in effect saturated. If they were removed then $r^2 = 0.88$.

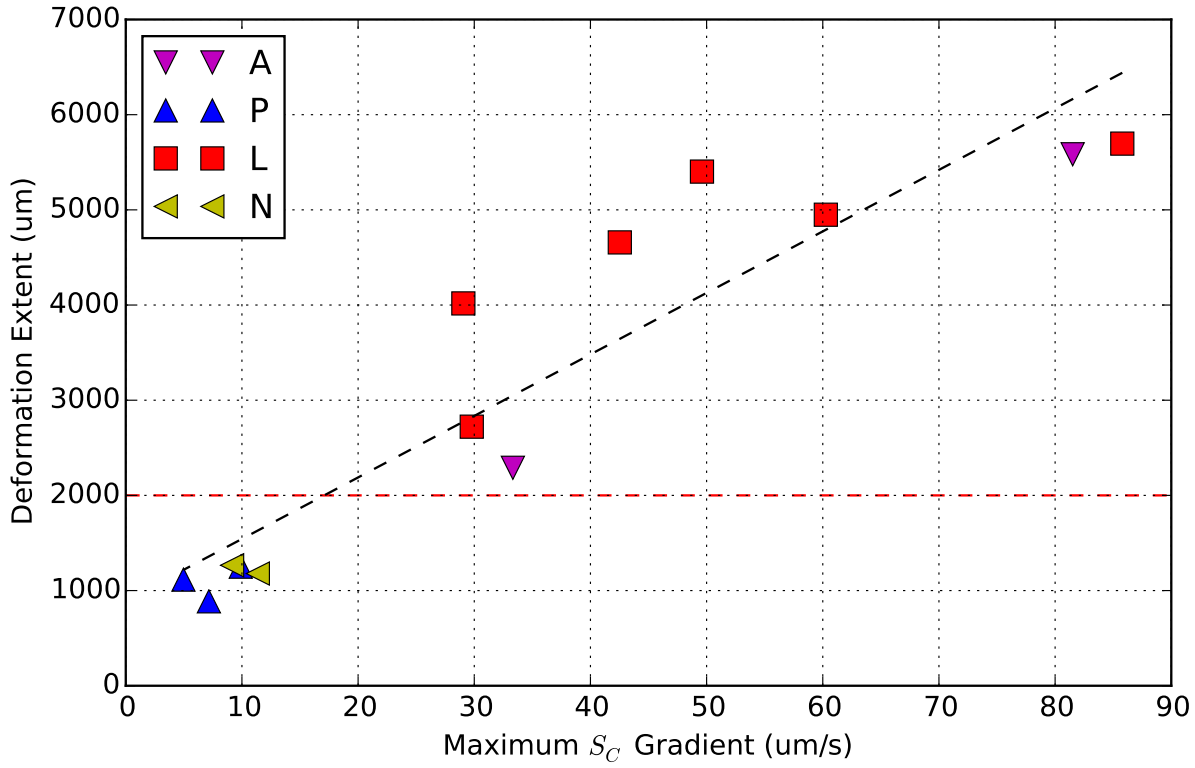

Figure 8.19: Deformation vs maximum S_C gradient. **A**: nanodroplets; **P**: PLGA nanoparticles; **L**: PLGA nanoparticle loaded DSEPC microbubble; **N:** nanocups. The dashed black line is a linear fit to the data, $y = 64.63x + 896.05$, $r^2 = 0.86$. PLGA nanoparticles were included for completeness. The red line separates the short and extended tunnel-type deformations according to deformation extent. Experiments A-1, A-2, and N-3 were excluded due to agarose cracking (A-2) and defective SIOS imaging (A-1 and N-3).

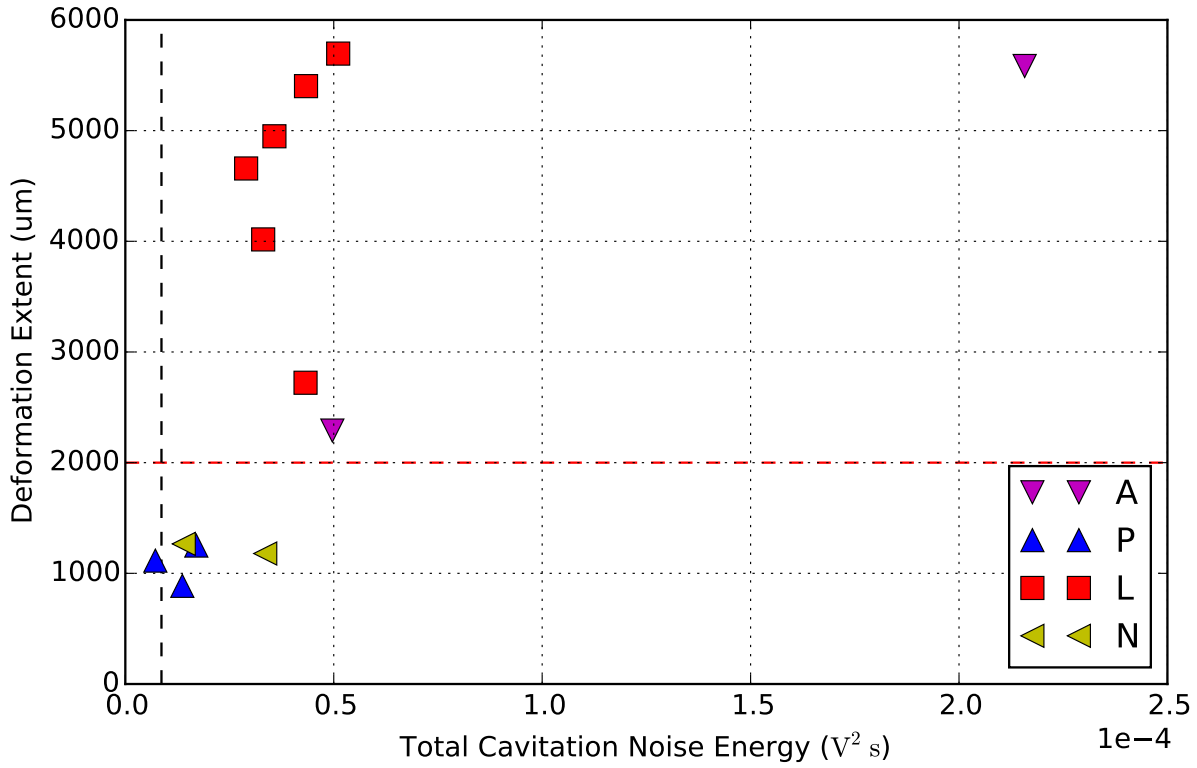

Figure 8.20: Deformation vs cavitation energy. **A**: nanodroplets; **P**: PLGA nanoparticles; **L**: PLGA nanoparticle loaded DSEPC microbubble; **N:** nanocups. The red line separates the short and extended tunnel-type deformations according to deformation extent. PLGA nanoparticles were included for completeness. The vertical dashed black line indicates noise floor of cavitation energy measurements. The red line separates the short and extended tunnel-type deformations according to deformation extent. Experiments A-1, A-2, and N-3 were excluded to maintain consistency with Figure 8.19.

ted here.

8.3.6.1 Single-bubble Tunnelling

Short tunnel-type deformations were first thought to be the result agarose erosion by single bubbles, accounting for the uniform width of the deformations. However, such bubbles would have produced significant cavitation activity, yet negligible cavitation noise was detected in PLGA nanoparticle experiments. Furthermore, microbubble tunnelling has been previously studied at similar frequencies, pressures and channel widths, and the reported mean width of the resulting tunnels was below 50 µm [5] in 0.75 % agarose (cf. 2.0 % agarose used in experiments presented here).

In addition to the lack of cavitation noise, there was also a lack of optical artefacts that would be expected from bubbles with a maximum size of 100 µm. Specifically, a large number of dark pixels would be expected at the ultrasound focus. No such artefacts were found, and no artefacts unique to experiments featuring short tunnel-type deformations were identified. It could be argued that, compared to the image acquisition time of the instrument, the period during which a bubble is at its maximum size is very short, and therefore the lack of artefacts is due to the low probability of the optical focus encountering the bubble at its maximum. However, optical artefacts are expected any time a bubble reaches a sufficient size whilst between the focus and the objective. Given a pulse-repetition frequency of 5 Hz and a scan line acquisition time of approximately 0.27 s, bubbles should reach their maximum size once per scan, and therefore should have been detected in experiments that produced tunnel-type deformations.

8.3.6.2 Agarose Destruction Due to Ultrasonic Pressure

An alternative hypothesis is that the short tunnel-type deformations are formed when the pressure due to ultrasound is sufficient to cause agarose destruction. Under this hypothesis, the uniformness of short tunnel-type deformations is due to the pressure field at the ultrasound focus and consistent alignment of the focus to the flow channel. If this hypothesis is correct, then the pressure field produced by the HIFU transducer

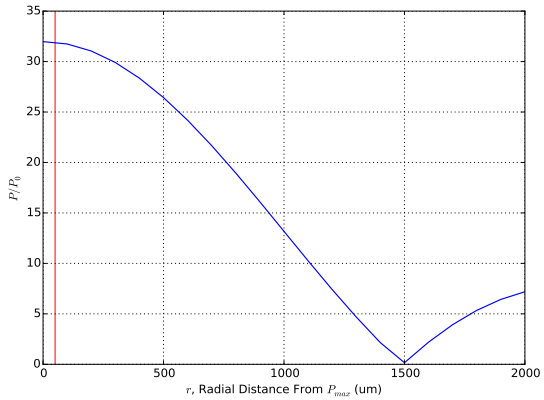

(a) Vertical red line indicates $r = 50\,\mu m$, and intercepts the pressure profile at $P/P_0 = 31.86$.

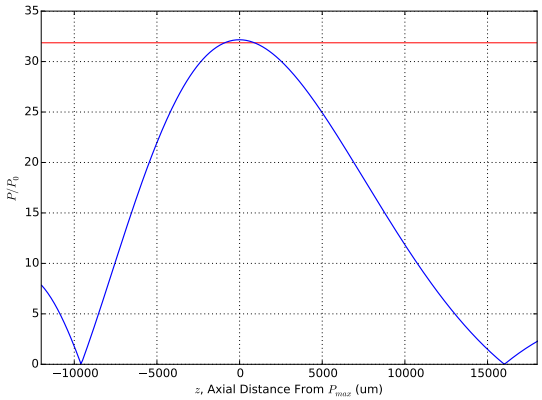

(b) The horizontal red line indicates $P/P_0 = 31.86$ and intercepts the pressure profile at $z = -897\,\mu m$ and $z = 910\,\mu m$.

Figure 8.21: Radial **(a)** and axial **(b)** pressure profile at the ultrasound focus. In (b) lower z values are towards the HIFU transducer. Profiles were numerically simulated using the technique described in [6].

should contain a contour with dimensions matching that of the deformations, i.e. approximately 100 µm wide and 1000 µm in length. To test the hypothesis, radial and axial pressure profiles at the focus of the HIFU transducer were numerically simulated [6] (Figure 8.21). A contour with a width of 100 µm can be found at $P/P_0 = 31.96$ (Figure 8.21a; P is pressure at the focus and P_0 is pressure at the surface of the transducer). However, this contour also has a length of 1807 µm (Figure 8.21b). Furthermore, a contour of this length would produce deformations extending away from and towards the HIFU transducer while only the former is observed.

The numerical simulation of the ultrasonic pressure at the focus was carried out by Joseph Blackmore at the Institute of Biomedical Engineering, Department of Engineering Science, University of Oxford.

8.3.6.3 Agarose Erosion Due to Acoustic Streaming

A variation on the previous hypothesis is agarose erosion due to acoustic streaming instead of ultrasonic pressure, whereby ultrasound induced streams in the liquid impinge on the agarose surrounding the flow channel, resulting in agarose erosion and deformation formation. The acoustic streaming hypothesis resolved the issue of non-symmetric deformation formation, as acoustic streaming occurs in the direction of ultrasound propagation; and because erosion only occurs where the streams interact

with agarose, the dimensions of the resulting deformation are not required to match a pressure contour.

Of the theories presented here, the acoustic streaming hypothesis best explains the various characteristics of short tunnel-type deformations, namely formation in the absence of cavitation, formation in the absence of optical artefacts, formation in the direction of ultrasound propagation, and the uniformity of deformation dimensions. However, as yet, short tunnel-type deformations have not been observed in negative control experiments utilising only de-ionised water and TRITC-Dextran.

8.3.7 Extended Tunnel-Type Deformations

The extended tunnel-type deformations produced in PLGA nanoparticle loaded DSEPC microbubble and nanodroplet experiments showed similar rates of growth, suggesting that they were produced by the same underlying mechanism. In Chapter 7, it was hypothesised that the formation of extended tunnel-type deformations was the result of increased bubble dynamic stability, allowing chamber-type deformations to develop into extended tunnel-type deformations. With loaded DSEPC microbubbles, the increase in bubble dynamic stability was due to PLGA nanoparticle loading. This hypothesis may also be applicable to nanodroplets, as the microbubbles that result from the vaporisation of perfluorohexane cores are partially encapsulated in polymer shells, potentially conferring the same benefits as PLGA nanoparticles with regards to bubble dynamic stability.

Compared to conventional gas microbubbles, significantly greater cavitation effects, by as much as an order of magnitude, was produced by PLGA nanoparticle loaded DSEPC microbubbles and nanodroplets, making these two cavitation agents the most promising in regards to promoting drug penetration.

8.3.8 Cavitation and Deformation

8.3.8.1 Cavitation Energy and Deformation

In general detected cavitation activity, measured by total cavitation energy, does not predict the magnitude of cavitation effect, measured by deformation extent in the dir-

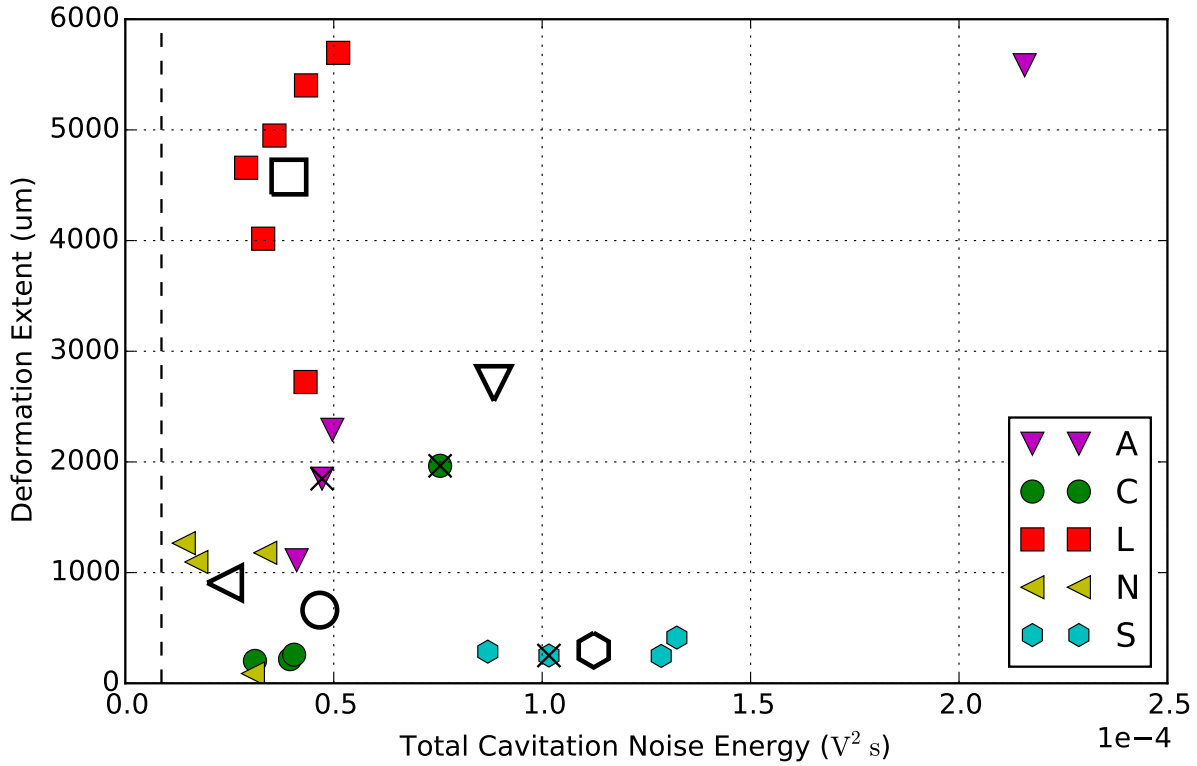

Figure 8.22: Detected cavitation energy and deformation extent produced by different cavitation agents. Widefield microscopy images were used to measure deformation extent in the direction of ultrasound. **A**: nanodroplets; **C**: unloaded DSEPC microbubble; **L**: PLGA nanoparticle loaded DSEPC microbubble**; N:** nanocups; **S**: SonoVue. Unfilled markers represent the arithmetic mean of each group. Data points overlaid with a $\times$ indicates experiments where agarose cracking occurred. The vertical dashed black line indicates cavitation energy in the absence of cavitation nuclei.

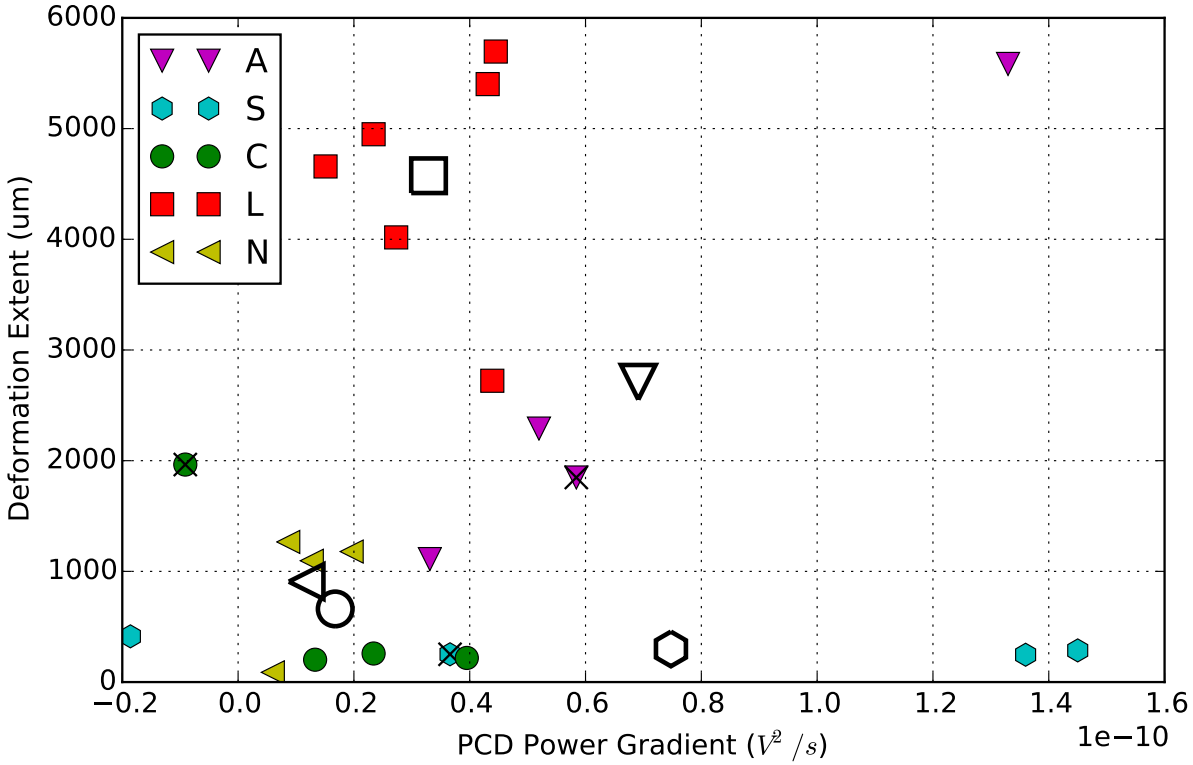

Figure 8.23: Deformation extent and cavitation power gradients produced by different cavitation agents. Widefield microscopy images were used to measure deformation extent in the direction of ultrasound. PCD power gradients were estimated from straight lines fitted to power curves. **A**: nanodroplets; **C**: unloaded DSEPC microbubble; **L**: PLGA nanoparticle loaded DSEPC microbubble**; N:** nanocups; **S**: SonoVue. Unfilled markers represent the arithmetic mean of each group. Data points overlaid with a $\times$ indicates experiments where agarose cracking occurred. The vertical dashed black line indicates cavitation energy in the absence of cavitation nuclei.

ection of ultrasound (Figure 8.22). However, in the nanodroplet, DSEPC microbubble, and PLGA nanoparticle loaded DSEPC microbubble experimental groups, total cavitation energy does bear some relation to the deformation extent. These findings are with those from Chapter 7.

As previously suggested, the lack of correlation between detected cavitation energy and deformation extent may be a limitation of the coaxial PCD arrangement, where cavitation agents within the flow channel shielded the passive cavitation detector from cavitation signals originating within deformations.

8.3.8.2 Cavitation Power and Deformation

Data from nanocups and nanodroplets suggests that the power gradient of PCD measurements could be used to predict the extent of deformations. However, when the ana-

lysis is applied to all cavitation agents, it was found that, like cavitation energy, PCD power gradients, in general, showed no correlation with deformation extent in the direction of ultrasound. Another similarity between PCD power gradient and cavitation energy is that, within specific experimental groups, namely nanocups, nanodroplets, and PLGA nanoparticle loaded DSEPC microbubbles, PCD power gradient did correlate with deformation extent.

While there was no overall relationship between PCD power gradient and deformation extent, it is possible that the onset of rapid deformation growth could have corresponding transient increases in PCD power. By visual inspection of spectrograms from all cavitation agent experiments, there were no features that could be used to consistently identify the onset of rapid deformation growth. For example, in experiment A-3 (Figure 8.17b), there was a transient increase in the PCD power at $t \approx 150\,\mathrm{s}$ that appears to corresponds with the onset of rapid deformation formation. However, a similar increase was also observed at $t \approx 110\,\mathrm{s}$.

8.3.8.3 Need For Better Monitoring Techniques

From a clinical perspective, monitoring of delivered cavitation effect in the target tissue is crucial to the safety and efficacy of ultrasound and cavitation mediated drug delivery. The results presented here show that, using a single-element coaxial transducer, PCD measurements cannot detect the onset of rapid deformation formation, nor predict their extent. These findings identify a need for better monitoring techniques with which to assess induced cavitation effects. One possibility is to improve on coaxial PCD by placing detectors orthogonal to the HIFU axis, thus avoid potential shielding effects and allow the use of transducers with wider field-of-views without sacrificing sensitivity or HIFU power. Clinically, however, this may not always be a practical solution as it would require two ultrasound windows into the target region. Other alternatives include passive acoustic mapping, which can overcome the shielding effect by using an array of transducers; restrict the use of cavitation agents to those that exhibit a correlation between cavitation energy and cavitation effect, e.g. nanodroplets; and engineering cavitation agents to produce a clear relationship between detected

cavitation energy and induced cavitation effect.

8.3.9 Multistage Deformation Formation

The real-time *in-situ* images of tunnel-type deformations, whether short tunnel-type deformations below 1500 µm or the extended tunnel-type deformations above 2000 µm, show for the first time that such deformation form in a multistage process. In the first stage, deformation growth is slow and below the detection limit of the system. This stage is then followed by a rapid growth stage, where the maximum rate of growth shows reasonable correlation ($r^2 = 0.86$) with the final deformation size.

The multistage formation of deformations suggests a feedback loop between the induced cavitation effects and the surrounding environment, whereby cavitation modifies the immediate environment in such a way that it leads to an amplification of cavitation effect through confinement or entrapment of cavitation agents (e.g. Chapter 7, Figure 7.19). The possibility of such positive feedback loops has safety implications for clinical applications of ultrasound and cavitation mediated drug delivery, where tissue damage beyond what is expected from *in vitro* and animal studies could occur if the targeted tissue is amenable to remodelling by cavitation.

8.4 Summary

The goal of this chapter was to document the commonalities and differences between the cavitation effects produced by different cavitation agents to enable comparisons and analysis. Based on the catalogue data, SonoVue and unloaded DSEPC microbubbles have similar cavitation effects, consistent with the fact that they have similar chemical compositions and sizes. In contrast, nanodroplets and PLGA nanoparticle loaded DSEPC microbubbles were found to produce deformations of similar extents with comparable growth rates despite the differences in their formulation, method of action, and size. Finally, the cavitation effects of nanocups were found to be very similar to those of PLGA nanoparticles, suggesting that under the conditions tested, they have no more effect than non-cavitating nanoparticles. Of the cavitation agents

studied, PLGA nanoparticle loaded DSEPC microbubbles and nanodroplets showed particular promise with regard to their ability to promote drug penetration, producing deformations that are up to 10 times larger than observed with conventional gas microbubbles.

PCD measurements, namely cavitation energy and cavitation power gradient, were found to correlate with deformation extent in some experimental groups. In general, however, there exists no correlation between cavitation activity, measured by cavitation energy, and cavitation effect, measured by deformation size, and no features in the cavitation spectrum or cavitation power curves could be used to reliably predict the onset of rapid deformation growth or deformation extent. This overall lack of correlations between coaxial single-element PCD measurements and cavitation effects identifies the need for more sophisticated monitoring techniques.

The ability to acquire real-time *in-situ* images of flow channels during ultrasound exposure allowed the maximum rate of deformation growth to be measured. It was found to be a reasonable predictor of final deformation size, and can also be used to distinguish between the short and extended tunnel-type deformations. The same images also showed that the formation of tunnel-type deformations, which are 2 to 10 times larger than chamber-type deformations, occurs in two stages: a stage of slow deformation growth followed by a stage of rapid expansion. This two-stage process implies interactions between cavitation and its surroundings, whereby cavitation modifies the immediate environment in such a way that the cavitation effects are amplified, resulting in further modification and amplification. The possibility of such positive feedback interactions must be taken into account when assessing the safety of ultrasound and cavitation mediated drug delivery, especially when the target tissue is amenable to remodelling by cavitation effects.

The availability of different cavitation agents increases the flexibility and applicability of ultrasound and cavitation mediated drug delivery. At the same time, they introduce new safety considerations, and more sophisticated techniques with which to monitor cavitation effects is required to safely and effectively utilise each cavitation agent.

Appendix

	Deformation Extent (µm)				
Experiment	e_C	S_C	Microscopy	Cavitation Energy (V^2 s)	Maximum S_C gradient (µm s^{-1})
S-1	340	404	413	1.32×10^{-4}	
S-2*	255	362	286	8.70×10^{-5}	
S-3*	128	256	247	1.29×10^{-4}	
S-4*	85	276	251	1.02×10^{-4}	
N-1	1340	1383	1179	1.34×10^{-4}	11.4
N-2*	128	64	88	1.22×10^{-4}	
N-3†	617	489	1096	6.81×10^{-5}	
N-4	1425	1469	1266	5.61×10^{-5}	9.15
A-1†	659	764	1111	4.11×10^{-5}	
A-2†	1127	1319	1848	4.72×10^{-5}	
A-3△	3211	3316	5584	2.16×10^{-4}	81.5
A-4	2233	2255	2290	1.99×10^{-4}	33.3
C-I†	1042	1126	1969	7.55×10^{-5}	
C-II*	213	212	202	3.11×10^{-5}	
C-III*	85	255	218	3.95×10^{-5}	
C-IV*	43	276	258	4.05×10^{-5}	
L-Ia△	2510	2676	4949	3.58×10^{-5}	60.3
L-Ib△	2531	2636	4017	3.31×10^{-5}	29.1
L-II†	1851	2022	2722	4.32×10^{-5}	29.8
L-III△	2701	2786	5402	4.33×10^{-5}	49.6
L-IVa△	2509	2701	4658	2.90×10^{-5}	42.5
L-IVb△	4358	4231	5696	5.11×10^{-5}	85.8

Table 8.2: Catalogue of deformation extent in the direction of ultrasound from all experiments as measured by SIOS and widefield fluorescence microscopy. S_C and e_C values at the end of ultrasound exposure are shown. (*) indicates cases where deformation is below the detection limit of 300 µm; (△) denotes cases where deformation extent exceeds the field-of-view; and (†) indicates cases where deformation deviated from SIOS imaging plane or where imaging was affected by external factors.

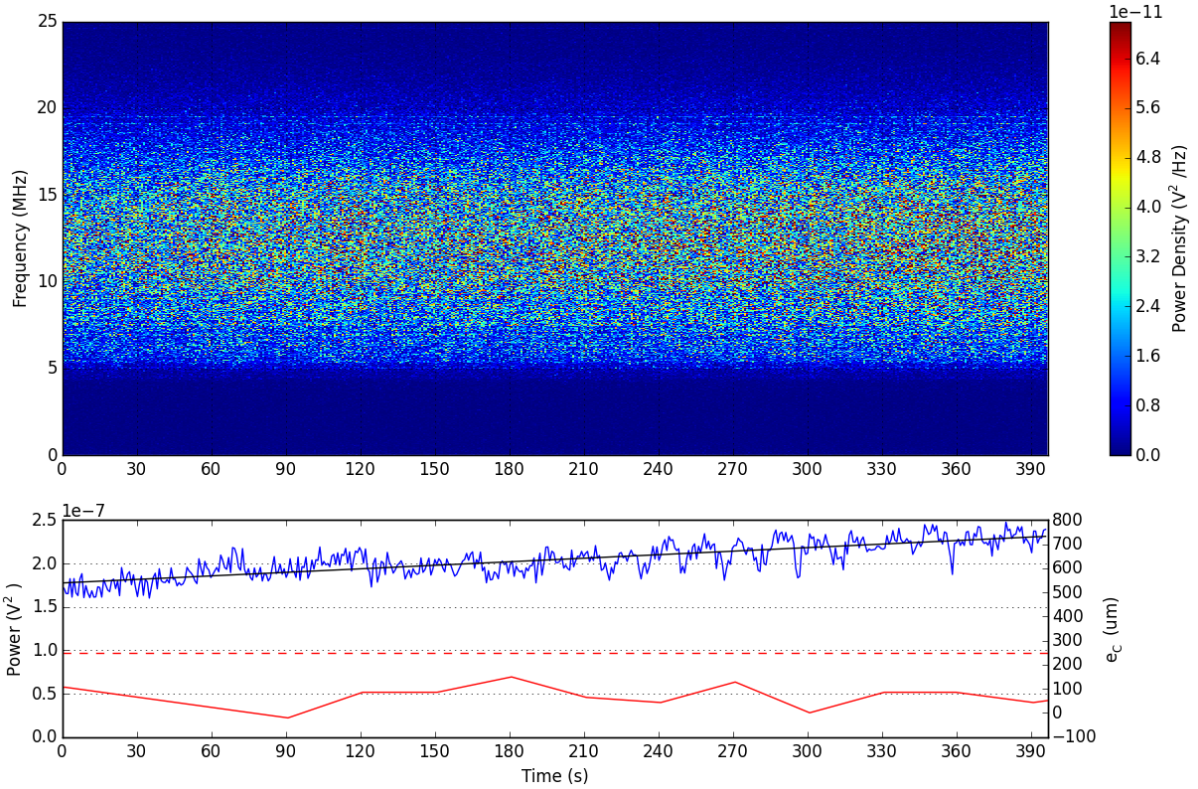

(a) S-3

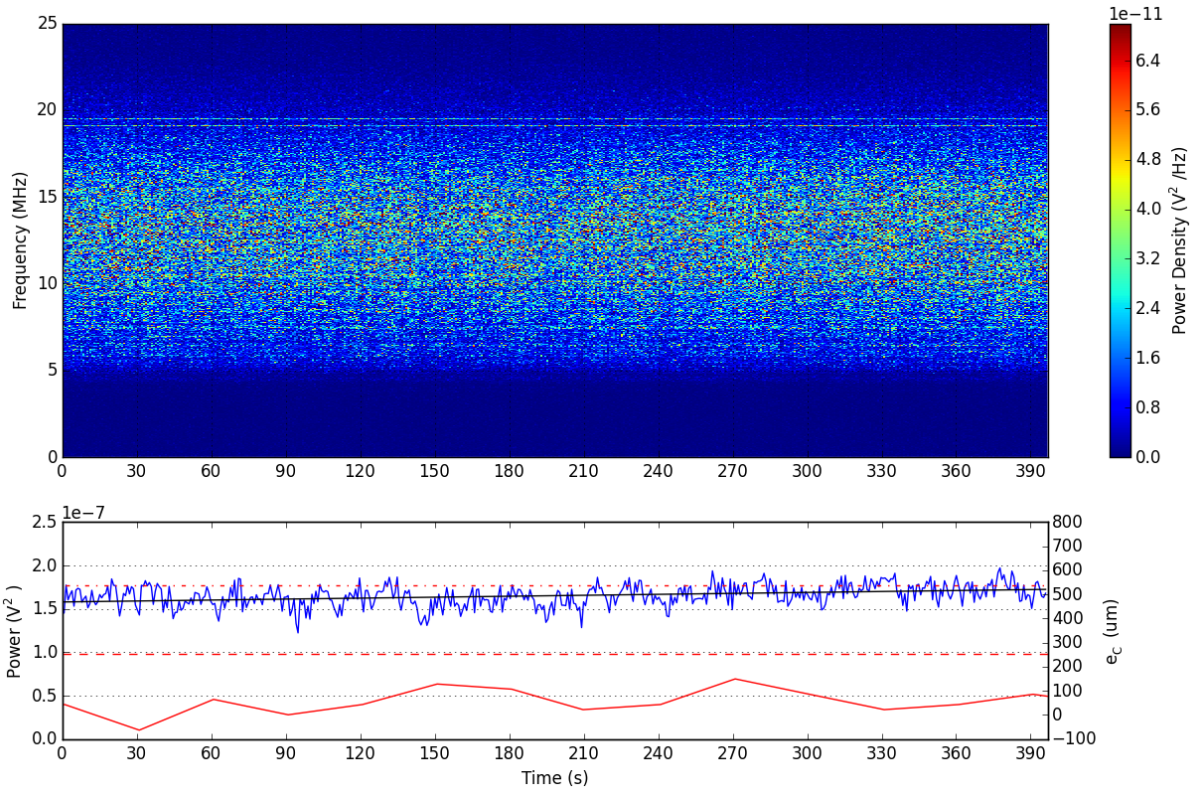

(b) S-4

Figure 8.24: PCD spectrogram and power in experiments S-3 and S-4 plotted together with the corresponding e_C values. Red dashed lines indicate deformation extent in the direction of ultrasound propagation measured using widefield microscopy. Power plots have been fitted with a 1st degree polynomial.

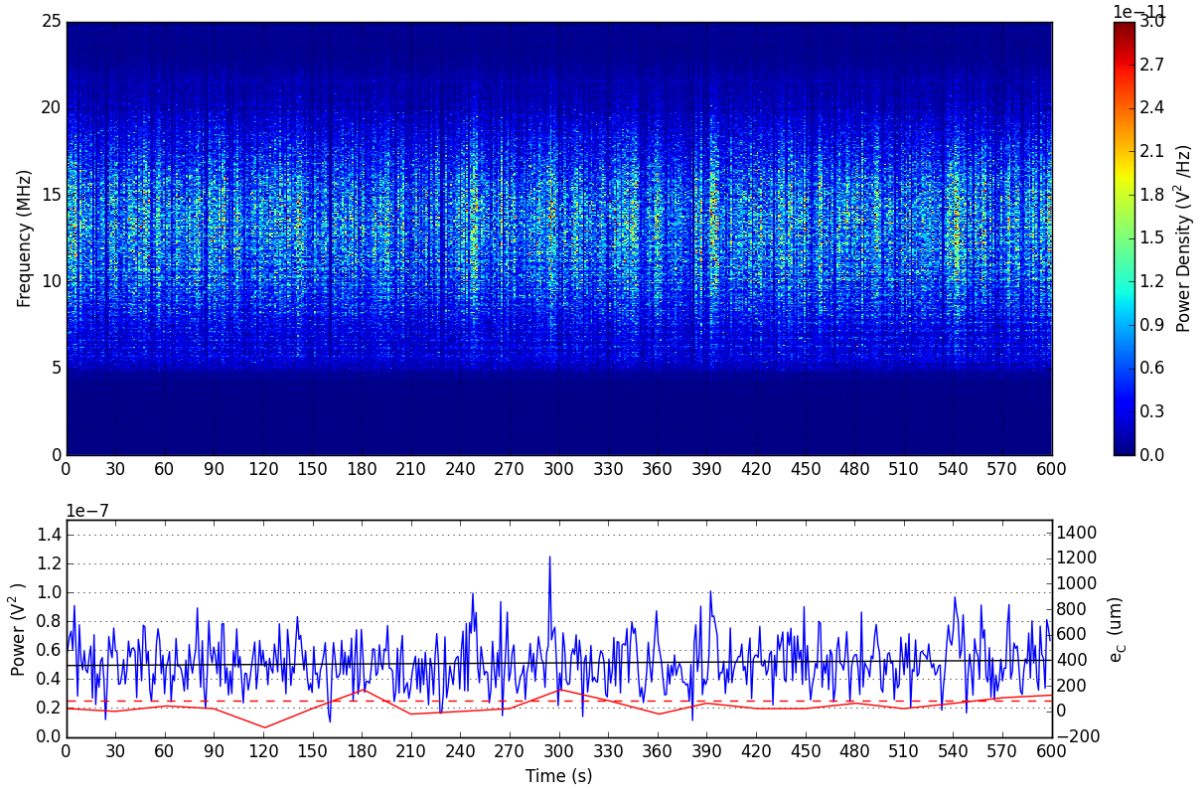

(a) N-2

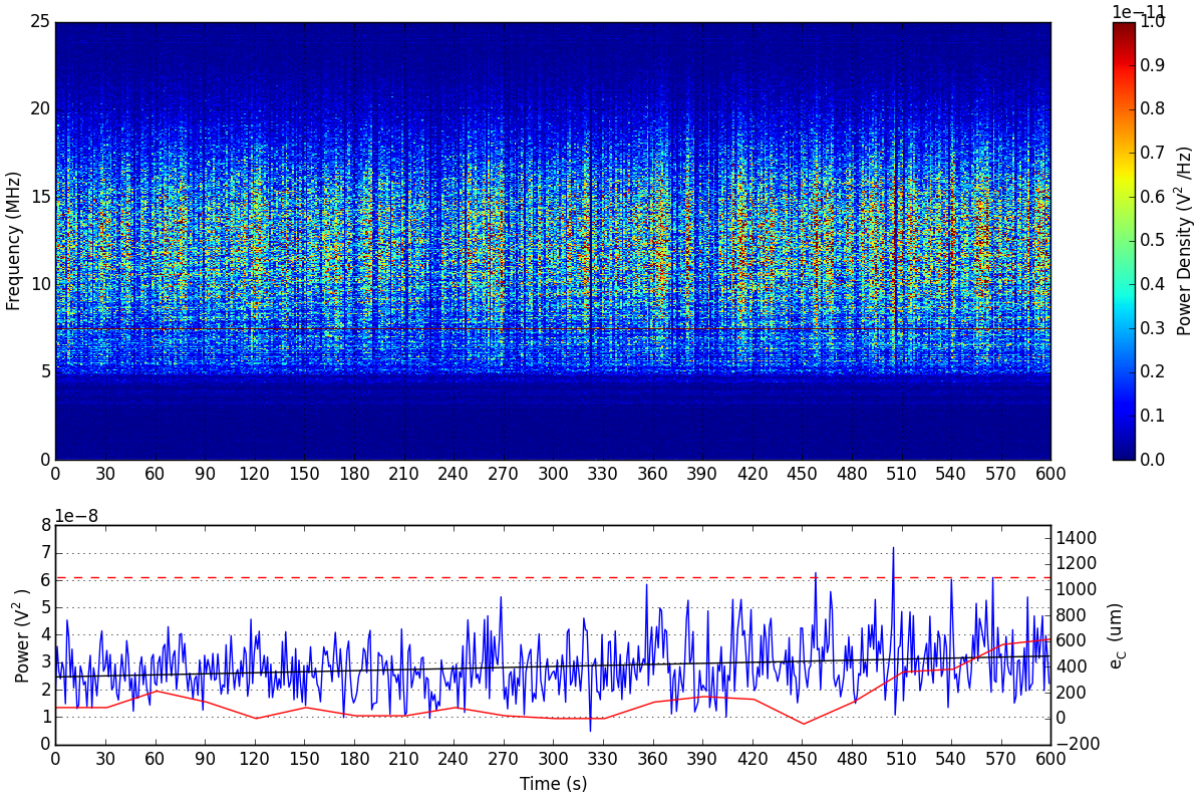

(b) N-3

Figure 8.25: PCD spectrogram and power from experiment N-2 to N-4 plotted with the corresponding e_C values. Red dashed lines indicate deformation extent in the direction of ultrasound propagation measured using widefield microscopy. Due to experimenter error, SIOS images in experiment N-3 was acquired with an X resolution of 100 µm instead of 50 µm, leading to an underestimate of the deformation extent. Power plots have been fitted with a 1st degree polynomial.

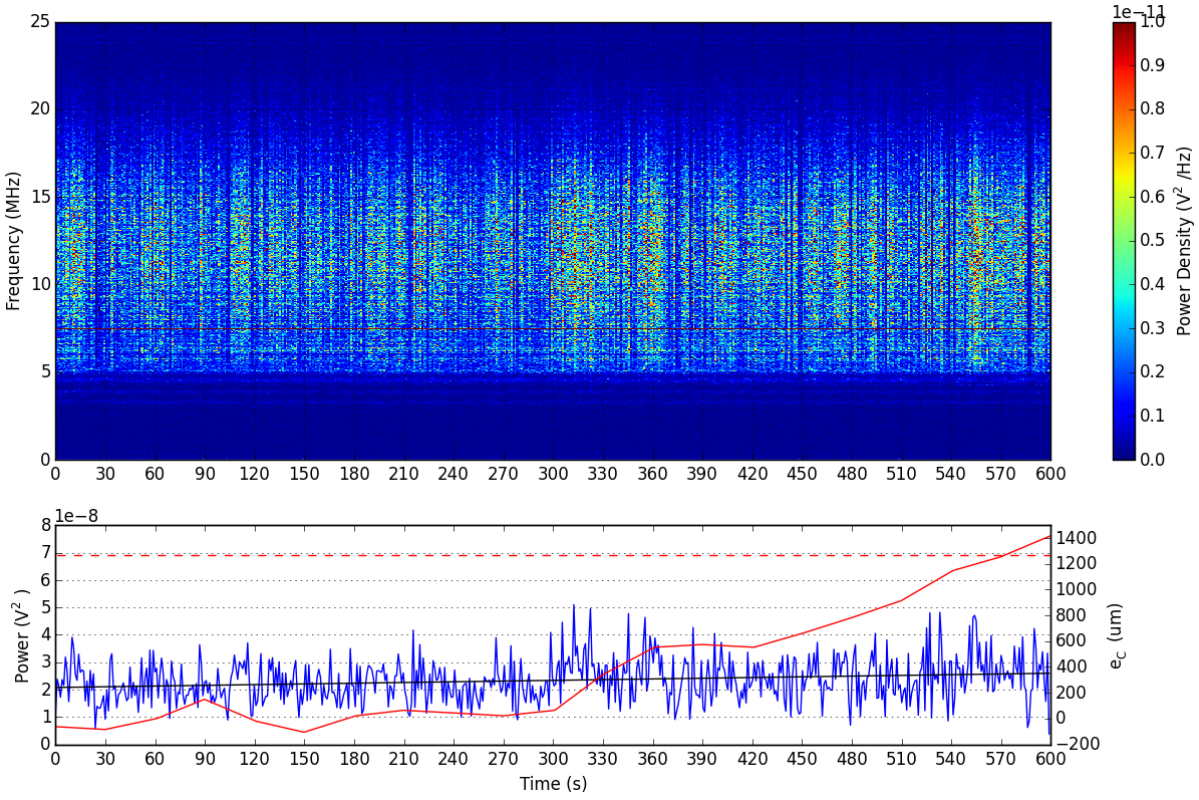

(c) N-4

Figure 8.26: (continued)

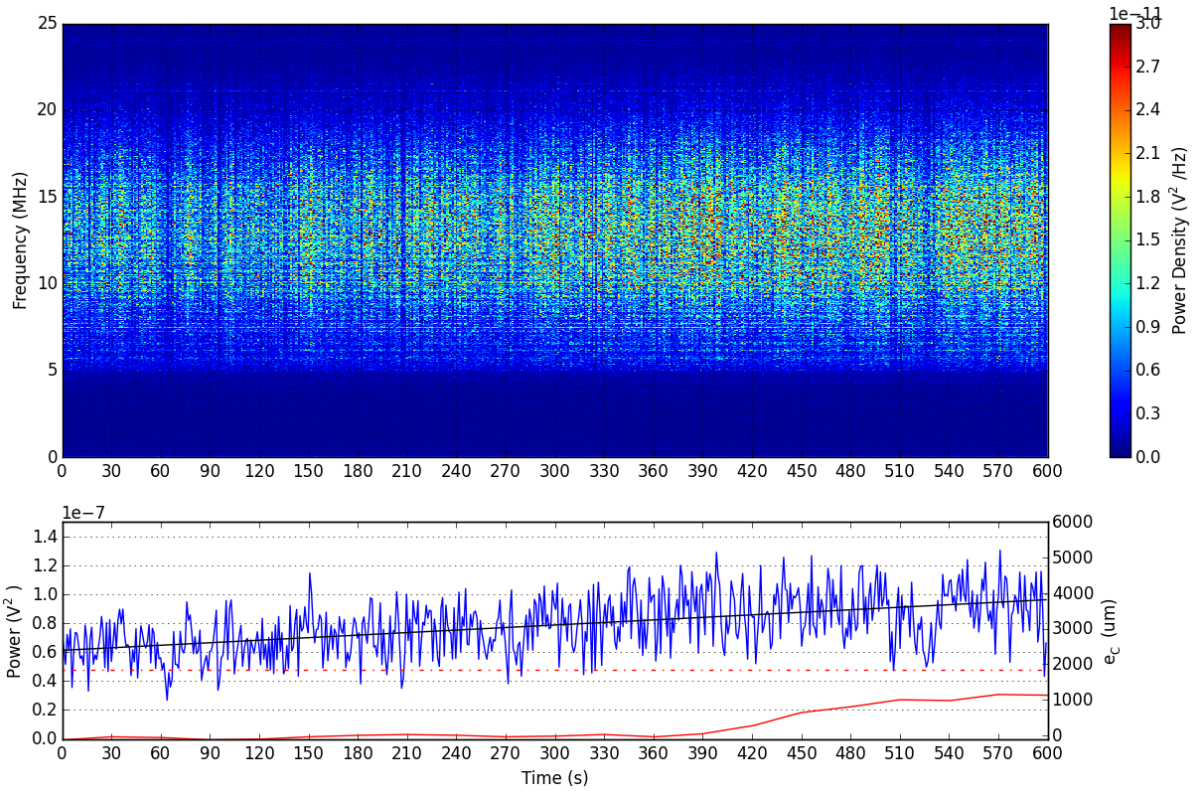

(a) A-2

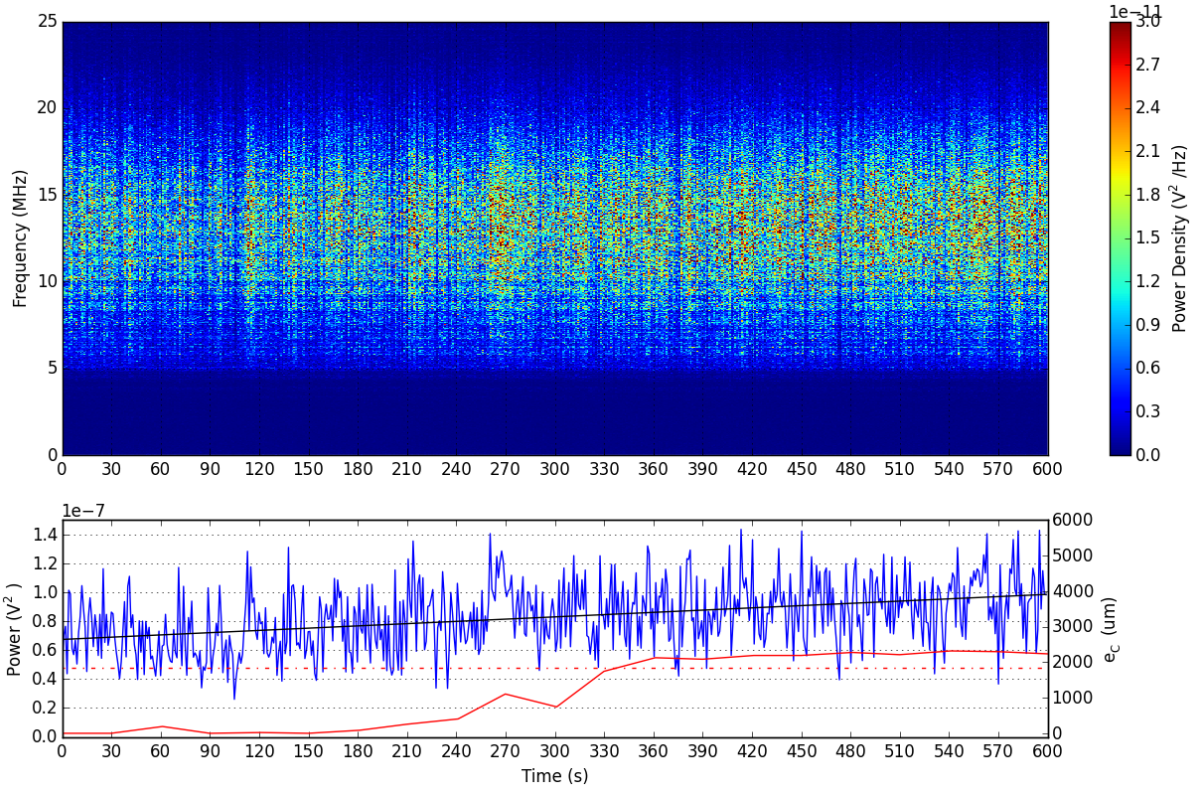

(b) A-4

Figure 8.27: PCD spectrogram and power from experiment A-2 and A-4 plotted with the corresponding e_C values. Red dashed lines indicate deformation extent in the direction of ultrasound propagation measured using widefield microscopy. Power plots have been fitted with a 1st degree polynomial.

References

[1] Susan K Hobbs, Wayne L Monsky, Fan Yuan, W Gregory Roberts, Linda Griffith, Vladimir P Torchilin, and Rakesh K Jain. Regulation of transport pathways in tumor vessels: role of tumor type and microenvironment. *Proceedings of the National Academy of Sciences*, 95(8):4607–4612, 1998.

[2] James J Kwan, Rachel Myers, Christian M Coviello, Susan M Graham, Apurva R Shah, Eleanor Stride, Robert C Carlisle, and Constantin C Coussios. Ultrasound-propelled nanocups for drug delivery. *small*, 11(39):5305–5314, 2015.

[3] Jeong Yu Lee, Dario Carugo, Calum Crake, Joshua Owen, Marie de Saint Victor, Anjali Seth, Constantin Coussios, and Eleanor Stride. Nanoparticle-loaded protein–polymer nanodroplets for improved stability and conversion efficiency in ultrasound imaging and drug delivery. *Advanced Materials*, 27(37):5484–5492, 2015.

[4] TG Leighton. The acoustic bubble. 1994. *ISBN: 0-12-44190-8*, 1994.

[5] Charles F Caskey, Shengping Qin, Paul A Dayton, and Katherine W Ferrara. Microbubble tunneling in gel phantoms. *The Journal of the Acoustical Society of America*, 125(5):183–189, 2009.

[6] Xucai Chen, Karl Q Schwarz, and Kevin J Parker. Radiation pattern of a focused transducer: A numerically convergent solution. *The Journal of the Acoustical Society of America*, 94(5):2979–2991, 1993.

Chapter 9

Concurrent Monitoring With Passive Acoustic Mapping

9.1 Introduction

In Chapter 8, a need for more sophisticated cavitation monitoring techniques beyond single-element passive cavitation detection (PCD) was identified. This need arises due to the inability of single-element PCD measurements to predict the onset of deformation formation or the final deformation size, a shortcoming that is possibly due acoustic shielding by cavitation agents within the flow channel and the narrow field-of-view (FOV) of a single-element PCD transducer. Passive acoustic mapping (PAM) is a cavitation monitoring technique that has the potential to overcome these issues. By using multiple transducers, PAM achieves a field of view that is substantially larger than that of a single element transducer, mitigating the effects of shielding by providing alternative lines-of-sight into the deformation region. In addition, by using beamforming techniques, PAM is able to locate sources of cavitation noise with high spatial resolution [1, 2].

To determine whether PAM can be used to reliably monitor cavitation activity and predict its effects, an experiment was conducted in which cavitation activity was monitored using PAM, and at the same time, cavitation effects were monitored using SIOS. This experiment will also provide a means of testing the utility of SIOS for evaluating cavitation monitoring techniques, and to the best of the author's knowledge, is the

first such application of concurrent spatiotemporal monitoring of cavitation activity and effect.

The author and Erasmia Lyka made equal contributions to the results presented within this chapter. In particular, Erasmia Lyka wrote the custom PAM software used and supplied all PAM data and related information.

9.2 Materials and Methods

9.2.1 Materials

9.2.1.1 Channel Model

An agarose channel model with a 370 µm embedded channel, as described in Chapter 5, was used. Due to resource constraints, this model was manufactured 72 h prior to the experiment.

9.2.1.2 Cavitation Agents

Three cavitation agents from Chapter 8 were used: SonoVue, nanodroplets, and nanocups. The concentration of each cavitation agent, in terms of agents per millilitre, was $1 \times 10^8\,\mathrm{mL}^{-1}$, $1 \times 10^7\,\mathrm{mL}^{-1}$ and $1 \times 10^8\,\mathrm{mL}^{-1}$ respectively. These concentrations were chosen using catalogue data from Chapter 8, with the goal of producing at least one deformation that extends more than 1000 µm in the direction of ultrasound.

Due to material shortage, the nanodroplets stock used was manufactured 7 days prior, while the same stock of nanocups used in Chapter 8 was used here. Consequently, the actual concentration of nanodroplets was likely to be lower than $1 \times 10^7\,\mathrm{mL}^{-1}$ as some droplets will have spontaneously vaporised in storage. No such reduction in concentration is expected for nanocups.

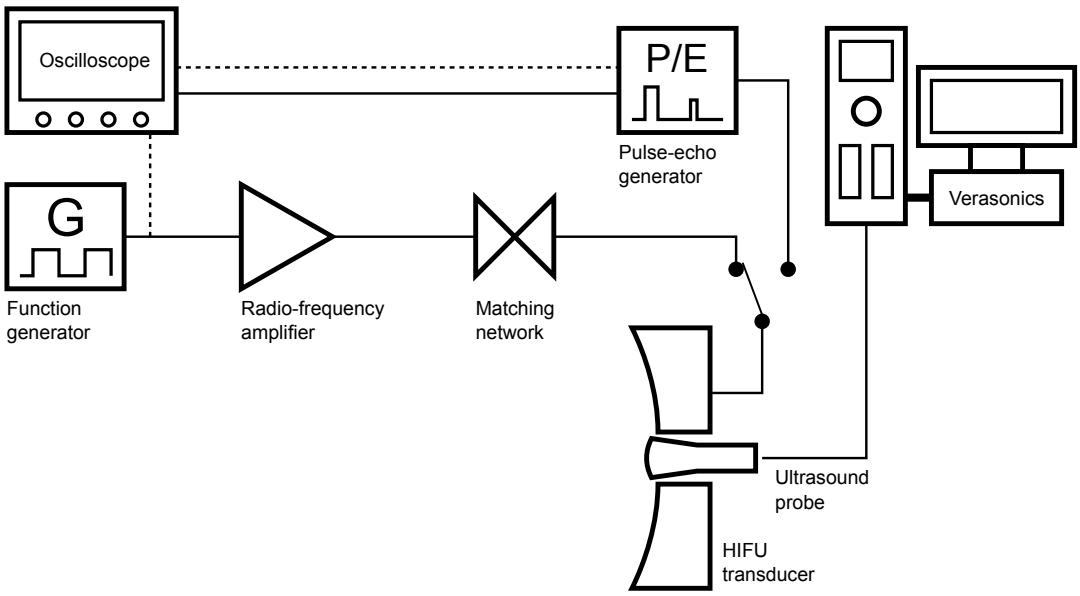

Figure 9.1: Ultrasound setup with PAM. **HIFU transducer**: H102-22B, Sonic Concepts; **Ultrasound probe**: L11-4v, Verasonics Inc, US; **Verasonics**: Verasonics Vantage Research Ultrasound System, Verasonics. For further information please see Figure 5.2 in Chapter 5.

9.2.2 Methods

9.2.2.1 Ultrasound Setup

The ultrasound setup used is shown in Figure 9.1, and is broadly similar to that described in Chapter 5. Differences include the addition of the Verasonics computer system and the use of an ultrasound probe instead of the single-element PCD transducer. The probe has a central frequency of 6.25 MHz with a -3 dB bandwidth of 4 to 11 MHz, and consists of 128 elements arranged linearly. Additionally, in order to accommodate the probe in a coaxial arrangement, a different HIFU transducer, featuring a central rectangular cutout, was used. This transducer also has a fundamental frequency of 1.067 MHz.

The system was aligned as described in Chapter 5, with the PCD transducer alignment step replace with alignment of the ultrasound probe, where the channel was bought into the probe's FOV under B-mode ultrasound imaging. To confirm the alignment, SonoVue was flowed through the channel and visualised under B-mode imaging.

9.2.2.2 Ultrasound Exposure and Monitoring

The flow channel was exposed to ultrasound three times, each time with a different cavitation agent and at a different exposure site. To minimise the effects of prior exposures, the flow channel model was translated along the X axis to place the ultrasound focus 1 to 2 mm upstream of the previous exposure site. SonoVue was the first cavitation agent used, followed by nanodroplets and finally nanocups. Between exposures, the flow channel was flushed with de-ionised water for 10 min.

For SonoVue and nanodroplets, ultrasound exposure was conducted at 1.067 MHz, 1.65 MPa peak-negative pressure, 5 Hz pulse-repetition frequency and 1.17 % duty-cycle for SonoVue and nanodroplets. For nanocups, the peak-negative pressure was increased to 1.90 MPa to ensure production of a deformation greater than 1000 µm.

22 XZ plane images of the flow channel were acquired by SIOS every 30 s, starting 30 s before ultrasound exposure. PAM signals were acquired simultaneously with ultrasound exposure, and a map of acoustic emissions was produced every 4 to 6 s.

9.2.2.3 PAM Software

PAM was carried out using custom software written by Erasmia Lyka. Briefly, the software first acquires cavitation noise measurements simultaneously from all transducer elements, then filters the recorded signals to remove harmonics [3]. Using the filtered signals, sources of acoustic emissions were then estimated using a data-adaptive beamforming algorithm [4], resulting in maps of acoustic emissions, also referred to as PAM images. By using a combination of CPU and GPU processing, the software was able to produce PAM images in real-time.

9.2.2.4 End-Point Widefield Microscopy

After completion of all ultrasound exposures, the flow channel was flushed with fluorescent beads then extracted for widefield imaging as described in Chapter 5.

Pairing of SIOS and PAM Images Each SIOS image was paired with a corresponding PAM image that was acquired during raster scanning of its central image region, where

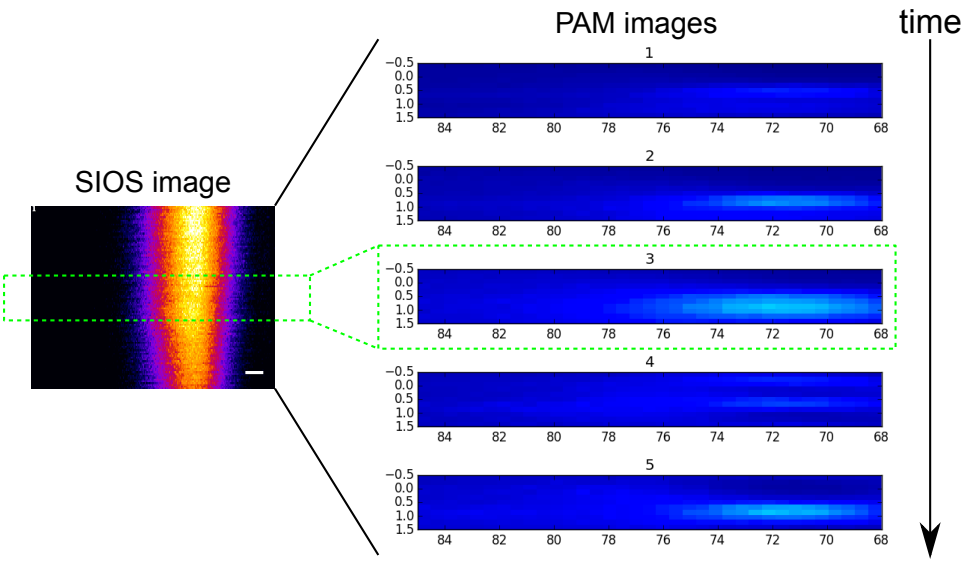

Figure 9.2: Pairing of SIOS and PAM images. Due to raster scanning, imaging of the central region, shown in green, occurs at the same time as the acquisition of the third PAM image, which is selected for pairing with the SIOS image.

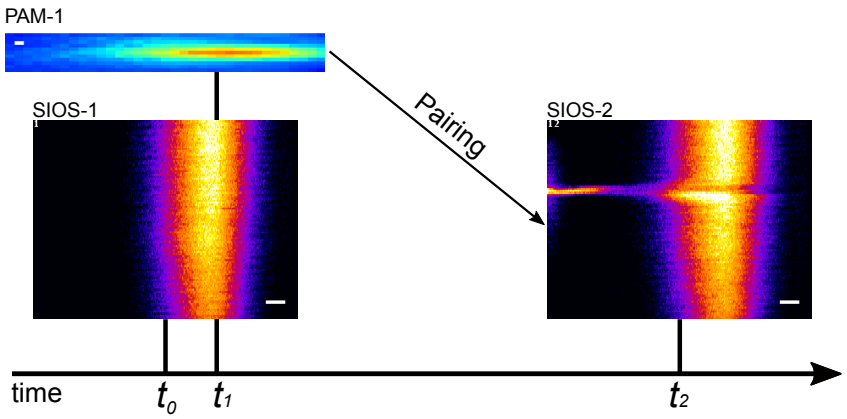

Figure 9.3: Capture of cause-and-effect relationship in SIOS and PAM images. At t_0 the central region of SIOS-1 was raster scanned. Immediately after, a cavitation event occurs at time t_1 and is captured by PAM-1. The deformation produced by the cavitation event is however not visible to SIOS until t_2, when the central region of SIOS-2 is scanned. To capture the fact that the cavitation event at time t_1 caused the deformation seen at time t_2, it is necessary to pair PAM-1 with SIOS-2 instead of SIOS-1.

deformations are expected (Figure 9.2). Furthermore, in order to guarantee capture of cause-and-effect, PAM images were offset by one before pairing (Figure 9.3).

9.3 Results

9.3.1 End-Point Widefield Microscopy Images

Figure 9.4 shows the deformations produced by SonoVue, nanodroplets and nanocups. Deformations due to SonoVue and nanocups were as expected, while nanodroplets failed to produce the same level of deformation previously seen in Chapter 8. The latter was attributed to the destruction of nanodroplets via spontaneous vaporisation whilst in storage.

Of the three cavitation agents, only nanocups produced a deformation greater than 1000 µm, and as such it will be the focus of analysis.

9.3.2 Real-Time SIOS and PAM Images

Paired SIOS and PAM images acquired during ultrasound exposure of nanocups are shown in Figure 9.5 (full data set in Appendix). The PAM images captured the distribution of cavitation activity and its strength, while the SIOS images monitored the effects of cavitation on the flow channel. During the ultrasound exposure of nanocups, the location and magnitude of cavitation activity corresponded with the deformation of the flow channel. Specifically, the amplitude of cavitation noise increased sharply with deformation formation, and at the same time, the spatial distribution of acoustic emissions extended in the direction of ultrasound propagation. The latter is indicative of cavitation activity within the deformation, and by extension, the presence of cavitation agents within the deformation.

9.3.3 Cavitation Activity and Deformations

During ultrasound exposure of nanocups, the level of cavitation activity, measured by taking the area integral of a PAM image, was found to increase with S_C, which meas-

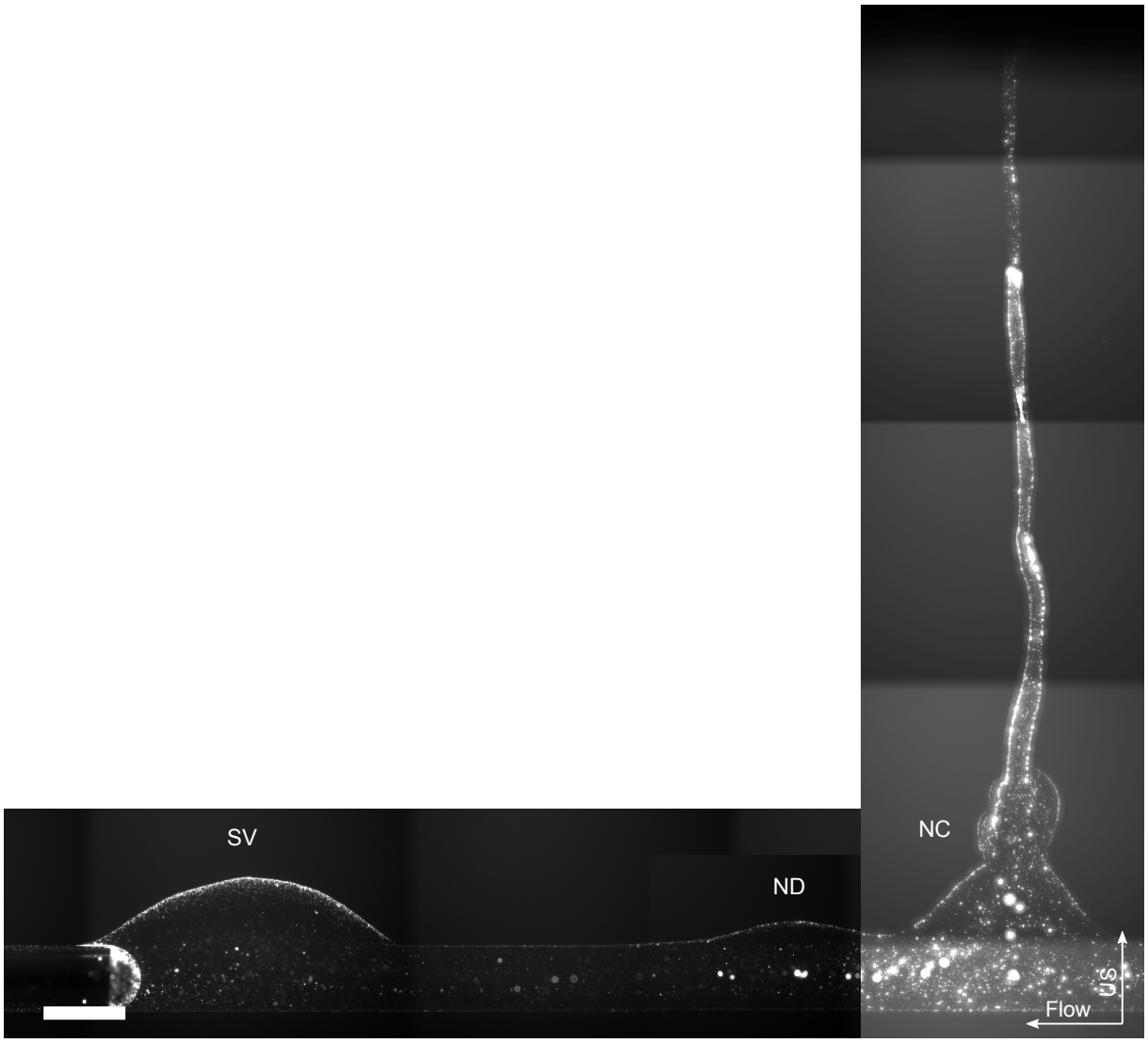

Figure 9.4: Widefield fluorescence microscopy of deformation produced by SonoVue (**SV**), nanodroplets (**ND**) and nanocups (**NC**). SonoVue and nanodroplets, at a concentration of $1 \times 10^7\,\mathrm{mL}^{-1}$, were exposed to a peak-negative pressure of 1.65 MPa; nanocups, at a concentration of $1 \times 10^8\,\mathrm{mL}^{-1}$ was exposed to a peak-negative pressure of 1.90 MPa. Left-to-right, deformation extends in the direction of ultrasound are 417 µm, 155 µm and 5382 µm. The image is a composite of three images each focused one a different exposure site. Scale bar is 500 µm.

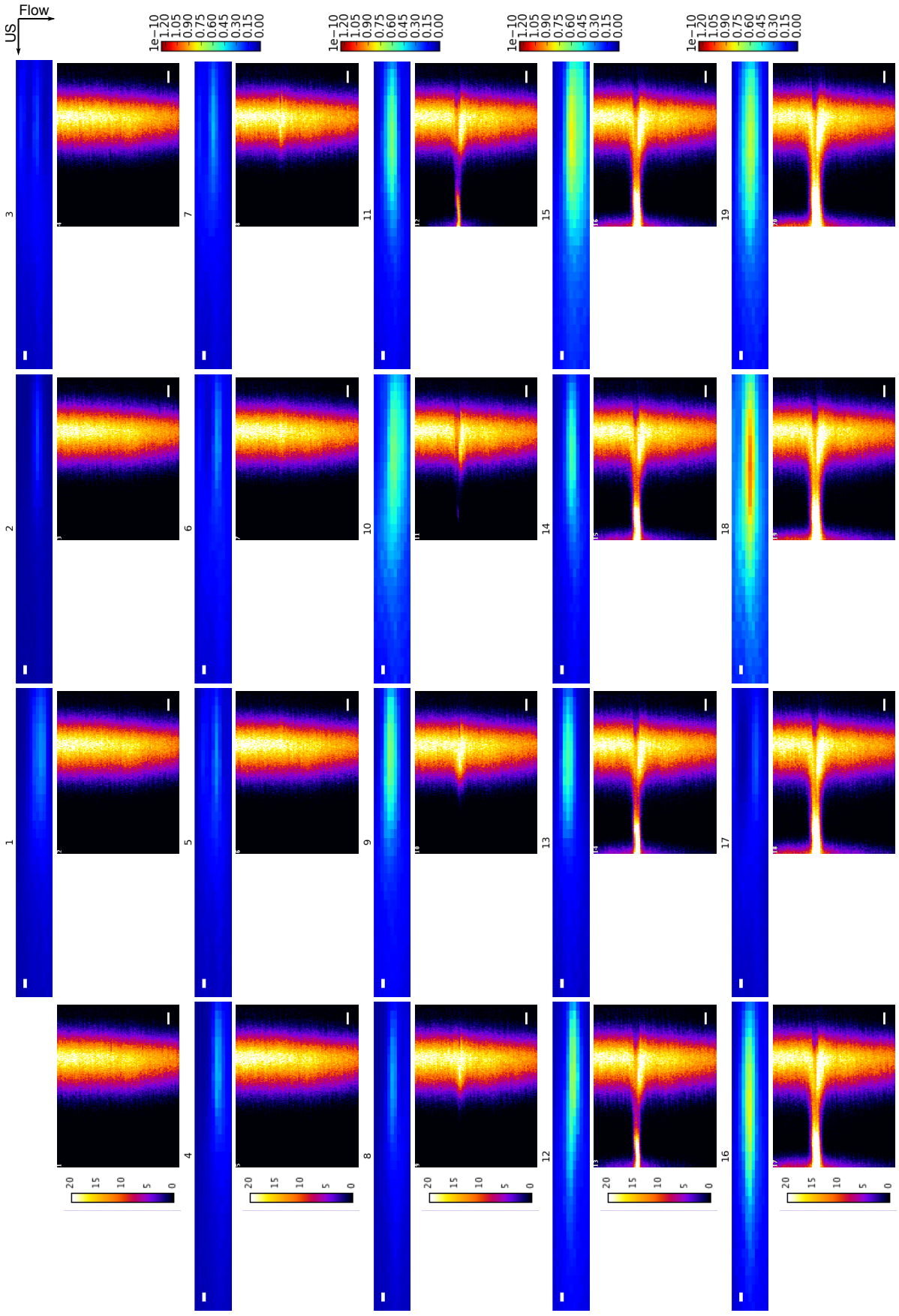

Figure 9.5: Paired SIOS and PAM images acquired during ultrasound exposure of nanocups. PAM images were transformed to match the orientation of SIOS images, then registered to SIOS images in the direction of ultrasound by aligning the location of maximum acoustic emissions to the location of maximum fluorescence. The fluorescence signal at the left edge of the latter SIOS images is caused by the fluorescent liquid leaking into the agarose-mylar interface due to the extent of the deformation. Scale bars are 500 µm.

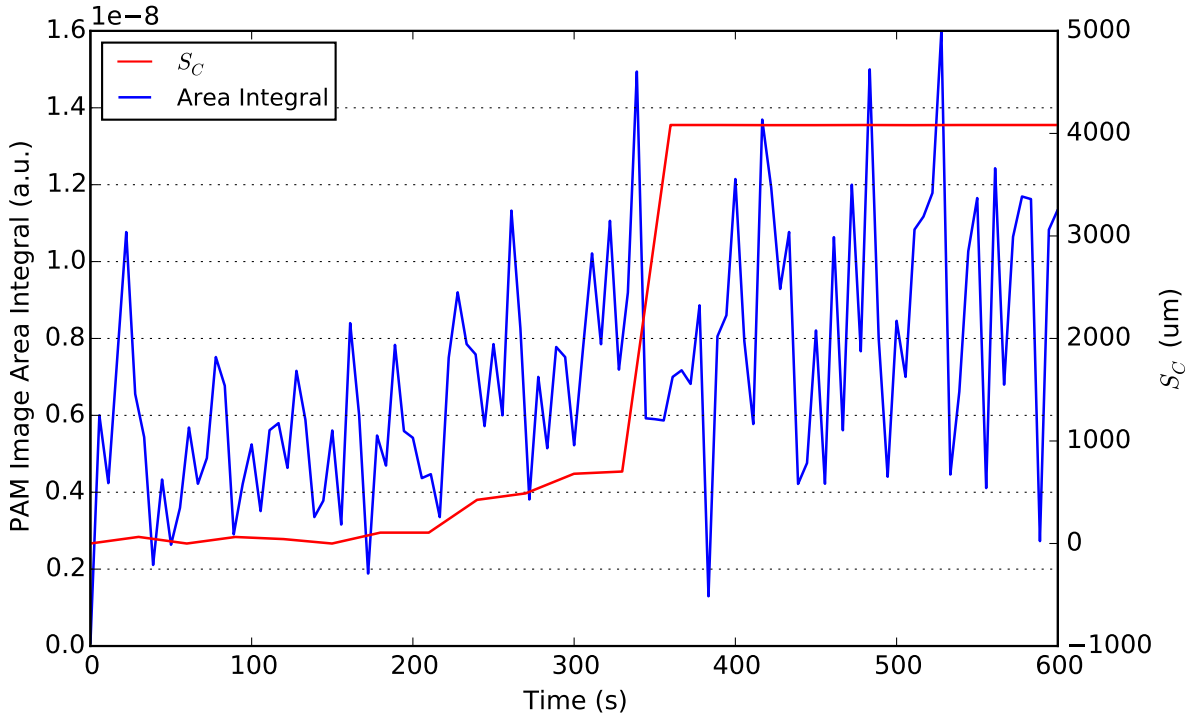

Figure 9.6: Cavitation activity vs deformation size during ultrasound exposure of nanocups. Cavitation activity is indirectly measured by the area integrals of PAM images while S_C measures the size of deformation extent in the direction of ultrasound.

Cavitation Agent	Total Detected Cavitation Activity	Deformation Extent (µm)
SonoVue	3.73×10^{-8}	417
nanodroplets	4.24×10^{-9}	155
nanocups	7.15×10^{-9}	5382

Table 9.1: Total detected cavitation activity and deformation extent. Cavitation activity was measured by summing the area integral of all PAM images. Deformation extent was measured using widefield microscopy (data in Appendix).

ures deformation extent in the direction of ultrasound propagation (Figure 9.6). This relationship was previously observed in Chapter 7, where detected cavitation power increased with deformation size in PLGA nanoparticle loaded DSEPC microbubble experiments. No similar increase was found for SonoVue or nanodroplets (data in Appendix).

Consistent with the previous findings in Chapter 8, total detected cavitation activity, measured by summing the area integrals of PAM images and adjusting for sampling rate, did not correlate with deformation size (Table 9.1).

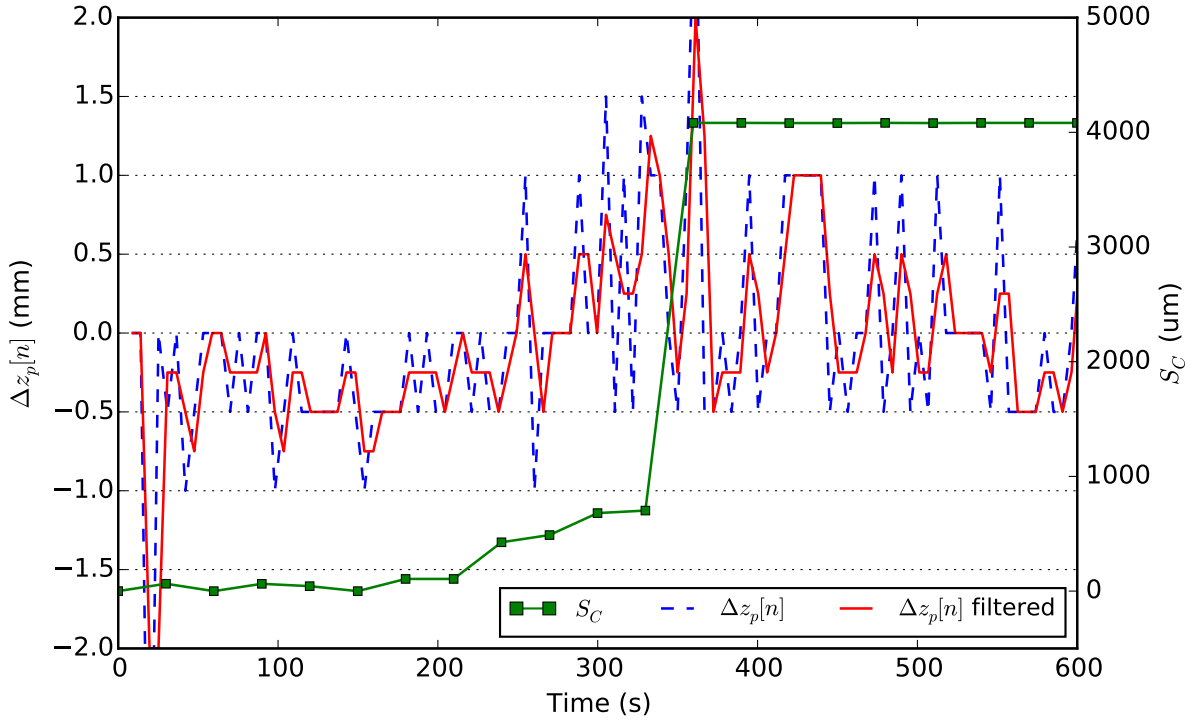

Figure 9.7: Displacement of the peak cavitation location ($\Delta z_p[n]$) and channel-centre fluorescence front displacement (S_C) during ultrasound exposure of nanocups. Filtering was done using an exponential filter with $\alpha = 0.5$. For clarity, the negative and positive outliers in have been clipped. An unclipped version of the plot can be found in the Appendix. Additionally, due to the deformation extending beyond the field-of-view of SIOS, S_C "saturates" at approximately 4200 µm.

9.3.4 Cavitation Peak Displacement and Deformations

For each PAM image obtained during the ultrasound exposure of SonoVue, nanodroplets and nanocups, the Z coordinate of peak cavitation noise was recorded ($z_P[n]$, $n = 0, 1, 2, \ldots$) and the displacement of the cavitation peak was calculated: $\Delta z_p[n] = z_p[n] - z_p[0]$. Due to the orientation of PAM images, higher $z_p[n]$ values are in the direction of ultrasound propagation. Therefore, a positive $\Delta z_p[n]$ indicates that the location of peak cavitation activity is shifting in the direction of ultrasound propagation.

When $\Delta z_p[n]$ is plotted against fluorescence front displacement, S_C, a correspondence exists in the measurements obtained during ultrasound exposure of nanocups, where the values of $\Delta z_p[n]$ increases with S_C (Figure 9.7). No similar correspondence was found for SonoVue or nanodroplets (data in Appendix).

9.3.5 Evaluation of PAM

Measurements from coaxial PAM, namely cavitation activity and cavitation peak displacement, indicate that PAM is able to predict the onset of deformation formation, provided that the deformations are sufficiently large along the acoustic axis. Practically, this ability enables more precise control over delivered cavitation effects, allowing ultrasound exposure to be discontinued when the onset of rapid deformation formation is detected. The same ability in a clinical setting enables more consistent enhancement of drug delivery and also provides a means of detecting when cavitation effects exceed safety limits.

While PAM detected deformation formation during ultrasound exposure of nanocups, it failed to do so during ultrasound exposures of SonoVue and nanodroplets. A possible explanation is that the axial resolution of PAM, approximately 5.9 mm, is much larger than the deformations produced by SonoVue or nanodroplets (0.417 mm and 0.155 mm respectively).

Compared with single-element coaxial PCD, PAM is a superior cavitation monitoring technique. However, it is also unable to predict the extent of deformations. This shortcoming could be attributed to the existence of mechanisms that play a role in deformation formation but are not cavitation dependent or have highly non-linear relationships with cavitation activity, e.g. acoustic streaming.

Overall, PAM has the potential to meet the need for more sophisticated cavitation monitoring techniques identified in Chapter 8.

9.4 Summary

The primary goal of this chapter was to investigate PAM was an alternative means of monitoring cavitation activity and effects. Results obtained during the ultrasound exposure of nanocups demonstrated that PAM measurements could be used to predict deformation formation. The results also suggest that cavitation does occur within deformations, i.e. cavitation agents are present within deformations. On the basis of these findings, PAM has the potential to meet the previously identified need for more

sophisticated cavitation monitoring techniques.

The results presented in this chapter also demonstrated the utility of SIOS in evaluating cavitation monitoring techniques, and represent the first instance in which real-time spatiotemporal measurements of cavitation activity and effects have been achieved in a flow channel model.

Appendix

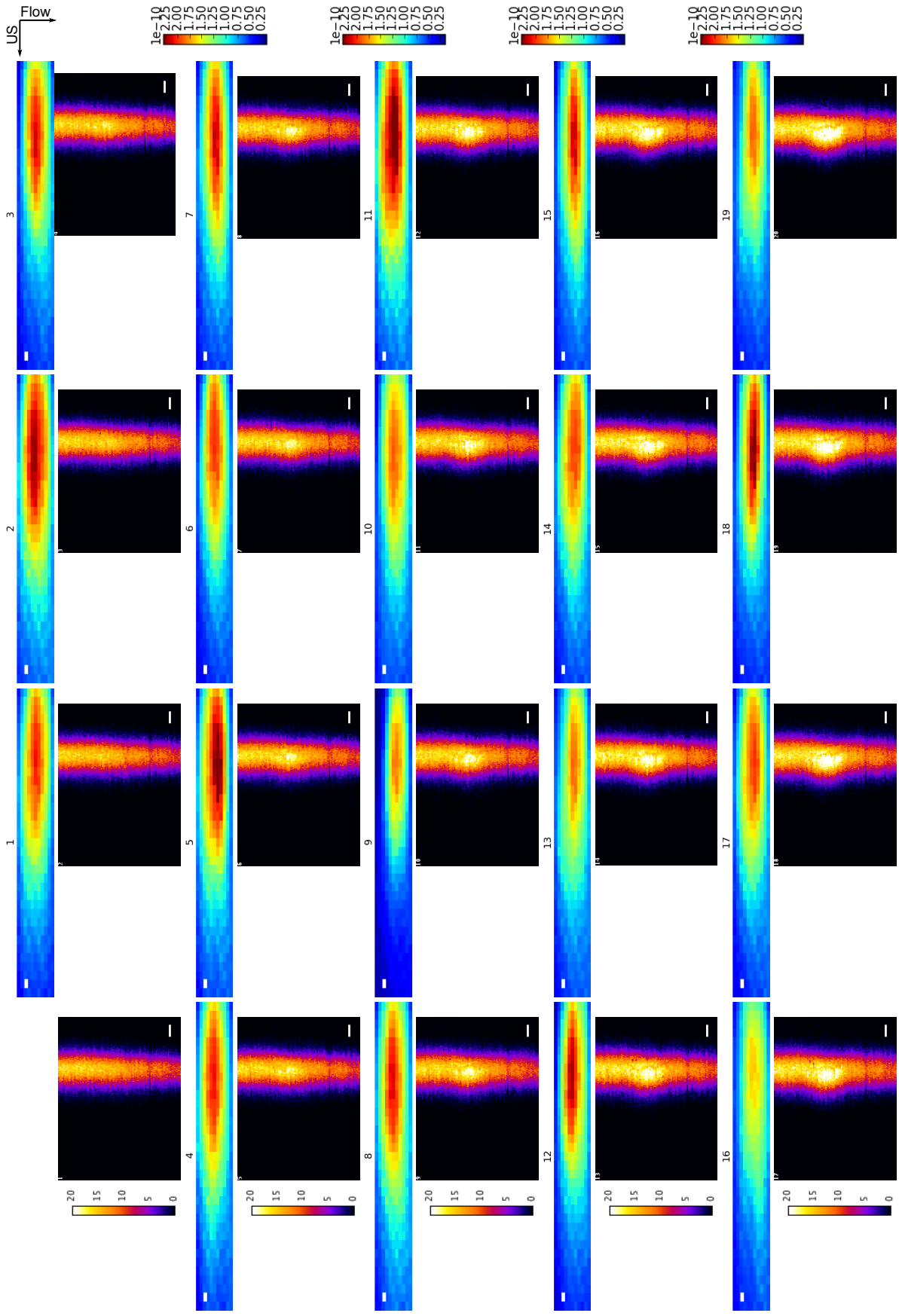

Figure 9.8: Paired SIOS and PAM images acquired during ultrasound exposure of SonoVue. PAM images were transformed to match the orientation of SIOS images, then registered to SIOS images in the direction of ultrasound by aligning the location of maximum acoustic emissions to the location of maximum fluorescence. Scale bars are 500 µm.

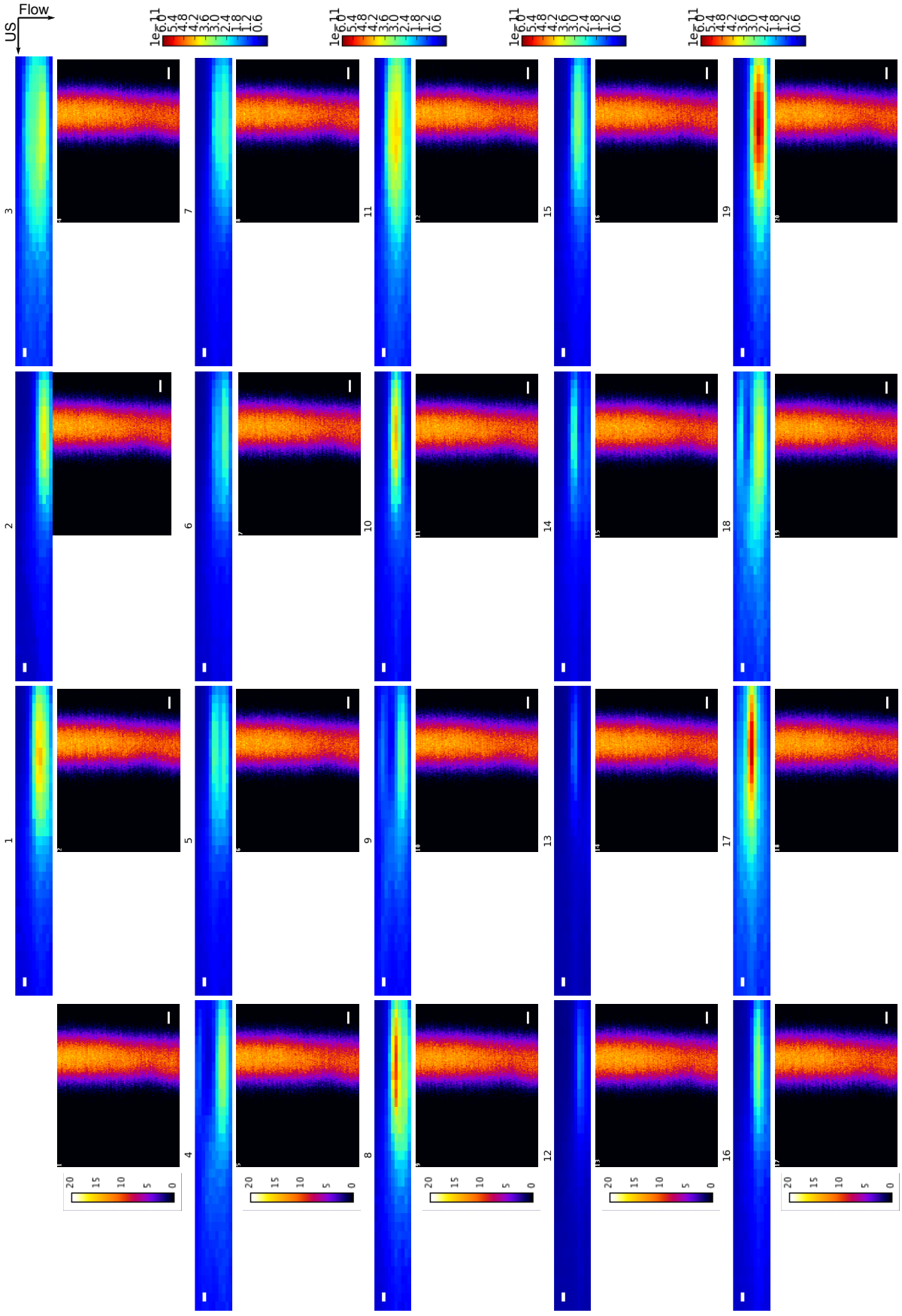

Figure 9.9: Paired SIOS and PAM images acquired during ultrasound exposure of nanodroplets. PAM images were transformed to match the orientation of SIOS images, then registered to SIOS images in the direction of ultrasound by aligning the location of maximum acoustic emissions to the location of maximum fluorescence. Scale bars are 500 µm.

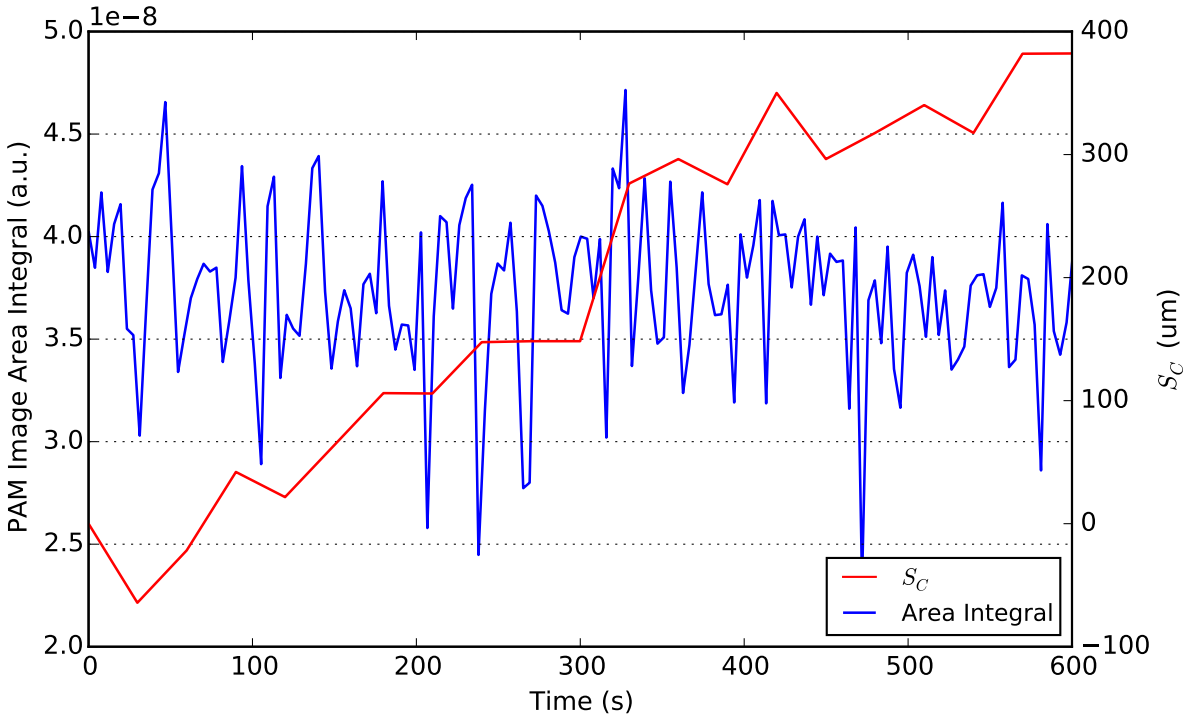

(a)

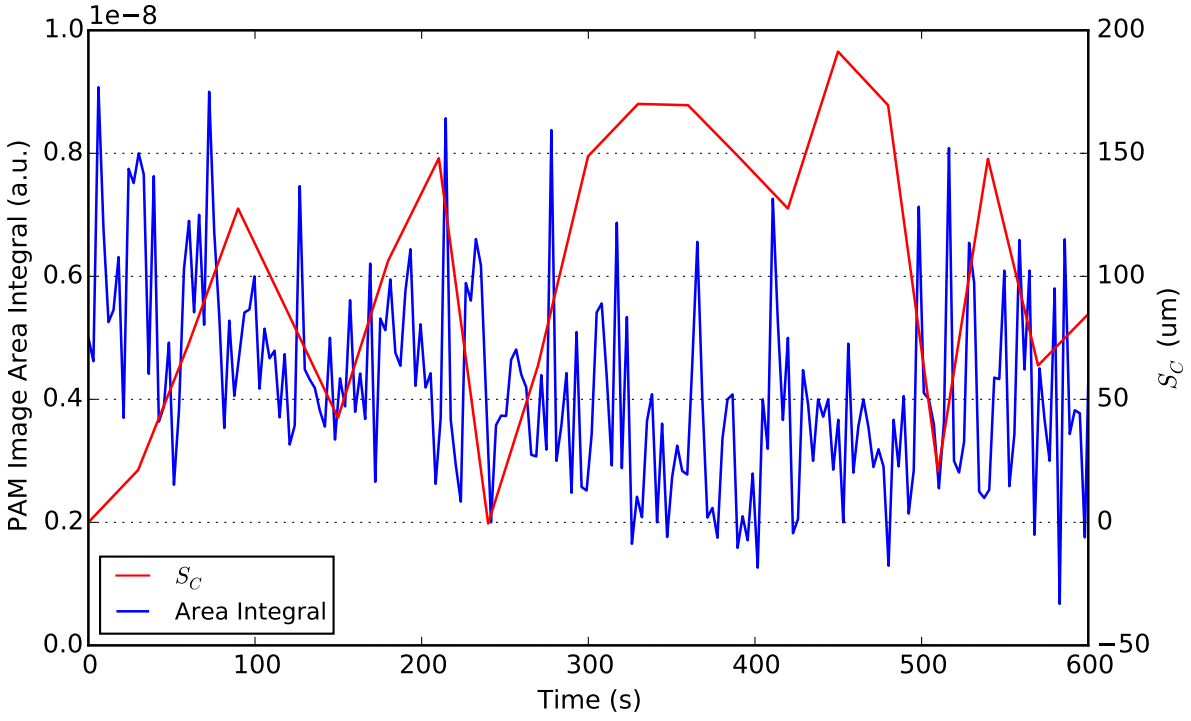

(b)

Figure 9.10: Cavitation activity vs deformation size during ultrasound exposure of **(a)** SonoVue and **(b)** nanodroplets. Cavitation activity was indirectly measured by the area integrals of PAM images, while S_C measured the size of deformation extents in the direction of ultrasound.

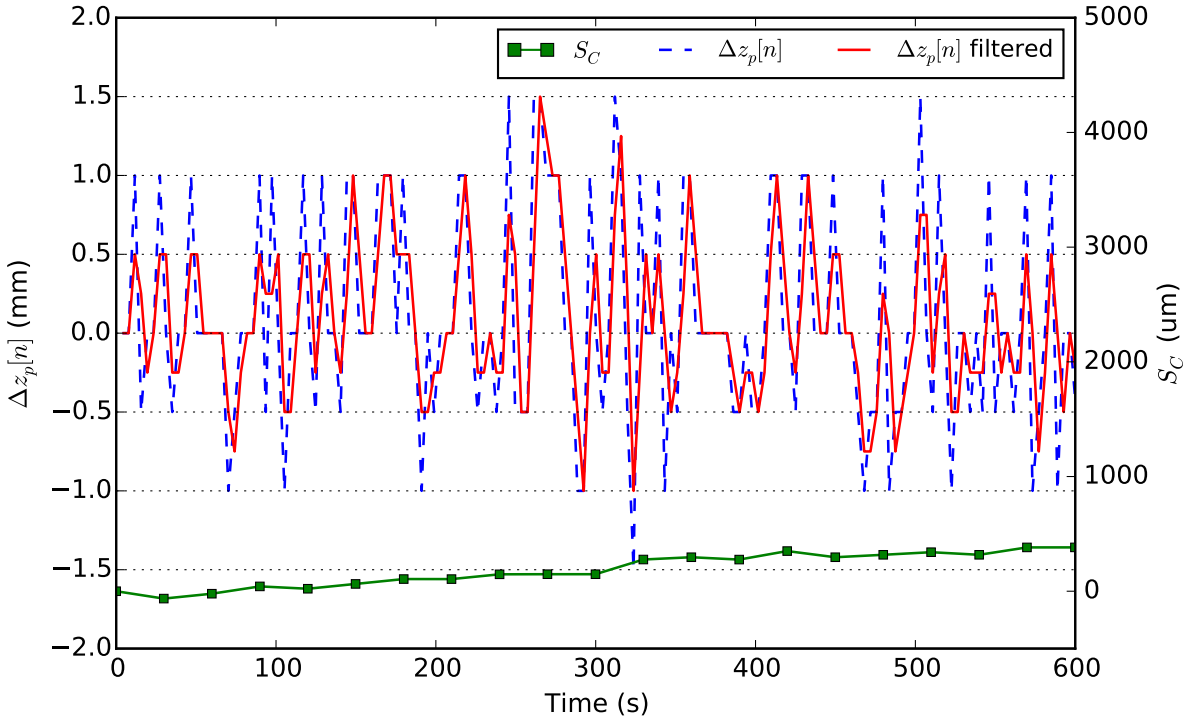

(a)

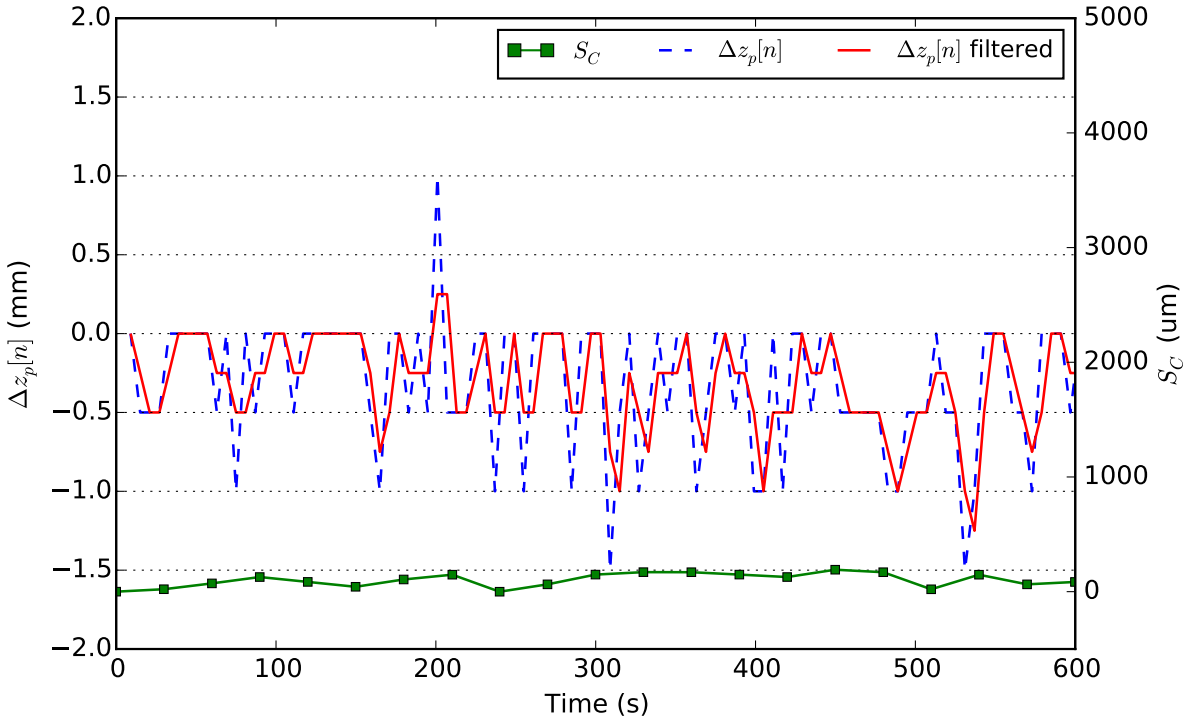

(b)

Figure 9.11: Change in cavitation peak location ($\Delta z_p[n]$) and channel-centre fluorescence front displacement (S_C) during ultrasound exposure of **(a)** SonoVue and **(b)** nanodroplets. Filtering was done using an exponential filter with $\alpha = 0.5$.

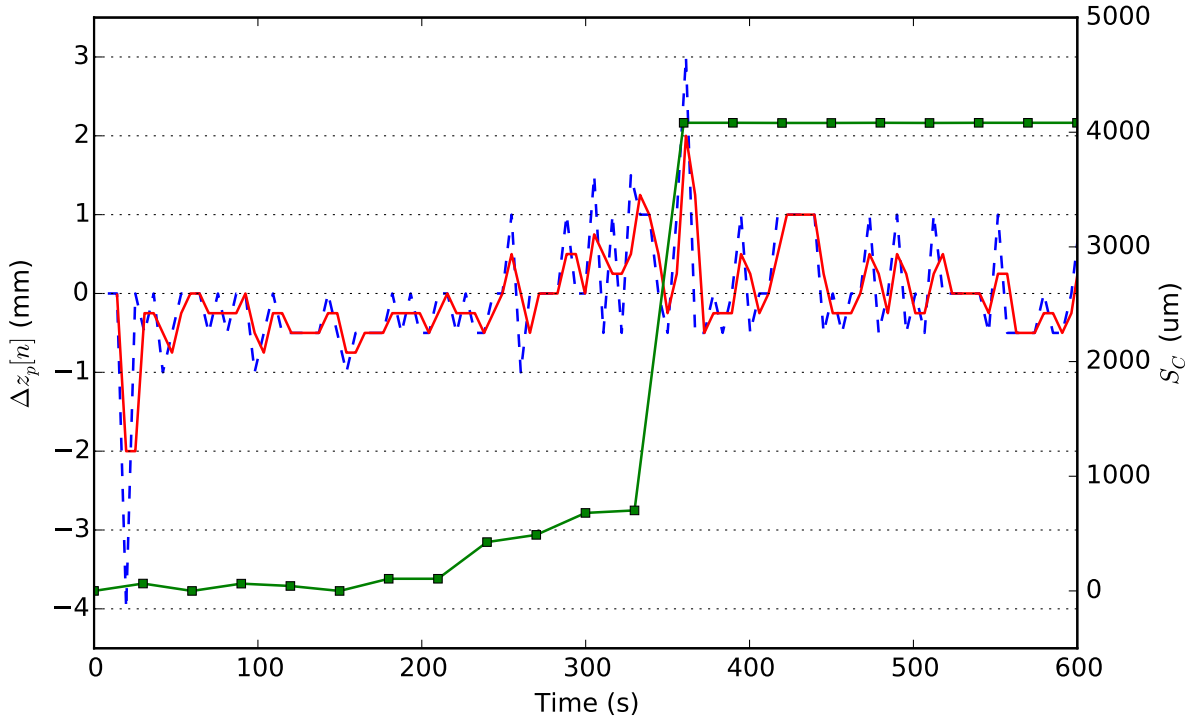

Figure 9.12: Unclipped version of Figure 9.7

References

[1] Carl R Jensen, Robert W Ritchie, Miklós Gyöngy, James RT Collin, Tom Leslie, and Constantin-C Coussios. Spatiotemporal monitoring of high-intensity focused ultrasound therapy with passive acoustic mapping. *Radiology*, 262(1):252–261, 2012.

[2] Miklós Gyöngy and Constantin-C Coussios. Passive spatial mapping of inertial cavitation during hifu exposure. *IEEE Transactions on Biomedical Engineering*, 57(1):48–56, 2010.

[3] Erasmia Lyka, Christian Coviello, Richard Kozick, and Constantin-C Coussios. Sum-of-harmonics method for improved narrowband and broadband signal quantification during passive monitoring of ultrasound therapies. *The Journal of the Acoustical Society of America*, 140(1):741–754, 2016.

[4] Christian Coviello, Richard Kozick, James Choi, Miklós Gyöngy, Carl Jensen, Penny Probert Smith, and Constantin-C Coussios. Passive acoustic mapping utilizing optimal beamforming in ultrasound therapy monitoring. *The Journal of the Acoustical Society of America*, 137(5):2573–2585, 2015.

Chapter 10

Conclusions

The goal of the present work was to produce an instrument that is capable of monitoring, in real-time and *in-situ*, the effects of ultrasound and cavitation on the distribution and penetration of drugs within a sample during ultrasound exposure. Such an instrument was realised in the form of a long working distance confocal laser scanning microscope. To determine the utility of the instrument, also referred to as SIOS, a number of experiments were performed.

Firstly, the pharmacokinetics of drug-eluting beads used for chemical embolisation was characterised with and without ultrasound exposure. The results from the instrument were found to be more physiologically relevant than those previously reported, and provided verification of SIOS' ability to monitor drug distribution *in-situ* in flow channel models. Additionally, no effects due to ultrasound were detected.

The instrument was then used to study the effects of nanoparticle loading on microbubble cavitation dynamics. It was found that PLGA nanoparticle loaded microbubbles produced significantly greater deformations than either unloaded microbubbles or PLGA nanoparticles. The real-time images provided by the instrument gave unique insights into the formation of these deformations, and revealed a lack of correspondence between single-element passive cavitation detection (PCD) measurements and deformation formation.

Following the previous investigation, SIOS was used to catalogue the cavitation effects produced by cavitation agents of different sizes, compositions and methods of action. The catalogue identified two cavitation agents, PLGA nanoparticle loaded

DSEPC microbubbles and nanodroplets, as particularly promising with regard to increasing drug penetration in cancerous tumours. Using the images provided by SIOS, it was determined that the deformations produced by these two cavitation agents formed via a two-stage process: a stage of slow deformation formation followed by an abrupt transition into a stage of rapid growth. This two-stage process is indicative of positive feedback interactions between cavitation effects and changes they induce in the surrounding environment, with safety implications for the *in-vivo* application of ultrasound and cavitation mediated drug delivery. Additionally, the maximum rate of deformation growth was found to correlate with the final deformation extent. Finally, the previous finding of a lack of general correspondence between single-element coaxial PCD measurements and deformation formation was strengthened, identifying a need for more sophisticated cavitation monitoring techniques.

Finally, SIOS was used to evaluate passive acoustic mapping (PAM), with the results indicating that PAM measurements could be used to predict the onset of rapid deformation growth, thus demonstrating PAM's potential in meeting the previously identified need for more sophisticated cavitation monitoring techniques.

Over the course of these experiments, the developed instrument's capability and utility was demonstrated, with the instrument suited not only to the study of ultrasound and cavitation effects on drug distribution and penetration, but also to the study and evaluation of cavitation monitoring techniques.

10.1 Summary of Contributions

- The design, development, and characterisation of a new instrument capable of monitoring in real-time and *in-situ* the effect of ultrasound and cavitation mediated drug delivery.
  - Development of a complete software stack for instrument control, data acquisition, and data processing.
  - Development of original electronics for signal acquisition and instrument control.
- New and more physiologically relevant data on the pharmacokinetics of drug-eluting beads used for chemical embolisation.
- Identified and documented a new phenomenon related to nanoparticle coating of microbubbles.
- Catalogue of cavitation effects from cavitation agents of different sizes, compositions and methods of action.
  - New data on the development of cavitation effects.
  - Identified a lack of correlation between single-element passive cavitation detection measurements and the magnitude of induced effects.
  - Identified a need for more sophisticated monitoring techniques
- Demonstrated the capabilities of passive acoustic mapping as a cavitation monitoring technique.

Chapter 11

Proposed Future Works

11.1 Instrument Development

In its current state, the instrument has the hardware required for 3D imaging, lacking only software support. This should be a relatively simple matter of automating the acquisition of XZ images at different Y coordinates, or YZ images at different X coordinates.

Optically, the placement of the dichroic mirror is sub-optimal as the light paths through it are not collimated. This can be resolved by collimating the laser's output prior to the dichroic mirror (Figure 11.1). Furthermore, the alignment of the fibre output is currently only possible along the X, Y and Z axes, while proper alignment requires tilt and rotation, an issue that can be solved with a more sophisticated fibre mount. These modifications, however, will not necessarily result in notable improvements if aberrations due to refractive index mismatch and agarose scattering are not well controlled.

The issue of refractive-index mismatch could be resolved if the instrument was mounted vertically so the optical axis is perpendicular to the water surface. This would allow the use of a water-immersion lens but would also require replacing or modifying the existing scan head as the Z axis can no longer be the fast axis of the system.

Lastly, alternatives to agarose that offer better optical properties while remaining ultrasound compatible, e.g. polyacrylamide, should be investigated as agarose scattering has significant adverse effects on the axial resolution.

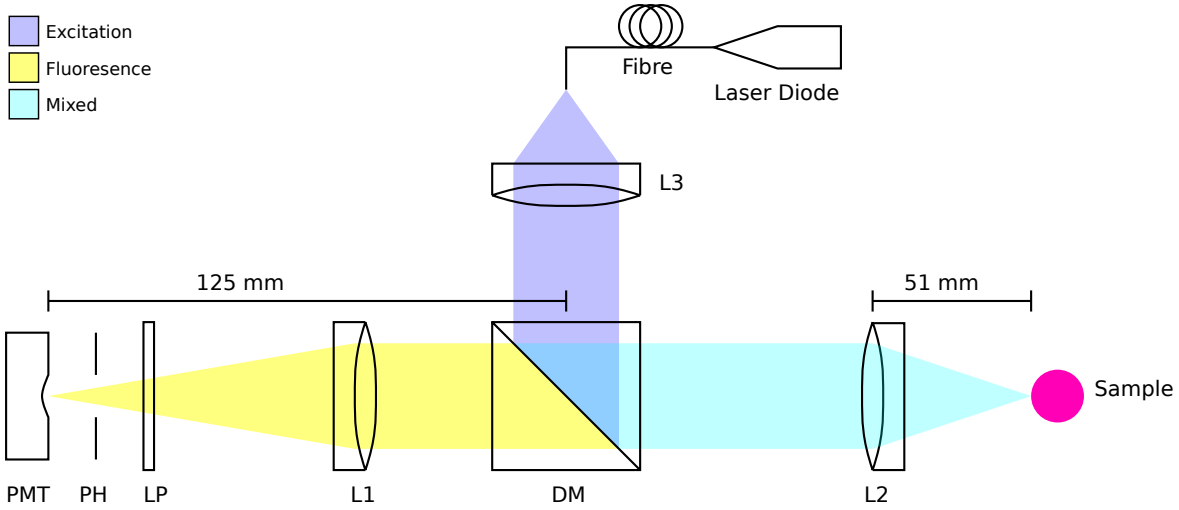

Figure 11.1: Proposed changes to the optical setup of SIOS. L3 has been added to collimate the laser diode output, allowing all light incident on the dichroic mirror to be collimated. **L1–L3**: lenses; **DM**: dichroic mirror; **LP**: long-pass filter; **PH**: pinhole; **PMT**: photomultiplier tube.

11.2 Pharmacokinetics of Drug-Eluting Beads

The agarose-alginate flow channel model in combination with SIOS is an attractive platform for *in-vitro* pharmacokinetic studies of drug-eluting beads and similar constructs prior to *in-vivo* trials. However, for clinical relevance, the platform's lower doxorubicin detection limit should be 10 µM or less, and it is currently 20 µM. Improvements can be made by implementing better light shielding to reduce the measurement noise floor, lowering the concentration of agarose to reduce optical scattering and attenuation, and increasing the number of exposures to increase instrument sensitivity.

The high variability in the presented results can obscure ultrasound effects if they are sufficiently small, leading to the present finding that ultrasound has no detectable effect on doxorubicin release or penetration. With more experiments and improved protocols, these small effects, if present, could be detected. However, the clinical relevance of these effects should be considered before conducting further experiments.

11.3 Effect of Nanoparticle Loading On Microbubbles

The proposed theory, that loading of PLGA nanoparticles increases the dynamic stability of DSEPC microbubbles, remains to be tested though is not without precedent.

In the literature microbubbles with gold nanoparticles incorporated into the shell were found to be significantly more stable in storage, with the effect attributed to reduced gas diffusion and interfacial tension [1].

The effect of loading nanoparticles with densities higher than PLGA should be investigated, as some clinical chemotherapy drugs, such as cisplatin, are metal based and have higher densities. The effect of high density nanoparticles on the cavitation behaviour of bubbles will inform on the safety and efficacy of using microbubbles to deliver such agents.

Lastly, if the rate of TRITC-Dextran diffusion can be slowed, the deformation detection limit can be improved. This may be possible by mixing additional compounds into the agarose hydrogel as was done in Chapter 6, where alginate was added to slow the diffusion of doxorubicin.

11.4 Cavitation Agent Catalogue

The causative mechanism behind the short tunnel-type deformations remains an open question, and further investigation is warranted in order to understand the circumstances in which deformation of the extent observed can be induced by ultrasound in the absence of cavitation noise.

The parameters of the catalogue should be expanded to better mimic clinical needs. For example, the ultrasound exposure parameters can be altered to reflect those available clinically, the agarose percentage can be varied to emulate different tissues types, and de-ionised water can be replaced with phosphate-buffered saline or other liquid that mimics the chemical and physical properties of human plasma.

Finally, a need for more sophisticated techniques for assessing cavitation effect was identified. Possibilities include spatially-discriminating cavitation detection techniques, e.g. passive-acoustic mapping, or cavitation agents engineered to exhibit a more predictable relationship between cavitation activity and cavitation effect.

11.5 Concurrent Monitoring With PAM

The findings regarding passive acoustic mapping (PAM) presented in Chapter 9 should be strengthened through replication, with future experiments limited to one flow channel model per cavitation agent and without the compromise made due to resource constraints. Additionally, PAM may achieve higher spatial resolution if the ultrasound probe is placed perpendicular to the direction of ultrasound propagation, potentially enhancing its ability to detect deformation formation.

11.6 Alternative Imaging Modalities

Based on the experience and knowledge gained from the present work, a new instrument using an alternative imaging modality could be built.

11.6.1 Widefield Microscopy

Widefield microscopy was previously rejected due to its poor optical sectioning capabilities. However, for the purpose of observing deformations that reliably form in the direction of ultrasound propagation, this may not be an issue. If the optical axis is perpendicular to both the ultrasound axis and the flow channel, then optical sectioning is implicitly provided by the confinement of fluorescent fluids within flow channels and deformations. Such a setup will have a faster imaging speed as well as a higher resolution when tracking deformation formation, but will also be ill-suited for measuring drug distribution and concentration.

11.6.2 Selective Plane Illumination Microscopy

Building on the experiences and expertise gained during the present work, it may be possible to implement selective plane illumination microscopy (SPIM) in an ultrasound compatible manner. A mockup of such system is shown in Figure 11.2. Anticipated challenges include the design and construction of the sample chamber, the water tank, and a means of tiling light-sheets to achieve a wide field-of-view. These challenges are

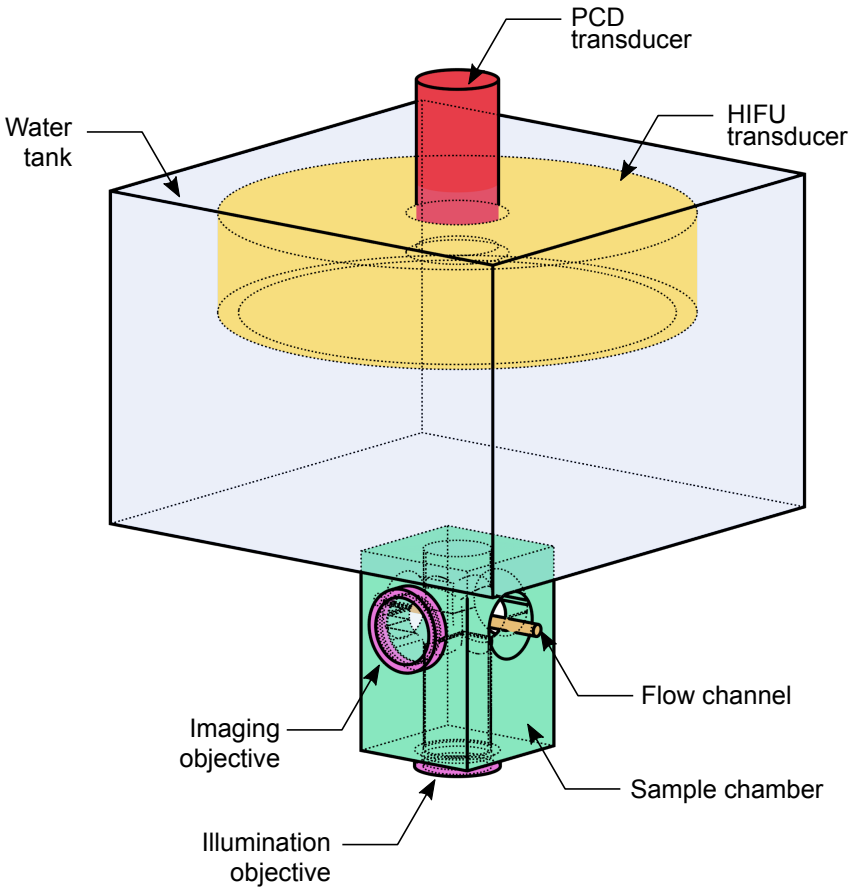

Figure 11.2: Mockup of an ultrasound compatible SPIM system. **HIFU**: high-intensity focused-ultrasound. **PCD**: passive cavitation detection.

expected to be difficult, they should also be surmountable.

References

[1] Graciela Mohamedi, Mehrdad Azmin, Isabel Pastoriza-Santos, Victoria Huang, Jorge Pérez-Juste, Luis M Liz-Marzán, Mohan Edirisinghe, and Eleanor Stride. Effects of gold nanoparticles on the stability of microbubbles. *Langmuir*, 28(39):13808–13815, 2012.